

Piezotronic Bicrystals and Hexagonal Nano-Platelets: A TEM Study on Structure and Chemistry of Functionalized Zinc Oxide

Vom Fachbereich Material- und Geowissenschaften
der Technischen Universität Darmstadt
zur Erlangung des akademischen Grades Doctor rerum naturalium (Dr. rer. nat.)
genehmigte Dissertation von
Maximilian Trapp
geboren in Kaiserslautern

Erstgutachter: Prof. Dr. Hans-Joachim Kleebe
Zweitgutachter: Prof. Dr. Jürgen Rödel

D17 - Darmstadt 2023



TECHNISCHE
UNIVERSITÄT
DARMSTADT

Piezotronic Bicrystals and Hexagonal Nano-Platelets: A TEM Study on Structure and Chemistry of Functionalized Zinc Oxide

Genehmigte Dissertation von Maximilian Trapp geboren in Kaiserslautern

1. Gutachten: Prof. Dr. Hans-Joachim Kleebe
2. Gutachten: Prof. Dr. Jürgen Rödel

Tag der Einreichung: 28.03.2023

Tag der Prüfung: 19.06.2023

Technische Universität Darmstadt

Fachbereich Material- und Geowissenschaften

März 2023 – Darmstadt – D 17

Bitte zitieren Sie dieses Dokument als:

URN: urn:nbn:de:tuda-tuprints-241930

URI: <https://tuprints.ulb.tu-darmstadt.de/id/eprint/24193>

Jahr der Veröffentlichung auf TUprints: 2023

Dieses Dokument wird bereitgestellt von tuprints,

E-Publishing-Service der TU Darmstadt

<http://tuprints.ulb.tu-darmstadt.de>

tuprints@ulb.tu-darmstadt.de

Die Veröffentlichung steht unter folgender Creative Commons Lizenz:

Namensnennung – Weitergabe unter gleichen Bedingungen 4.0 International

<https://creativecommons.org/licenses/by-sa/4.0/>

This work is licensed under a Creative Commons License:

Attribution – ShareAlike 4.0 International

<https://creativecommons.org/licenses/by-sa/4.0/>

Erklärung gemäß § 8 Abs. 1 lit. c, d und § 9 Abs. 1, 2 der Promotionsordnung der TU Darmstadt

Hiermit versichere ich, Maximilian Trapp, die vorliegende Dissertation ohne Hilfe Dritter und nur mit den angegebenen Quellen und Hilfsmitteln angefertigt zu haben. Alle Stellen, die Quellen entnommen wurden, habe ich eindeutig als solche kenntlich gemacht. Ich versichere, dass zu einem vorherigen Zeitpunkt noch keine Promotion versucht wurde und dass die vorliegende Dissertation in gleicher oder ähnlicher Form noch keiner Prüfungsbehörde vorgelegen hat. Ich versichere, dass die schriftlichen und elektronischen Kopien der eingereichten Dissertation identisch sind.

Ort, Datum:

Unterschrift:

Darmstadt, 28.03.2023

Maximilian Trapp



Contents

List of Abbreviations	VIII
List of Symbols	X
Preface	XIII
Kurzfassung	XV
Abstract	XVII
1. ZnO – Background & Fundamentals	1
1.1. Mineralogy, structure and general properties	1
1.1.1. Remarks on Miller and Bravais indices	3
1.2. Piezoelectric properties	5
1.3. Semiconducting properties	7
1.4. Varistor effect and varistor ceramics.....	10
1.5. Doping of varistor ceramics.....	14
1.6. Piezotronics and piezotronic modulation of potential barriers	16
1.7. ZnO bicrystals and (0001) inversion boundaries	18
1.8. Nanocrystals	21
2. Aims, Motivation and Thesis Concept	23
3. Experimental Methods	25
3.1. Synthesis	25
3.1.1. B/DB bicrystals	25
3.1.2. EST bicrystals.....	27
3.1.3. Hexagonal platelets & rod-shaped twins	28
3.2. TEM and SEM sample preparation.....	29
3.2.1. Bicrystals	29
3.2.2. Hexagonal platelets & rod-shaped twins	30
3.3. Analytical methods.....	30

3.3.1.	SEM	30
3.3.2.	TEM	32
3.3.3.	CEP-method.....	43
3.3.4.	I-V characterization	45
4.	ZnO Bicrystals – Results & Discussion	47
4.1.	Undoped DB bicrystals	47
4.1.1.	Undoped DB bicrystal in O O orientation (B-I)	47
4.1.2.	Undoped DB bicrystal in Zn Zn orientation (B-II)	48
4.1.3.	Undoped DB bicrystal in Zn O orientation (B-III).....	51
4.1.4.	I-V measurements.....	54
4.1.5.	Discussion and Summary	54
4.2.	Doped DB bicrystals	58
4.2.1.	Doped DB bicrystal in O O orientation I (DB-I).....	58
4.2.2.	Doped DB bicrystal in O O orientation II (DB-II).....	61
4.2.3.	Doped DB bicrystal in O O orientation III (DB-III).....	63
4.2.4.	I-V measurements.....	64
4.2.5.	Discussion and Summary	66
4.3.	EST bicrystal.....	70
4.3.1.	EST bicrystal in O O orientation.....	70
4.3.2.	I-V measurements.....	77
4.3.3.	Discussion and Summary	78
4.4.	Doped DB bicrystals with reduced coherency.....	85
4.4.1.	Doped DB bicrystal in a c orientation (DB-a c)	87
4.4.2.	Doped DB bicrystal in Zn Zn orientation with 26° tilt (DB-26).....	90
4.4.3.	I-V measurements.....	93
4.4.4.	Discussion and Summary	95
5.	ZnO Hexagonal Platelets & Rod-shaped Twins – Results & Discussion.....	98
5.1.	Hexagonal platelets	98
5.2.	Rod-shaped twins.....	103

5.3. Discussion and Summary	104
6. Final Summary, Conclusive Remarks and Outlook	107
7. References	111
List of Figures	126
List of Tables.....	137
Acknowledgment.....	138
Curriculum vitae	139

List of Abbreviations

ABF	Annular bright field
AFM	Atomic force microscopy
BF	Bright field
BSE	Back scattered electrons
CBED	Convergent-beam electron diffraction
CCD	Charge-coupled device
ccp	Cubic close packing
CEP	Concentric electron probe (method)
CLAHE	Contrast-limited adaptive histogram equalization
CRLP	Coincidence of reciprocal lattice points
CSL	Coincidence site lattice
CSLP	Coincidence site lattice point
DB	Diffusion bonding
DF	Dark field
DSB	Double Schottky barrier
EDS (EDX)	Energy dispersive X-ray spectroscopy
EELS	Electron energy-loss spectroscopy
EST	Epitaxial solid-state transformation
FEG	Field emission gun
FFT	Fast Fourier transform
FOLZ	First order Laue zone
GB	Grain boundary
HAADF	High-angle annular dark field
hcp	Hexagonal close packing
HMTA	Hexamethylenetetramine
HOLZ	Higher order Laue zone
HR	High resolution
IB	Inversion boundary
I-V	Current-voltage
MOV	Metal oxide varistor
NBED	Nano-beam electron diffraction
PC	Polycrystal
PLM	Polarized light microscopy
SAED	Selected area electron diffraction
SB	Schottky barrier
SC	Single crystal
SE	Secondary electrons
SEM (REM)	Scanning electron microscopy
SOLZ	Second order Laue zone

STEM	Scanning transmission electron microscopy
TEM	Transmission electron microscopy
WBDF	Weak-beam dark field
WDS	Wavelength dispersive X-ray spectroscopy
XPS	X-ray photoelectron spectroscopy
XRD	X-ray diffraction
ZOLZ	Zero order Laue zone

List of Symbols

a, b, c	Crystallographic lattice constants
α	Non-linearity coefficient (varistor)
α, β, θ	Beam angles (ion-milling, electron microscopy)
A^*	Richardson constant
C_s	Spherical aberration
C_c	Chromatic aberration
γ	Interfacial energy
Γ	Interfacial excess of segregating species
d	Effective chemical width (CEP method)
$d_{(hkl)}/d_{(hkil)}$	Lattice plane distance
$d_{ijk}/d_{i\lambda}$	Piezoelectric strain tensor / Piezoelectric charge tensor
δ_{gap}	Interface width (Schottky contact)
e^-	Electron
e	Elementary charge
e_{ijk}	Piezoelectric stress tensor
ϵ_0	Vacuum permittivity
ϵ_{Int}	Relative permittivity of the interface region
ϵ_r	Relative permittivity
ϵ_ξ	Fermi-level in adjoining grains
E	Electric field strength
E_C	Energy level (conduction band)
E_F	Fermi level
E_V	Energy level (valence band)
E_{Vac}	Energy level (vacuum)
ΔE	Energy spread of the electron beam
θ	Dihedral wetting angle
F	Mechanical force
f_i	Ionicity
$g/g_{hk(i)l}$	Reciprocal lattice vector / reflection
h, k, l	Miller indices (indexing of crystallographic planes)
h, k, i, l	Bravais indices (indexing of crystallographic planes)
h^+	Electron hole
Φ_B	Barrier height
Φ_{SB}	Schottky barrier height
Φ_{DSB}	Double Schottky barrier height
Φ_M	Work function (metal)
Φ_S	Work function (semiconductor)
I	Electric current
I	Intensity (electron microscopy, CEP method)

J	Electric current density
k	Boltzmann constant
$k (= \lambda^{-1})$	Wave vector (electron microscopy)
k_m	k -factor matrix element species (CEP method)
k_s	k -factor solute element species (CEP method)
l	Zn-O Bond length in wurtzite structure
λ	Wavelength
L	Length of square scanning area (CEP method)
μ	Chemical potential
N_D	Density of donor states
N_I	Interfacial trap states (unoccupied)
P	Piezoelectric polarization
q	Elementary charge
Q_{ijkl}	Electrostriction tensor
Q_I	Interfacial sheet charge
Q_P	Piezoelectric polarization charge
R	Electrical resistance
R	Intensity ratio of matrix/solute signal (CEP method)
r_1, r_2, r_3	Unit vectors / basis vectors of an orthonormal coordination system
r	Beam radius (CEP method)
ρ	Specific electrical resistance
ρ_{piezo}	Piezoelectric charge density
Σn	Coincidence parameter (CSL)
s	Excitation error
S_{jk}	Strain tensor
σ_{jk}	Stress tensor
t	Sample thickness
T	Temperature
u	Internal parameter of the wurtzite structure
u, v, w	Miller indices (indexing of crystallographic directions)
u, v, t, w	Bravais indices (indexing of crystallographic directions)
V	Sample volume (CEP method)
V / U	Voltage
V_A	Acceleration voltage (electron microscopy)
V_C	Critical voltage / Breakdown voltage / Switching voltage (varistor)
w	Width of a planar defect, interface or boundary (CEP method)
W_{piezo}	Width of piezoelectric charge distribution
x	(Bulk) solid solubility
χ	Electron affinity (semiconductor)
Z	Atomic number



Preface

Zinc oxide is quite a versatile material, which almost every one of us surely encounters every day in at least one of its many applications. For example, being antibacterial and well-tolerable, it is a common ingredient in ointments, lotions or toothpaste, and also in sunscreen, as it absorbs UV-A and UV-B radiation. It is also used as a food additive since zinc is an essential trace element for humans. Non-medicinal applications are, for example, its utilization as a component in thermal conductive paste or in the vulcanization process in industrial rubber production. Furthermore, it is used as a white pigment (*zinc white*) in paints and makeup. Doped with cobalt, it additionally serves as a green pigment (*zinc green* or *cobalt green*).^a The latter, also known as *Rinman's green*, was discovered by Swedish chemist Sven Rinman in 1780 upon heating mixtures of ZnO and CoO. Later, in 1912, this very compound took a main role in the development of solid-state chemistry as a scientific discipline in its own right, when Johan Arvid Hedvall realized that the reaction of ZnO and CoO occurred between the solid phases without the mediation of a gas or liquid and additionally lead to the formation of a solid solution; a novel concept at this time.^{1, 2, 3}

In this thesis, solid solutions (i.e., doping of ZnO) play a major role as well: Besides the mentioned applications, doped zinc oxide is an interesting electroceramic, due to its intrinsic semiconducting, piezo- and pyroelectric as well as non-linear properties. The latter refers to the particular current-voltage (*I-V*) characteristics of specifically doped polycrystalline ZnO ceramics, which show, instead of being ohmic ($R = const$) and linear ($U = R \cdot I$), an exponential increase in current once a certain critical voltage is applied ($R \neq const$). Materials exhibiting such behavior are termed *varistors* and in fact, ZnO is THE varistor material applied and investigated for decades. However, the combination and utilization of ZnO's varistor properties with its intrinsic piezo- and semiconducting properties sparked new research and led to the development of so-called *piezotronics*, where electrical properties are mechanically tuned and manipulated via piezoelectric charges. Such piezotronic devices, i.e., piezotronically tuned varistor bicrystals to be more precise, are the main subject of this thesis. They are investigated with a special focus on interface structure and dopant segregation, which are both essential for the generation of varistor properties in the first place. In doing so, an important question is dealt with, which might be expressed as "*How to dope with insoluble dopants?*" and refers to the circumstance that the most important varistor dopant, bismuth, is actually insoluble in ZnO.^{4, 5} Besides that, ZnO nanocrystals with the shape of hexagonal platelets and twinned rods are investigated. These depict only two examples of the remarkable range of different morphologies nanocrystalline ZnO can establish, but the hexagons in particular hold potential for the development of novel devices, as they can – in principle – tessellate and form functional thin-films with similar interesting electrical properties as mentioned above. However, a continuous

^a The term "cobalt green" is ambiguous, as it is used for two different cobalt-containing green pigments, which are $Zn_{1-x}Co_xO$ with wurtzite structure and $(Mg,Zn,Co)_2TiO_4$, which has inverse spinel structure.

tessellation has high demands on the quality of the hexagons in terms of uniform size and shape, which in turn, is sensitive to the synthesis conditions. In contrast, the rod-shaped twins cannot tessellate, but being twins they represent a case of inversion boundary bicrystals, similar to the piezotronic bicrystals and therefore, might be of interest for future application as well.

Kurzfassung

Um den Zusammenhang zwischen Grenzflächenstruktur und elektrischen Eigenschaften zu studieren, wurden an piezotronischen ZnO Bikristallen TEM und REM Untersuchungen durchgeführt. Der Begriff „piezotronisch“ bezieht sich hierbei auf die Manipulation und Anpassung elektrostatischer Potentialbarrieren an dotierten Varistorkorngrenzen mittels piezoelektrischer Ladungen, welche durch mechanische Belastung erzeugt werden. Zu diesem Zweck wurden Varistorbikristalle in „tail-to-tail“ $(000\bar{1})|(000\bar{1})$ und „head-to-head“ $(0001)|(0001)$ Orientierung, d.h. mit einer Invertierung der c-Achse orthogonal zur Korngrenze, hergestellt, was für Belastungen entlang $\langle 0001 \rangle$ eine optimale piezotronische Reaktion gewährleistet. Es wurden verschiedene Synthesemethoden verglichen und zusätzlich undotierte Referenzbikristalle und Bikristalle mit spezifischen Kipporientierungen begutachtet. Des Weiteren wurden Untersuchungen an ZnO Nanokristallen durchgeführt, welche die Form hexagonaler Plättchen und stäbchenförmiger Zwillinge haben und denen, ebenso wie den Bikristallen, ein großes Potenzial für Funktionalisierungen im Rahmen der Entwicklung neuartiger elektrischer Bauteile zugesprochen wird. Darüber hinaus ist der Varistoreffekt selbst, welcher den piezotronischen Anwendungen zu Grunde liegt, noch nicht final aufgeklärt – trotz jahrzehntelanger Forschung. Diesbezüglich stellen die untersuchten Bikristalle gut geeignete Modellsysteme dar, um spezifische Dotanden/Korngrenzsituationen zu studieren.

Da der Varistoreffekt auf der Ausbildung von Potentialbarrieren an dotierten Korngrenzen basiert, wurden die entsprechenden Grenzflächen mittels atomar aufgelöster HAADF-STEM untersucht; die Hauptmethode dieser Thesis, welche sowohl strukturelle als auch chemische Informationen liefert. Im Hinblick auf eine vollständige Charakterisierung und Kontrolle des Syntheseprozesses, wurden diese Messungen durch konventionelle TEM, ABF-STEM, Elektronenbeugung und EDX-Methoden vervollständigt. Die TEM-Resultate wurden dann mit den Ergebnissen korrespondierender elektrischer Messungen verglichen und interpretiert. Dabei wurde der Fokus auf das erfolgreiche Dotieren mit Bismut gelegt, welches für das Auftreten von Varistoreigenschaften und damit auch für eine piezotronische Manipulation derselben eine notwendige Bedingung darstellt.

Als Hauptergebnis wurde festgestellt, dass das Dotieren mit Bi, welches in ZnO unlöslich ist, keineswegs trivial ist und angepasste Synthesemethoden und/oder Bikristallkonfigurationen erforderlich sind, um für Bi geeignete Segregationsplätze zu erzeugen, da es ansonsten von der Grenzfläche abgezogen wird und elektrisch inaktive Sekundärphasen bildet. Es wurde beobachtet, dass entsprechende Segregationsplätze in Abhängigkeit von der strukturellen Kohärenz der jeweiligen Korngrenze auftreten. Während hochkohärente Grenzflächen undotiert blieben, wurde ein deutlicher Einbau von Bi an semi- oder inkohärenten Grenzflächen vorgefunden, was sich auch in den elektrischen Messungen widerspiegelte, die dementsprechend ein Ausbleiben bzw. ein Auftreten des Varistoreffekts nachwies. Die notwendige Inkohärenz konnte entweder durch eine besondere Synthesemethode (epitaktische

Festkörpertransformation) erzeugt werden, welche zu einer stark gekrümmten, defektreichen Korngrenze führte, oder durch eine gezielte Kipporientierung für Bikristalle mit flacher Korngrenze herbeigeführt werden. Für Letzteres konnten zwei Fälle unterschieden werden: Semikohärente Konfigurationen, bei denen sich ein Koinzidenzgitter (CSL) ausbildet und dessen Punkte als semiperiodische Segregationsplätze fungieren, sowie hochinkohärente Grenzflächen, deren Struktur eine deutliche Unordnung beinhaltet. Zusätzlich zur strukturellen Charakterisierung wurden thermodynamische Aspekte betrachtet, welche darauf hinweisen, dass alle drei Arten von Bi-Segregation (gekrümmt, flach-semikohärent, flach-hochkohärent) durch die Gibbsche Adsorptionsisotherme qualitativ erklärt werden können. Diese Gleichung beschreibt die Verringerung von Ober- oder Grenzflächenenergien durch die Anlagerung von Fremdatomen. Für den besonderen Fall eines unlöslichen Dotanden, welcher aber quasi-unendlich zur Verfügung steht gegenüber einer limitierten Anzahl von Segregationsplätzen, hängt die Segregation ausschließlich von a) der Energiedifferenz zwischen unbesetzter und besetzter Korngrenze, sowie von b) der Menge an verfügbaren Segregationsplätzen ab. Dabei sind a) und b) jeweils höher für inkohärente Grenzflächen und gehen gegen null für den Fall maximaler Kohärenz. Ein Vergleich mit einschlägiger Literatur zeigt, dass sowohl die TEM Ergebnisse, als auch die thermodynamischen Betrachtungen nicht nur mit den Resultaten früherer Bikristallstudien, sondern auch mit denen völlig verschiedener Materialsysteme übereinstimmen, weswegen sie als generalisierbar angesehen werden.

Mit dem Ziel einer Langmuir-Blodgett Abscheidung einer sich selbstassemblierenden Monolage von Kristalliten, wurden eine Syntheseroute für hexagonalen ZnO Plättchen bestimmt. Im Zuge dessen wurden TEM Untersuchungen durchgeführt, um die entstandenen Mineralisationsprodukte zu charakterisieren und die Synthese entsprechend zu optimieren. Dafür wurden dieselben Methoden wie bei den Bikristallen angewandt, insbesondere ABF-STEM und NBED zur Bestimmung der absoluten Ausrichtung der *c*-Achse. Dies war sowohl für die Hexagone, wo Inversionszwillinge ausgeschlossen werden mussten, als auch für die stäbchenförmigen Zwillinge, deren Zwillingsscharakter so bestimmt werden konnte, von besonderer Bedeutung. Des Weiteren wurde bei den TEM Untersuchungen festgestellt, dass die ZnO Hexagone eine Oberflächenbelegung mit residualem Material der Fällungssynthese aufwiesen, welche durch eine entsprechend konzipierte, zusätzliche Calcinierung entfernt werden konnte, die zeitgleich für eine Verbesserung der Oberflächenqualität der Facetten von rau zu quasi atomar eben sorgte. Im Hinblick auf die stäbchenförmigen Zwillinge, bei denen es sich eigentlich um ein Nebenprodukt der Syntheseexperimente für die Hexagone handelt, konnte gezeigt werden, dass es sich ausschließlich um präzise ausgerichtete „tail-to-tail“ Inversionszwillinge mit antiparallelen *c*-Achsen handelt, deren Grenzfläche eine gewisse Unordnung aufweist. Damit könnten diese in der Lage sein Dotanden, wie Bi einzubauen und somit für ähnliche Anwendungsszenarien wie die der piezotronischen Bikristalle interessant sein, vor allem im Hinblick auf die Tatsache, dass es sich bei den ursprünglichen piezotronischen Elementen bereits um ZnO Nanokristalle (Nanodrähte) handelte.

Abstract

TEM and SEM investigations of piezotronic ZnO bicrystals were conducted with the aim to study the relationship between interface structure and electrical properties. In this context, the term “piezotronic” refers to the manipulation and tuning of electrostatic potential barriers at doped varistor-type grain boundaries via piezoelectric charges generated upon mechanical load. To this end, varistor-type inversion-boundary bicrystals were synthesized in tail-to-tail $(000\bar{1})|(000\bar{1})$ or head-to-head $(0001)|(0001)$ orientation with respect to the c -axis, providing an optimized piezotronic response for load applied in $\langle 0001 \rangle$ directions. Different synthesis methods are compared and specific tilt configurations as well as undoped reference bicrystals were examined. Furthermore, ZnO nanocrystals, i.e., hexagonal platelets and rod-shaped twins, were investigated, as both the bicrystals and the nanocrystals hold a large potential for functionalization and the development of novel devices. Finally, the dopant-related varistor-effect itself, which underlies the piezotronic applications, is – despite decades of research – still not completely elucidated and the examined bicrystals are well-suited model systems for respective studies on specific dopant/grain-boundary situations.

Since the varistor-effect is attributed to potential barriers at doped grain-boundaries, respective interfaces were investigated by atomic-resolution HAADF-STEM; the main method in this thesis, capable of delivering structural as well as chemical information. These measurements were complemented with conventional TEM, ABF-STEM, electron diffraction and EDS methods in order to fully characterize the bicrystals as well as control and verify their successful synthesis. The TEM results were interpreted with respect to the findings from corresponding electrical measurements. In doing so, the focus laid upon the successful doping with bismuth, which is essential to obtain varistor behavior and hence, for the subsequent piezotronic manipulation.

As a main result, it was found that doping with Bi, being insoluble in ZnO, is by no means trivial and demands appropriate synthesis procedures and/or bicrystal configurations, which provide suitable segregation sites. Otherwise, Bi retracts from the interfaces and forms electrically inactive secondary phases. The presence of such segregation sites was found to be related to the respective structural coherence of the grain boundary. While highly coherent interfaces did not feature any significant Bi doping, semi- or incoherent interfaces exhibited a clear Bi decoration, which was also reflected by the electrical measurements revealing the absence or occurrence of varistor behavior, respectively. The required incoherency could be introduced either via a special synthesis procedure (epitaxial solid-state transformation) leading to a strongly curved defect-rich interface or by applying specific tilt configurations to diffusion-bonded bicrystals with a flat interface. The latter comprises two different cases: Semi-coherent configurations, where a coincidence-site lattice (CSL) is formed and CSL points act as semi-periodic segregation sites, and highly incoherent situations, where the interface structure is strongly and irregularly disordered. In addition to the structural characterization, thermodynamic aspects were considered, indicating that all three types of Bi-segregation

(curved, flat-semicoherent, flat-incoherent) can be explained qualitatively by applying Gibbs adsorption isotherm, which describes the lowering of surface or interface energies depending on the decoration by impurity atoms. Due to the special case of an insoluble dopant, which is available in a quasi-infinite reservoir with respect to the limited amount of segregation sites, the segregation of Bi depends only on a) the energy difference between the undecorated and decorated interface, and b) the actual quantity of segregation sites. Both a) and b) are higher for incoherent interfaces and approach zero for the case of maximum coherency. The TEM results as well as the thermodynamic considerations were found to be not only in perfect agreement with previous ZnO bicrystal studies but also with comparable situations in other, completely different material systems. In consequence, they are considered to be applicable to all cases of interfacial segregation of insoluble dopants.

The main goal behind the synthesis of the hexagonal ZnO platelets is their self-assembled tessellation upon Langmuir-Blodgett deposition. However, a synthesis route needed to be established first. TEM investigations were performed in order to characterize the obtained mineralization products and provide feedback for the optimization of the synthesis. In doing so, the same methods as for the bicrystals could be employed, in particular, ABF-STEM and NBED for determining the absolute direction of the *c*-axis. This was an important issue for both the hexagonal platelets, where inversion twinning needed to be ruled out, as well as for the rod-shaped twins, whose twinning character could be identified this way. In addition, the TEM investigations revealed a surface coverage of the hexagonal facets by residuals from the precipitation process. In consequence, an additional calcination step was added to the synthesis procedure, which was shown to successfully remove this coverage and simultaneously increase the quality of the surfaces from rough to almost atomically flat. Regarding the rod-shaped twins, actually a side-product of the synthesis experiments, the TEM findings revealed a situation similar to the piezotronic inversion-boundary bicrystals. In all cases, the crystallites were found to be accurate tail-to-tail inversion twins with anti-parallel *c*-axes and a disordered interface, probably capable of incorporating dopants such as Bi. In consequence, they are seen as holding potential for further development in their own right, especially against the background that the original “piezotronics” were established based on ZnO nanocrystals (nanowires).

1. ZnO – Background & Fundamentals

1.1. Mineralogy, structure and general properties

At ambient conditions, the inorganic compound ZnO, i.e., zinc(II) oxide, crystallizes in the hexagonal wurtzite structure with space group No. 186 $P6_3mc$ and lattice constants $a = 3.2496 \text{ \AA}$ and $c = 5.2042 \text{ \AA}$.⁶ The characteristic symmetry elements in the three viewing directions $[0001]$, $\langle 2\bar{1}\bar{1}0 \rangle$ and $\langle 10\bar{1}0 \rangle$ of the hexagonal system, are a 6_3 -screw axis parallel to $[0001]$, a mirror plane in $\{2\bar{1}\bar{1}0\}$ and a c -type glide plane in $\{10\bar{1}0\}$.^a ZnO crystals exhibit perfect cleavage on $\{10\bar{1}0\}$ planes and parting as well as twinning on $\{0001\}$ faces.^b The general fracture is conchoidal. Being stable over a wide range of temperature and pressure, the wurtzite modification is the crystal structure typically associated with ZnO and its naturally occurring equivalent *zincite* (Figure 1-1). Typical zincite localities are contact metamorphic ore deposits, with Sterling Hill in Ogdensburg, New Jersey and Mine Hill in Franklin, New Jersey being the most prominent ones.⁷

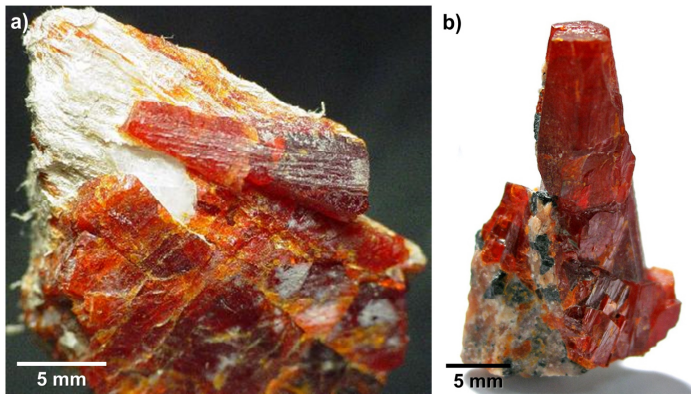


Figure 1-1: a) and b) zincite specimens from Sterling Mine, Sterling Hill, Ogdensburg, Franklin Mining District, Sussex County, New Jersey, USA. The red color is due to iron and manganese impurities. Reworked after Robert M. Lavinsky.^{8,9}

Two other ZnO modifications are known, which are a cubic zincblende (No. 216 $F\bar{4}3m$)¹⁰ and a cubic rock-salt structure (No. 225 $Fm\bar{3}m$)¹¹.

Whereas the zincblende polymorph can be obtained exclusively by heteroepitaxial growth on appropriate cubic substrates, such as ZnS,¹² GaAs/ZnS¹³ or Pt/Ti/SiO₂/Si,¹⁴ the rock-salt polymorph is the thermodynamically favored modification at high pressures $> 10 \text{ GPa}$.¹¹ In both the wurtzite and the zincblende structure, Zn and O atoms have the coordination number 4, which corresponds to the formation of tetrahedra with one atom species being placed in the center, while the other is located at the tips, where the tetrahedra are connected. Although this tetrahedral coordination is often indicative of sp^3 hybridization with covalent bonds, the Zn-O bonding features a considerably strong polarity due to the high electronegativity of oxygen. As a consequence, its ionicity resides in the ionic regime but is nevertheless close to the borderline to covalent bonding ($f_i = 0.62$ Phillip's scale, $f_i = 0.59$ Pauling's scale)^{15, 16}. The difference between the wurtzite and zincblende modification is found in the sublattice, which causes a disparity in the second coordination sphere. Both atomic species form interpenetrative close-packings and mutually occupy one-half of their tetrahedral sites. In the case of zincblende,

^a Using Miller indices (hkl), the viewing directions are $[001]$, $\langle 100 \rangle$ and $\langle 210 \rangle$. The symmetry elements are a 6_3 -screw axis along $[001]$, a mirror plane in $\{2\bar{1}0\}$ and a c -type glide plane in $\{100\}$.

^b In general, *cleavage* is an inherent property of a crystal's symmetry, atomic structure and bonding conditions, while *parting* is due to structural defects in real crystals, hence the latter is only indirectly related to the crystal structure.

cubic close-packings (ccp) are formed, while hexagonal close-packings (hcp) are present in the wurtzite structure. These packing types directly correlate with the cubic or hexagonal crystal system of the respective ZnO modification. For the wurtzite structure, the shift between the interpenetrating close-packings in c -direction equals the anion-cation distance, i.e., the Zn-O bond length, and is represented by the so-called *internal parameter* u , which is connected to the ratio of the c - to the a -axis.¹⁵ In the case of an idealized structure, the tetrahedral geometry determines the axes ratio to be $c/a = (8/3)^{1/2} = 1.633$ and $u = (1/3) \cdot (a^2/c^2) + 1/4 = 0.375$, with the Zn-O bond length l being $l = c \cdot u$ for all four bonds within a single coordination tetrahedron. However, the c/a ratio and u deviate from the ideal values in real ZnO as well as in other wurtzite crystals, with a decreasing c/a ratio causing an increasing parameter u and vice versa. In consequence, the tetrahedra are slightly distorted and the c -axis directed bond length $l = c \cdot u$ differs from the off-axis bond lengths $l' = \sqrt{\frac{1}{3}a^2 + (\frac{1}{2}-u)^2 c^2}$, as shown in Figure 1-2.¹⁷ Applying lattice constants $a = 3.2496 \text{ \AA}$ and $c = 5.2042 \text{ \AA}$,⁶ the axis ratio $c/a = 1.6015$ is $\sim 2\%$ lower than the ideal value. For the internal parameter u , values in the region of $u = 0.3817$ up to $u = 0.3856$ are reported, with the experimentally determined values being typically lower compared to those from ab initio or first-principle calculations.^{6, 18-21} With respect to $u = 0.3819$,⁶ for example, which is about $\sim 2\%$ higher than the ideal value, the on- and off-axis bond lengths are $l = 1.9875 \text{ \AA}$ and $l' = 1.9743 \text{ \AA}$.

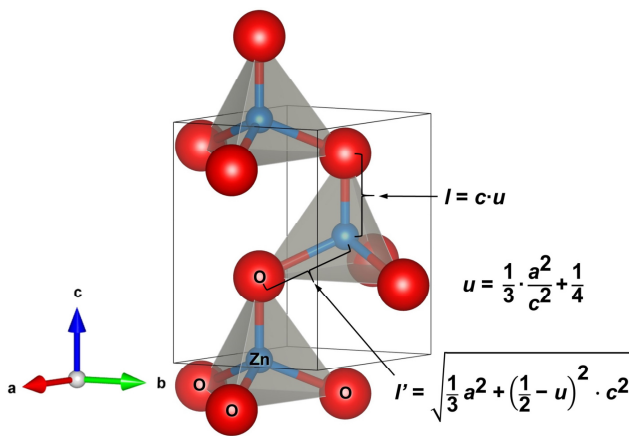


Figure 1-2: The crystal structure of wurtzite ZnO. Zinc and oxygen atoms form interpenetrative hcp and mutually occupy one-half of their tetrahedral sites. In contrast to an ideal tetrahedral coordination, the close-packings are slightly shifted along the c -axis, leading to non-uniform bond lengths l and l' in c -axis and off-axis direction, respectively.^a

As a consequence of space group $P6_3mc$,^b the substantial ionic character of the Zn-O bonding as well as the deviation of the internal parameter u from the ideal value

$u = 3/8$, wurtzite structures exhibit piezo- and pyroelectricity with a spontaneous polarization, i.e., a non-vanishing electric dipole moment, which is present even under load-free conditions. Since this characteristic is of special interest to this work, it is discussed in more detail in section 1.2 (pp. 5).

Due to the alternate stacking of cation and anion layers, wurtzite crystals with idealized structure terminate in c -axis direction with a pure cation layer on one side and a pure anion layer on the other. In the case of ZnO, the positive c -axis direction is conventionally assigned to the cation-terminated side, which results in an indexing of Zn-terminated surfaces as (0001)

^a Image created with the free software VESTA 3.5.7.²²

^b Space group $P6_3mc$ (No. 186) is non-centrosymmetric and features a polar c -axis, i.e., no inversion symmetry exists and the c -axis has a defined direction.

and O-terminated surfaces as $(000\bar{1})$ planes. However, surface reconstruction is common for real ZnO crystals and, besides ion adsorption (e.g. H^+ and OH^-), partial charge transfer, impurity atoms and surface defects, it is a well-reported stabilization mechanism for the otherwise electrostatically unstable surfaces.²³⁻²⁶ It should be noted that these various linked and partly competing mechanisms are sensitive to and determined by the chemophysical environment and, furthermore, can be expected to influence the interfacial properties of derived ZnO devices. Regarding the synthesis of (functionalized) ZnO crystals, not only surface reconstructions may need to be taken into account, but also the different growth rates for different crystallographic directions. Preferential growth typically occurs along the c -axis, often leading to the formation of columnar structures, which complicates the fabrication of atomically smooth and flat ZnO surfaces.²⁷ However, while ZnO exhibits the highest growth rate in the positive c -axis direction $[0001]$, the lowest growth rate is in the negative c -axis direction $[000\bar{1}]$.^{28, 29} As a further consequence of their polar nature, Zn- and O-terminated surfaces also exhibit different chemical behavior. Prominent examples are the orientation-dependent etching patterns, which can be utilized to unambiguously differentiate between (0001) Zn- and $(000\bar{1})$ O-faces, since the latter exhibits a significantly higher etching rate with uniformly distributed and well-pronounced hillock-like etch figures.^{30, 31} In this thesis, etching with 10 % HCl_{aq} for ~ 1 s was used to check and reveal polycrystalline structures and grain boundaries in EST bicrystals (cf. pp. 27), as exemplarily shown in Figure 1-3.

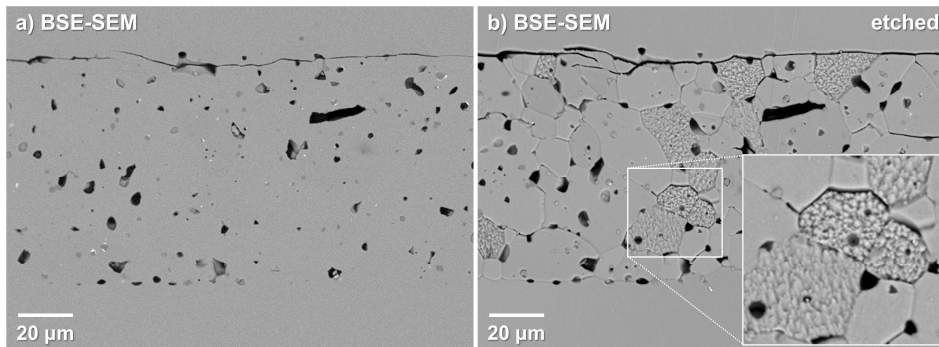


Figure 1-3: a) and b) BSE-SEM images of the interface layer in an EST bicrystal (cf. pp. 27) before and after etching with 10 % HCl_{aq} for about 1 s. Etching indicates the incomplete transformation to a bicrystal by revealing the polycrystalline state of the interfacial layer by highlighting grain boundaries as well as the different orientation of ZnO grains, as reflected by the etching pits and hillocks (inset), which occur exclusively at the O-terminated $[000\bar{1}]$ side.

1.1.1. Remarks on Miller and Bravais indices

In the case of the hexagonal crystal family^a, indexing of crystallographic planes or directions can be done by using either the common Miller indices h, k, l or the four-digit Bravais indices h, k, i, l . Due to the special geometry of the hexagonal unit cell with $a = b \neq c$, $\alpha, \beta = 90^\circ$, $\gamma = 120^\circ$, a third symmetry equivalent a -axis can be introduced with conditions $-a_1 + -a_2 = a_3$ and $a_1 + a_2 + a_3 = 0$, as illustrated in Figure 1-4.

^a The hexagonal crystal family contains both the hexagonal and trigonal crystal systems, since all related crystal structures can be displayed within a hexagonal unit cell.

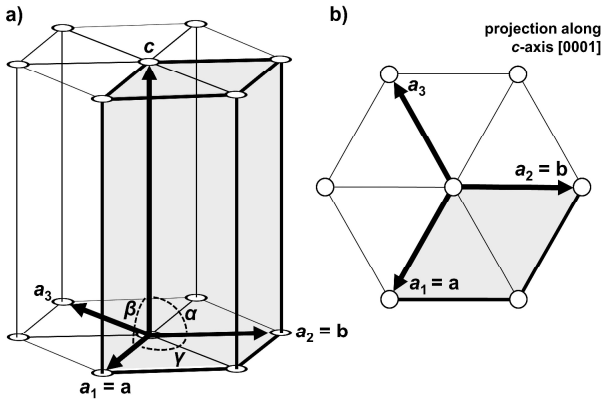


Figure 1-4: a) Illustration of the hexagonal unit cell according to Bravais notation using three equivalent axes a_1 , a_2 , a_3 and the unique c -axis. The small circles mark Bravais lattice points. As highlighted by the grey color, the regular primitive hexagonal unit cell hP is set up by $a_1 = a$, $a_2 = b$ and c . b) Projection of the hexagonal unit cell along the c -axis, for a better depiction of the equivalence of a_1 , a_2 and a_3 .

The additional index i corresponds to a_3 like h, k, l correspond to a_1, a_2 and c . Index i is not essential as it is already defined by $i = -(h + k)$. However, its application has a major advantage. In Miller notation, certain planes of the hexagonal unit cell are indexed by a different set of h, k, l digits, although they are symmetry equivalent. For example, (100) and $(1\bar{1}0)$ belong to the same family of planes and are identical, which, however, only becomes clear when Bravais notation is used. In this case, the planes are indexed as $(10\bar{1}0)$ and $(1\bar{1}00)$ and their symmetry relationship is denoted by the same set of permuted h, k, i, l digits. Throughout this work, Bravais notation is used exclusively, since it is much more convenient to express hexagonal symmetry relations. Yet, vector calculations are easier if Miller indices are used, omitting the redundant index i . The conversion for arbitrary planes and directions is shown in Eq. 1.1, Eq. 1.2 and Eq. 1.3, with upper- and lower-case letters referring to Miller and Bravais notation, respectively.

$$\begin{pmatrix} H \\ K \\ L \end{pmatrix}_{Miller} = \begin{pmatrix} h = H \\ k = K \\ i = -(H + K) \\ l = L \end{pmatrix}_{Bravais} \quad \text{Eq. 1.1}$$

$$\begin{bmatrix} U \\ V \\ W \end{bmatrix}_{Miller} \cong \begin{bmatrix} u = \frac{1}{3}(2U - V) \\ v = \frac{1}{3}(2V - U) \\ t = \frac{1}{3}(-U - V) \\ w = W \end{bmatrix}_{Bravais} \quad \text{Eq. 1.2}$$

$$\begin{bmatrix} u \\ v \\ t \\ w \end{bmatrix}_{Bravais} \cong \begin{bmatrix} U = 2u + v \\ V = 2v + u \\ W = w \end{bmatrix}_{Miller} \quad \text{Eq. 1.3}$$

Please note, while the conversion of planes is straightforward in both ways, the conversion of directions is more complicated. Some converted directions need to be multiplied by 3 or $\frac{1}{3}$ to obtain integers for h, k, i, l . In consequence, the length is altered and hence, the vectors are not identical when converted from Miller to Bravais notation and back. However, the direction is maintained, which is sufficient for most crystallographic applications. Table 1-1 comprises an overview of the most important directions in both Miller and Bravais notation for wurtzite ZnO.

Table 1-1: Overview of basic directions and planes in wurtzite ZnO in both Miller and Bravais notation. As indicated by the corresponding lengths, lattice plane distances and color code, only Bravais notation allows direct identification of families of symmetry equivalent directions and planes by their shared set of $[uvtw] / (hkil)$ digits.

Direction / plane	Miller notation $[uvw]/(hkl)$	Bravais notation $[uvtw]/(hkil)$	Length / lattice plane distance [Å]
a_1 (a)	[100]	$[2\bar{1}\bar{1}0]$	3.2496
a_2 (b)	[010]	$[\bar{1}2\bar{1}0]$	3.2496
a_3 ($-a-b$)	$[\bar{1}\bar{1}0]$	$[\bar{1}\bar{1}20]$	3.2496
c	[001]	[0001]	5.2042
plane $\perp a_1$	$(2\bar{1}0)$	$(2\bar{1}\bar{1}0)$	1.6248
plane $\perp a_2$	$(\bar{1}20)$	$(\bar{1}2\bar{1}0)$	1.6248
plane $\perp a_3$	$(\bar{1}\bar{1}0)$	$(\bar{1}\bar{1}20)$	1.6248
plane $\perp c$	(001)	(0001)	5.2042
plane $\parallel a_2, c$ ($a_2 \times c$)	(100)	$(10\bar{1}0)$	2.8142
plane $\parallel a_1, c$ ($a_1 \times c$)	(010)	$(01\bar{1}0)$	2.8142
plane $\parallel a_3, c$ ($a_3 \times c$)	$(\bar{1}10)$	$(\bar{1}100)$	2.8142

1.2. Piezoelectric properties

Piezoelectric materials respond upon dimensional change, that is, strain in consequence of mechanical stress, with the generation of polarization charges and hence, display a voltage or electric field, which is the so-called *direct* piezoelectric effect. Vice versa, if an electric field is applied to a piezoelectric material, the polarization will cause a dimensional change, which is termed *inverse* piezoelectric effect or *electrostriction*. In general, the polarization P_i is (at electric field $E = \text{const}$, “short circuit” condition) a linear function of all components of the stress tensor σ_{jk} coupled by the piezoelectric strain or charge tensor d_{ijk} as described by^a

$$P_i = \sum_{j,k} d_{ijk} \sigma_{jk}; \quad i, j, k = 1, 2, 3 \quad \text{Eq. 1.4}$$

If strain instead of stress is considered (also $E = \text{const}$, “short circuit” condition), the polarization P_i is a function of the strain tensor S_{jk} and the piezoelectric stress coefficients e_{ijk}

$$P_i = \sum_{j,k} e_{ijk} S_{jk}; \quad i, j, k = 1, 2, 3 \quad \text{Eq. 1.5}$$

^a The indices of the tensors P_i , σ_{jk} , d_{ijk} , etc. always refer to directions and planes within an orthonormal coordination system with basis vectors r_1, r_2, r_3 , and not to a crystallographic unit cell. In other words, it considers a (macroscopic) cubic bulk piece of the material (cf. Figure 1-6, p. 7). $j = k$ indicates normal stress and $j \neq k$ shear stress. Thus, $\sigma_{11}, \sigma_{22}, \sigma_{33}$ refer to normal stress applied on planes (surfaces) perpendicular to r_1, r_2 and r_3 , respectively. σ_{13} refers, for example, to shear stress in direction of r_1 applied on the plane perpendicular to r_3 .

Due to the stress tensor's inner symmetry $\sigma_{jk} = \sigma_{kj}$ and if the crystal symmetry is taken into account, at most 18 of the 27 piezoelectric charge coefficients d_{ijk} can remain independent. In addition, all components of a polar third-order tensor d_{ijk} disappear for crystal classes with a center of inversion and due to $d_{ijk} = d_{ikj}$, also for point group 432. In consequence, 12 of the 32 crystal classes do not feature piezoelectricity. Furthermore, of the remaining 20 piezoelectric crystal classes, only 10 are polar and exhibit spontaneous polarization, which implies them being pyroelectric.^a Considering the direction of polarization and applied force, the piezoelectric coefficients can be further divided into four different groups, representing either a longitudinal or a transversal orientation of the polarization vector towards normal and shear forces, respectively (Figure 1-5).

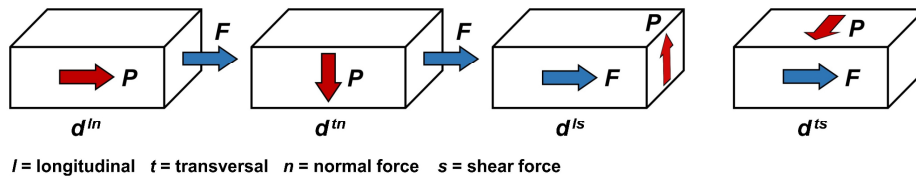


Figure 1-5: Illustration of the four different types of the piezoelectric effect, which are classified by the two components of the corresponding piezoelectric coefficient d . These components are the applied force F , which is either a normal or a shear force, and the direction of the resulting polarization P , which is either longitudinal or transversal to F . Redrawn after "Bild. 4.12" by Kleber.³²

Analogous to the direct effect, the inverse piezoelectric effect can be described by the resulting strain tensor S_{jk} being a linear function of the applied electric field E_i coupled by the piezoelectric strain coefficients d_{ijk} :

$$S_{jk} = \sum_i d_{ijk} E_i; \quad i, j, k = 1, 2, 3 \quad \text{Eq. 1.6}$$

Although an accurate mathematical expression for the inverse piezoelectric effect would require the application of the electrostriction coefficients Q_{ijkl} , the same piezoelectric coefficients as for the direct effect can be utilized ($d_{ijk}^{\text{direct}} = d_{ijk}^{\text{inverse}}$) if simplifying assumptions are made, which are, in particular, "mechanically free" conditions (stress $\sigma = \text{const}$) for the inverse effect.³³

Wurtzite ZnO does not only meet all requirements necessary for the occurrence of piezoelectricity and pyroelectricity, that is, a non-centrosymmetric point group and a polar axis (which implicates the deviation of the internal parameter u from the ideal value of $3/8$), it is also well known for the strength of its piezoelectric effect. It is reported to be indeed the largest among the II-VI compounds with wurtzite structure and comparable to those of III-V nitrides, which characteristically exhibit large piezoelectric coefficients.^{34, 35} The same is true for the zinc oxide's spontaneous polarization P_s , which induces negative charges on the Zn-terminated and positive charges on the O-terminated side. According to ab initio calculations, P_s is typically in the region of -0.047 C/m^2 up to -0.057 C/m^2 , depending on the applied structural data and, in particular, the internal parameter u .^{35, 36}

^a As a side remark, it should be noted that only pyroelectric crystals, such as wurtzite ZnO, show piezoelectricity if the applied mechanical load is an all-side hydrostatic pressure.

Due to space group $P6_3mc$ (crystal class $6mm$), only the three piezoelectric charge coefficients d_{311} , d_{333} and d_{131} remain independent, hence, using Voigt's notation,^a which reduces the two indices j and k to λ , the tensor d_{ijk} can be written as

$$d_{i\lambda} = \begin{pmatrix} 0 & 0 & 0 & 0 & d_{15}^{ts} & 0 \\ 0 & 0 & 0 & d_{15}^{ts} & 0 & 0 \\ d_{31}^{tn} & d_{31}^{tn} & d_{33}^{ln} & 0 & 0 & 0 \end{pmatrix} \quad \text{Eq. 1.7}$$

l = longitudinal, t = transversal, n = normal strain, s = shear strain

Please note, the directions indicated by the coefficients' indices do not (directly) relate to the wurtzite unit cell, but to a derived orthonormal coordination system with basis vectors $r_1 \parallel [2\bar{1}\bar{1}0]$, $r_2 \parallel [01\bar{1}0]$ and $r_3 \parallel [0001]$,^b as exemplarily shown for the stress tensor σ_{jk} in Figure 1-6.

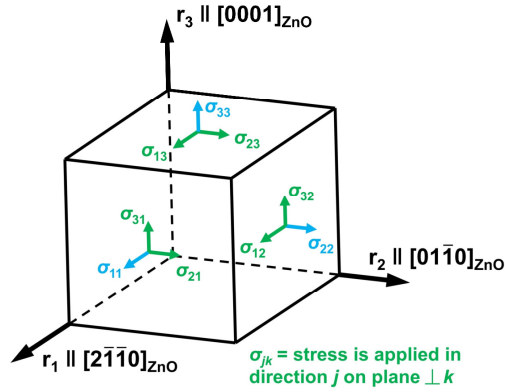


Figure 1-6: Illustration of the components of the stress tensor σ_{jk} for wurtzite ZnO. The directions and planes indicated by j and k correspond to an orthonormal coordination system, which relates to the hexagonal unit cell as shown in the figure. Normal and shear components are highlighted in blue and green color, respectively. Reworked after "Bild 4.10" by Kleber.³²

In consequence, the two coefficients d_{31} represent the transversal piezoelectric contribution to the c -directed polarization component P_3 for normal strain along the a -axes on $\{10\bar{1}0\}$ planes, whereas d_{33} relates to the longitudinal contribution to P_3 for normal strain along the c -axis on the basal planes $\{0001\}$. The d_{15} coefficients denote the transversal contribution to P_1 and P_2 upon shear strain on the basal planes $\{0001\}$ in a -axis direction. Experimentally determined values for the piezoelectric coefficients, obtained by resonance-antiresonance measurements, were found to be in the range of $d_{31} = -4.7$ pC/N to -5.2 pC/N, $d_{33} = 10.6$ pC/N to 12.4 pC/N and $d_{15} = -8.3$ pC/N to -13.9 pC/N.³⁷⁻⁴⁰ In contrast to the c -axis, which points from the O- towards the Zn-terminated basal plane, the sign of the polarization tensor is defined to be positive in the opposite direction, that is, from the cation to the anion side. Note, the shear strain contributions to P_1 and P_2 are often neglected for the sake of simplification, hence the total polarization P_i is solely determined by the c -directed component P_3 .

1.3. Semiconducting properties

Besides being piezo- and pyroelectric, (undoped) zinc oxide is also known to be a semiconducting material with n-type characteristics and a wide band gap in the range of 3.3 eV to 3.44 eV.^{41, 42} However, although often reported to be an *intrinsic* n-type semiconductor, it is not finally clarified yet, whether this is true in the narrower sense, which excludes any kind of

^a The first index i refers to a (piezo)electric parameter of the crystal in a certain direction, while j and k , or λ in Voigt's notation, refer to a mechanical parameter (stress or strain) in a certain direction. In Voigt's notation, $\lambda = 1, 2, 3, 4, 5, 6$ denotes pairs of $jk = 11, 22, 33, 23, 13, 12$ with $23 = 32, 13 = 31$ and $12 = 21$.

^b Using Miller notation $[uvw]$, these directions are $r_1 \parallel [100]$, $r_2 \parallel [120]$ and $r_3 \parallel [001]$.

impurity doping, being intentional or not. Originally, the n-type characteristics were discussed as being the consequence of intrinsic donor defects, such as zinc interstitials Zn_i or oxygen vacancies V_O .⁴³⁻⁴⁷ Though this appears to be a likely as well as reasonable explanation for a semiconducting oxide, later results indicated that these native defects have rather high formation energies in n-type ZnO and therefore are unlikely to form and presumably not the origin of the intrinsic conductivity.^{48, 49} The same is true for other native defects, such as zinc antisites Zn_o (donor), oxygen interstitials O_i (acceptor) and oxygen antisites O_{Zn} (acceptor), which have even higher formation energies and therefore are not expected to play any role in equilibrium or near-equilibrium conditions.⁵⁰ According to the cited reports,^{48, 49, 50} V_O is a deep donor 1 eV below the conduction band and may act as compensating defect in p-type doped ZnO, but is most likely not able to provide the observed intrinsic n-type doping. Furthermore, Zn_i is reported to be a shallow donor and fast diffuser, which makes it probably unstable. On the contrary, V_{Zn} has a comparably low formation energy, but is a deep acceptor and therefore a compensating defect in n-type ZnO. In summary, the native defects are seen as sources of self-compensation, but not as the origin of the intrinsic semiconducting characteristics in as-grown ZnO. Consequently, unintentional doping by impurity atoms is suggested as an alternative explanation. The most likely candidate is hydrogen,⁴⁸ although a large variety of residual impurities can be thought of, for example, silicon or aluminum, which may originate from the source material, growth equipment or the often applied sapphire substrates during epitaxial ZnO growth.^{27, 51} While being an *amphoteric* species in other semiconductors, and therefore counteracting the respective p- or n-type conductivity via incorporation as donor H^+ or acceptor H^- , respectively, hydrogen occurs exclusively as donor H^+ in ZnO according to more recent first-principle calculations.^{52, 53} On the one hand, experimental studies confirmed the presence of hydrogen and specified on its states and species (starting already in the 1950s),⁵⁴⁻⁵⁷ but on the other hand the native defects re-entered the discussion upon newer findings indicating that strong *attractive interaction* between V_O and Zn_i significantly lowers their formation energies and therefore, renders them possible candidates for the intrinsic n-type conductivity again.⁵⁸ In addition, the experimental studies on hydrogen in ZnO also yielded rather complex, partly inconsistent results, most likely due to the high sensitivity of respective H-related defect species (e.g. donor vs. inactive) and hence, of the observed conductivity towards the material source, synthesis and annealing conditions.⁵⁹ In consequence, the nature of zinc oxide's "intrinsic" n-type conductivity, which is probably related to both impurities and native defects in varying degrees, remains still under debate.

Considering the manifold applications of ZnO in semiconducting devices, such as transparent electrodes in solar cells, thin-film transistors, UV-LEDs, nanogenerators, piezoelectric sensors and varistor ceramics,⁶⁰⁻⁶³ it is mandatory to control and tune the *extrinsic* semiconducting properties by different doping strategies. Whereas n-type doping is readily achievable, considering the intrinsic properties, reliable p-type doping is comparably challenging.^{15, 46, 50, 64} Although native defects may not act as responsible donors for the intrinsic semiconducting

properties, they are likely present as compensating species in this case. For example, V_O is reported to have a low formation energy in p-type ZnO and is in consequence an abundantly present donor compensating for the respective extrinsic acceptor dopants.^{47, 48} Furthermore, hydrogen likely counteracts p-type doping, since it is either non-amphoteric and always a donor, if the reports prove to be correct, or it is amphoteric and therefore a donor as well in p-type ZnO.^{52, 53, 65} Aside from that, TEM investigations on dislocations in ZnO indicated a high line charge and, since respective dislocation states are reported to act amphoteric, they probably support self-compensation.⁶⁶ Thus, dislocations might contribute to the difficulties obtaining p-type doping, if they are present in high quantity. In addition, measuring (bulk) p-type conductivity in ZnO is reported to be complicated, for example, by the possible formation of surface electron accumulation layers and the conductivity's general sensitivity towards surface states and modifications.^{46, 50, 64, 67-69} Although many reports were published on effective p-type doping, the results were (according to the shared view of the cited review papers) often not reproducible, were considered as partly unrealistic or, at least, did not lead to the successful formation of p-n junctions, which is a main goal for the further development of ZnO-based devices.^{27, 46, 50, 64} Nevertheless, some progress had been made and the most promising methods addressing the p-type problem rely on either nitrogen doping^{70, 71, 72} or on the formation of heterojunctions with appropriate materials,⁴⁶ which avoids the doping issue as, for example, in ZnO/AlGaN UV-LEDs⁷³ or ZnO/NiO UV detectors.⁷⁴ In principle, various elements appear suitable for ZnO p-type doping, e.g., Mg or Cu,^{75, 76} but especially group-I elements (Li, Na, K) for Zn substitution and group-II elements (N, P, As, Sb) for O substitution are often considered.¹⁵ However, due to the smaller atomic radii, group-I elements typically occupy interstitial instead of the intended substitutional sites and hence, they act as donors. Furthermore, their larger bond length causes lattice strain and, in consequence, increases the density of compensating lattice defects. Similarly, group-V elements, with the exception of nitrogen, prefer donor-like antisites over the substitutional sites and, if in an acceptor state at all, form deep acceptors.⁶⁴ Therefore, (co)-doping with nitrogen is reported as the most promising route towards stable p-type ZnO, though it should be noted that this is also not straightforwardly accomplished. The solubility of N in ZnO is obstructively low,¹⁵ N_2 molecules on O sites are compensating double donors^{77, 78} and there are also reports of high N-concentration, but nevertheless n-type conductivity, probably due to the formation of nitrogen-induced deep trap states.⁷⁹ As a final remark, though new reports on the successful fabrication of acceptor doped ZnO and p-n homojunctions are published now and then,⁸⁰⁻⁸⁵ a conclusive breakthrough was not achieved so far and p-type doping still has to be considered a non-trivial issue.

In contrast, extrinsic n-type doping is reliably attained with group-III elements (B, Al, Ga, In) substituting Zn and group-VII elements (F, Cl, Br, I) substituting O.^{15, 46, 50, 64, 86, 87} Supreme results are typically obtained with group-III dopants and among these, Ga is probably the best-suited element due to the very similar bond lengths of Ga-O (1.92Å) and Zn-O (1.97 Å). A

typical example is the application of Ga-doped ZnO as conductive transparent oxide thin-film in solar cells.⁸⁸ Finally, considering its role as a donor in nominally undoped ZnO, hydrogen can be utilized as well to obtain highly conductive extrinsic n-type ZnO.⁸⁹

1.4. Varistor effect and varistor ceramics

The term *varistor* (a portmanteau word formed from “**variable resistor**”) describes a material or electric component with an electrical resistance, which varies depending on the applied voltage. Generally speaking, they are isolators up to a certain voltage, which is the so-called *switching* or *breakdown voltage*, at which they become quasi-instantaneously conducting. This is an intrinsic, characteristic and – if long-term degradation is neglected – a reversible effect,⁹⁰ hence their field of application is typically found in protecting electrical systems from voltage peaks. Regarding their function, they are equivalent to back-to-back Zener diodes, although relying on a different mechanism of electron transport.⁹⁰

After the fabrication of the first varistors in the 1930s, which were based on CuO/Cu and SiC,^{91, 92, 93} Matsuoka published a detailed study on the varistor properties of doped ZnO in 1971 and attracted attention to this material.⁹⁴ In the course of the following years, a large effort was put into research and commercial development of ZnO-based varistors with great success. Especially for high-voltage applications, ZnO is the main component in most of today’s metal-oxide-varistors (MOV), due to its superior current-voltage (*I-V*) characteristics and large non-linearity coefficients of $\alpha = 30 - 100$.⁹⁵

Whereas an ideal ohmic material will show a perfectly linear graph in current-voltage (*I-V*) measurements, varistors exhibit a non-linear response with three distinguishable regions (Figure 1-7).⁹⁰

I. Pre-switch region

Below the switching voltage, varistors show ohmic behavior and pass only a comparably small leakage current, which is mainly governed by the respective grain-boundary resistances.

II. Switching region

When the applied voltage exceeds the switching voltage, the material becomes highly conducting. Small voltage changes cause drastic increases in current density, which are typically in the range of several orders of magnitude. This region is also called the non-linear regime. It is described by the non-linear coefficient α according to the relation

$$I \propto V^\alpha \quad \text{or} \quad \alpha = \frac{d \ln(I)}{d \ln(V)} \quad \text{Eq. 1.8}$$

III. High-current region

At very high voltages, the varistor behavior is ohmic again ($\alpha = 1$), but in contrast to the pre-switch region, the current flow is mainly determined by the specific grain resistance and hence the semiconducting properties of the bulk.

The origin of this *varistor effect* is attributed to electrostatic potential barriers at grain boundaries, where dopant-induced acceptor-like defect states trap charge carriers, i.e., electrons.^{90,96} This phenomenon can be understood as the formation of double Schottky-barriers (DSB), which is – with some modifications, as shown in the following – the commonly accepted model explaining the specific charge carrier transport across varistor grain boundaries.

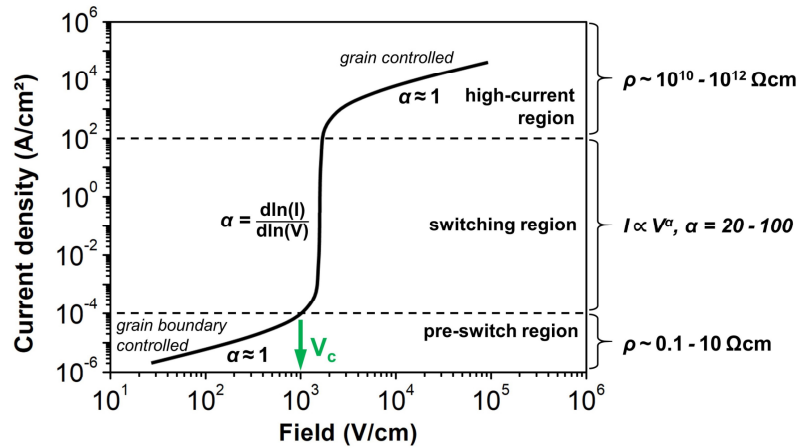


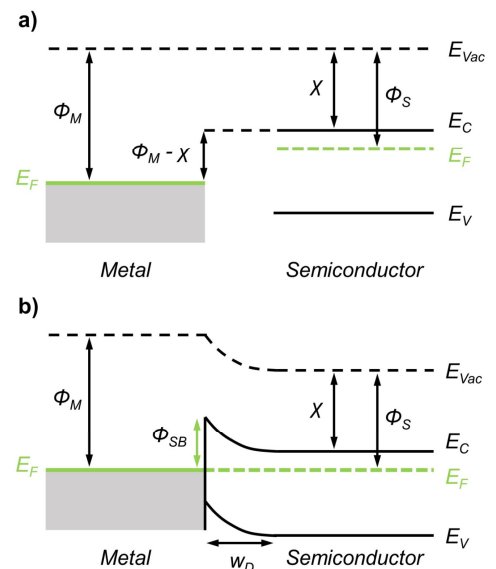
Figure 1-7: Typical I-V curve of a commercial polycrystalline varistor. In the pre-switch and high-current regime, where the current is controlled by the grain boundaries and the grain's bulk properties, respectively, the electrical behavior is quasi-ohmic with $\alpha \approx 1$. In the switching region, the current I increases proportionally to V^α . Reworked after Fig 1 by Clarke.⁹⁰

The properties of regular single Schottky barriers, which

occur at metal-semiconductor contacts, are in principle governed by the difference between the work function of the metal (Φ_M) and the workfunction (Φ_S) and electron affinity (χ) of the semiconductor.^{97, 98} In the case of an n-type semiconductor with $\Phi_M > \Phi_S$, electrons are transferred from the semiconductor to the metal side of the junction, leaving a depletion layer behind of width W_D and hence induce a potential barrier with height $\Phi_{SB} = \Phi_M - \chi$ according to the Schottky-Mott rule (Figure 1-8).^{99, 100}

Figure 1-8: Band diagram of a Schottky barrier at a metal/n-type semiconductor junction a) before and b) after contacting. Due to $\Phi_M > \Phi_S$, electrons are transferred to the metal side in the course of Fermi level equalization, which causes band bending and formation of a potential barrier Φ_{SB} and a depletion layer W_D . Reworked after Figure 2-3 by Keil.¹⁰¹

In contrast to that, a (small) ohmic contact is formed for an n-type/metal junction with $\Phi_M < \Phi_S$, since electrons are transferred from the metal to the semiconductor accumulating at the boundary causing an inverse band bending.¹⁰² For a p-type/metal contact, the converse relationship applies with a Schottky barrier for $\Phi_M < \Phi_S$ and an ohmic contact for $\Phi_M > \Phi_S$. However, the situation at real junctions is significantly complicated by additional effects, such as image force barrier lowering or,¹⁰³ to an especially large extent, by the so-called Fermi-level pinning due to the presence of a high density of gap states or polarized chemical bonds at the interface.^{104, 105, 106} In the latter case, the actual barrier height is found to be largely independent of the metal's work function since the semiconductor's band structure rather depends on the surface or metal-interface states instead of the metal's bulk properties. In particular, the fabrication of good-



quality (low) ohmic contacts, which are needed for accurate electric measurements, can be hindered that way.

In the DSB concept for ZnO varistors, originally developed by Pike and Seager^{107, 108} and refined by Blatter and Greuter,^{109, 110} two n-type semiconducting grains are separated by an (infinitely thin) layer of grain-boundary material, which is the same material as the adjacent grains and hence has the same band gap, but is considered to be comparably rich in acceptor-like defect states (Figure 1-9 a)). In consequence, the Fermi-level is different for the grains and the grain-boundary material. Furthermore, the latter features additional electronic states in the band gap region with those above the Fermi-level being unoccupied. After joining these three pieces, electrons are transferred from both sides to the grain boundary, occupying the defect states and equalizing the Fermi-level throughout the entire resulting bicrystal. Consequently, a negative sheet charge with adjacent positive space-charge regions is formed, which gives rise to a symmetric potential barrier centered at the interface, resembling the semiconductor part of an n-type Schottky barrier mirrored at the grain boundary (Figure 1-9 b)).

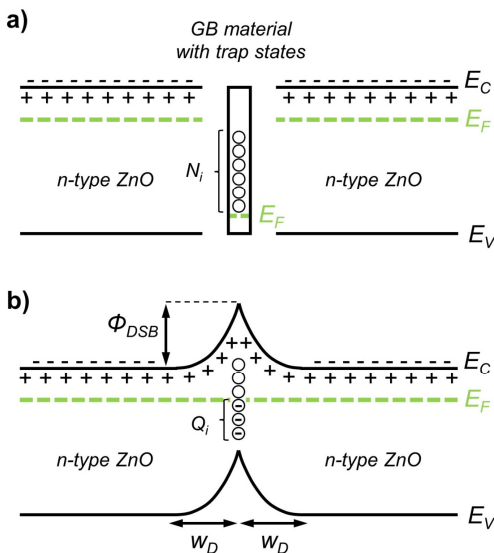


Figure 1-9: Band diagram of a double Schottky barrier at a varistor-type interface a) before and b) after contacting. a) Two n-type ZnO grains are separated by GB material with additional unoccupied trap states N_i and hence a lower Fermi level. Upon contacting and Fermi level equalization, the trap states get filled by electrons from both sides, leading to a negative sheet charge Q_i at the interface, depletion layers W_D on both sides and, in consequence, the formation of a double Schottky barrier. Reworked after Figure 14-6 by Pike.¹⁰⁸

The key similarity to Schottky barriers is the mechanism of charge carrier transport, which can be described by the thermionic emission model, i.e., the surmounting of potential barriers by electrons of sufficiently high kinetic energy.^{97, 111} In doing so, thermionic emission across DSBs is able to largely

explain the varistor charge carrier transport in the pre-switch and in the high-current regions, as well as the corresponding temperature dependence.⁹⁰ However, it is insufficient to fully explain the characteristic varistor behavior in the non-linear regime. Therefore, Pike and Seager included a feedback process of minority charge carriers, i.e., holes, generated by “hot” electrons, which facilitates the barrier breakdown.^{107, 108} An entire sweep through all three regimes of varistor I - V characteristics is summed up in the following:

Starting with an ideal symmetric varistor DSB, the band structure is deformed and the energy level positions of the electronic trap states are changed upon application of an external voltage as shown in Figure 1-10. Thus, the depletion layer width is altered and the barrier height would be reduced. However, Fermi-level pinning occurs if trap states, which remained unoccupied so far, get successively filled by electrons when their level is lowered. As long as these states are not completely filled, the additionally trapped electrons counteract a decrease of the barrier

potential. In consequence, no significant change in barrier height occurs and the varistor remains in the pre-switch region and the current flow across the boundary still corresponds to regular thermionic emission. However, applying a sufficiently high voltage – the switching voltage V_C – eventually causes the trap states to be entirely filled and the potential barrier becomes sensitive to a further voltage increase, hence the varistor enters the non-linear regime. In contrast to the pre-switch region, electrons are now not only transported across the barrier by thermionic emission but also gain sufficient kinetic energy to cause impact ionization of valence and acceptor states in the depletion region. Thus, holes (electron-hole pairs) are created, which are attracted by the electrostatic field at the boundary, hence diffusing as minority charge carriers back to the potential barrier where they compensate for trapped negative charges. In consequence of this avalanche-like effect, the barrier is lowered disproportionately fast and the current flow is increased, which provides the characteristic non-linear electron transport of varistor materials. Finally, in the high-current regime, the conductivity is dominated (or rather limited) by the bulk conductivity of the ZnO grains, which naturally depends on the doping level, especially the number of shallow donors (cf. pp. 7). Neglecting the asymmetries present in real, non-idealized grain boundaries, the mechanism is exactly the same for an inverse polarization of the applied voltage, and hence – in contrast to single diodes (Schottky or else) – no distinct forward or backward bias exists.

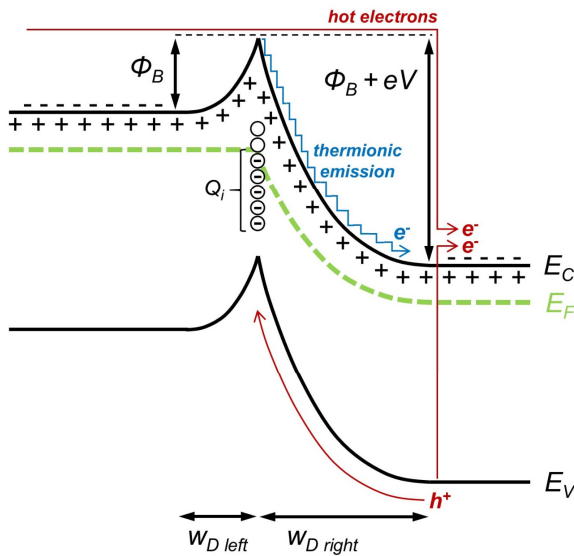


Figure 1-10: Illustration of the breakdown mechanism for varistor-type potential barriers under voltage application. Below the critical voltage V_C , the band structure is deformed and unoccupied trap states get successively filled, counteracting a barrier decrease. Current is governed by thermionic emission. Reaching the critical voltage, hot electrons occur, which ionize valence states and thus, generate electron-hole pairs. Being attracted by the electrostatic field, h^+ diffuse to and counteract the negative sheet charge, leading to an exponentially fast lowering of the potential barrier. Reworked after Figure 14-10 by Pike.¹⁰⁸

A detailed derivation and discussion of the mathematical expressions for the described model is found in the work of Pike and Seager^{107, 108} and in the publications by Blatter

and Greuter.^{109, 110, 112} Here, only the main resulting formulas for barrier height and electron transport shall be mentioned according to the simplified model presented in the much-valued review paper on ZnO varistor ceramics by Clarke.⁹⁰ Based on thermionic emission, the current density J across the boundary is

$$J = A^*T^2 \exp\left(\frac{-(q\Phi_B(V) + \epsilon\xi)}{kT}\right) \cdot \exp\left(\frac{-qV}{kT}\right) \quad \text{Eq. 1.9}$$

The barrier height Φ_B can be approximated in terms of a critical voltage V_C as

$$\Phi_B(V) = \frac{V_C}{4} \left(1 - \frac{V}{V_C}\right)^{1/2} \quad \text{Eq. 1.10}$$

1.5. Doping of varistor ceramics

In order to create sufficient trap states at the grain boundary, which are necessary for the varistor effect as discussed in section 1.4 (pp. 10), appropriate doping is essential. In the case of ZnO varistors ceramics, there are four main doping systems based on praseodymium, vanadium, barium and bismuth, respectively.¹¹³ Commercial varistors, however, are mostly based on either praseodymium or bismuth, with the latter being the most common doping system.⁹⁵ Although the details of the defect state formation mechanism are still not completely clarified, a certain consensus has emerged comprising the application of bismuth or praseodymium as a „grain boundary activator“ in combination with further transition metal elements such as manganese, cobalt or nickel.^{90, 96} Whereas the latter are “only” added for the purpose of improving the varistor performance regarding non-linearity and stability to degradation, the key role in the formation of the required defect states is attributed to the large-ion dopants (Bi, Pr) and the oxygen concentration at the interface. However, there is still some lack of clarity regarding the nature of the corresponding defects, their energies and hence their position in the band gap.⁹⁶ Nevertheless, there is a general agreement on the existence of three different states, which are two shallow bulk trap states and one deep trap state at the interface. The shallow bulk traps are assigned to positions at ~ 0.14 eV and ~ 0.24 eV below the conduction band according to Chen et al.,¹¹⁴ though it should be noted that a variety of results are reported on this issue,⁹⁰ which is probably due to differences in the respective chemical composition, treatment and applied investigation method. For example, admittance spectroscopy indicated the states to occur at ~ 0.20 eV and 0.34 eV.¹¹⁵ Their microscopic origin is also still under debate, since indications were found that they might not be due to zinc interstitials Zn_i and oxygen vacancies V_O as originally suggested by earlier studies.^{90, 116, 117} The deep trap state was also found at different positions ranging from 0.6 – 0.7 eV to ~ 1.1 eV below the conduction band.^{115, 118} However, a notable result was obtained by Tsuda and Mukae,¹¹⁹ who found the energy level of this deep trap state to be the same in both Bi- and Pr-doped varistors, which points towards an interpretation attributing the defect state rather to a dopant-influenced interface structure than to the dopant itself. This is consistent with earlier results by Gambino et al.,¹¹⁸ who obtained similar values for the deep trap state in Bi- and Pr-based varistors. Furthermore, first-principle-calculations by Carlsson et al.¹²⁰ indicated that Bi does not form the required defect states directly, but lowers the formation energy of acceptor-type defects, such as zinc vacancies (V_{Zn}) and oxygen interstitials (O_i), due to the formation of an interfacial ($Bi_{Zn} - V_{Zn} - O_i$) defect complex. Although Bi_{Zn} itself is a donor-type defect, the defect complex overall exhibits acceptor characteristics. In addition, similar results were reported for Pr,¹²¹ as well as for cobalt impurities, which form donor-type Co_{Zn} defects, but promote and stabilize acceptor-type V_{Zn} .¹²² Since these defects are commonly associated

with (local) oxygen excess, these results elucidate the connection between dopants, defect states and the characteristic oxygen excess in varistor ceramics. It was observed multiple times that highly non-linear properties correlate with, or even more, require excess oxygen at the grain boundaries.^{123, 124, 125} Complementary, XPS measurements by Stucki and Greuter¹²⁶ on degraded samples with little to no varistor behavior showed a significant oxygen deficiency. In addition, experiments by Sonder and Austin¹²⁷ showed that degradation occurs in reducing environments already at comparably low temperatures (150 – 500 °C), whereas annealing in oxidizing atmosphere restores the original varistor properties, although higher temperatures (500 – 700 °C) are required. In summary, the reported results point out that the role of the metal dopants is, in the simplest case, to provide excess oxygen (O_i) at the interfaces in order to facilitate and maintain the p-type nature of the grain boundary material.^{126, 128}

Especially in commercial polycrystalline varistor ceramics, the (successful) doping with Bi or comparable elements as well as the barrier formation is often associated with segregation towards grain boundaries, triple junctions and the formation of amorphous or crystalline secondary phases and (continuous) interfacial films.¹²⁹⁻¹³⁵ However, the idea of a continuous, grain-separating 3D network of intergranular secondary phases being mandatory for the varistor effect was ruled out via TEM studies by Clarke (although he showed simultaneously that the interfaces, nevertheless, feature a thin Bi-rich film).^{130, 136} Furthermore, varistor behavior is also reported for interfaces free of both secondary-phases and thin-films,¹³⁷⁻¹⁴⁰ which indicates that the presence of discrete amorphous or crystalline dopant phases is not essential for the varistor effect. Therefore, the decoration of the interfaces with respective dopant atoms or the incorporation of those into the adjacent crystals appears to be sufficient in principle. It should be noted that this is perfectly consistent with the widely accepted model by Pike and Seager¹⁰⁸ for varistor-type barrier formation, which just presupposes „*grain-boundary material*“ with appropriate defect states and not necessarily distinct secondary phases or films.

Nevertheless, in polycrystalline ceramics, the presence and constitution of such secondary dopant-phases at varistor grain boundaries influence the electrical properties in various ways.¹⁴¹ For example, degradation and asymmetric I - V behavior of individual varistor grain boundaries were found to be influenced by the modification of Bi_2O_3 present at the interface.^{142, 143} Furthermore, a continuous 3D-network of Bi-rich intergranular phases may provide additional current pathways bypassing the true varistor boundaries.¹⁴⁴⁻¹⁴⁷ Therefore, it can distinctively affect the leakage current and the overall breakdown voltage, depending on the intergranular material's conductivity, which is (among other factors) determined by its structure, the predominant Bi_2O_3 modification¹⁴² and the concentration of other dopants phases, such as Y_2O_3 or Al_2O_3 .^{148, 149} In addition, the constitution of such 3D intergranular networks also determines the transport of (excess) oxygen to the grain boundaries during annealing, which is of particular importance for the varistor effect as mentioned above.^{90, 123, 144} Finally, dopants or *additives*, as they are sometimes referred to when explicitly considered as non-soluble secondary phases, indirectly influence the resulting electrical characteristics by affecting the sintering process. In

a polycrystalline ZnO varistor, the total breakdown voltage is determined by the interaction of all individual varistor boundaries in the respective current path. Both switching voltage and energy-handling capacity increase with an increasing number of grains per area, which renders grain-growth control an important aspect in the fabrication of varistor ceramics.⁹⁰ In consequence, certain dopants, such as Sb_2O_3 and CeO_2 or MnO_2 and TiO_2 are mainly added for their respective promoting or inhibiting effect on grain growth, although they often have an effect on electrical and other properties (e.g. degradation, stability, inversion boundary formation, etc.) as well, which self-evidently needs to be considered.^{94, 123, 150-153}

1.6. Piezotronics and piezotronic modulation of potential barriers

Originally introduced by Wang in 2007,^{154, 155} the term *piezotronic* refers to the coupling of piezoelectric and semiconducting properties, which enables the tuning of electrostatic potential barriers via the application of mechanical stress. In other words, the charge carrier transport at metal-semiconductor (Schottky) or p-n junctions is controlled by the generation of piezoelectric charges, which modulate the barrier height. This mechanism offers the possibility to develop novel devices based on the piezotronic effect, such as strain-gated transistors, pressure sensors or various opto-electronics and is closely related to the fabrication of nanogenerators and self-powered nanosystems, which likewise utilize the combination of piezoelectricity and semiconduction.^{156, 157} Due to zinc oxide's unique characteristics, which include both semiconducting and piezoelectric properties as well as a large variety of easily producible nanostructures (nanowires, -belts, -rings, -springs, -cages, etc.), it is seen as one of the best suited and most promising materials in the field of piezotronics.^{158, 159} For example, a single ZnO nanowire (grown along the polar *c*-axis) can be used as a strain-gated transistor when contacted at both ends, i.e., (0001) and (000 $\bar{1}$), with an appropriate metal ($\Phi_M > \Phi_{\text{ZnO}}$), hence forming two Schottky barriers (Figure 1-11).¹⁶⁰

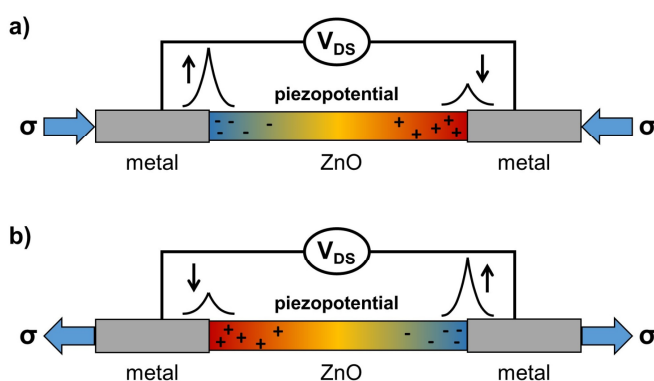


Figure 1-11: Piezotronic application of a single ZnO nanowire as a strain-gated transistor. Two contacts suffice since the gate voltage is adjusted via mechanical load. a) Compressive stress: piezoelectric charges increase the Schottky barrier at one side (left) while decreasing the other (right). b) Tensile stress: reversed piezo-charges and impact on the Schottky barriers, hence inverse operation of the transistor is possible.

In contrast to regular field-effect transistors, which require a third gate electrode, the two contacts (drain and source) suffice, since the gate voltage controlling the carrier transport is replaced by the piezopotential, which is adjusted via an externally applied stress. In doing so, generated piezoelectric charges increase one Schottky barrier while simultaneously decreasing the other depending on the orientation and if tensile or compressive strain is used. Consequently, the transistor's function is controlled, including the possibility of an inverse operation.

Regarding the fundamental theory of the piezotronic effect, two main models are reported, which are both capable of providing an applicable mathematical description of the Schottky barrier height modulation due to the influence of piezoelectric charges.¹⁰¹ The main difference between them is how the piezoelectric charges are considered. In contrast to the “classic” theory of piezoelectricity, which regards the polarization charge as a surface charge, the model developed by Zhang et al.¹⁶¹ assumes a spatial charge distribution with a defined width W_{piezo} and a Schottky barrier height Φ_{SB} according to

$$\Phi_{SB} = \Phi_{SB}^0 - \frac{q^2 \rho_{piezo} W_{Piezo}^2}{2\varepsilon_r \varepsilon_0} \quad \text{Eq. 1.11}$$

On the contrary, the model by Pintilie and Alexe¹⁶² still regards the polarization charge as a surface (or sheet) charge, but introduces a finite distance δ_{gap} between them and the physical interface of the metal, with the barrier height given as

$$\Phi_{SB} = \Phi_{SB}^0 - q \frac{\delta_{Gap} Q_p}{\varepsilon_{Int} \varepsilon_0} \quad \text{Eq. 1.12}$$

It should be noted that both models assume the modulation not only being dependent on the sheer amount of generated piezoelectric charges but also on the interfacial distance between them and the (negative) sheet charge on the metal side, as expressed by the spatial distribution width W_{piezo} and the distance δ_{gap} , respectively.

Considering the piezotronic effect on Schottky barriers and the unique suitability of ZnO, it is straightforward to extend the former on double Schottky barriers in varistor ceramics. In this case, the piezotronic modulation corresponds to the modification of the interfacial sheet charge by the piezoelectric charges contributed from both adjacent grains, as described by Verghese and Clark.¹⁶³ Although this mechanism could be underpinned by experimental results in principle,¹⁶⁴ the respective model needed to be extended as shown by Baraki et al.,¹⁶⁵ who included the effects of Fermi-level pinning and voltage application. Upon low mechanical stress, the DSB height was found to be insensitive to the generated piezoelectric charges up to a specific value, which is explained by Fermi-level pinning in similarity to the general varistor breakdown mechanism (cf. pp. 12). Positive piezoelectric charges lower the barrier just as the energy level of the varistor trap states, hence previously unoccupied states get successively filled by free charge carriers (electrons), which partially compensate and impede a change in barrier height until they are completely below the Fermi-level. However, voltage application has an analogous effect and can therefore be utilized to change the barrier’s sensitivity to mechanical load. Thus, an increasing electric field decreases the mechanical stress necessary to induce significant changes in the barrier height (for the case of a configuration that generates positive piezo-charges at the interface). According to this model,¹⁶⁵ the voltage-dependent DSB height is

$$\Phi_{DSB}(V) = \frac{\left((Q_i + Q_p)^2 - 2qN_D V \varepsilon_r \varepsilon_0 \right)^2}{8qN_D \varepsilon_r \varepsilon_0 (Q_i + Q_p)^2} \quad \text{Eq. 1.13}$$

1.7. ZnO bicrystals and (0001) inversion boundaries

The investigation of zinc oxide bicrystals represents the backbone of this work. In contrast to polycrystalline samples, bicrystals have several unique advantages. Foremost, they provide the possibility to synthesize interfaces with well-defined orientation and chemistry. Thus, different orientations and doping strategies as well as special grain-boundary configurations can be analyzed. By featuring exactly one interface, ZnO bicrystals are well-suited for electrical measurements investigating the respective piezotronic and varistor properties. Compared to polycrystalline materials, where every grain boundary differs in terms of orientation, structure and probably doping as well, the attribution of measured electrical characteristics to specific structural or chemical features is significantly simplified, especially if combined with analyzation and imaging techniques such as TEM. Besides being a model system for special grain-boundary configurations, ZnO bicrystals also hold the potential for the development of novel piezotronic devices, as they allow tailoring orientation as well as doping in accordance with the respective requirements.

In the case of zinc oxide, (0001) and (000 $\bar{1}$) inversion-boundary configurations are of particular interest for piezotronic bicrystals, as they allow an optimization of the piezotronic effect upon compressive stress, which is beneficial for both fundamental studies as well as for possible applications. Such a configuration contains two ZnO crystals with opposing, anti-parallel c -axis, joined at their (0001) or (000 $\bar{1}$) basal planes (Figure 1-12). Since the terminating (0001) layer in the positive c -axis direction is always a Zn layer and in the opposite direction, the terminating (000 $\bar{1}$) layer is always an O layer, these orientations are also referred to as *head-to-head* or $Zn|Zn$ and *tail-to-tail* or $O|O$, respectively.^a Such a bicrystal could also be regarded as an artificial basal plane inversion twin, similar to the naturally occurring {0001} twinning of zincite. Such bicrystal configurations are also referred to as *inversion domain boundaries* in some literature reports, which emphasize the aspect of inverted polarity, but are synonymous with *inversion boundaries* (IB), as they are termed within this work.

Due to the inversion symmetry, compressive stress applied parallel to the c -axis causes the generation and accumulation of piezoelectric charges at the interface, which are negative in the case of a $Zn|Zn$ and positive for an $O|O$ configuration (Figure 1-12). In doing so, a varistor-type potential barrier at the interface can be modulated piezotronically (cf. pp. 16). Whereas negative charges add to the trapped electrons and thus, increase the barrier height, positive charges compensate trapped electrons, leading to a decrease in barrier height. In consequence, the electrical conductivity is modulated as well, which provides, in the ideal case, the possibility to mechanically switch between an on and off, or a conductive and a non-conductive state. In

^a Please note, in the ZnO literature, the “head” and “tail” denotation is sometimes assigned to the opposite directions. In these cases, the authors do not refer to the c -axis, but to the direction of the (spontaneous) polarization P_3 , which has its positive direction pointing towards the O-terminated (000 $\bar{1}$) side instead of (0001). Please note, throughout this work, “head” and “tail” always refer to the c -axis with the positive, i.e., “head”, direction towards the Zn-terminated side (0001).

the context of varistors, this corresponds to the high-current and pre-switch regions, respectively.

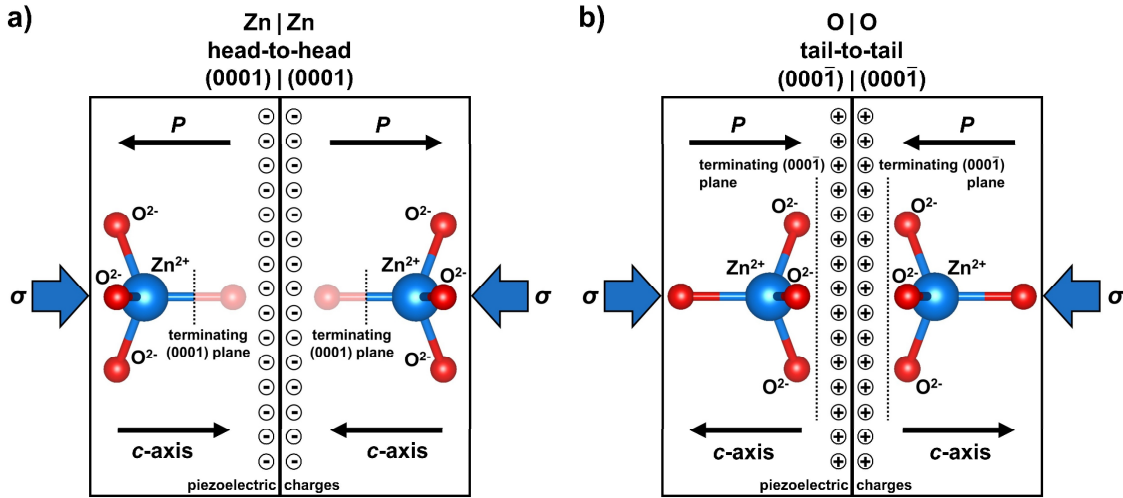


Figure 1-12: Illustration of the two main configurations of ZnO bicrystals investigated in this work: a) Zn|Zn terminated bicrystal with an (0001)|(0001) interface corresponding to a head-to-head orientation of the c-axes. b) O|O terminated bicrystal with an (000 $\bar{1}$)|(000 $\bar{1}$) interface corresponding to a tail-to-tail orientation of the c-axes. Both orientations provide an optimized piezoelectric response (polarization P) upon compressive stress applied along the c-axes, causing the accumulation of negative and positive piezo-charges at the interface for a Zn|Zn and O|O configuration, respectively.

Although zinc oxide as a varistor or semiconductor material was extensively researched and the corresponding literature is vast,⁶⁰ dedicated bicrystal studies are rare. Being probably the first attempt to model a ZnO varistor grain boundary using a bicrystal approach, Schwing and Hoffmann investigated samples synthesized from pairs of ZnO single crystals with an intermediate metal oxide layer and a ceramic binder.^{166, 167} The intermediate layer contained the common varistor dopants Bi₂O₃, Co₃O₄ and MnO₂, and corresponding *I-V* measurements revealed a breakdown voltage of 3.5 V and a coefficient of non-linearity $\alpha = 8 - 11$, which are typical values for a single grain boundary. However, in the strict sense, this was not a true bicrystal as the metal oxide layer remained after sintering with a thickness of 5 – 20 μm . Lee and Maier reported on the *I-V* characteristics of various undoped and doped bicrystal configurations, at which doping with Mn, Co and Ni was performed by sputter deposition of 50 nm thin films on both single crystals.¹⁶⁸ Further studies on varistor bicrystals were conducted by Cheng et al., who investigated *coincidence site lattice* (CSL)^a twist boundaries with a focus on

^a CSL: Between two overlaid crystal lattices, which are tilted or twisted with respect to each other, special orientations exist, at which sites of both lattices coincide. These coincidence sites define a new lattice, that is, the *coincidence site lattice*; a kind of superstructure with its own unit cell. The relation between the number of lattice points in the CSL unit cell and the regular unit cell defines the type of CSL and is denoted by the coincidence parameter Σn with $n = 1, 3, 5, 7, \dots$. In other words, Σn is the CSL cell volume expressed in units of regular cell volume. Σn unambiguously defines the relative orientation of the two original lattices and $\Sigma 1$ denotes a perfect fitting with both lattices merging completely, like in a perfect single crystal. Between two grains in $\Sigma n \geq 3$ orientation, boundaries exist, which form periodic structures at the interface related to the coinciding sites. These “partly fitting” interfaces are energetically favorable to arbitrary interfaces and hence, twinning or faceted boundaries typically correspond to such CSL boundaries. With higher n , fitting and coherency are reduced. Please note, as the atomic structure is not rigid, small misalignments from Σn , theoretically extremely incoherent, are compensated by lattice distortions or dislocations. Such cases, often close to $\Sigma 1$, are denoted as *small angle grain boundaries*.

asymmetrical I - V characteristics, degradation and dielectric behavior.^{169, 170, 171} The most comprehensive TEM studies on ZnO bicrystals, addressing structure, doping and origin of the varistor effect, were performed by Sato et al.^{138, 139, 172-177} and also published in a summary paper.¹⁴⁰ They investigated undoped and sputter-doped bicrystals with praseodymium and cobalt, both single and co-doped. Furthermore, they applied various bicrystal orientations with different CSL configurations, achieved by specific twist and symmetric tilt of the crystals, with most of them being derived from (0001) IBs, but also from a - a and a - c bicrystals with parallel a -axes and c -axes. Their results revealed that certain Σ boundaries provide segregation sites for the large Pr atoms, which are normally incompatible and insoluble in the ZnO lattice. Moreover, they found a distinct relationship between the coherency of the interface, the amount of incorporated Pr and hence the varistor properties. Whereas highly coherent configurations, such as $\Sigma 1$, were dopant-free and ohmic ($\alpha \approx 1$), less-coherent interfaces, e.g. $\Sigma 7$ and a - c , featured praseodymium at the interface as well as non-linear characteristics with $\alpha = 1.8$ and $\alpha = 3.9$, respectively. Subsequently, they designed specifically misoriented $(8\bar{5}\bar{3}0)|(11\bar{2}0)$ and $(2\ 11\ \bar{1}\bar{3}\ 0)|(0001)$ bicrystals with maximized incoherency, which showed the highest Pr segregation and non-linearity ($\alpha > 20$) among their entire set of samples. These results are important, since they point out the previously unrecognized importance of grain-boundary coherency for the doping with insoluble large-ion elements, such as Pr or Bi.

The typical piezotronic or varistor application implies doping in any case, but besides its importance for trap-state and potential-barrier formation (cf. pp. 14), dopants might also be essential for the bonding of an $\{0001\}$ IB, since this configuration demands the bonding of two identical atom layers. As carriers of the same charge naturally repel each other, it is difficult if not impossible to consider a ZnO IB without either severe reconstruction or the addition of dopants and probably a distinct interfacial layer. In polycrystalline ZnO ceramics, Zn|Zn IBs are well-known to form spontaneously upon antimony doping and – to a lesser extent – upon tin and titanium doping, as shown and intensively studied by Recnik et al.¹⁷⁸⁻¹⁸³ However, to the author's knowledge, a truly undoped inversion boundary has never been verified in the literature. Lee and Maier report on the electrical characteristics of nominally undoped bicrystals with a purity of >99.99 wt%.¹⁶⁸ Nevertheless, they observed non-ohmic behavior attributed to small contaminations (~ 10 ppm) in some of the undoped samples and considering that they did not check the interfaces by appropriate methods such as analytical (S)TEM, it is doubtful if the interfaces were actually undoped. In the paper by Kim and Goo on IBs in zinc oxide,¹⁸³ the aspect of doping is misleadingly not addressed, but they used Sb-doped ZnO as a matter of fact, which is described in a related paper and explains the observed IB formation.¹⁸⁴ Please note, the bicrystal studies by Sato et al. did feature one undoped $\{0001\}$ IB according to their experimental section, but the aspect of inversion is neither explicitly mentioned or discussed, nor is it verified with appropriate methods revealing the c -axis polarity.^{140, 172, 175} Furthermore, no chemical measurements, such as EDS or EELS, were performed for the undoped interface and only HR-TEM images are shown, which do – in contrast to HAADF-STEM (cf. pp. 39) – not

provide chemical information. Therefore, a contamination, such as shown in Figure 4-7 (p. 52) for example, which might originate from a preceding mechanochemical polishing, would remain unnoticed. Preliminary to the studies on piezotronic bicrystals presented in this thesis, an undoped polycrystalline ZnO sample was extensively investigated by TEM regarding the occurrence of IBs. However, none were observed.

Presently, the only substantial indication of whether and how undoped {0001} IBs might be realized is found by Rohrer and Albe, which performed density functional theory calculations on this very question.¹⁸⁵ Their results yielded three possible models for the Zn|Zn case, which depend on the chemical potential of oxygen, and one model for the O|O case. The favorable models of both configurations are isomorphic (Zn and O positions can be exchanged) and contain an interlayer with half the sites occupied and 4-fold bonding conditions similar to the bulk. However, experimental evidence for these configurations and the formation of truly undoped IBs is still pending.

1.8. Nanocrystals

Doped as well as undoped nanocrystalline ZnO particles, formed from solution via different precipitation methods, are well-known to crystallize within a large variety of possible shapes and sizes, depending on the applied synthesis procedure.^{186, 187} These different morphologies range from simple geometries, such as single-crystalline platelets to complex, often polycrystalline and sometimes twinned arrangements, e.g., sea-urchin-like assemblages of acicular ZnO crystals. Among this variety of forms, ZnO sheets, discs and platelets attract special interest, since they are (quasi) 2D structures holding a large potential for application in various fields, such as catalysis, opto- and piezoelectronics or chemical sensing.^{186, 188} This is not only due to zinc oxide's inherent semiconducting and piezoelectric properties, but especially to the prospect of fabricating well-defined, equally sized 2D particles,^a hexagons in particular, which may provide access to innovative bottom-up techniques in the designs of novel devices via self-assembly into functionalized 2D or 3D arrays.^{189, 190, 191} For example, such a self-assembled close-packed monolayer of hexagonal crystallites could be achieved via Langmuir-Blodgett deposition in case of β -Co(OH)₂,^b which additionally allowed the transformation into CoO by post-annealing and showed remarkable properties in electric resistivity switching.¹⁹² Likewise, a Langmuir-Blodgett deposition of ZnO hexagonal platelets should be possible. However, for ZnO, no appropriate synthesis route providing suitable hexagons is established so far, as the obtained mineralization products typically suffer from heterogeneity, low quantity or contamination by other phases (byproducts or additives).¹⁹³⁻¹⁹⁸ In addition to the lack of an

^a Extended, homogenous and complete arrays or layers have naturally high demands on the uniformity of their individual tiles, i.e., the crystallites, since every deviation implies a failure or interruption of the tessellation. In the case of functionalized films, such deviations (i.e., heterogeneity of the crystallites) can plausibly be seen as detrimental, as they might adversely affect the respective properties and limit the maximum achievable size of a single undisturbed array.

^b The β -phase of Co(OH)₂ has brucite (Mg(OH)₂) structure and hence, crystallizes in space group No. 164 $P\bar{3}m1$. Therefore, although being trigonal, it belongs to the hexagonal crystal family and can adopt (pseudo)-hexagonal morphologies similar to wurtzite ZnO crystallites.

adequate synthesis route, the actual effect of dopants and additives on the atomic level is also not completely elucidated, despite the fact that the general ZnO platelet formation via thermohydrolysis is well established, including the effects of different reaction parameters. Thus, summarizing the cited reports, the crystallization process can be best controlled by the application of strong coordinating anions, such as citrate or acetate, by the solvent, which should be either N,N-dimethylformamide or ethanol/water mixtures and finally, by doping with cobalt or magnesium. Nevertheless, more research is required to define and understand the right combination of growth modifiers in order to obtain well-defined, equally sized ZnO hexagons, which meet the demands of the pursued self-assembly by Langmuir-Blodgett deposition, dip-coating or other eligible techniques.

2. Aims, Motivation and Thesis Concept

The background behind this work is the development of and research into novel piezotronic bicrystals, which enable the tuning of varistor-type potential barriers via coupling of piezoelectric, semiconducting and varistor properties.^{101, 199} The main motivation to conduct TEM investigations on the respective samples can be attributed to the nature of the varistor effect itself. As detailed in the introductory chapter, varistor behavior is an interface-related effect (cf. pp. 10). However, since an “interface” between two grains is naturally limited to the terminating atomic planes and their direct vicinity, investigations on the very important issues of structure and doping, for example, are by no means trivial and demand atomic resolution in the end. In this regard, (S)TEM stands out in the pool of characterization methods, as it is capable of simultaneously delivering structural and chemical information with a spatial resolution down to the atomic level (cf. pp. 32). In doing so, TEM is complementary to electrical measurements, which characterize the resulting properties but remain “macroscopic” at the same time. High-resolution HAADF-STEM employing C_s -correction is probably the best-suited TEM method in this context, and thus, frequently used in this thesis, since it straightforwardly combines interpretable images of the atomic structure with chemical information, easily extended by pinpoint precise EDS measurements. Nonetheless, other TEM methods, such as SAED, ABF-STEM, two-beam imaging, HR-TEM, NBED, etc. are likewise indispensable for a complete characterization, which is not only useful in understanding the piezotronic bicrystals but also regarding the still not completely elucidated varistor effect itself. Finally, TEM provides feedback on the synthesis procedure and can be reliably used to check and verify whether aspired properties have been achieved. Where reasonable, TEM was complemented by SEM, e.g., for imaging and surveys at the mesoscale ($> 1 \mu\text{m}$). In consequence, the aims are:

- Verification of the successful synthesis of bicrystals
- Studying the bicrystal interfaces in terms of:
 - atomic structure: bonding conditions, defects, disorder
 - presence of interfacial films and secondary phases
 - presence of dopants (Bi in particular); conditions of doping
- Correlation of the TEM results with the electrical properties (I - V measurements).

In the case of the nanocrystalline hexagonal platelets, where the background is the establishment of a synthesis route appropriate for a subsequent self-assembled tessellation (cf. pp. 21), the focus of the TEM investigations lies on the characterization of the obtained mineralization products in terms of chemical (EDS) and structural (BF-/HR-TEM, SAED) homogeneity. In doing so, the main goal is to provide feedback for an optimization of the synthesis procedure. Furthermore, as twinning of nanocrystals was observed for nearly all variations of the synthesis route, the verification of the hexagons’ single-crystallinity is of special interest. Since this twinning is expected to be related to a c -axis inversion, the same TEM methods as for the bicrystal studies can be applied, in particular, NBED and ABF-STEM, which

allow the determination of the *c*-axis' absolute polarity. In addition, the investigations are extended on rod-shaped nanotwins, which were also obtained as mineralization products from the hexagon-synthesis experiments. The main task was to identify their twinning character, which is a fundamental question against the background that they might hold potential for future applications in their own right. Therefore, TEM studies are performed with the following aims:

- Structural and chemical characterization of the mineralization products at different reaction stages (hexagon synthesis)
- Verification of the successful synthesis of hexagonal ZnO platelets and, in particular, their single-crystallinity with respect to possible twinning
- Determination of the twinning character and twin-boundary conditions of the rod-shaped crystallites.

Addressing these research questions, the main part of this thesis deals with TEM investigations of ZnO bicrystals. After a description of the synthesis methods (pp. 25), including some preliminary findings, and an introduction to the applied characterization methods (pp. 30), the bicrystal results are presented. Following the undoped reference samples (pp. 47), the various doped specimens, subdivided by their respective synthesis procedure, are shown and discussed (pp. 58, pp. 70 and pp. 85). In doing so, the main results of this thesis are deduced from a comparison of two bicrystals (DB-I and EST-O|O, cf. pp. 78), which represent opposing cases of grain-boundary configuration, Bi segregation and *I-V* characteristics. In addition, a qualitative analysis of the thermodynamical aspects of the Bi-segregation, attained by applying Gibb's adsorption isotherm, is included (pp. 80) as well as a comparison with literature examples of diverse material systems showing that the obtained insights on interfacial segregation can be generalized (pp. 82). Subsequently, the hexagonal platelets and nanotwins are examined (pp. 98). At the end of each (sub-)chapter, a short summary is given (green boxes) as well as a final résumé in chapter 6 (pp. 107), which sums up the entire results, including some conclusive remarks and a short outlook on the addressed topics.

.

3. Experimental Methods

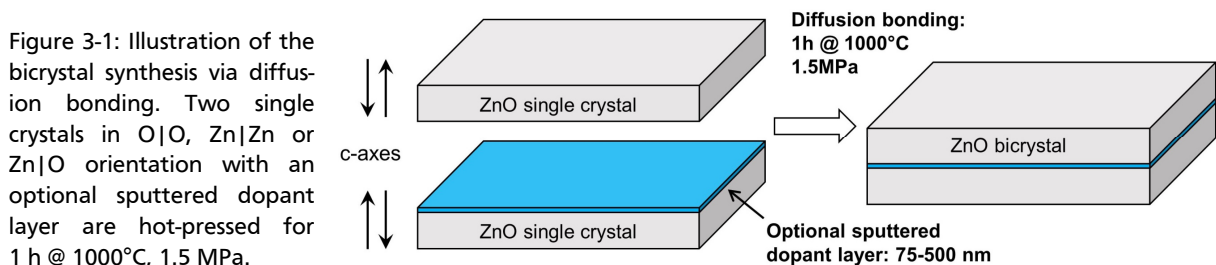
3.1. Synthesis

With respect to the applied synthesis methods, which are *epitaxial solid-state transformation* (EST) and *diffusion bonding*, two types of ZnO bicrystals were fabricated. The corresponding samples are denoted by the prefixes EST and B/DB in the following, with B referring to undoped and DB to doped diffusion-bonded bicrystals. The synthesis of all ZnO bicrystals presented in this work was devised and performed by Peter Keil,^a except for samples DB-a|c and DB-26, which were synthesized by Maximilian Gehringer.^a In the case of sample DB-26, suggestions by the author, regarding the degree of tilt, were taken into account (cf. pp. 85). The synthesis of the ZnO hexagons and nano-twins was devised and performed by Dr. Rudolf Hoffmann^b.

The following description of the synthesis procedure reproduces and largely equates to the description as given in the corresponding publications.^{199, 200, 201}

3.1.1. B/DB bicrystals

The diffusion-bonded bicrystals were synthesized by directly hot-pressing two 5 mm × 5 mm × 0.5 mm ZnO single crystals in the desired orientation at 1000 °C for 1 h under a load of 1.5 MPa (Figure 3-1). This synthesis method is sometimes also referred to as *hot-joining* or *hot-pressing* in the related literature and can be considered the most common and straightforward approach for synthesizing ZnO bicrystals.^{140, 168, 169}



Undoped reference bicrystals were fabricated in all three possible $\{0001\}|\{0001\}$ -IB configurations, that is, O|O, Zn|Zn and Zn|O. Doped bicrystals were prepared in either Zn|Zn or O|O orientation, however, only O|O bicrystals could be used for TEM investigations appropriately, as all Zn|Zn samples were either unsuccessfully bonded or fractured from either the load-dependent *I-V* measurements or sometimes even the hot-pressing.^c For the tilted DB bicrystals, specific asymmetrical tilts were introduced via rotation and respective cutting of one single crystal, while the other was fixed in its respective tail or head position (Figure 3-2). The

^a In affiliation with the group *Nonmetallic-Inorganic Materials* of Prof. Rödel, Institute of Material Science, Technical University of Darmstadt, Darmstadt, Germany.

^b In affiliation with the group *Inorganic & Mesoscopic Chemistry* of Prof. Schneider, Department of Chemistry, Technical University of Darmstadt, Darmstadt, Germany.

^c Please note that this is not an indication of a higher stability or better bonding of O|O bicrystals in contrast to Zn|Zn. There were just much more O|O bicrystals fabricated, as the piezotronic effect was found to be much stronger for this configuration (cf. pp. 77).¹⁹⁹

cutting procedure was performed using a 4240 Benchtop diamond wire-saw^a at a wire speed of 0.8 m/s and sufficient large single crystals to obtain 2.5 mm x 2.5 mm x 0.5 mm pieces, matching the dimensions of the non-rotated crystals.

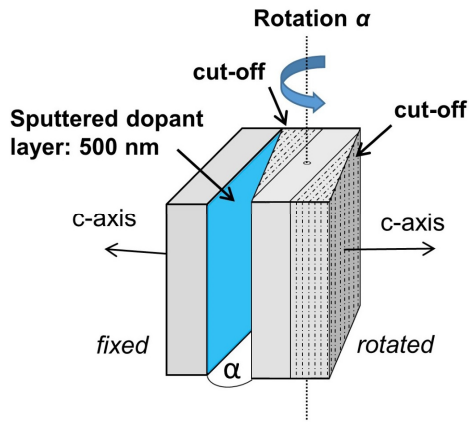
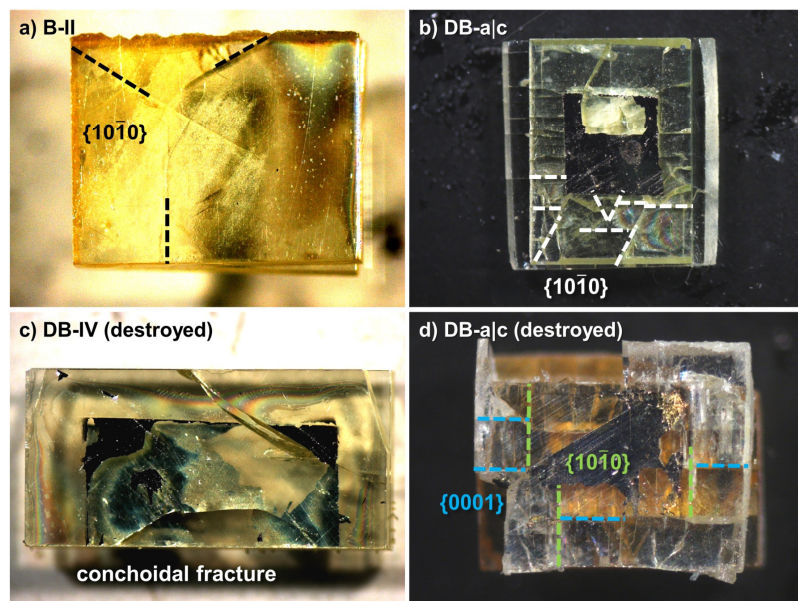


Figure 3-2: Illustration of the synthesis for the tilted DB-bicrystals. An asymmetrical tilt is introduced, at which one crystal with a sputtered dopant layer remains fixed in “head” or “tail” position, while the other is rotated by a specific angle α . For the rotated crystals, larger specimens were used, which allowed cutting them to match the size of the fixed crystal and to obtain a plain and flat interface.

Originally, all tilted DB bicrystals were devised to have an O|O configuration, but sample DB-26 was accidentally bonded in Zn|Zn configuration (cf. p. 91). Besides sample DB-26, only one other tilted DB bicrystal (DB-a|c) was found to be suitable for TEM investigations, due to a large extent of cracks and fracture from the hot-pressing and load-dependent *I-V* measurements or due to incomplete bonding of the other samples. For all DB bicrystals, doping was achieved by depositing Zn-Bi-Co-O films on the {0001} surface of one of the single crystals by RF magnetron sputtering prior to bonding. The composition of the sputtering target was 90 % ZnO, 5 % Bi₂O₃, 5 % Co₃O₄ for samples DB-I and DB-IV, 98 % ZnO, 1 % Bi₂O₃, 1 % Co₃O₄ for sample DB-II and 80.0 % ZnO, 10.0 % Bi₂O₃, 10 % Co₃O₄ for sample DB-III (all values in mol%). The sputtered film thicknesses were nominally 25 nm (DB-IV), 75 nm (DB-I), 300 nm (DB-II) and 500 nm (DB-III). Both tilted samples DB-a|c and DB-26 feature a 500 nm sputtered dopant layer with a composition of 97.27 ZnO, 0.6 Bi₂O₃, 0.63 Co₃O₄, 0.55 Mn(C₅H₇O₂)₂, 0.35 Cr₂O₃, 0.6 NiO (all values in mol%), which corresponds to a typical varistor composition as applied in commercial fabrication.¹²³

Figure 3-3: Some examples of bicrystals, as provided for this thesis. All bicrystals featured cracks and fractures as a consequence of zinc oxide’s perfect {10 $\bar{1}$ 0} cleavage and the load during bonding or *I-V* measurements. a) Sample B-II; no *I-V* measurement performed; cracks are from bonding. b) Sample DB-a|c; highly fractured from load-dependent *I-V* measurements. c) DB-IV bicrystal in O|O orientation with conchoidal fracture; destroyed during TEM sample preparation. d) Second DB bicrystal in a|c orientation; destroyed during TEM sample preparation; direction of view (and applied force) is along the a-axis, which caused additional parting along {0001}.



^a Well Diamantdrahtsäge GmbH, Mannheim, Germany.

It should be noted that all investigated ZnO crystals were highly fragile and featured cracks and fractures to some extent, which mostly followed zinc oxide's perfect $\{10\bar{1}0\}$ cleavage,^a as shown in Figure 3-3. However, conchoidal fracture was observed in a few cases, as well. As stated above, this was found to be a severe impediment to the TEM preparation and hence limited the number of bicrystal samples usable for TEM investigations.

3.1.2. EST bicrystals

For the EST-O|O bicrystal, a doped polycrystalline ZnO ceramic (PC) of $100\ \mu\text{m}$ thickness is placed between two $5\ \text{mm} \times 5\ \text{mm} \times 0.5\ \text{mm}$ ZnO single crystals (SC), which are in tail-to-tail (O|O) orientation of the c -axis (Figure 3-4). Under a load of 1.5 MPa, the sample is diffusion bonded at $1100\ ^\circ\text{C}$ for 2 h in air to achieve a well-bonded SC–PC–SC stack. Subsequently, the stack is annealed at $1100\ ^\circ\text{C}$ for 65 h in a powder bed of the same composition as the polycrystalline layer to prevent an evaporation of dopant elements. This annealing step promotes grain growth of the single crystals into the sacrificial polycrystalline layer until the latter is consumed completely. In consequence, a doped (0001)|(0001) ZnO bicrystal with a single grain boundary is formed.

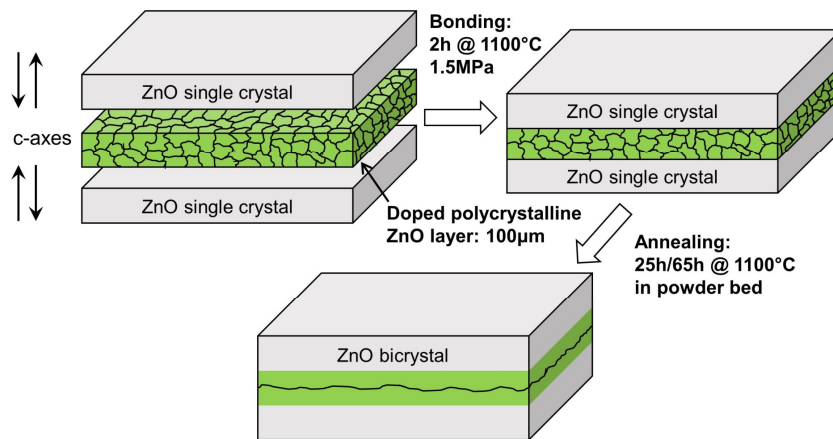


Figure 3-4: Illustration of epitaxial solid-state transformation (EST). Two single crystals in O|O or Zn|Zn orientation with a doped polycrystalline interlayer of $100\ \mu\text{m}$ thickness form a single-poly-single crystalline stack bonded for 2 h @ $1100\ ^\circ\text{C}$, 1.5 MPa. Upon the subsequent annealing step of 25 h (Zn|Zn) or 65 h (O|O) @ $1100\ ^\circ\text{C}$, the single crystals grow at the expense of the sacrificial interlayer, which is epitaxially transformed until a bicrystal is obtained.

Doping is controlled by the composition of the polycrystalline sacrificial layer, which was 97.27 ZnO, 0.6 Bi₂O₃, 0.63 Co₃O₄, 0.55 Mn(C₅H₇O₂)₂, 0.35 Cr₂O₃, 0.6 NiO (all values in mol%), being a typical varistor composition as in commercial applications.¹²³

In addition to EST-O|O, an EST bicrystal in head-to-head (Zn|Zn) orientation was synthesized, applying the same conditions except for the annealing step, which was adjusted to 25 h @ $1100\ ^\circ\text{C}$ according to the higher growth rate in [0001] direction. However, the epitaxial transformation was found to be incomplete, as revealed by polarized light microscopy (PLM) and SEM (Figure 3-5). In consequence, no distinct bicrystal grain boundary could be identified and the sample was not subjected to further TEM investigations. Nevertheless, corresponding I - V measurements showed a typical bicrystalline response and therefore, were added to the results in section 4.3.2 (pp. 77) for comparative reasons.

^a The possible angle between various $\{10\bar{1}0\}$ planes (as visible in [0001] viewing direction) is $n \cdot 60^\circ$ with $n = 1, 2, 3, \dots$

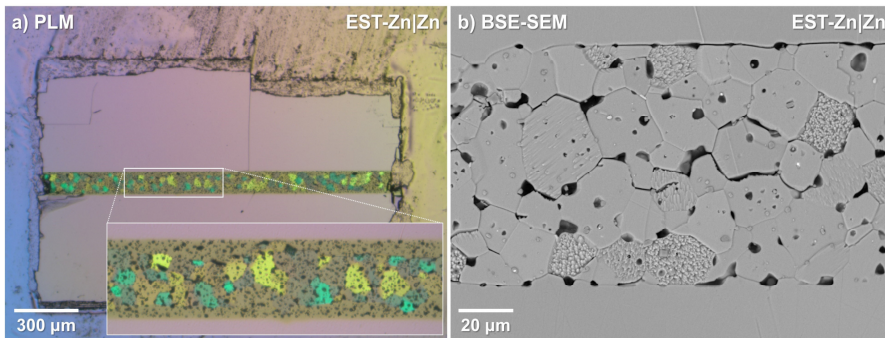
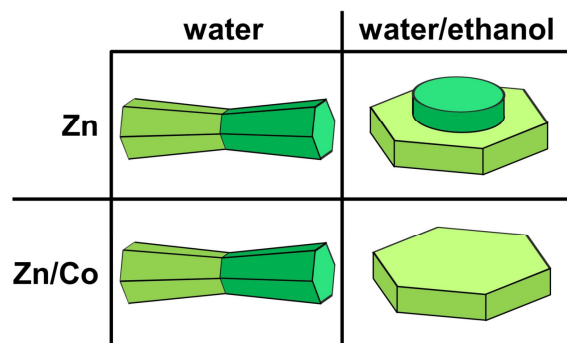


Figure 3-5: a) PLM image of the EST-Zn|Zn bicrystal after polishing. It is revealed that the sacrificial interlayer is still polycrystalline. b) Corresponding BSE-SEM image of the interlayer after etching with 10 % HCl_{aq} for about 1 s, which highlights grain boundaries as well as different grain orientations.

3.1.3. Hexagonal platelets & rod-shaped twins

Both the hexagonal ZnO platelets and the rod-shaped twins were synthesized as precipitates by a hydrolytic reaction (thermohydrolysis) from solutions of zinc and cobalt acetates in an ethanol/water mixture in the presence of hexamethylenetetramine (HMTA). Depending on the addition of cobalt and the ethanol/water ratio, different morphologies were obtained as well as twinning could be suppressed or triggered. Various combinations of reaction parameters were tested and the resulting mineralization products were analyzed by SEM. A simplified overview of the resulting precipitates is shown in Figure 3-6.²⁰¹

Figure 3-6: Schematic illustration of the reaction products obtained from thermohydrolysis of Zn/Co-acetates, depending on the employed solvent and optional cobalt doping. Whereas the application of water lead to the formation of rod-shaped nanotwins, independent of Co doping, the latter was found to be mandatory to suppress the twinning of hexagons, which were formed using a water/ethanol mixture. Redrawn after Figure 1 by Hoffmann et al.²⁰¹



For the hydrolytic reaction, zinc acetate dihydrate (0.439 g, 2 mmol) and cobalt acetate tetrahydrate (0.030 g, 0.12 mmol) were dissolved in 70 ml of demineralized water.^a In a second vessel, HMTA (1.400 g, 10 mmol) was dissolved in 30 ml absolute ethanol. The aqueous solutions of the metal salts were transferred to a two-neck flask with a reflux condenser and inserted in a preheated oil bath at 95 °C. Both the 70:30 ratio of the water/ethanol mixture as well as the 95 °C reaction temperature were found to be optimal for the synthesis of precipitates with well-defined hexagonal shape.²⁰¹ After 5 min, when the first visible precipitation started, the HMTA solution was added. This procedure, i.e., combining the educts not before the desired reaction temperature is reached, was applied owing to the low solubility of the metal salts in ethanol and to avoid local oversaturation leading to inhomogeneous reaction conditions. After a defined reaction time, the proceeding mineralization was terminated by removing the flask from the oil bath and subsequently quenching it in an ice bath. The precipitates were isolated by centrifugation and washing with a water/ethanol mixture. Afterward, the centrifugation tube was stored in a

^a Since cobalt was found to be mandatory for the formation of platelets,²⁰¹ Co-free (undoped) ZnO samples were not subjected to TEM investigations.

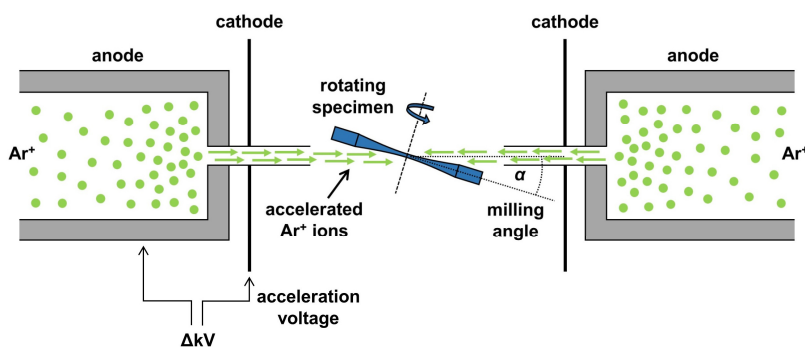
drying cabinet at 40 – 45 °C overnight, allowing to isolate 70 – 100 mg of the final product in form of an off-white (≤ 30 min reaction time) or greenish powder (≥ 45 min reaction time). In the case of the ZnO hexagons, three different samples were fabricated at different reaction stages, corresponding to 15 min and 45 min reaction times and one 45 min sample, which was additionally subjected to calcination at 300 °C in air. For the rod-shaped twins, the same procedure and educt quantities were employed with the exception of omitting the ethanol addition, as only water was used as the solvent. Therefore, HMTA was added directly to the aqueous solution. The reaction time was 60 min.

3.2. TEM and SEM sample preparation

3.2.1. Bicrystals

For TEM investigations, cross sections of the bicrystals were cut out in $[\bar{1}2\bar{1}0]$ and $[01\bar{1}0]$ directions and polished down to a thickness of 10 μm using an Allied MultiPrep polishing system^a with diamond lapping films of grain sizes from 15 μm down to 0.1 μm . Subsequently, the thin-foils were mounted on supporting 75-mesh or 100-mesh molybdenum TEM grids^b and argon ion-milled (Figure 3-7) using a DuoMill 600^c until electron transparency of the interface regions was reached. Low acceleration voltages of 4 kV and a milling angle of 14° were applied, to avoid the unintended removal of possibly present amorphous interface films as reported by Chiang et al.¹²⁹ for polycrystalline ZnO varistor ceramics. For the final 10 min of the ion-milling procedure, both acceleration voltage and angle were further lowered to 1.5 kV – 2 kV at 12°. In addition, it should be noted that the DuoMill 600 has an unfocused ion-beam, which generally provides a rather “gentle” milling.

Figure 3-7: Schematic of the ion-milling procedure. A thin-foil TEM sample is placed between opposing ion guns, where Ar⁺ ions are accelerated on the rotating specimen under a certain milling angle α and an acceleration voltage ΔkV . Sample material is continuously removed until one or more holes are generated featuring electron transparent regions at their edges.



As shown in Figure 3-8, the bicrystal grain-boundaries were positioned in the center of the meshes and parallel to a row of meshes on the supporting grid. Thus, several holes being electron transparent at the edges could be obtained per sample. For the EST bicrystal, an additional $[01\bar{1}0]$ oriented cross-section was surface polished and lightly carbon coated^d for SEM investigations, whereas the ion-milled TEM samples were also used for the SEM studies in the case of the DB-I and DB-26 bicrystals.

^a Allied High Tech Products Inc, Rancho Dominguez, CA, USA.

^b Plano, Wetzlar, Germany.

^c Gatan, Pleasanton, CA, USA.

^d Carbon coating was performed using a Med 010, Balzers Union, Balzers, Liechtenstein.

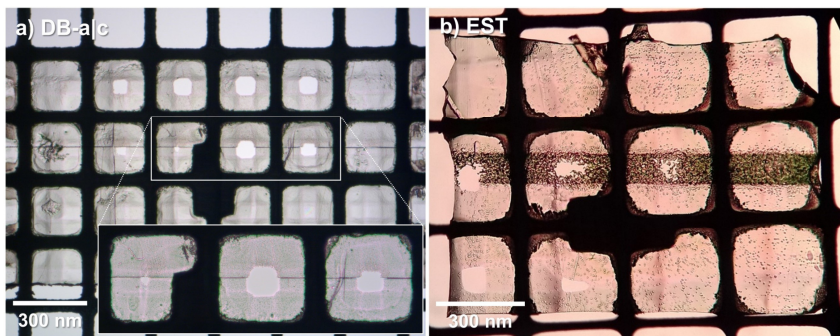


Figure 3-8: a), b) Samples DB-a|c and EST-O|O after ion-milling. Grain-boundary and interlayer were carefully positioned parallel & centered with respect to a row of meshes. In consequence, several holes formed along the interface upon ion-milling, thus providing a maximum yield of electron transparent regions.

3.2.2. Hexagonal platelets & rod-shaped twins

For TEM preparation of the ZnO hexagons and rod-shaped twins, ethanol suspensions of the respective powder samples were dispersed in an ultrasonic bath for 10 min. One drop of each suspension was deposited on a copper TEM grid^a with a supporting holey carbon film (400 mesh). Cross-sections were prepared by embedding the sample material in epoxy resin and cutting out 3 mm discs, which were mechanically polished down to a thickness below 20 μm using an Allied MultiPrep polishing system^b with diamond lapping films of grain sizes from 15 μm down to 1 μm . Subsequently, the disc was mounted on a copper TEM grid^a (200 mesh) and argon-ion milled (Figure 3-7) using a DuoMill 600^c until electron transparency was reached (5 kV acceleration voltage, 15° milling angle). For the final 10 min of the ion-milling procedure, both acceleration voltage and angle were lowered to 2.5 kV and 13° in order to remove possibly amorphized material.

3.3. Analytical methods

Electron microscopy provides a multitude of characterization techniques, hence covering an exceptionally wide range of material-scientific research questions which can be addressed. Its main advantage is the combination of an in general high spatial resolution, obtained by utilizing a beam of accelerated electrons, with the versatile analytical power constituted by the various signals generated upon beam radiation. Scanning electron microscopy (SEM) and transmission electron microscopy (TEM) in particular, which represent the core of this work, provide unique methods to reveal, analyze and understand the structure of the investigated piezotronic bicrystals, covering scales from tenths of microns down to the Angstrom region on the atomic level.

3.3.1. SEM

In scanning electron microscopy (SEM), the surface of a sample is scanned by an electron beam causing beam-matter interactions, which comprise – among other effects – the emission of *secondary* (SE) and *back-scattered electrons* (BSE) within a certain pear-shaped excitation volume of typically 1 – 2 μm depth (Figure 3-9). The SE and BSE are collected by respective

^a Plano, Wetzlar, Germany.

^b Allied High Tech Products Inc, Rancho Dominguez, CA, USA.

^c Gatan, Pleasanton, CA, USA.

detectors and represent the two main imaging modes of an SEM. It should be noted that SEM images are not optical images but generated by electric and computational data processing, which assigns a certain brightness value to every pixel, depending on the measured signal intensity. Secondary electrons have rather low kinetic energies of only a few eV and hence are unable to pass large distances through the sample material. In consequence, detected SE always originate from the atoms of the upper or outer few nanometers of the sample, therefore almost exclusively providing information on surface and topography, however, with a high spatial resolution. In contrast to that, BSE are reflected or back-scattered electrons from the electron beam itself, hence having a kinetic energy up to the applied acceleration voltage (e.g., 5 – 30 kV), depending on the amount of energy-loss they have experienced. Consequently, they deliver information from a larger and deeper part of the excitation volume, down to a few hundred nanometers. The intensity of the BSE signal is mainly determined by the atomic number Z of the excited material, thus respective images contain chemical information, with regions of higher average Z appearing brighter. Furthermore, in crystalline materials, the crystal-beam orientation additionally influences the BSE intensity via (back-scatter) diffraction and electron-channeling effects.

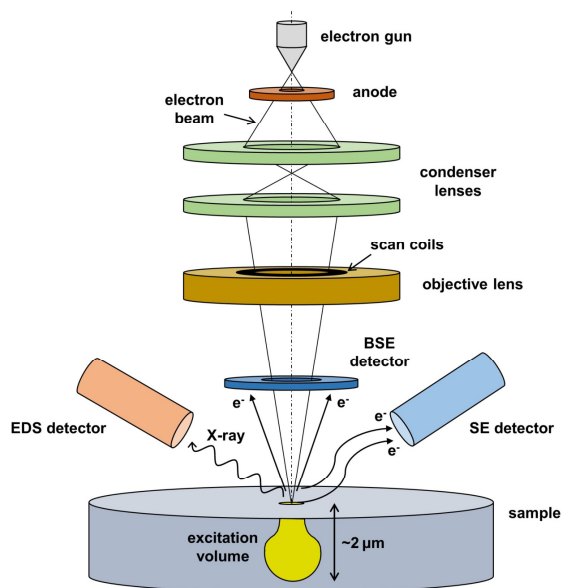


Figure 3-9: Schematic sketch of a typical SEM. An electron gun generates an electron beam focused by a set of lenses and scanned across the sample. Within a certain pear-shaped excitation volume, beam-matter interactions cause (among other effects) the generation of secondary and back-scattered electrons as well as characteristic X-rays, whose detection is used for imaging and chemical analysis.

While an efficient collection of the fast, high-energy BSE requires an annular detector centered around the primary beam, the SE detector can be placed more freely, for example, at the side, but also in the column above the BSE detector. This is possible since the low-energy SE can easily be deflected and attracted by a sufficient positive “suction” voltage (e.g., +300 V) applied at the detector, ensuring efficient detection rates. Vice versa, applying a negative voltage at the BSE detector screens it from unwanted SE.

Typical lateral resolutions are in the region of 1 nm for modern (uncorrected) SEMs equipped with field-emission guns (FEG) for electron beam generation. In addition to imaging, most SEMs are equipped with further detectors for chemical analysis, such as energy- or wavelength-dispersive X-ray spectrometers (EDS/WDS).

All SEM investigations presented in this study were performed using a JEOL JSM 7600F^a equipped with a FEG and an X-Max 80 EDS detector,^b operated at 15 kV.

^a JEOL, Tokyo, Japan.

^b Oxford Instruments, Abingdon, UK.

3.3.2. TEM

The basic principle of a transmission electron microscope (TEM, cf. Figure 3-10) is the illumination of ultrathin samples (<100 nm) with a high-energy beam of electrons (80 – 300 kV). In this case, the electrons are able to pass through the sample material and the transmitted, scattered and diffracted beams can be utilized to image and analyze the material's structure and properties.

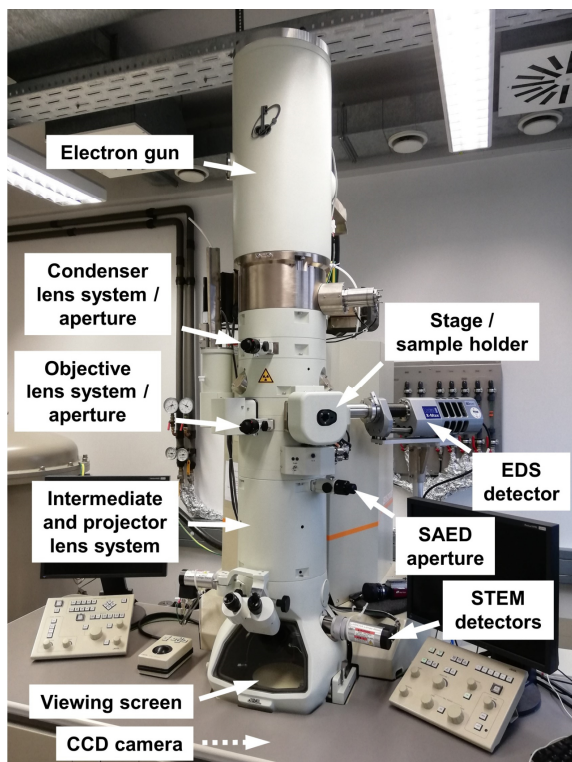


Figure 3-10: Components and general setup of a TEM, showing the Jeol 2100F instrument used for this work. The electron gun generates an electron beam, which is focused by electromagnetic lenses. In order to adjust brightness, spot size and beam convergence, the condenser lens system and aperture can be used, while the objective lens system and aperture allow adjustment of image contrast and DF-imaging. The intermediate lens features the ability to switch instantaneously between image and diffraction mode. If required, the SAED aperture limits the sample area contributing to the diffraction pattern. Typically, a double-tilt holder is used, which allows tilting of the sample to desired zone axes or directions. The resulting image or diffraction pattern is magnified and displayed on the viewing screen or CCD camera by the projector lens system. For scanning mode, special scan coils (condenser system) and STEM detectors are used. Both TEM and STEM images can be complemented by chemical analysis via EDS.

In consequence, not only features at or near the surface can be detected – as it is the case for SEM – but also those located in or related to the material's bulk can be revealed. Considering the

various signals generated due to beam-matter interaction as well as the diverse imaging modes providing different and complementary information, TEM can be considered less a single method, but rather a collective term for an extensive set of microscopy characterization techniques. Combined with its extraordinarily high resolution down to the atomic level, which results from the small wavelength of the electron beam ($\lambda = 2.51 \text{ pm}$ at 200 kV), TEM is unique in terms of imaging and versatility for spatially resolved analytics. If striving for completeness, even a basic introduction to TEM is an extensive matter and hence, by far out of the scope of this work. Therefore, the interested reader and those who remain with open questions after this section are referred to the excellent as well as comprehensive textbook by D. B. Williams and C. B. Carter.²⁰² Moreover, a complete and detailed introduction in German language is provided by J. Thomas and T. Gemming.²⁰³ Regarding the specialties of scanning transmission electron microscopy (STEM), the textbook by S. J. Pennycook and P. D. Nellist is recommended.²⁰⁴ For brief introductions to the basic principles of TEM, the reader is referred to the introductory article by H.-J. Kleebe, S. Lauterbach and M. Müller²⁰⁵ and the book chapter by A.-K. Fetzer, M. Trapp, S. Lauterbach and H.-J. Kleebe,²⁰⁶ with me as a co-author. However, those aspects of TEM which are of direct relevance for this work are presented briefly in the following, but only as far as it is necessary to basically understand the presented TEM results.

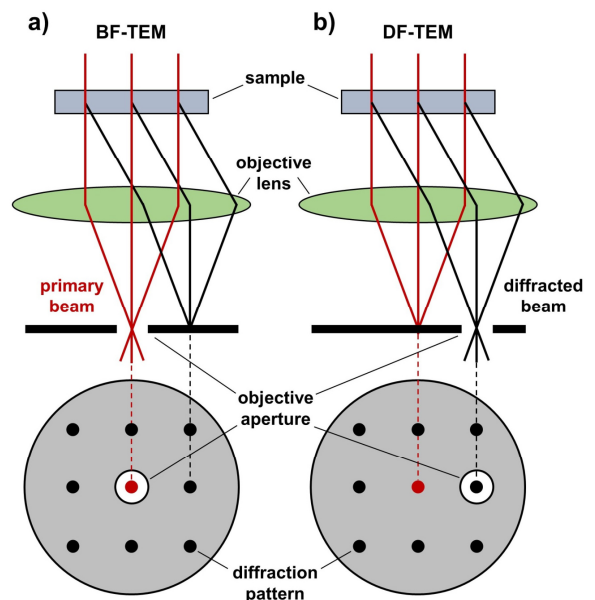
Bright- and dark-field imaging

Bright-field imaging (BF-TEM) can be considered the basic imaging mode in TEM. The respective image contrast, also referred to as *amplitude contrast*, corresponds to variations in the beam intensity due to mass-thickness effects and electron diffraction. A higher mass (atomic weight) of the specimen's atoms corresponds to a higher probability of electron-matter interaction, that is, scattering in particular. In consequence, heavier sample regions scatter electrons more often and under higher angles. Naturally, the probability of interaction also rises with increasing sample thickness. In the case of crystalline materials, diffraction additionally occurs, causing electrons to be deflected from the optical axis under certain angles. Different degrees of image contrast can be adjusted by applying different objective apertures centered around the optical axis (primary beam), which absorb the stronger scattered electrons depending on their diameter, hence defining certain acceptance angles for the electron beam (Figure 3-11 a)). In BF images, sample areas of different mass-thickness and diffraction conditions appear with differently intense dark contrast on a bright background.

Figure 3-11: a) Sketch illustrating the formation of a bright-field TEM image (BF-TEM). The objective aperture is centered on the primary beam and absorbs scattered and diffracted beams depending on its diameter. The smaller the diameter is, the more electrons are absorbed and the higher is the resulting image contrast. b) For dark-field imaging (DF-TEM), a small objective aperture is shifted on the position of a diffracted beam excluding the primary beam. In the corresponding image, only those parts of the sample, which contribute to the diffracted beam, appear bright and the background is dark.

For *dark-field* imaging (DF-TEM),^a the objective aperture (typically a small one) is not centered on the primary beam but on one of the diffracted beams of a crystalline sample (Figure 3-11 b)). In consequence, the primary beam and hence, all unaffected transmitted electrons are excluded as well as all other diffracted or scattered beams. In this case, only those sample regions, which scatter or diffract electrons in such a way that they pass the aperture, contribute to the image and thus, appear bright while everything else constitutes a dark background.

For both BF- and DF-TEM imaging of individual crystalline grains, the beam-sample orientation is highly important as the contrast is mainly determined by diffraction effects. Therefore, the adjustment of certain orientations is often reasonable, which typically correspond to either *zone-axis* or *two-beam* conditions. To obtain a zone-axis image, a zone-axis of the grain's crystal structure needs to be oriented parallel to the incident beam (the viewing direction). Then, all



^a Here, only so-called *off-axis* DF-TEM is discussed, which refers to the fact that the utilized diffracted beam is not centered on the optical axis. Applying a certain beam tilt, it is possible to shift this beam on the optical axis (instead of the primary beam). In this case, the method is called *on-axis* DF-TEM.

lattice planes corresponding to this zone-axis fulfill Bragg condition^a and respective reflections are present in the corresponding diffraction pattern as well as all related diffraction effects are incorporated in the real-space image. In the case of a two-beam condition, only one certain reflection \vec{g}_{hkl} is oriented in Bragg condition instead of an entire zone-axis. The practical advantage is that many probably obstructive or unwanted diffraction-contrast effects are reduced and especially defects and grain boundaries are imaged as well-resolved fine lines. In the case of screw or edge dislocations, two-beam imaging can also be used to identify the Burger's vector \vec{b} and the dislocation character if several images are recorded using appropriately different reflections \vec{g}_{hkl} . Then, the so-called *invisibility criterion* allows to deduce \vec{b} . While it is simply $\vec{g} \cdot \vec{b} = 0$ for (pure) screw dislocations, $\vec{g} \cdot \vec{b} \times \vec{u} = 0$ must be additionally fulfilled for edge dislocations to be invisible. The dislocation character, i.e., screw vs. edge vs. mixed, can be determined from the angle between the dislocation line \vec{u} (known from the images) and \vec{b} , with $\angle(\vec{b}, \vec{u}) = 90^\circ$ for pure edge and $\angle(\vec{b}, \vec{u}) = 0^\circ$ for pure screw dislocations. Angles between 0° and 90° indicate a mixed character. In addition to two-beam imaging, *weak-beam dark field* (WBDF-TEM) is a commonly applied method, as it allows imaging of dislocations as bright, fine lines on a dark background at a well-defined position close to the true dislocation core. To obtain a WBDF image, the sample is tilted from a perfect two-beam condition towards an orientation, at which the respective reflection \vec{g}_{hkl} is almost not excited anymore. However, due to the presence of the dislocation, lattice planes (hkl) are bent back into Bragg condition near the dislocation core and hence, are imaged with high intensity relative to the background (weakly excited bulk). The WBDF-TEM images shown in this thesis were recorded applying the typically used $\vec{g}(3\vec{g})$ weak-beam condition, i.e., in a systematic row of reflections, the Ewald sphere passes through the $3\vec{g}_{hkl}$ reflection, which is hence strongly excited (small or no excitation error), while \vec{g}_{hkl} is very weak with a large excitation error (cf. pp. 35).

In many cases, TEM thin-foil specimens are bent, which produces the so-called *bending contours* in both BF and DF mode, as the diffraction conditions will be unequal for different locations in the bent crystal due to the varied local orientation. Furthermore, since the intensity distribution between primary and diffracted beams depends and periodically varies with decreasing (or increasing) sample thickness, the so-called *thickness fringes* occur if an individual grain has a non-uniform (e.g., a wedge-shaped) thickness.

High-resolution imaging and phase contrast

The mechanism providing contrast in *high-resolution* TEM imaging (HR-TEM) is quite different from the *amplitude contrast* in regular BF-/DF-TEM (low and medium magnifications). At high magnifications of $M > 150.000x$, *phase contrast* is dominating and responsible for the lattice-

^a Actually, the Bragg condition is NOT fulfilled, when the beam is perfectly parallel to the lattice planes. It is a specialty of electron diffraction (in contrast to XRD, for example) that small deviations from the Bragg condition still produce constructive interference and hence, reflections. This effect is due to the small wavelength of the electron beam (large Ewald sphere) in combination with the so-called *excitation error* (cf. pp. 35).

resolving resolution of HR-TEM. The phase of the incident beam (a plane wave in this case) is altered by the *crystal potential* ϕ , which is the potential energy of an electron within a crystal, depending on its position and the positions of the atoms, ions and other electrons surrounding it. Due to the 3D periodicity of crystal structures, the crystal potential has also this periodicity. Those “parts” of the incoming plane wave, which experience a different potential by propagating along or between atom columns, experience a phase shift. Diffracted beams are phase-modulated as well, but in a different way, as they propagate through the crystal in a different direction. Upon interference of the phase-modulated direct wave with waves of diffracted beams, phase contrast is transformed into amplitude contrast. This interference can be induced and controlled by defocusing the objective lens, providing an additional phase shift between the direct and the diffracted waves. Please note, the transformation to amplitude contrast is important, as neither the viewing screen nor the CCD camera is able to detect phase contrast. The resulting amplitude contrast and hence the corresponding image strongly depend on the conditions of the wave interference, which in turn, depends on several factors. It is influenced not only by the defocus, but also by lens aberrations, sample thickness and the distance, or rather the spatial frequency of the imaged objects (lattice planes or atom columns). In consequence, bright contrast in HR-TEM images does not necessarily correspond to the atom positions. Depending on the applied defocus, the atom columns might appear dark and the space between them bright, or the other way around. In addition, such a contrast inversion might also occur for different spatial frequencies. Therefore, image simulations and calculations are mandatory to fully interpret HR-TEM images. Nevertheless, for well-aligned low-indexed zone axes, which feature large lattice plane distances and large projected distances between the atom columns, the periodicity of the crystal structure is normally correctly represented. Thus, it is possible to work with HR-TEM images anyhow, for example, to distinguish amorphous from crystalline regions, determine orientations and directions or identify deviations in the periodicity, such as defects, grain boundaries or interfaces.

Electron diffraction

Electron diffraction is a special case of coherent elastic scattering within a crystalline specimen, caused by the interference of electron waves with each other and the crystal structure. While the common Bragg model is well-suited to describe single diffraction events at individual lattice planes, like in XRD, the peculiarities of electron diffraction in TEM are best illustrated by the so-called Ewald sphere. The Ewald sphere is constructed in the reciprocal space, which contains the reciprocal lattice and corresponds to a Fourier transformation of the real space and the direct crystal lattice. All parallel lattice planes of the same distance have their specific individual position in the real space but are transformed to a single point in the reciprocal space, as they are “assorted” by their directional spatial frequency in this case and not by their location as before.^a Denoted by the reciprocal vector \vec{g}_{hkl} , the distance between this single point and the

^a To be more precise, lattice planes (hkl) are actually not transformed to a point, but rather to a direction specified by a vector \vec{g}_{hkl} . Upon transformation from direct to reciprocal space, planes become directions and directions become [...]

origin of the reciprocal lattice reflects the spatial frequency, which is the reciprocal value of the real space lattice plane distance. In other words, the reciprocal lattice consists of points (hkl) corresponding to sets of lattice planes (hkl) . A reciprocal lattice vector \vec{g}_{hkl} points on (hkl) and is perpendicular to the corresponding lattice planes (hkl) in real space. Its length specifies the spatial frequency and reciprocal lattice plane distance. In rotational corrected TEMs,^a it is therefore possible to directly identify and correlate planes and directions when comparing images and diffraction patterns.

Regarding the Ewald sphere construction, the incoming electron beam is represented by a wave vector \vec{k} with length λ^{-1} pointing to the origin of the reciprocal lattice (000) in its respective incident direction (Figure 3-12). Its starting point defines the center of the Ewald sphere, which has a radius of λ^{-1} , thus always cutting (000). Diffraction maintains the wavelength, hence the wave vectors \vec{k}' for diffracted beams always point from the center to the surface of the Ewald sphere, just like \vec{k} , but with a different direction, as they are scattered under a certain angle. If a reciprocal lattice point (hkl) lies on the surface of the Ewald sphere and the wave vector \vec{k}' fulfills the condition $\vec{k}' = \vec{k} + \vec{g}_{hkl}$, diffraction occurs. In other words, the Bragg condition is met for those lattice-plane sets (hkl) , which are cut by the Ewald sphere's surface.

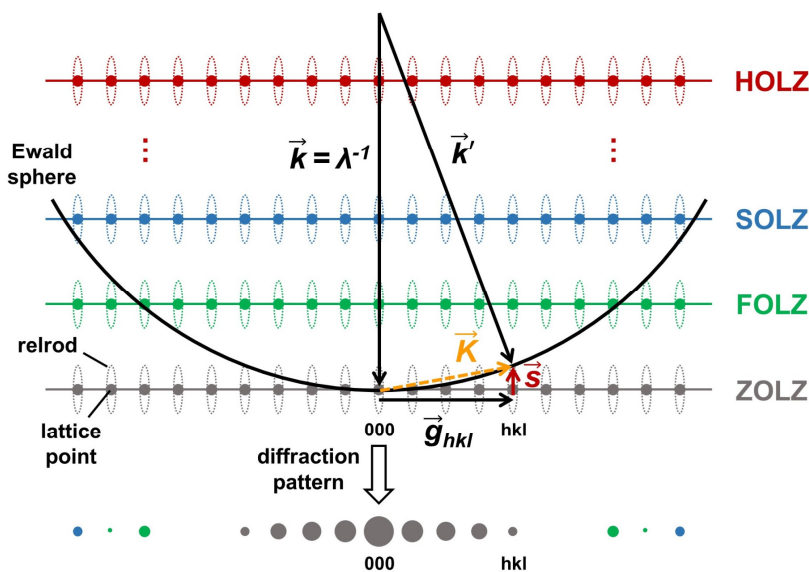


Figure 3-12: Illustration of the Ewald sphere and diffraction in TEM. A 2D cross-section of the reciprocal lattice is shown with Zero, First, Second, ..., and Higher Order Laue Zones (ZOLZ, etc.). The Ewald sphere has radius $\vec{k} = \lambda^{-1}$ pointing to the (000) reflection, i.e., the spot of the primary beam. Diffraction occurs for all reciprocal lattice points (hkl) intersecting the sphere's surface with $\vec{k}' = \vec{k} + \vec{g}_{hkl}$. Due to thin-foil effects, lattice points are elongated to relrods, allowing a certain excitation error \vec{s} , which relaxes the diffraction condition to $\vec{K} = \vec{g}_{hkl} + \vec{s}$ and $\vec{k}' = \vec{k} + \vec{K}$.

Two specialties arise in TEM. Firstly, due to thin-foil effects, the reciprocal lattice points are expanded and elongated into so-called *relrods* (reciprocal lattice rods).^b In consequence, diffraction conditions are relaxed as it is sufficient if the relrod instead of the exact point is cut

[...] planes and vice versa for the retransformation. The endpoints of the reciprocal vectors, if shifted on a joint origin, build up the reciprocal lattice. However, regarding them as transformed into points is often more illustrative.

^a Due to the spiral path of electrons in the TEM column, images and diffraction patterns rotate upon changing the magnification or camera length. However, more or less all machines are rotation corrected nowadays.

^b Relrods are (empirically) necessary to explain diffraction in TEM. However, it can also be shown mathematically that thin-foil effects, resulting from TEM specimens being quasi-infinitely large in x and y direction (relative to the size of a unit cell), while being very thin in z direction (parallel to the incoming beam), lead to an abnormal reciprocal lattice with z -elongated relrods of finite length instead of points.

by the Ewald sphere, hence some deviations from the ideal Bragg condition are tolerated. This is described by the *excitation error* \vec{s} and the diffraction vector $\vec{K} = \vec{g}_{hkl} + \vec{s}$. Diffraction occurs for $\vec{k}' = \vec{k} + \vec{K}$. Secondly, the radius λ^{-1} of the Ewald sphere is very large in TEM, due to the very small wavelength λ . Therefore, it is nearly flat in the region around (000) and not only a few but a multitude of relrods are cut in the so-called *zero order Laue zone* (ZOLZ).^a That is why electron diffraction in TEM, in contrast to XRD, allows the recording of entire reflection patterns at once without any sample tilt required. Furthermore, combined with a TEM's unique possibility to instantaneously switch between diffraction and imaging mode, via focusing the so-called intermediate lens on either the image or the diffraction plane of the objective lens, it becomes possible to easily record corresponding sets of real space images and diffraction patterns.

Sample tilt corresponds to a rotation of the reciprocal lattice around the origin. If a low-angle sample tilt, or rather a misalignment of the zone-axis condition, is present, the Ewald sphere and the ZOLZ will be slightly twisted relative to each other. In consequence, only a few relrods are cut, resembling the circular intersection line of the Ewald sphere and the ZOLZ. The radius of this circular intersection, often referred to as the “radius of the ZOLZ”, allows approximating the tilt or misalignment α according to^b

$$\alpha = \tan^{-1}(R/L) = \tan^{-1}(\lambda \cdot R^{-1}) \quad \text{Eq. 3.1}$$

α = angle of sample tilt or misalignment, R = real space radius on screen, L = camera length, λ = wavelength, R^{-1} = radius in reciprocal space

The regular way of obtaining diffraction patterns in TEM is the so-called *selected area electron diffraction* (SAED), at which a certain aperture, the SAED aperture, is used to select a specific sample area illuminated by a parallel beam.^c Only this area contributes to the pattern, which for example, can be a zone-axis pattern if a respective orientation is adjusted. A characteristic of such SAED patterns is their point symmetry, which does not only apply to the position but also to the intensity of reflections. Therefore, it is normally not possible to distinguish between so-called *Friedel pairs* (hkl) and ($\bar{h}\bar{k}\bar{l}$). This is also known as Friedel's law. However, if a polar axis is present, as in the case of wurtzite ZnO, Friedel's law is violated under certain conditions, as illustrated in Figure 3-13.

^a The reciprocal plane containing the (000) point is the ZOLZ. Parallel planes within the Ewald sphere are the first (FOLZ), second (SOLZ) or higher order Laue zones (HOLZ).

^b The camera constant $C = L \cdot \lambda$ connects camera length L and wavelength λ . It also relates the radius R , measured on the screen, to the lattice plane distance d of a reflection via $C = R \cdot d$, or to the respective reciprocal distance d^{-1} via $C = R / d^{-1}$. With $L = C / \lambda$ and $R = C \cdot d^{-1}$, the result is $R / L = \lambda \cdot d^{-1}$. Considering that the measured reciprocal radius of the ZOLZ R^{-1} can be treated similarly to a reciprocal distance d^{-1} , as the geometric relationship is the same, $R / L = \lambda \cdot R^{-1}$ is obtained. Using the well-known general geometric relation $\tan(2\theta) = R / L$, it is possible to approximate the tilt. In other words, the tilt angle is calculated as if there was a reflection corresponding to a beam diffracted under the very same angle. For 0° tilt, such a virtual reflection coincides with (000) but is located further away by a certain distance d^{-1} with increasing tilt and spans up the ZOLZ intersection circle, whose center it is.

^c Using a parallel beam, reflections occur as spots. Converging the beam causes the reflections to spread into discs. This is a diffraction method of its own, called *convergent-beam electron diffraction* (CBED).

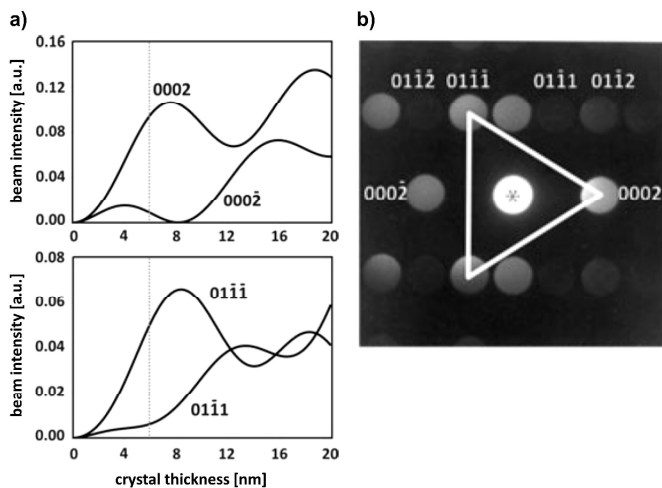


Figure 3-13: a) Intensity difference of Friedel pair (0002) & (000̄2) and Bijvoet pairs {10̄1̄1̄} & {10̄11} due to multiple scattering in very thin samples. b) Sketch of the resulting diffraction pattern which allows to deduce the c -axis polarity. Reworked after Fig. 4 by Recnik et al.¹⁸⁰

As shown by Recnik et al.,^{178, 180, 207} *nano-beam electron diffraction* (NBED)^a of very thin sample regions of about $t \approx 8$ nm thickness is able to detect and identify the absolute direction of the polar c -axis in ZnO. Best results are obtained using a

$\langle \bar{1}2\bar{1}0 \rangle$ zone-axis orientation,^b at which the (0002) reflection corresponding to the Zn-terminated “head” direction exhibits a significantly higher intensity compared to the (000̄2) reflection, which relates to the O-terminated “tail” direction. In addition, reflections (10̄1̄1̄) and (̄101̄1̄), which lie on the tail side, show a higher intensity than their Bijvoet-related counterparts (10̄11) and (̄1011) on the head side.^c Thus, the polarity of the c -axis can be deduced directly from the NBED patterns in rotational corrected TEMs. Otherwise, the rotation needs to be measured and considered. In this regard, all NBED patterns presented in this work were rotated by 180°, as the used machine (JEOL 2100F) is indeed rotation corrected, but still features a 180° rotation between diffraction patterns and real space images.^d

For the sake of completeness: In order to identify IBs in ZnO, Kim and Goo also used a method related to the violation of Friedel’s law.¹⁸³ Under multibeam condition, i.e., in zone axis orientation, the alternating dark-bright contrast of thickness fringes crossing an IB is reversed in the corresponding DF-TEM images using the (0002) reflection. However, as it does not allow distinguishing between head-to-head and tail-to-tail orientation, this method is considered inferior to the NBED or the ABF-STEM (cf. pp. 40) technique and thus, was not applied in this work.

^a NBED utilizes a convergent beam like CBED, but with a rather small convergence angle and hence, a resulting small disc size, since overlapping of discs needs to be avoided and intensity comparison is easier if discs are not too large. Due to these quasi-parallel conditions, the applied method is termed NBED for distinction from regular CBED with higher convergence angles.

^b In principle, every zone axis containing {0002} can be used. However, a $\langle \bar{1}2\bar{1}0 \rangle$ projection is the most advantageous, since it shows the most pronounced effect, as it features two sets of {10̄1̄1̄} reflections in addition.

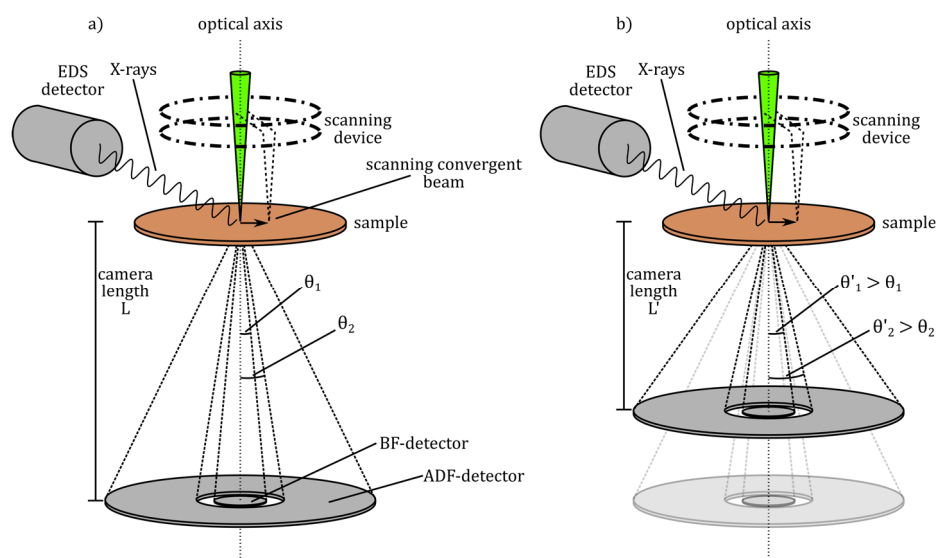
^c **Bijvoet pairs:** Reflection intensities can be equivalent due to the symmetry of the crystal structure and/or due to the (additional) inversion symmetry of the diffraction pattern (Friedel’s law). While the former is always true, the latter only applies to normal diffraction conditions. In a crystal structure without a center of inversion, the two reflections of a Friedel pair (hkl) and ($\bar{h}\bar{k}\bar{l}$) exhibit the same intensity only due to Friedel’s law. However, if the crystal contains other symmetry elements (mirror planes, rotation axes, ...), further always-equivalent reflections might exist for each member of a Friedel pair, forming two groups, which have the same intensity under normal, but not under anomalous conditions. A pair of reflections, one from each group, is called a *Bijvoet pair*. Thus, all Friedel pairs are Bijvoet pairs, but only Bijvoet pairs related by inversion symmetry are Friedel pairs. Here, the Bijvoet pairs are (10̄1̄1̄) & (10̄11) and (̄101̄1̄) & (̄1011).

^d Normally, this 180° rotation is irrelevant and remains unnoticed, due to Friedel’s law.

Scanning transmission electron microscopy

In conventional TEM, the investigated sample volume is illuminated at once with a parallel or convergent electron beam and an optical image is obtained. In contrast to that, the respective sample volume, or to be more precise, the sample surface is scanned by an electron probe in *scanning transmission electron microscopy* (STEM). Special STEM detectors are used to count the transmitted signal for every beam position of the scanned raster pattern and a respective intensity value is assigned to each corresponding pixel. Therefore, STEM images are not optical images, but the result of electronic signal processing. However, at first, the image contrast is created similarly to conventional TEM, as the same beam-matter interactions determine the intensity of the transmitted beams. Mass-thickness and diffraction are mainly responsible for the different intensities at different beam positions and hence, for the respective brightness values of the corresponding image pixels. Bright-field and dark-field imaging can be realized in STEM as well, although this is accomplished in a different way than in TEM. STEM detectors are centered on the optical axis and, in consequence of the applied camera length (the distance between sample and detector) and their circular or annular shape, only rays within a certain angular range are collected (Figure 3-14). For BF-STEM, a circular detector is used, which records the primary beam and beams scattered or diffracted under typically rather small angles. The resulting image has a bright background with a dark contrast for those sample regions that scatter strongly.

Figure 3-14: a) Sketch illustrating a typical STEM setup with an EDS detector. Via special scanning coils, a small convergent electron beam (probe) is scanned across the sample. BF and DF detectors are located below the sample collecting transmitted beams within a certain angular width. b) By changing the (virtual) camera length, the acceptance angles θ of the detectors can be adjusted, e.g., for HAADF or Z^2 -contrast conditions.



For DF-STEM, an annular detector is used, which lets the primary beam pass and collects only those transmitted beams, which are scattered within the angular range defined by the inner and outer acceptance angles. Thus, the image has a dark background with only those parts of the sample being bright, which sufficiently scatter or diffract the electron beam on the detector. The acceptance angles for both BF- and DF-STEM can easily be adjusted by changing the (virtual) camera length or inserting limiting apertures. Using very small camera lengths, only

beams scattered under comparably high angles >50 mrad are recorded by the DF detector. This setting is known as *high-angle annular dark field* (HAADF) and has some important advantages.

At such high angles, mostly inelastically scattered electrons are collected and effects of diffraction and other elastic scattering processes are largely reduced as they typically involve smaller scattering angles. In consequence, the image contrast mainly depends on the probability of inelastic scattering and hence, on the (average) atomic weight Z of the sample with the recorded intensity being $I \sim Z^2$.^a Therefore, this is called Z - or Z^2 -contrast and HAADF is sometimes also referred to as Z -contrast imaging. In contrast to HR-TEM, which involves the possibility of contrast inversion between atoms and background, HAADF-STEM images always feature bright atoms on a dark background. Together with the reduced effects of elastic scattering, image interpretation is significantly simplified. Furthermore, due to the Z^2 -contrast, images readily deliver chemical information, as shown by the example in Figure 3-15.

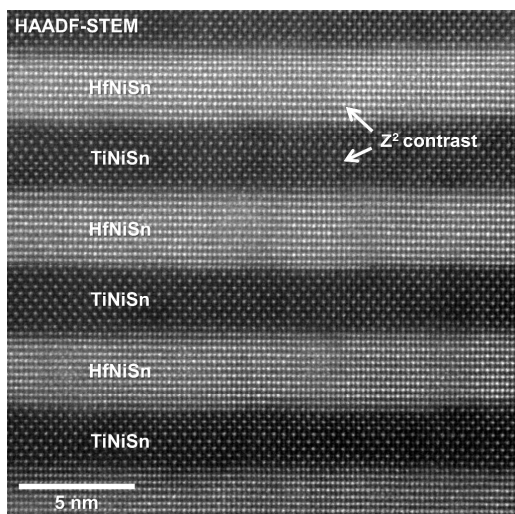


Figure 3-15: FFT-filtered HAADF-STEM image of alternating layers of TiNiSn and HfNiSn. Both layer types feature exactly the same crystal structure but a different average atomic weight Z . Therefore, they exhibit a strong Z^2 -contrast due to $I \sim Z^2$.

The resolution in STEM is mainly determined by the diameter of the electron probe. If lens aberrations of the condenser system are corrected, which refers to the spherical aberration C_s in particular,^b it is possible to obtain a sufficiently small electron beam at still adequate beam currents, hence providing atomic resolution in scanning mode (HR-STEM). However, it should be noted that, for atomic resolution, the sample needs to be in perfect, ideally low-indexed zone-axis orientation to obtain well-resolvable atom columns aligned parallel to the electron beam (viewing direction). In this regard, HR-STEM is much more sensitive to the orientation than HR-TEM (phase-contrast imaging), since electron channeling/de-channeling^{208, 209} influences the image contrast more strongly and, since the atom columns are projected on the image plane, tilted columns naturally appear indistinct if not indistinguishable, even for rather small misorientations.

In this work, a special mode for BF-STEM, which is called *annular bright field* (ABF), was used to determine the absolute direction of the polar c -axis in ZnO crystals. The image contrast of light elements, such as oxygen, which cause low-angle scattering, can be increased in BF-STEM images by excluding the inner part of the primary beam. This can be accomplished either by

^a In fact, it is rather $I \sim Z^{1.7}$, but often rounded up to Z^2 in the respective literature.

^b C_s is the dominant lens aberration limiting (S)TEM resolution. Its correction is not straightforward and requires special equipment and training. In fact, it was considered impractical or even impossible for decades, although research by Otto Scherzer started already in the 1940s. It was not until the 1990s that the first C_s -corrected TEM was built by Harald Rose together with Max Haider and Knut Urban. Nowadays, it is state-of-the-art and sometimes even combined with C_c -correction (chromatic aberration) for sub-atomic resolution.

special annular BF detectors or by inserting a circular beam stopper of appropriate diameter above a regular BF detector.

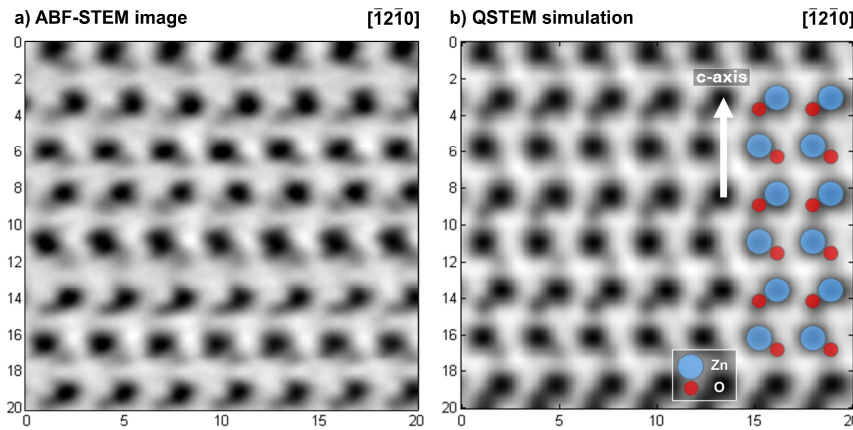


Figure 3-16: a) ABF-STEM image of wurzite ZnO in $[\bar{1}2\bar{1}0]$ zone-axis orientation recorded with a C_s -corrected ARM 200F at a camera length of 6 cm and with the beam stopper inserted, which limits the BF acceptance angles to 11 – 22 mrad. b) Corresponding QSTEM image simulation for a ZnO slab of 30 nm thickness, an acceptance angle of 11 – 22 mrad, a beam convergence angle of 24 mrad, $C_s = 0.001$, $C_c = 1.4$ and an energy spread of $\Delta E = 0.8$ eV. A comparison of both images verifies the ABF-STEM technique to be capable of identifying the absolute c -axis direction via the orientation of the Zn-O dumbbells, as highlighted in b).

In principle, atomic resolved ABF-STEM allows imaging of the oxygen positions in ZnO and hence, the orientation of Zn-O dumbbell pairs, which in turn reveal the absolute c -axis direction.²¹⁰ As shown in Figure 3-16, which features an ABF-STEM image and a corresponding QSTEM image simulation^a for comparison, it is indeed possible to deduce the c -axis direction directly from the Zn-O dumbbell orientation in $\langle \bar{1}2\bar{1}0 \rangle$ zone-axis orientations.

FFT filtering

The quality of HR-(S)TEM images, which depict the crystal lattice, can often be improved by *fast Fourier transform* (FFT) filtering (Figure 3-17).

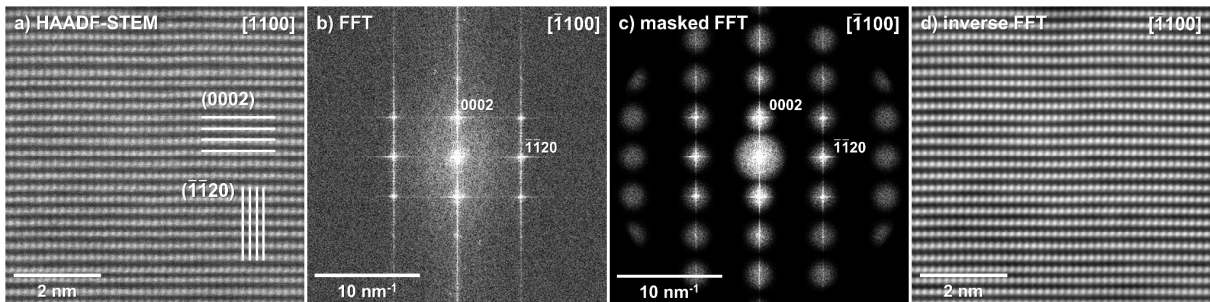


Figure 3-17: Illustration of the FFT filtering procedure used to increase the quality of HR-(S)TEM images. a) Raw HAADF-STEM image of ZnO in $[\bar{1}100]$ zone-axis condition. b) FFT of the HAADF-STEM image. Similar to reflections in a diffraction pattern, spots occur related to periodic image features, such as atomic columns or lattice planes, e.g., (0002) and $(\bar{1}\bar{1}20)$. c) The same FFT after the application of a mask filtering out background noise and amorphous contributions. d) Inverse FFT recreating the filtered real space image.

The real-space image information is translated into spatial frequency data via FFT. If periodic image features are present, such as atom columns or lattice planes sharing the same spatial frequency, corresponding spots occur in the FFT image, similar to reflections in a diffraction pattern. Non-periodic image elements, such as amorphous regions or irregular disturbances, do not share a certain spatial frequency. They are represented as “diffuse” intensity between the

^a QSTEM: a free software package for quantitative TEM/STEM simulations by Christoph Tobias Koch.²¹¹

spots in the FFT image. Image processing software can be used to filter these parts of the FFT, while the periodic spots are retained. Applying an inverse FFT recreates a real-space image from the filtered FFT pattern, which depicts the lattice more clearly with reduced amorphous or irregular parts.

Energy-dispersive X-ray spectroscopy

Energy-dispersive X-ray spectroscopy (EDS) is a chemical analysis technique based on the detection of characteristic X-rays generated upon electron beam radiation. It is a standard method in both TEM and STEM. In contrast to comparable (S)TEM methods, such as *electron energy-loss spectroscopy* (EELS), it allows measuring signals from all elements of the periodic table simultaneously, since it covers a wide range of X-ray energies detectable at once (e.g., 0 – 40 keV). In addition, detecting heavy elements ($Z > 25$), such as bismuth, is much more efficient in EDS than in EELS. This is due to the underlying signal-generating deexcitation processes being competitive and X-ray emission being favored for higher Z . In addition, EELS is much more demanding on the sample quality and requires especially thin sample regions, suffering from bad signal/background ratios otherwise. With respect to bismuth ($Z = 83$) doping being the main topic and the necessity to work with rather thick sample regions in many cases, EDS was the preferred method for chemical analysis throughout this work, while the (occasionally tested) application of EELS was found to be inferior at all times.

In contrast to SEM, the excitation volume for TEM-EDS is not significantly larger than the corresponding illuminated sample area, due to the high acceleration voltage, the thin-foil samples and the small probe diameter (in the case of STEM). However, if the highest spatial resolution of EDS data is required, e.g., for quantification, beam broadening and the size of the excitation volume might be relevant. A technique to address this problem, the CEP method, is presented in section 3.3.3 (pp. 43).

TEM machines, settings and software

All TEM investigations within this work were performed on a JEOL JEM 2100F^a and a C_s -corrected JEOL JEM ARM 200F^a both equipped with a Schottky field emission gun (FEG) and an energy-dispersive X-ray spectroscopy system (JEM 2100F: TEM 250 SDD^b, ARM 200F: JED 2300T^a). The SEM used is a JEOL JSM 7600F^a equipped with an X-Max 80^b EDS detector. For HAADF-STEM imaging, a camera length of 6 cm and 8 cm were used, which corresponds to inner and outer detector acceptance angles of 90 – 174.5 mrad and 68 – 174.5 mrad, respectively.^c ABF imaging was conducted using acceptance angles of 11 – 22 mrad.

^a JEOL, Tokyo, Japan.

^b Oxford Instruments, Abingdon, UK.

^c 174.5 mrad is the maximum ensured acceptance angle of the ARM 200F. Theoretically, the DF-detector allows 370 mrad and 280 mrad, respectively.

Image processing, FFT filtering and measurements were performed using Digital Micrograph 3.21^a and ImageJ 1.52.²¹² The insets in Figure 4-27, Figure 4-29 b) and Figure 4-41 were additionally processed using *contrast-limited adaptive histogram equalization* (CLAHE) for a better depiction of the presented features.²¹³ EDS measurements were conducted and evaluated using the INCA^b software for the 2100F and the 7600F, while the Analysis Station 3.8.0.30^c software was used for the ARM 200F. Both software packages feature an automatic drift-correction, which was applied for all STEM-EDS measurements.

3.3.3. CEP-method

The *concentric electron probe* method (CEP), sometimes also referred to as *ConceptEM*, is a powerful technique for the accurate quantification of segregated solute atoms at well-defined planar defects, such as straight interfaces, grain boundaries or stacking faults.^{214, 215, 216} It is based on recording a series of EDS or EELS spectra with different electron beam radii centered on the respective defect in edge-on orientation (Figure 3-18). In consequence of the different interaction volumes, different ratios of matrix to solute atoms are probed. Larger beam radii imply a proportionately larger fraction of the matrix, while smaller beam radii cause a proportionately larger fraction of the solute being detected, since

$$V_{\text{defect}}(r) = 2r \cdot d \cdot t \quad V_{\text{matrix}}(r) = r^2 \pi \cdot t - (2r \cdot d \cdot t) \quad \text{Eq. 3.2}$$

V = volume, r = beam radius, t = sample thickness, d = (chemical) width of planar defect $d, t = \text{const.}$

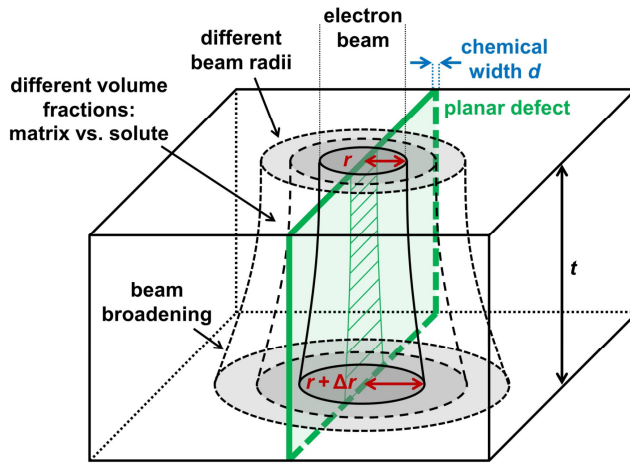


Figure 3-18: Sketch illustrating the CEP method for the quantification of solute segregation to planar defects or interfaces. A series of EDS or EELS measurements is recorded using different radii r for the electron beam, which is centered on the planar defect in edge-on orientation. In consequence, different matrix/solute ratios are probed. From the obtained data, the chemical width d of the solute-covered planar defect can be calculated, which allows quantifying the segregation. The main advantage of the CEP method is its independence from beam broadening $r + \Delta r$, which can, depending on the thickness t , be a large obstacle for EDS or EELS point measurements. Redrawn after Figure 1 by Walther et al.²¹⁷

As shown in Figure 3-19, the k -factor weighted (effective) intensity ratios $R = I_m^* k_s / I_s^* k_m$ of the matrix-to-solute elements are plotted against the respective beam radius (full-width half maximum, imaged on CCD camera). The slope $\partial R(r) / \partial r$ of a linear regression function yields the so-called *effective chemical width* d by

$$d = \pi / \left(2 \cdot \frac{\partial R(r)}{\partial r} \right) \quad \text{Eq. 3.3}$$

^a Gatan Microscopy Suite, Gatan, Pleasanton, CA, USA.

^b Oxford Instruments, Abingdon, UK.

^c JEOL, Tokyo, Japan.

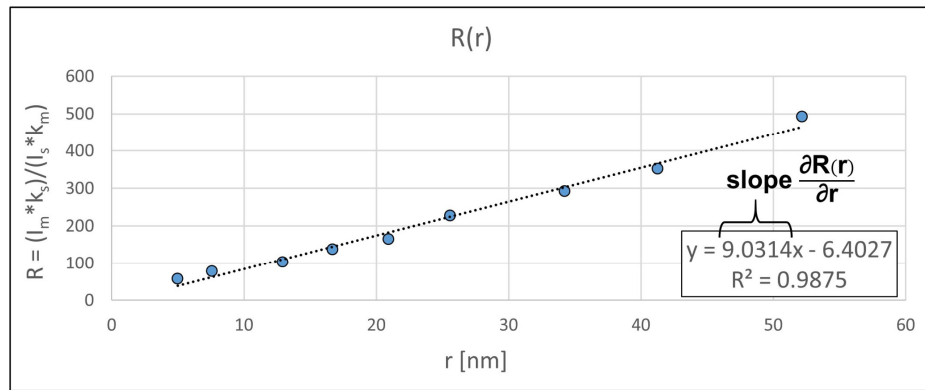
as derived from the general relationship

$$R = [(1 - x)(\pi r^2 - 2rd)] / [(2rd + \pi r^2 x)] \approx r \cdot \pi / (2d) - 1 \quad \text{Eq. 3.4}$$

assuming a bulk solubility of $x \approx 0$ for the segregating species.

The chemical width d corresponds to the product of the width of the respective defect and its coverage or substitution by solute atoms. Thus, it can be further translated into a site occupancy, if the defect width in terms of atom layers (monolayer, bilayer, etc.) is known from corresponding HR-TEM or atom-resolved STEM images. For example, when the measured chemical width is $d = 0.1301$ nm and the width of the planar defect is one monolayer of Zn in ZnO, which corresponds to the lattice plane distance $d_{(0002)} = 0.2602$ nm, the site occupancy is $d/d_{(0002)} = 0.1301 \text{ nm} / 0.2602 \text{ nm} = 50\%$.

Figure 3-19: Plot of a CEP measurement series (EDS). The intensity ratios $R = I_m \cdot k_s / I_s \cdot k_m$ are plotted against the respective beam radius. The slope $\partial R(r) / \partial r$ of a linear regression function yields the chemical width d according to Eq. 3.3.



However, the stated simplification and relationship between chemical width and slope holds true only for elements with very low to zero bulk solubilities of $x < 20$ ppm. For elements with larger x , but within the limits $0 < x \ll 1$ and beam radii fulfilling $r \gg d$, the following relationship is derived from Eq. 3.4 using the simplifications $\pi r^2 \gg -2rd$ and $(1 - x) \approx 1$

$$R^{-1} \approx \frac{1}{r} \cdot 2d / \pi + x \quad \text{Eq. 3.5}$$

In this case, the y -axis intercept of a linear regression of R^{-1} plotted against r^{-1} yields the solubility limit of the segregated element, since $r^{-1} \rightarrow 0$ implies $r \rightarrow \infty$, which corresponds to the case of an infinitely large beam and hence, extrapolates the matrix/solute ratios to the case of a pure bulk measurement. Again, the slope of the linear fit provides the chemical width d by

$$d = \left(\pi \cdot \frac{\partial R^{-1}(r^{-1})}{\partial r^{-1}} \right) / 2 \quad \text{Eq. 3.6}$$

However, the linear regression yields more reliable values for plots of $R(r)$ and therefore Eq. 3.3 should be used, when $x \approx 0$ is confirmed by Eq. 3.5. This is due to data points with large r being squeezed near the ordinate in an $R^{-1}(r^{-1})$ plot, hence causing larger errors for the linear regression. It should also be noted that the CEP method can be applied to STEM as well, using different square scanning-areas of length $L = 2r$ instead of concentric beams.²¹⁸ In consequence of the different geometry, the respective planar defect does not need to be centered within the

scanning area, it is sufficient to align it parallel to one of the edges. While the underlying equations remain principally valid, the factor π needs to be substituted by 4 yielding

$$R \approx L/d - 1 \quad \text{for } x \approx 0 \quad \text{Eq. 3.7}$$

$$R^{-1} \approx d/L + x \quad \text{for } 0 < x \ll 1 \text{ and } L \gg d \quad \text{Eq. 3.8}$$

Within the solubility condition $x < 20$ ppm and beam-radii range $5 \text{ nm} < r < 100 \text{ nm}$, typical R^2 values for the linear fits are >0.99 in theoretical simulations and >0.90 to >0.99 in practical measurements corresponding to a relative error of $\sim 2\%$, which converts to 0.01 monolayer or 0.25 atoms/nm.^{215, 217, 219} Significantly lower R^2 values may indicate the limits of application for the CEP method, such as high solid solubilities x or that segregation to the respective defect may have occurred very inhomogeneously. This means low R^2 do not necessarily indicate failed measurements, since respective data can nevertheless be informative and interpretable if the results from corresponding TEM images are taken into account.²¹⁶

The main advantage of the CEP method is its insensitivity to the adverse effect of beam broadening, which is in the region of several nanometers and more; even for the typically small sample thicknesses and high acceleration voltages in TEM.²²⁰ In consequence, quantifications of simple point measurements, especially in EDS, tend to significantly underestimate the actual amount of solute atoms at such planar defects. However, a main drawback of the CEP method is its limitation to structurally well-defined interfaces, boundaries or defects. In cases of irregular, non-uniform segregation, for example, if the solute concentration along the boundary significantly varies, or where no distinct number of occupied atom layers can be determined, the obtained data is prone to large errors.

For the actual application of the CEP method in this work, the K_{α} -lines of Si and Zn were used and the respective intensities (counts) and k -factors were exported from the raw data using the INCA software for EDS analysis (cf. p. 42). CCD images of the concentric beams were taken at the respective measurement position, so that beam broadening has been considered in determining the beam radii, which were sized using the Digital Micrograph (cf. p. 42) and ImageJ software.²¹²

3.3.4. I-V characterization

All current-voltage (I - V) measurements presented in this work were devised and performed by Peter Keil^a, except those of samples DB-a|c and DB-26, which were measured by Maximilian Gehringer^a. Al/Au-based low-ohmic contacts were prepared by sputter deposition (Q300TD, Quorum Technologies Ltd, Laughton, UK) on the outer surfaces of the bicrystals. Electrical measurements were conducted using a Keithley 2450^b source measurement unit in a voltage

^a In affiliation with the group *Nonmetallic-Inorganic Materials* of Prof. Rödel, Institute of Material Science, Technical University of Darmstadt, Darmstadt, Germany.

^b Keithley Instruments Inc, Cleveland, USA.

range between 0.1 – 5 V or 0.1 – 10 V, while the current output was limited to 100 mA.^a For stress-dependent measurements, a screw-driven Zwick Z010^b load frame was used applying compressive stress from 5 – 250 MPa or from 5 – 300 MPa, in steps of 50 MPa after an initial 45 MPa step. 5 MPa was the minimum applied stress and necessary to ensure contact of the sample within the load frame and measurement device (Figure 3-20). Respective measurements are considered “stress-free” throughout this work. All measurements were performed using the d_{33} -arrangement, at which load is applied parallel to the c -axes to achieve a maximum piezoelectric polarization in c -axis direction (cf. pp. 5).

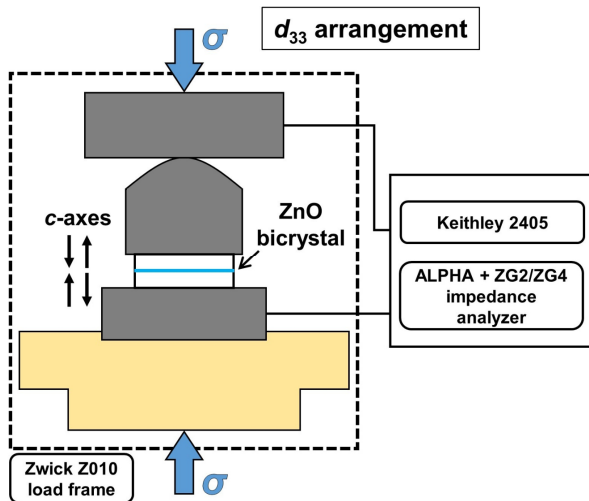


Figure 3-20: Sketch of the setup for the load-dependent I-V measurements used for the electrical characterization of the ZnO bicrystals. All measurements were performed using the d_{33} -arrangement, at which load is applied parallel to the c -axes.

All I-V measurement-related data evaluation within this Ph.D. thesis, which includes the creation of I-V plots and the calculation of the respective non-linearity coefficients α , was performed by the author. The data evaluation focuses on the determination of α_{\max} and the breakdown voltage V_C , since these parameters can be used for straightforward correlations of

electrical properties with the structural data obtained from TEM investigations. Whereas α_{\max} reflects the “quality” of the obtained varistor properties, according to a simple “the higher, the better” rule, the breakdown (switching) voltage V_C relates to the number of grain-boundaries involved in the current path and is reported to be ~ 3.5 V per single boundary.^{90, 221} Further details on the measurements, additional data from impedance spectroscopy and in-depth discussions of the electrical properties are found in the Ph.D. thesis “*Mechanically tuned conductivity in piezoelectric semiconductors*” by Peter Keil and his corresponding publications.^{101, 199} Likewise, additional information can be found in the M.Sc. thesis “*Preparation of varistor-type bicrystal interfaces by sputter deposition of dopants*” by Maximilian Gehringer.²²²

^a As a consequence of these threshold values, the I-V plots presented in this thesis do not include the high-current regime, but only the pre-switch and switching region of the investigated varistor bicrystals (cf. pp. 10).

^b Zwick GmbH & Co KG, Ulm, Germany.

4. ZnO Bicrystals – Results & Discussion

4.1. Undoped DB bicrystals

With the focus on grain-boundary structure and bonding, undoped reference bicrystals will be discussed in the following, comprising all three possible configurations of $\{0001\}|\{0001\}$ -type interfaces, i.e., O|O, Zn|Zn and Zn|O.

4.1.1. Undoped DB bicrystal in O|O orientation (B-I)

Figure 4-1 a) depicts a BF-TEM image of the interface in the tail-to-tail (O|O) oriented undoped bicrystal sample B-I in $[\bar{1}2\bar{1}0]$ zone-axis orientation. At this scale, the interface appears straight and free of inclusions, as expected for an undoped, diffusion-bonded sample. No special contrast features were observed in zone-axis or two-beam condition. Using SAED imaging, a misalignment of 1° tilt between the $[\bar{1}2\bar{1}0]$ zone-axes of the bicrystal halves was determined.

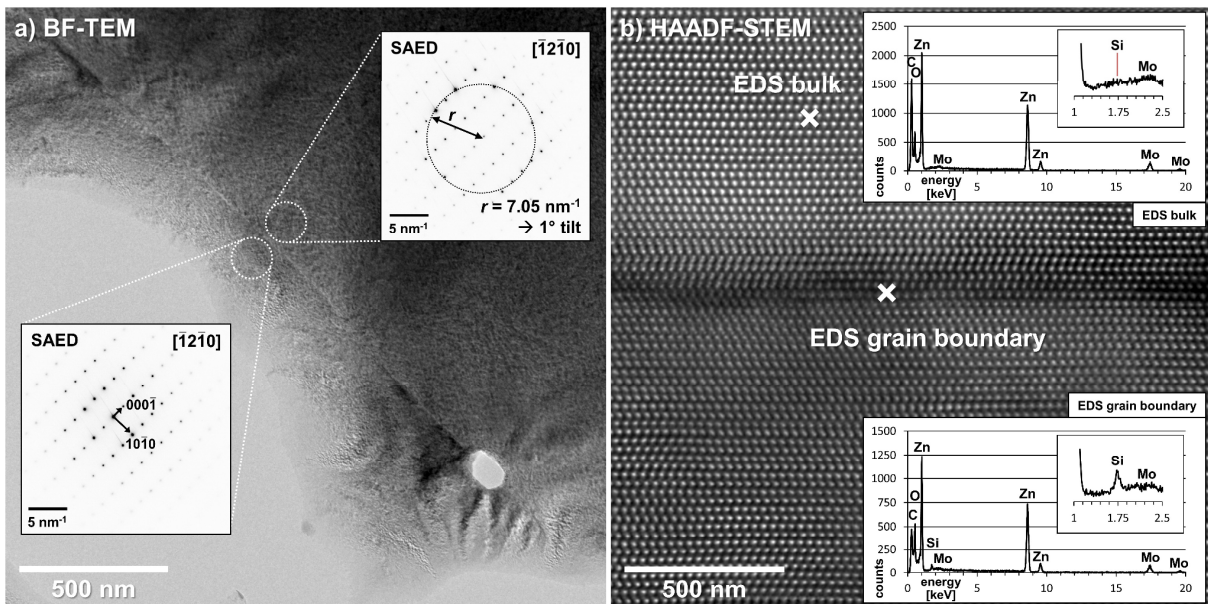


Figure 4-1: a) BF-TEM image of the interface in the O|O oriented undoped bicrystal B-I in $[\bar{1}2\bar{1}0]$ zone-axis orientation. SAED reveals a misalignment of 1° tilt (insets). b) FFT-filtered HAADF-STEM image of the interface showing a lower intensity for the grain boundary compared to the bulk, which indicates a locally lower average atomic weight. EDS measurements verify the presence of silicon ($Z = 14$) at the grain boundary, whereas no silicon was detected in the bulk. Except for minor lattice distortions, the interface is predominantly straight and defect free.

The HAADF-STEM image in Figure 4-1 b) reveals on the one hand an atomically well-bonded and defect-free interface (with the exception of a few minor lattice distortions), but on the other hand, the comparably low intensity in the vicinity of the interface indicates a locally lowered average atomic weight (Z^2 -contrast). With respect to the EDS point measurements, this is attributed to a substitution of zinc atoms by silicon, although electron de-channeling due to lattice distortions could in principle contribute to the reduced intensity.^{208, 209} While no Si was detected in the bulk region, the interface is clearly enriched and according to density functional calculations by Lyons et al.⁵¹, silicon can reasonably be expected to occupy Zn sites. However, the exact limits of the interfacial Si-enrichment, as reflected by the Z^2 -contrast, are rather diffuse, especially in comparison with samples B-II and B-III (cf. Figures p. 49 and 52).

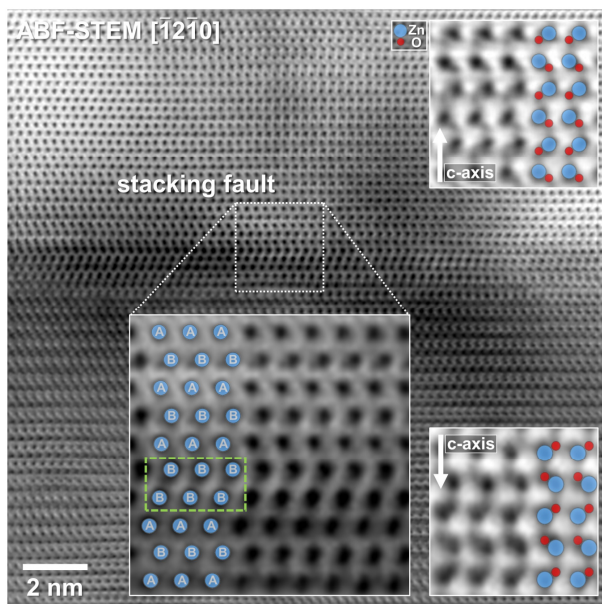


Figure 4-2: FFT-filtered ABF-STEM image of the interface in sample B-I in $[\bar{1}2\bar{1}0]$ zone-axis orientation showing a predominantly straight and well-bonded grain boundary. Here, a stacking fault is observed as presented in the large inset in the middle. The two small ABF insets on the right verify the tail-to-tail orientation by revealing the direction of the Zn-O dumbbells.

ABF-STEM imaging was used to determine and verify the tail-to-tail orientation of the bicrystals via imaging of the oxygen positions. The results presented in Figure 4-2 also confirm the observation of a predominantly straight, well-bonded and defect-free boundary. The large inset in the middle depicts a basal plane stacking fault, which

was found to be a typical feature of this and other bicrystal interfaces (cf. p. 53). Considering the low formation energies of such stacking faults²²³ and the neglectable distortion they cause, their presence is seen as neither unexpected nor contradicting to the above-stated general low-defect condition. As presented in the small insets to the right, the oxygen positions (dark grey) with respect to the zinc atoms (black) unambiguously confirm the O|O orientation.

4.1.2. Undoped DB bicrystal in Zn|Zn orientation (B-II)

In the case of the undoped bicrystal sample B-II, which has a head-to-head (Zn|Zn) orientation, a periodic contrast variation was revealed at the interface by two-beam imaging with $\vec{g} = (0002)$. This periodic contrast variation occurred symmetrically along the grain boundary in both bicrystal halves. With respect to the SAED measurements, which evidence a large misalignment of 2.8° tilt between the two $[\bar{1}2\bar{1}0]$ zone-axes, the periodic contrast is interpreted as strain contrast, caused by the comparably large mismatch between the bicrystal halves. Nevertheless, the atomically resolved HAADF-STEM image in Figure 4-3 b) displays a straight, well-bonded and rather defect-free interface. The absence of visible strain effects in Figure 4-3 b) might be due to two reasons: Firstly, lattice relaxation might have occurred in the very thin sample regions near the edge, where the image was taken. Secondly, the strain periodicity is comparably large (>50 nm), hence the effect on the lattice might be locally too weak to be visible at higher magnifications. Please note, due to the large misalignment, only one bicrystal side can be oriented in zone-axis condition, which impedes the simultaneous imaging of well-resolved atom columns on both sides. Furthermore, although having the same chemistry, the off-axis side yields a significantly lower intensity, which is related to the effect of electron channeling and de-channeling in the oriented and unoriented crystal, respectively.

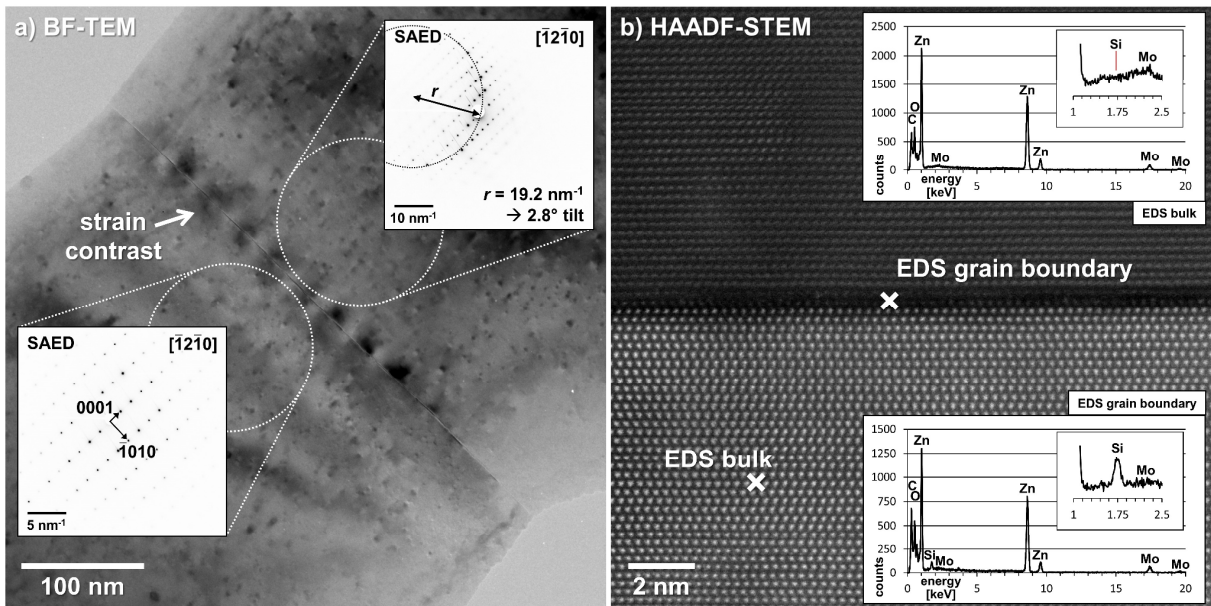
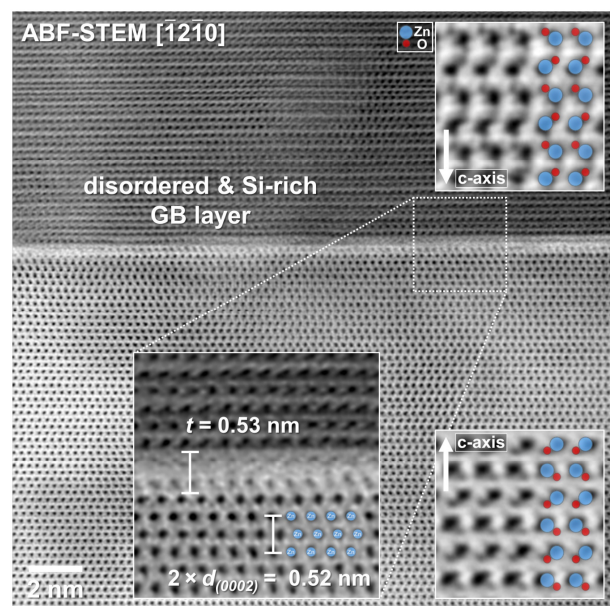


Figure 4-3: a) BF-TEM image of the interface in the Zn|Zn oriented undoped bicrystal B-II in $\bar{g} = (0002)$ two-beam condition. SAED measurements indicate a misalignment of 2.8° tilt between the $[\bar{1}2\bar{1}0]$ zone axes (insets). The periodic contrast variations at the interface are interpreted as strain contrast generated by the large mismatch. b) FFT-filtered HAADF-STEM image of the interface in $[\bar{1}2\bar{1}0]$ orientation, which appears straight and rather defect-free. Due to the large misalignment, only the lower crystal is in zone-axis orientation with resolvable atom columns. Z^2 -contrast and EDS measurements reveal a distinct Si enrichment at the interface.

As for the undoped sample B-I, Z^2 -contrast and EDS measurements indicate a distinct silicon enrichment. Although the same considerations regarding Zn-substitution apply here as well (cf. p. 47),⁵¹ the Si-enriched region features a distinctively different shape, with better-pronounced limits and notably uniform width. In addition, both the peak-to-background ratio in the EDS measurement as well as the more intense Z^2 -contrast indicate a higher quantity of silicon compared to the O|O interface in B-I. The uniform width of the Si-enriched grain-boundary layer is especially well visible in the ABF-STEM image in Figure 4-4.

Figure 4-4: FFT-filtered ABF-STEM image of the interface in bicrystal B-II in $[\bar{1}2\bar{1}0]$ zone-axis orientation. In contrast to Figure 4-3 b), ABF imaging indicates a rather disordered interface with diffuse atom columns. However, the disordered region is limited to two Zn layers, hence corresponding to the dimensions of one unit cell in c -axis direction. The ABF insets depict the head-to-head orientation by revealing the direction of the Zn-O dumbbells.

As shown by the large inset in the middle, the Si enrichment comprises two Zn-layers in c -axis direction, which corresponds to the distance of two (0002) lattice planes and therefore to the height of one unit cell. In contrast to the HAADF-STEM image in Figure 4-3 b), the interface region appears notably disordered in ABF mode, featuring atomic columns at the boundary, which are even more diffusely displayed and hence locally distorted than those in the bulk regions (even compared



to the misaligned side). This can be explained by ABF imaging being more sensitive to lattice distortions since it includes – in contrast to HAADF-STEM – signals from light elements, oxygen in particular, as well as electrons diffracted at low angles (11 – 22 mrad). As illustrated by the small insets on the right, ABF-STEM also verified the head-to-head orientation of bicrystal B-II.

Since the Si-enriched region features an approximately uniform width, hence resembling a well-defined planar defect, the CEP method (cf. pp. 43) was applied to quantify the actual silicon content. Three measurement series were recorded at three different positions. According to the general SiO₂-ZnO phase diagram, no significant solid solubility exists for Si in ZnO in equilibrium conditions,^{224, 225} hence the <20 ppm criterion for the CEP method was expected to be fulfilled. However, the linear regression of an $R(r)$ plot of series A (Figure 4-5 a)) shows a notably low R^2 value of about 0.43, which is interpreted as an indication of an actually higher solubility limit.^a Consistent with that, a linear regression of an $R^{-1}(r^{-1})$ plot yields $x = 0.0033 = 3300$ ppm (Figure 4-5 b)). In order to exclude errors due to failed centering of the interface or wrongly determined beam radii, which could in principle contribute to low R^2 values, measurement series B & C were conducted in STEM mode, which is easier in application in this regard and additionally features an automatic drift correction. However, the results showed similar or even lower R^2 values in $R(r)$ plots, while the experimental finding of a non-neglectable Si-solubility was reproduced. As determined from the $R^{-1}(L^{-1})$ plots in Figure 4-6, the solubility limits are $x = 0.0041 = 4100$ ppm for series B and $x = 0.0054 = 5400$ ppm for series C.

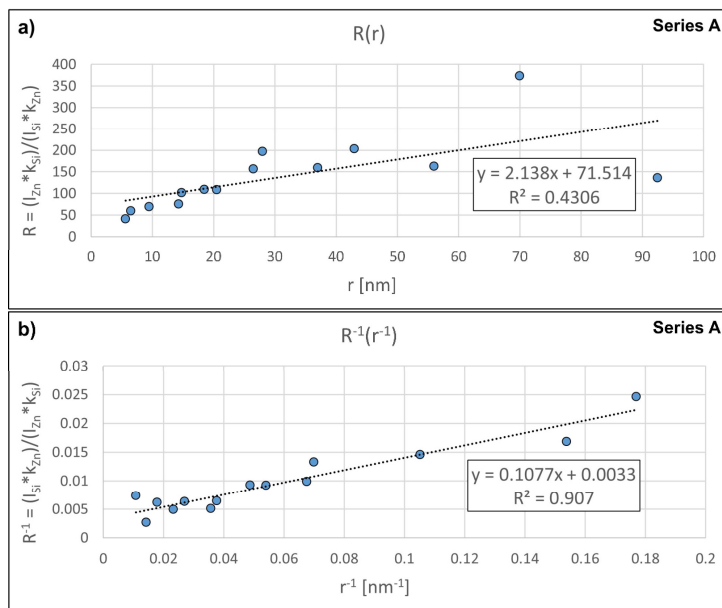


Figure 4-5: a) $R(r)$ plot of CEP measurement series A conducted in TEM mode. The low R^2 value is seen as an indication of a solid solubility of Si in ZnO $\gg 20$ ppm. b) The linear regression of an $R^{-1}(r^{-1})$ plot of the same measurement series confirms this consideration by indicating a solid solubility limit of $x = 0.0033 = 3300$ ppm. In consequence, the chemical width $d = (\pi \cdot 0.1077) / 2 = 0.1692$ is determined from $R^{-1}(r^{-1})$ instead of $R(r)$.

In consequence of $x \gg 20$ ppm, the chemical width d cannot be determined from $R(r)$ or $R(L)$ plots as recommended, but needs to be derived from $R^{-1}(r^{-1})$ and $R^{-1}(L^{-1})$ instead. Series A yields: $d = 0.1692$,

series B: $d = 0.1918$ and series C: $d = 0.2805$. Assuming a constant width of $t = 0.53$ nm for the Si-enriched region, which corresponds well with two Zn layers (cf. Figure 4-4), the chemical widths relate to site occupancies of 31 % (series A), 36 % (series B) and 53 % (series C). Since the measurements were carefully performed within the recommended limits and series B & C

^a Such low R^2 values could also be explained by a very inhomogeneous Si enrichment with varying concentrations along the interface. However, this appears to be unlikely or, at least, only a subsidiary reason in this case, as the uniform width and contrast of the Si-enriched interface layers indicate a rather homogeneous segregation (cf. Figures 4-3 b) and 4-4).

were additionally conducted in STEM mode with drift correction, the results are seen as reliable, although the obtained occupancies may exceed expected values and the R^2 values are also low in the $R^{-1}(r^{-1})$ plots. However, the determined solubility limits are notably close to values reported by Clatot et al.,²²⁶ who found $x = 0.0028 - 0.0054$ in doped thin films,^a which supports the correctness of the obtained CEP data. Therefore, it is assumed that both the determined solubility limits as well as the unexpectedly large variation in the high Si occupancy being approximately $1/3$ to $1/2$ of the Zn sites, indeed represent the real situation.

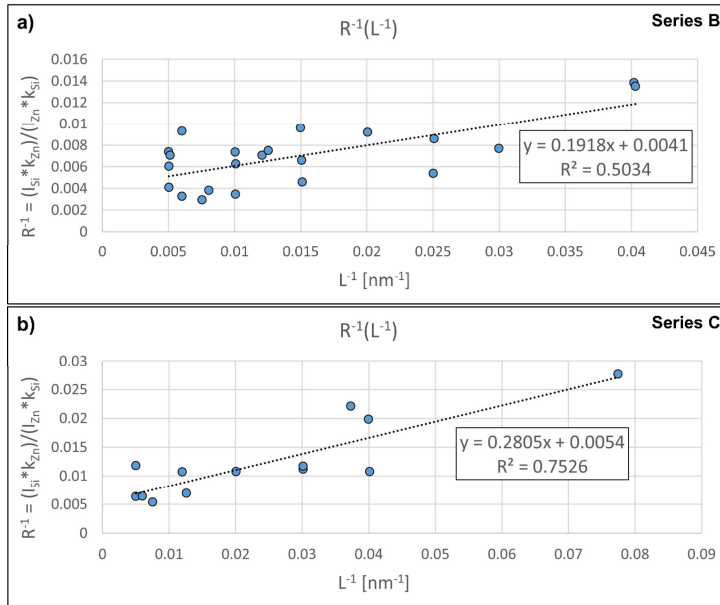


Figure 4-6: a) $R^{-1}(L^{-1})$ plot of CEP measurement series B conducted in STEM mode. The R^2 value of the respective linear regression is considerably low, although a solubility $x \gg 20$ ppm is already considered. This is attributed to a varying Si concentration at the interface. However, the obtained values $x = 0.0041$ and $d = 0.1918$ are in the same region as for series A & C and hence appear plausible. b) $R^{-1}(L^{-1})$ plot of CEP measurement series C conducted in STEM mode. The solubility of Si and the chemical width were determined as $x = 0.0054$ and $d = 0.2805$.

4.1.3. Undoped DB bicrystal in Zn|O orientation (B-III)

Due to its head-to-tail orientation, which was originally unintended, as a Zn|Zn configuration was aimed for, the undoped Zn|O sample B-III represents a single crystal with an artificial subgrain boundary rather than a real bicrystal. Nevertheless, its investigation featured some interesting findings, such as the segregation of Si, for example, and additionally, it was an extraordinarily well-suited sample for testing and verifying TEM methods to distinctively reveal the (true) directions of the polar c -axes. Furthermore, this sample was subjected to CEP measurements in order to gain more data on the solubility and segregation of Si in ZnO.

As shown by the insets in Figure 4-7 a), bicrystal B-III is well-aligned with no measurable zone-axis tilt between the bicrystal halves. Nevertheless, the displacement of the bending contour at the interface in the two-beam BF-TEM image indicates a very small tilt, which is, however, estimated to be $\ll 1^\circ$, since no effect is seen in the SAED patterns. The interface itself appears straight and free of any inclusions. As expected from these findings, the atom-resolved HAADF-STEM image in Figure 4-7 b) reveals a highly coherent, well-bonded and defect-free boundary,

^a The thin-films were actually over-doped, but for Si concentrations above $\sim 0.5\%$, the samples were found to be increasingly amorphous, which indicates Zn substitution up to this level, but the creation of disorder (insolubility) for higher contents. The quantity of “active” Si_{Zn} sites with $x = 0.0028 - 0.0054$ was determined by Hall measurements.

which almost reaches the crystalline quality of a single-crystal, though it should be noted that basal-plane stacking faults are invisible in $[\bar{1}100]$ orientation. Similar to samples B-I and B-II discussed in sections 4.1.1 (pp. 47) and 4.1.2 (pp. 48), a significant silicon enrichment is present at the interface, as revealed by Z^2 -contrast and EDS measurements. Likewise, Si is presumed to substitute Zn atoms. According to the alternating brighter and darker regions along the boundary in Figure 4-7 b), the Si content varies locally, with darker regions corresponding to higher concentrations. With respect to the distortion-free and highly coherent interface, electron de-channeling effects lowering the intensity can be ruled out in this case. The average width of the Si-containing region comprises three Zn layers in approximation, which corresponds to $3 \cdot d_{(0002)} = 0.78 \text{ nm}$.

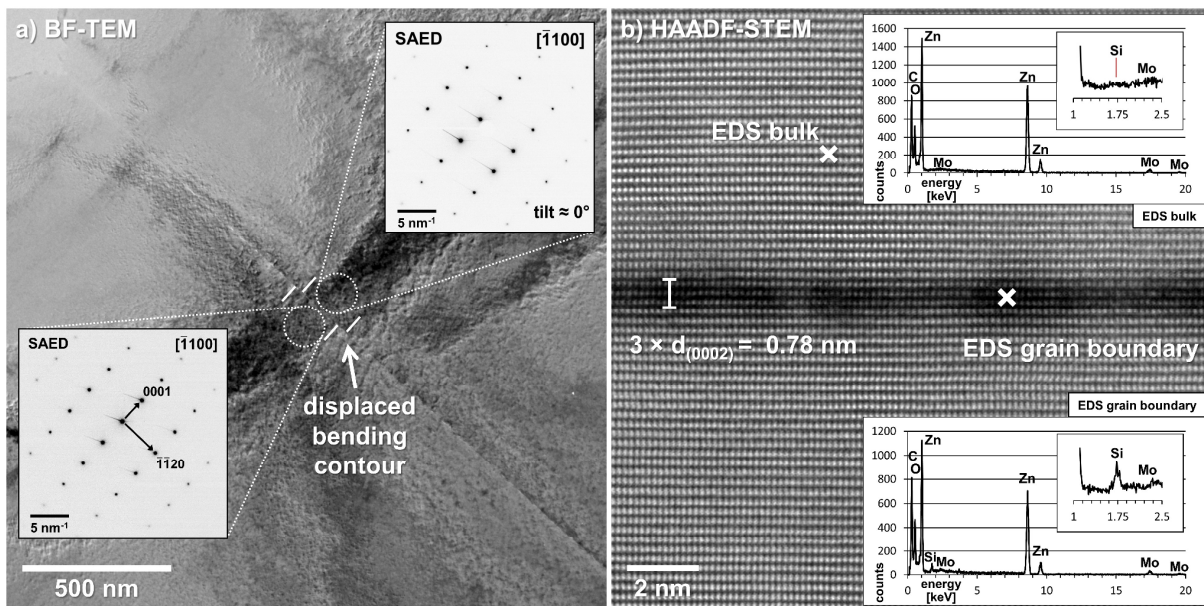


Figure 4-7: a) BF-TEM image of the interface in the head-to-tail (Zn|O) oriented undoped bicrystal B-III in $\vec{g} = (0002)$ two-beam condition. SAED indicates a quasi-perfect fitting with zero tilt (insets). Nevertheless, a small displacement of bending contours at the interface indicates a very slight mismatch, which however is non-measurable and estimated to be $\ll 1^\circ$. b) FFT-filtered HAADF-STEM image of the interface in $[\bar{1}100]$ orientation. Consistent with the observed tilt-free configuration, the interface appears straight and defect-free. However, Z^2 -contrast and EDS measurements reveal a distinct Si enrichment, which varies along the boundary, according to the alternating darker and brighter regions. The width of the Si-containing interface comprises approximately three Zn layers corresponding to $3 \cdot d_{(0002)} = 0.78 \text{ nm}$.

In order to verify or disprove the originally intended Zn|Zn orientation, two methods were applied to identify the directions of the c -axes. Firstly, a specimen in $[\bar{1}2\bar{1}0]$ direction was prepared and investigated by ABF-STEM. As shown by the insets in Figure 4-8 a), the positions of the oxygen atoms, i.e., the direction of Zn-O dumbbells, are clearly identifiable and confirm a Zn|O configuration. In addition, NBED was used to both support this finding as well as test it as a complementary method to determine the axis polarity (cf. pp. 38). The violation of Friedel's law, which successfully proves the head-to-tail orientation in this case, is illustrated in Figure 4-8 a) and b). In contrast to Figure 4-7 b), a basal-plane stacking fault is also observed at the interface in Figure 4-8 a), which clearly distinguishes the boundary region from the bulk. However, such stacking faults have low formation energy, cause low to zero distortion and hence are not unexpected.²²³

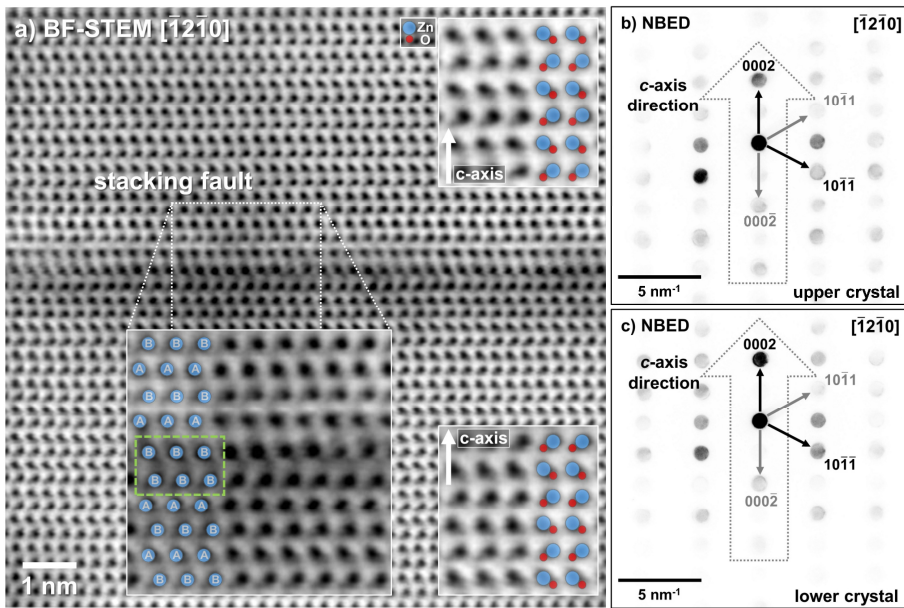


Figure 4-8: a) FFT-filtered ABF-STEM image of the interface in bicrystal B-III in $[\bar{1}2\bar{1}0]$ zone-axis orientation. Imaging along $[\bar{1}2\bar{1}0]$ provides to possibility to identify basal-plane stacking faults (large inset in the middle) as well as the Zn-O dumbbell orientation (insets on the right). Contrary to the intended Zn|Zn orientation, ABF imaging revealed a Zn|O bicrystal. As shown in b) and c), NBED revealing the violation of Friedel's law was applied, verifying this finding.

With respect to the findings in sample B-II, two CEP measurement series were performed to verify the obtained solid-solubility limit of silicon in ZnO as well as to determine the chemical width and respective occupancy of Zn sites at the interface. The results are shown in Figure 4-9 a) and b). Both series, performed at different positions, yield similar values from $R^{-1}(r^{-1})$ plots, which are $x = 0.0032$, $d = 0.0979$ and $x = 0.0034$, $d = 0.1323$. Assuming a constant width of 0.78 nm for the Si-containing interface layers (cf. Figure 4-7 b)), the chemical widths translate to site occupancies of 12,55 % and 16,96 %. Please note, these results represent mean values, since the CEP method averages the locally varying Si-content (cf. Figure 4-7 b)) as well as the corresponding chemical width along the measured interface. Regarding the obtained solubility limits of $x = 0.0033 - 0.0054$, there is a notable agreement with the Zn|Zn-bicrystal B-II (cf. pp. 50), although the site occupancies differ.

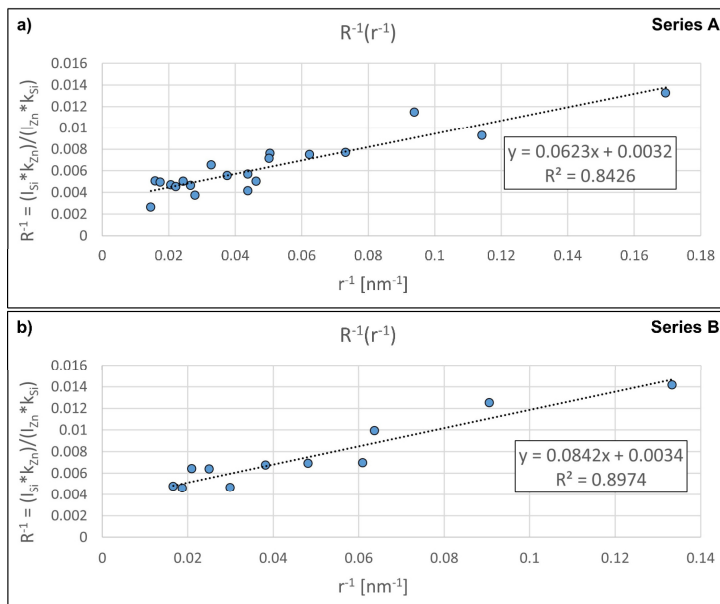


Figure 4-9: a) and b) $R^{-1}(r^{-1})$ plots of CEP measurement series A and B conducted in TEM mode. Whereas the obtained values for the solubility limit $x = 0.0032$ and $x = 0.0034$ are in the same region as the results from the Zn|Zn bicrystal (cf. pp. 50), the chemical widths $d = (\pi * 0.0623) / 2 = 0.0979$ and $d = (\pi * 0.0623) / 2 = 0.1323$ are significantly lower. The R^2 -values are both < 0.9 , which is seen as a consequence of the non-uniform silicon segregation along the interface.

4.1.4. I-V measurements

Among the undoped reference samples, only B-III was subjected to load-dependent I - V measurements.^a As expected for an undoped bicrystal and, in particular, for a perfectly aligned head-to-tail (Zn|O) orientation, sample B-III exhibits ideal ohmic behavior ($\alpha_{\max} \approx 1.0$), independent of the applied load, ranging from 5 MPa to 100 MPa, as shown in Figure 4-10. The leakage current of $8 \cdot 10^{-4}$ A (measured at 0.1 V) is likewise independent and constant throughout all measurements.

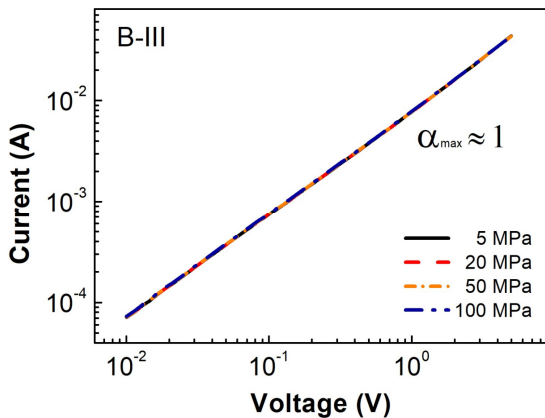


Figure 4-10: Stress-dependent I - V characteristics of the undoped reference bicrystal B-III. An ideal ohmic behavior ($\alpha_{\max} \approx 1.0$) is observed independent of the applied mechanical load ranging from 5 MPa to 100 MPa. Likewise, the leakage current of $8 \cdot 10^{-4}$ A (measured at 0.1 V) remains unchanged.

Among all investigated bicrystals, the undoped sample B-III shows the highest electrical conductivity (cf. p. 65, 77 and 94), which can be explained by the head-to-tail orientation. Due to the missing inversion symmetry and the perfect alignment, the Zn|O interface is – with the exception of the local silicon enrichment – nothing else than a single stacking fault and hence, the bicrystal is structurally rather a single crystal.

In consequence, the measured electrical conductivity is governed by the bulk conductivity only, similar to the high-current regime of a varistor. Furthermore, Si_{Zn} is reported to act as a double donor and hence, the extensive Si contamination is expected to support charge transfer across the interface.⁵¹ However, this remains without any measurable effect, as the current is always limited by the adjacent, undoped bulk regions.

4.1.5. Discussion and Summary

Interfacial silicon – origin, solid solubility, relevance for varistor and piezotronic ZnO

The Si enrichment at the bicrystal interface is a prominent feature shared by all three undoped samples. Although it appears to be influenced by the bicrystal orientation and misalignment (cf. p. 49 and 52), its occurrence by itself is obviously independent of that, since it was observed in the well-aligned, single-crystal-like sample B-III as well as in the misaligned O|O and Zn|Zn samples B-I and B-II. Considering that the supplier (MaTeck GmbH, Jülich, Germany) standardly applies an epi-polishing step on the {0001} surfaces of their ZnO single crystals, probably performed with a silicon-based polishing agent,^b the most likely source for the silicon content is a surface contamination prior to bonding. Thus, an additional cleaning step, utilizing

^a At this time, sample B-III was still mistakenly considered to have Zn|Zn configuration, hence the question was if piezoelectric charges alone, without the effect of additional dopants, are sufficient to introduce a potential barrier upon mechanical load or at least, change the electrical characteristics. In the case of symmetric {0001}|{0001} type interfaces, this is indeed theoretically possible, but naturally not in a Zn|O bicrystal, as generated charges will cancel each other out.

^b A request to the company which polishing agent was used remained unanswered.

acetone, ethanol and an ultra-sonic bath, was performed for samples B-I and B-II prior to bonding, which was found to be ineffective, however. In terms of a recommendation for future bicrystal synthesis (not tested in this work), a more effective cleaning might be achieved via a short ion-milling procedure (low angle, low to medium kV) or a re-polishing of the surfaces with, for example, a diamond lapping film or suspension. Residual carbon or diamond material is expected to be removed by forming CO or CO₂ upon annealing under air, which might be introduced as an additional step prior to bonding.

In general, silicon is considered to be insoluble in zinc oxide.^{224, 225} However, the CEP measurements of samples B-II and B-III, strongly indicate a low but non-neglectable solid solubility of 3200 ppm – 5400 ppm, which is in accordance with a report by Clatot et al. on doped ZnO thin-films.²²⁶ On the one hand, it should be mentioned that it is questionable whether annealing for 10h @ 1000 °C was sufficient to achieve equilibrium conditions. On the other hand, silicon is assumed to originate from a surface contamination and in case of a solubility $x \approx 0$, a complete retraction from the interface would be expected, as it was, for example, observed for bismuth (cf. pp. 58). However, the Si enrichment clearly spreads over a few atomic layers (cf. p. 52). Furthermore, since no radii $r > 100$ nm were applied in the CEP method, Si diffusion is considered to provide near-equilibrium conditions for the respective bulk area in the interface's vicinity, which is hence assumed to be saturated in silicon. In consequence, as excess silicon at the “planar defect” does not hinder the solubility determination by CEP (cf. pp. 43), the obtained solubility limits are seen as reliable. Nevertheless, with site occupancies of 10 % – 50 %, these solubility limits are exceeded by far by the Si content of the interfacial Zn layers, which is a further strong indication for a surface contamination. Interestingly, no lattice distortions were observed in sample B-III, which features around 15 % Si_{Zn} per zinc layer, although XRD analysis of Si-doped ZnO thin-films by Clatot et al.²²⁶ indicated a distinct and fast decrease in ZnO crystallinity for Si contents > 0.5 %; a value which correlates well with the obtained solubility limits by CEP. However, in sample B-II, the very high Si content of $\frac{1}{3}$ to $\frac{1}{2}$ appears to be related with pronounced lattice distortions and reduced crystallinity (cf. p. 49), although it is not possible to say if misalignment and distortion facilitate the Si incorporation or if it is the other way around. In any case, the Si-enriched interfacial layers clearly differ from the bulk and must be considered a special case of overdoping.

Regarding the synthesis of piezotronic and varistor-type bicrystals, the presence of silicon at the interface might be of relevance, as Si_{Zn} is reported to act as a shallow double-donor and aids the (intrinsic) n-type semiconduction.⁵¹ Though a deeper analysis of the implications for the electrical characteristics is beyond the scope of this work, it is suggested that a high content of donor Si_{Zn} located at the interface interferes with the acceptor-type trap-states inducing the potential-barrier formation and hence, could be detrimental for varistor performance and leakage current. Therefore, the aspect of silicon contamination as well as an adapted cleaning procedure should be considered in future piezotronic or varistor bicrystal studies.

{0001}|{0001} interfaces – bonding and misalignment

In principle, the bicrystal synthesis worked well for all undoped samples and all three types of {0001}|{0001} interfaces. All samples featured atomically well-bonded interfaces without interfacial films or phases, which is in agreement with the results by Sato et al.^{140, 172, 175} However, in samples B-I and B-II, stacking faults and lattice distortions were observed as typical features, apparently scaling with the degree of misalignment between the bicrystal halves, which was found to be 1° and 2.8°, respectively. Although these values might be considered rather low, they appear to have an actual effect on the interface structure. Sample B-II, featuring the highest misalignment, shows also the highest and most distinct distortion of the interfacial layers. This seems to correlate with the amount of incorporated silicon, although it is unclear if a large amount of silicon contamination induced the distortion or whether the misalignment facilitated the Si incorporation and hence, (more) Si remained after bonding and annealing. Independent of that, the fact that just the non-inverted Zn|O boundary in sample B-III was perfectly bonded without any measurable misorientation, whereas the inversion bicrystals B-I and B-II feature misalignment and distortions, is probably related to the issues of IB bonding in ZnO, as discussed in section 1.7 (pp. 18). Naturally, a $\Sigma 1$ (0001) Zn|O boundary is energetically as well as structurally the most favorable configuration and hence, will aid a respective bicrystal bonding. Contrary, (undoped) Zn|Zn and O|O IBs require at least some reconstruction, that is, in the simplest case, lattice distortions and defects. In fact, the HR-TEM image of the undoped (0001) IB shown by Sato et al. (Fig. 15c in the publication),¹⁴⁰ also features clearly visible lattice distortions, which are, however, not mentioned in the paper. In addition, deviations from perfect (0001) IB orientations (in the range of 1° – 5°, similar to B-I and B-II), are also reported by Lee and Maier, and it appears that the synthesis of perfectly aligned IB bicrystals is in general, not a trivial task.¹⁶⁸ Due to the silicon contamination, the question of whether and how the bonding of truly undoped {0001} inversion boundaries would structurally be realized remains unsolved in this study. No indications for the formation of the DFT calculated structures by Rohrer and Albe were observed,¹⁸⁵ which is, however, no surprise, considering that the group-IV element Si might induce both local distortions and different bonding conditions.

UNDOPED DB BICRYSTALS - SUMMARY

- ABF-STEM and NBED were used to successfully verify and determine the bicrystal orientations O|O (B-I), Zn|Zn (B-II) and Zn|O (B-III).
- All samples featured straight and atomically well-bonded interfaces without the presence of interfacial films or secondary phases.
- SAED was used to determine the bicrystal misalignment, which was 1° (B-I), 2.8° (B-II) and 0° (B-III).
- Lattice distortions were observed proportional to the degree of misalignment. In sample B-III, a disordered region of uniform width (2x Zn layers; $2x d_{(0002)} = 0.52\text{nm}$) was formed.
- All samples featured a distinct silicon contamination at the interface. The Si atoms substitute Zn sites in the direct vicinity of the interface.⁵¹ No secondary Si-phases were observed.
- The CEP method was used to quantify the Si content in samples B-II and B-III,^a yielding local Zn-site occupancies of 31 % – 53 % and 13 % – 17 %, respectively. These findings indicate a strong overdoping of interfacial Zn layers.
- The CEP method was used to determine the solid solubility of Si in ZnO, which was found to be in the range of 3200 ppm – 5400 ppm, which is in accordance with data from overdoped thin-films,²²⁶ but contradicts the general literature, which reports Si to be insoluble.^{224, 225}
- Si is reported to act as a double donor and aids ZnO's intrinsic n-type properties.⁵¹ Therefore, a high Si content at the interface is assumed to detrimentally interact with the varistor-type potential barrier formation.
- The *I-V* measurement of sample B-III reflects the bulk conductivity of the employed undoped ZnO single crystals and confirmed a completely ohmic behavior ($\alpha_{\text{max}} \approx 1.0$).

^a For sample B-I, the CEP method was considered inapplicable as the limits of the interfacial Si-enrichment were rather diffuse, hence lacking the required “planar character”.

4.2. Doped DB bicrystals

All three diffusion-bonded samples, which could successfully be prepared for TEM measurements, feature a tail-to-tail (O|O) orientation and are doped with bismuth and cobalt (cf. pp. 25). However, they differ from each other in terms of bonding and annealing conditions as well as in the amount of added dopants.

4.2.1. Doped DB bicrystal in O|O orientation I (DB-I)

After sample preparation, but prior to the TEM/STEM investigations, the diffusion-bonded bicrystal DB-I in tail-to-tail (O|O) orientation with a sputtered interfacial dopant layer (target concentration: 5 mol% Bi₂O₃, 5 mol% Co₃O₄, ~75 nm thickness) was subjected to SEM analysis to obtain overview images including the areas non-accessible by TEM. As shown in Figure 4-11, BSE-SEM revealed a straight grain boundary decorated by isolated Bi-rich inclusions, as determined by EDS measurements.

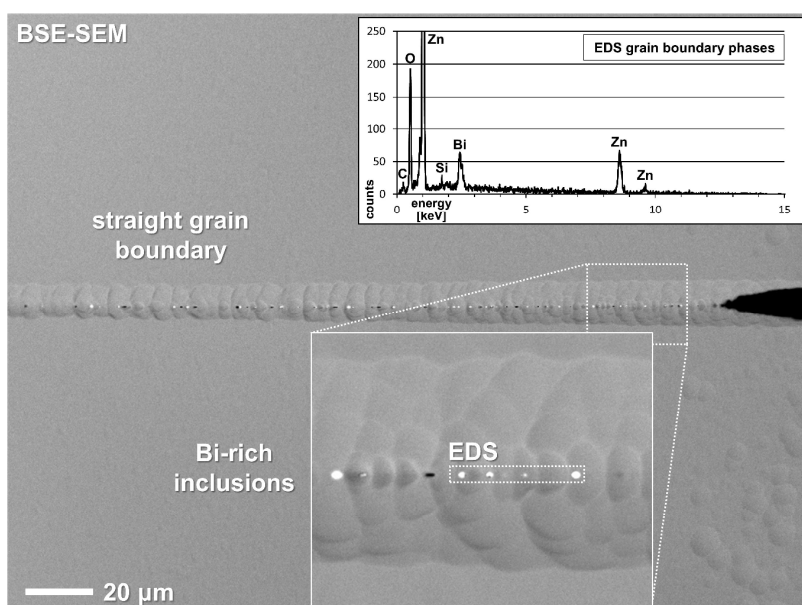


Figure 4-11: BSE-SEM image of the interface in the O|O oriented doped bicrystal DB-I subsequent to TEM-sample preparation and ion-milling. A straight interface is revealed, decorated by Bi-rich inclusions, as determined by EDS measurements (upper inset). A small silicon signal was detected in addition to bismuth. The crater-like structure of the interface region is a preparation artifact due to ion-milling.

Similar to the undoped samples, a small silicon signal was detected at the interface (cf. pp. 47). The crater-like structures in the vicinity of the interface are artifacts of the ion-milling procedure, which typically affects “weak spots” like grain boundaries or interfaces stronger than bulk regions.

HAADF-STEM imaging combined with EDS (Figure 4-12 a)) confirms the presence of Bi-rich inclusions at the bicrystal interface and electron diffraction (SAED inset) clearly identifies them as δ -Bi₂O₃ grains. Especially the superlattice reflections occurring at $\frac{1}{3}$ (hkl) positions are characteristic for the δ -modification, which is a defective fluorite structure rich in anion vacancies, hence being predestinated to ordering phenomena leading to superlattice structures.^{227, 228} In this case, a 3x3x3 supercell was formed as illustrated in the ABF-STEM image in Figure 4-13. However, it remains unclear if this superlattice is formed by a dopant-independent ordering of vacancies or due to impurities.

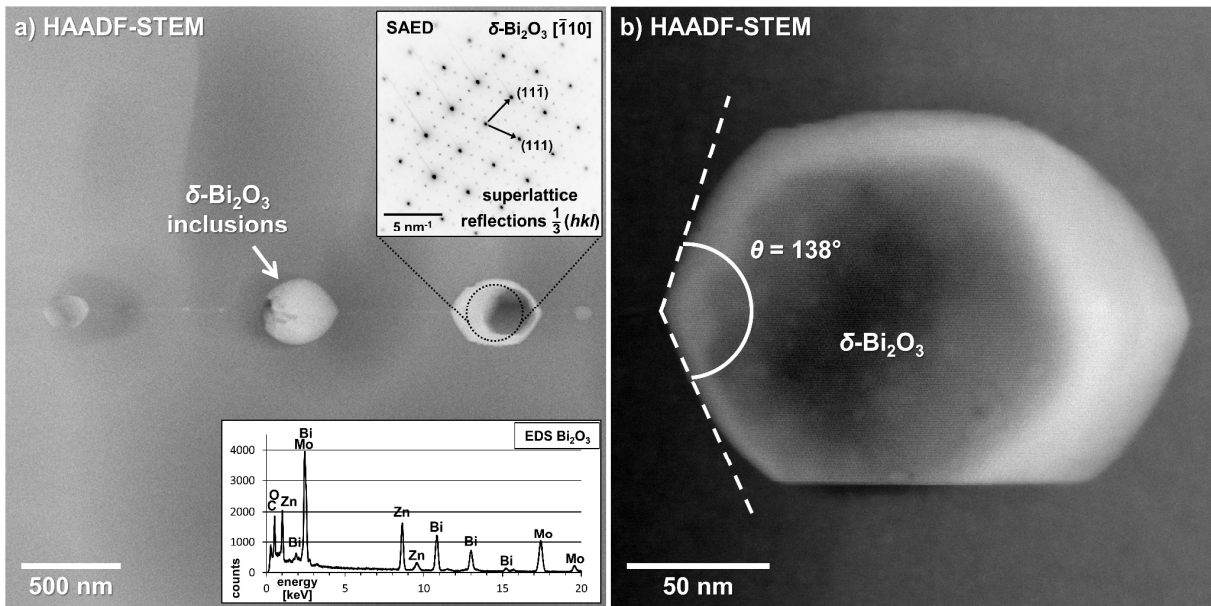


Figure 4-12: a) HAADF-STEM image of the Bi-rich inclusions at the interface of the O|O oriented bicrystal DB-I, doped by sputtering a 75 nm dopant layer with 5 mol% Bi₂O₃ and 5 mol% Co₃O₄ (target composition). δ -Bi₂O₃ is clearly and unambiguously identified by EDS and electron diffraction (lower & upper inset). The superlattice reflections at $\frac{1}{3}(hkl)$ positions are characteristic for the δ -modification of Bi₂O₃.²²⁷ b) HAADF-STEM image of an individual δ -Bi₂O₃ grain revealing a large dihedral angle of $\theta = 138^\circ$ at the interface, which indicates a non-wetting behavior.²²⁹

On the one hand, respective impurity elements, which are typically metal ions with high valences, such as Nb, Ta or W,^{227, 228} were neither added nor detected by EDS. On the other hand, in a few rare cases, cobalt is also reported as a dopant in Bi₂O₃ and probably promoted the superlattice formation.^{230, 231} However, no information on the solid solubility of Co in δ -Bi₂O₃ is found in the respective literature, except the formation of γ -Bi₂O₃ phases such as CoBi₂₅O₄₀ or Co₁₆Bi₁₀O₃₈, which are ruled out via SAED.^{232, 233} If cobalt induced the superlattice formation, its concentration in the Bi₂O₃ grains must be below the detection limit of EDS.

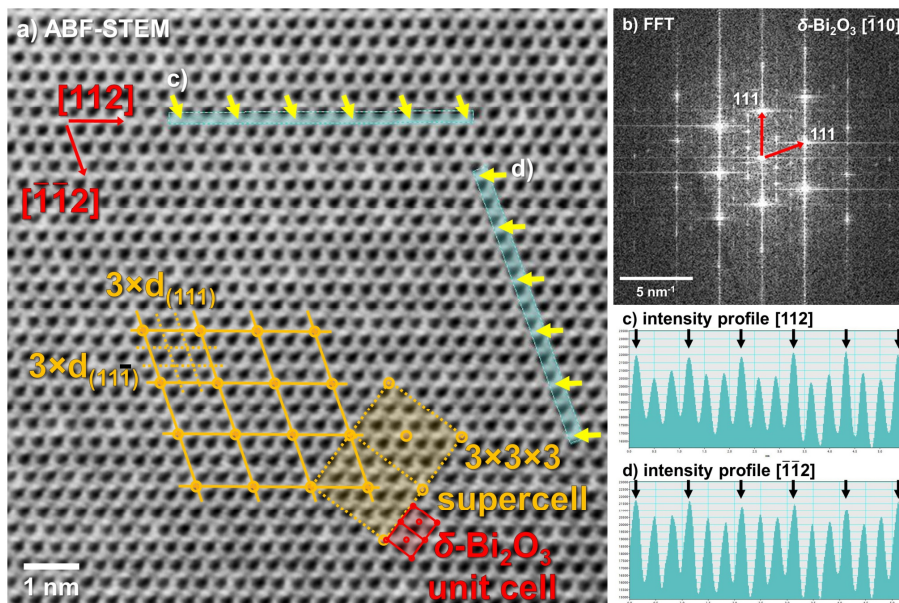


Figure 4-13: a) FFT-filtered ABF-STEM image of δ -Bi₂O₃ in $[\bar{1}10]$ orientation depicting the $3 \times 3 \times 3$ supercell compared to the regular unit cell. b) FFT of the ABF-STEM image showing the crystallographic directions as well as small additional spots at $\frac{1}{3}(hkl)$ positions corresponding to the $3 \times 3 \times 3$ superlattice. c) and d) show plots of the intensity profiles along the $[112]$ and the $[\bar{1}\bar{1}2]$ directions illustrating the threefold-periodic intensity variation defining the supercell in the ABF-STEM image.

It should be noted that the δ -modification is the high-temperature phase of Bi_2O_3 , which is normally unstable at room temperature and transforms either to the α -phase or – depending on cooling rate and temperature path – to the metastable β - or γ -modification.²³⁴ In addition, the incorporation of ZnO is reported to lead to the formation of γ - Bi_2O_3 , although later studies did not find any evidence for stable γ - Bi_2O_3 .^{5, 235} Thus, the finding of δ - Bi_2O_3 is somewhat unexpected, but might be explained by the results of Watanabe, who reports that the transition rates of δ - Bi_2O_3 exhibit a certain “sluggishness”.^{236, 237} In consequence, it is easily and probably unintentionally quenched, even if no special quenching procedure was applied. Consistently with that, the δ as well as the α -, β - or γ -phases are reported to occur in typical ZnO varistor ceramics.^{133, 142, 238} However, in the case of bicrystals, the finding of δ - Bi_2O_3 is of special relevance for the interface doping and hence, the varistor properties, since it exhibits non-wetting properties for ZnO grain boundaries.¹³³ As shown in Figure 4-12 b), the large dihedral wetting angles ($\theta = 138^\circ$), which are typical for Bi_2O_3 grains in this sample, confirm the non-wetting behavior.²²⁹ Regarding cobalt, the second dopant element in this sample, distinct phases were not observed at the investigated interface regions, which is seen as an indication of Co being largely dissolved in the ZnO crystal lattice. Although its solubility limit is $\ll 1$ mol% at room temperature, it is >10 mol% at the applied bonding temperature of 1000°C .^{239, 240}

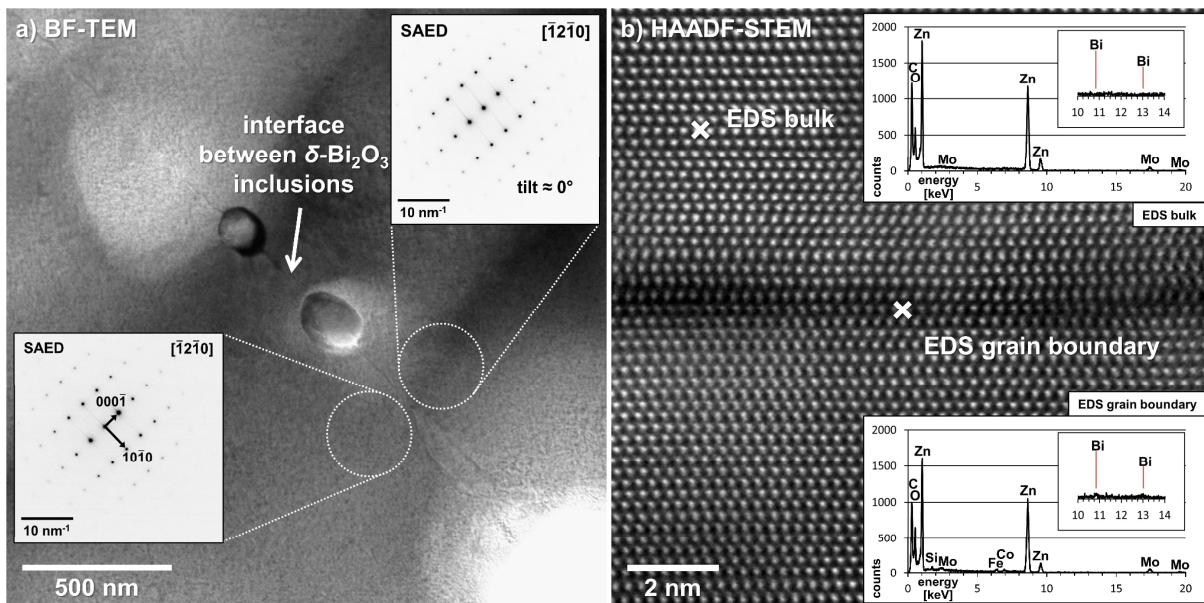


Figure 4-14: a) BF-TEM image of the interface in the O|O bicrystal DB-I in $[\bar{1}2\bar{1}0]$ zone-axis orientation. Electron diffraction indicates a perfect alignment of the bicrystal halves with zero zone-axis tilt (SAED insets). b) FFT-filtered HAADF-STEM image of the interface section between the δ - Bi_2O_3 inclusion revealing an atomically well-bonded and coherent grain boundary. No interfacial films or any kind of distinct Bi segregation is observed. However, silicon is detected at the interface indicating a Si segregation as previously observed in undoped bicrystals (cf. pp. 47), which explains the reduced intensity (Z^2 -contrast) at the interface.

This is in agreement with EDS featuring only very small cobalt peaks (lower inset Figure 4-14 b)), which relates to a low local concentration being the consequence of bulk diffusion and dilution during the annealing. The quality of the bicrystal alignment was found to be remarkably precise with no measurable zone-axis tilt between the bicrystal halves, as determined by SAED

(Figure 4-14 a)). Consistent with that, TEM images in both zone-axis and two-beam condition did not feature any indications of misalignment, such as strain contrast or fringe displacement at the interface. According to the STEM image in Figure 4-14 b), the interface section between the δ -Bi₂O₃ grains is free from any crystalline or amorphous film. Furthermore, it is atomically well-bonded and highly coherent with only minor lattice distortions, as expected from the perfect (000 $\bar{1}$)|(000 $\bar{1}$) bicrystal alignment. Bismuth was neither detected by EDS measurements nor indicated by the Z²-contrast of HAADF-STEM, hence no significant bismuth segregation or incorporation occurred at the bicrystal interface. However, silicon is found at the grain boundary by EDS, along with a reduced intensity in HAADF-STEM, which is hence seen as Z²-contrast. Regarding the segregation of silicon, it is assumed that the same considerations as for the undoped bicrystals apply here as well (cf. pp. 54).

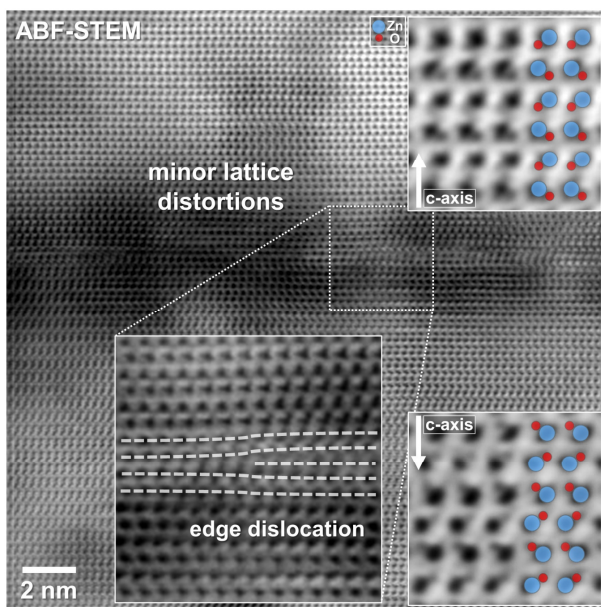


Figure 4-15: FFT-filtered ABF-STEM image of the interface in bicrystal DB-I in $[\bar{1}2\bar{1}0]$ zone-axis orientation. Except for a single edge dislocation and minor lattice distortions, the interface is predominantly straight and atomically well-bonded. The two small ABF insets on the right depict a tail-to-tail orientation as revealed by the directions of the Zn-O dumbbells.

Figure 4-15 features an ABF-STEM image of an interface section between δ -Bi₂O₃ grains different from the position shown in Figure 4-14. Here again, the interface does not exhibit any indication of crystalline or amorphous films or any other types of dopant inclusion or segregation. Besides a single edge dislocation and minor lattice distortions, the

grain boundary appears straight and coherently bonded. Furthermore, the tail-to-tail orientation is confirmed.

4.2.2. Doped DB bicrystal in O|O orientation II (DB-II)

Similar to bicrystal DB-I, sample DB-II is diffusion bonded in tail-to-tail (O|O) orientation with a sputtered interfacial dopant layer. However, two important differences exist: Firstly, the doping parameters were different with a significantly lower dopant concentration of only 1 mol% Bi₂O₃ and 1 mol% Co₃O₄ in the sputtering target, but a four times higher layer thickness of \sim 300 nm. Nevertheless, this corresponds to lower doping in total. Secondly, the misalignment of the bicrystal halves is rather high with 2.8° tilt between the $[\bar{1}100]$ zone axes, as determined by electron diffraction measurements (Figure 4-16 a). However, TEM and STEM imaging revealed a straight, rather uniform grain boundary. Whereas no individual cobalt or bismuth phases were found at the actual interface, they were observed in the near bulk region several times, but always on the same side. This finding indicates different growth rates for both bicrystal sides, causing an overgrowth of the dopant phases during bonding and annealing. It

is assumed that the bicrystal half with the dopant layer sputtered-on is well-aligned in relation to the interface, whereas the other half is rather misaligned since it is placed on the probably uneven surface of the sputtered layer.

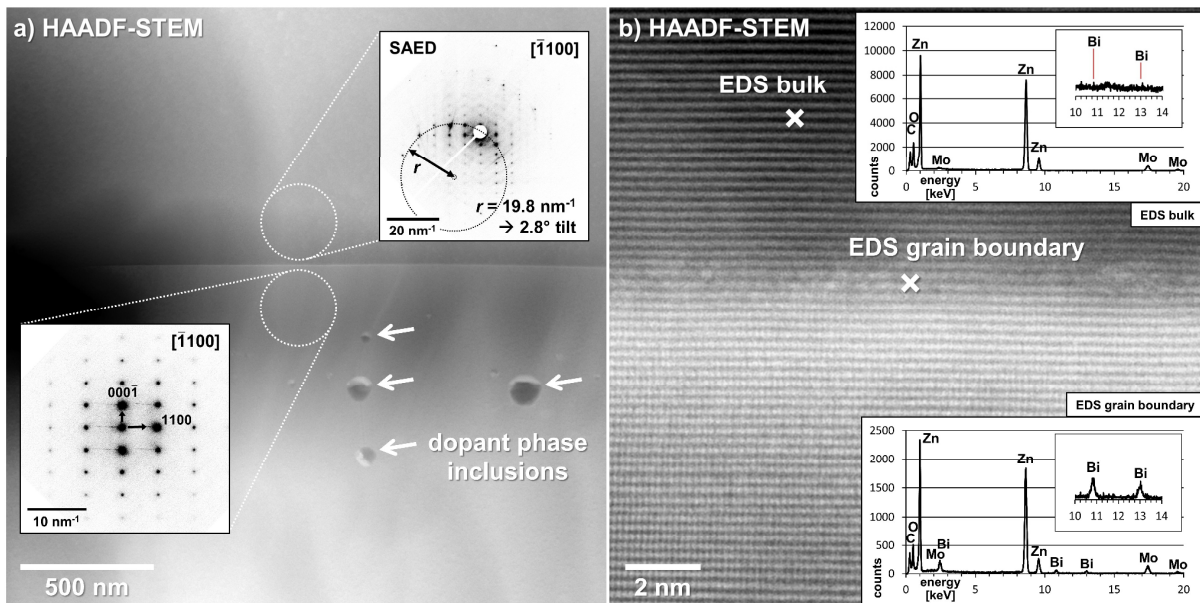


Figure 4-16: a) HAADF-STEM image of the interface in the O|O oriented doped bicrystal DB-II in $[\bar{1}100]$ zone-axis orientation. The sample was doped by sputtering a (nominal) 300 nm thick dopant layer with 1 mol% Bi_2O_3 and 1 mol% Co_3O_4 (target composition). SAED was used to determine a misalignment of 2.8° tilt (insets). Dopant phases were found as inclusions in the near bulk, but not at the actual interface and only on one side, indicating a one-directional (over)growth. b) FFT-filtered HAADF-STEM images (Z^2 -contrast) indicate the presence of heavy elements, i.e., Bi. EDS measurements comparing bulk and interface reveal a distinct Bi accumulation at the grain boundary. Due to the large misalignment, the atomic structure of the interface could hardly be resolved.

Assuming a uniformly flat surface for the entire dopant layer appears unlikely, especially if its high thickness is considered, which might vary and is at least partially larger than the intended 300 nm, since an approximately 500 nm wide distance is measured between dopant inclusions perpendicular to the interface. In consequence, it is expected that the sputtered bicrystal half features a better alignment and connection to the dopant layer than the other and therefore, exhibits faster growth and recrystallization of the (at this point still polycrystalline) ZnO fraction in the sputtered layer.^a This would explain the shift of the final interface from the center towards the misaligned bicrystal half, including the observed overgrowth of dopant phases. It should also be noted that a true $(000\bar{1})|(000\bar{1})$ alignment was not achieved for this sample, which renders the simultaneous atom-resolved imaging of both bicrystal halves and hence the atomic structure of the interface impossible, as it can be seen in Figure 4-16 b). Nevertheless, respective HAADF-STEM images (Z^2 -contrast) clearly indicate the presence of heavy elements at the interface, which appears bright compared to the bulk. EDS measurements confirm the presence of bismuth at the interface, while it is absent in the bulk. Cobalt was neither detected at the interface nor in the immediate vicinity. Therefore, it must be either diluted below the detection limit or “left behind” during overgrowth. In contrast to that, bismuth is still present at the interface.

^a Please note, the sputter target contains 1 mol% Bi_2O_3 , 1 mol% Co_3O_4 and 98 mol% ZnO.

4.2.3. Doped DB bicrystal in O|O orientation III (DB-III)

The doped bicrystal DB-III, which has tail-to-tail (O|O) orientation with a sputtered dopant layer of 500 nm thickness, represents an example of incomplete bonding. The dopant concentration in the target was 10 mol% Bi₂O₃ and 10 mol% Co₃O₄. As shown in Figure 4-17 a), the bicrystal halves are not directly bonded but still separated by a polycrystalline layer of about 1 μm thickness.

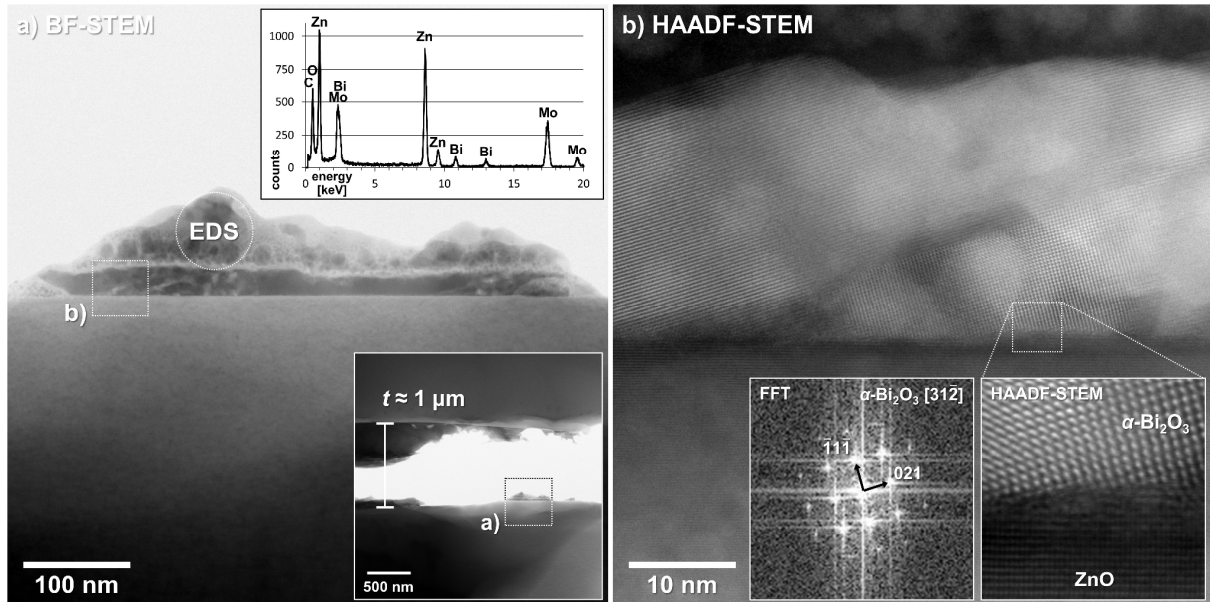


Figure 4-17: a) BF-STEM image of the interface in the O|O oriented doped bicrystal DB-III revealing an incomplete bonding. Doping was achieved by sputtering a 500 nm layer on the interface prior to bonding with 10 mol% Bi₂O₃ and 10 mol% Co₃O₄ (target composition). The thickness of the dopant layer was, however, determined to be about 1 μm (lower inset). The interfacial material mainly consists of polycrystalline Zn- and Bi-rich grains according to EDS measurements (upper inset). b) α-Bi₂O₃ is identified by high-resolution HAADF-STEM and corresponding FFT images (insets).

Similar to the situation in sample DB-II (cf. p. 62), the actual dopant layer thickness is significantly larger than intended. Although cobalt phases were occasionally detected (not shown here), the majority of the grain-boundary material comprises ZnO and Bi₂O₃, as indicated by EDS. Atom-resolved HAADF-STEM and corresponding FFT images identified the bismuth phase being the α-Bi₂O₃ modification, as expected for a non-quenched sample at room temperature (Figure 4-17 b).²³⁴ No special orientation relationship was observed between ZnO and α-Bi₂O₃, hence their interface is incoherent and disordered, as it can be seen in the inset on the lower right in Figure 4-17 b). Regarding the bicrystal misalignment, no information can be given, as both sides are widely separated and bending of the TEM thin-foil becomes dominant. Thus, SAED measurements would not represent the true (mis)alignment, but the foil bending. In contrast to the other samples, sample B-III could be utilized to verify and roughly evaluate the diffusion of cobalt into the ZnO lattice for two reasons: Firstly, due to the incomplete bonding, the interface between sputtered dopant layer and ZnO is still present and easy distinguishable; hence, it can be used as a reference and starting point for EDS measurements. Secondly, the higher cobalt content of 10 mol% provides a stronger signal and a more

pronounced decrease from the dopant layer towards the inner bulk regions. The results are shown in Figure 4-18.

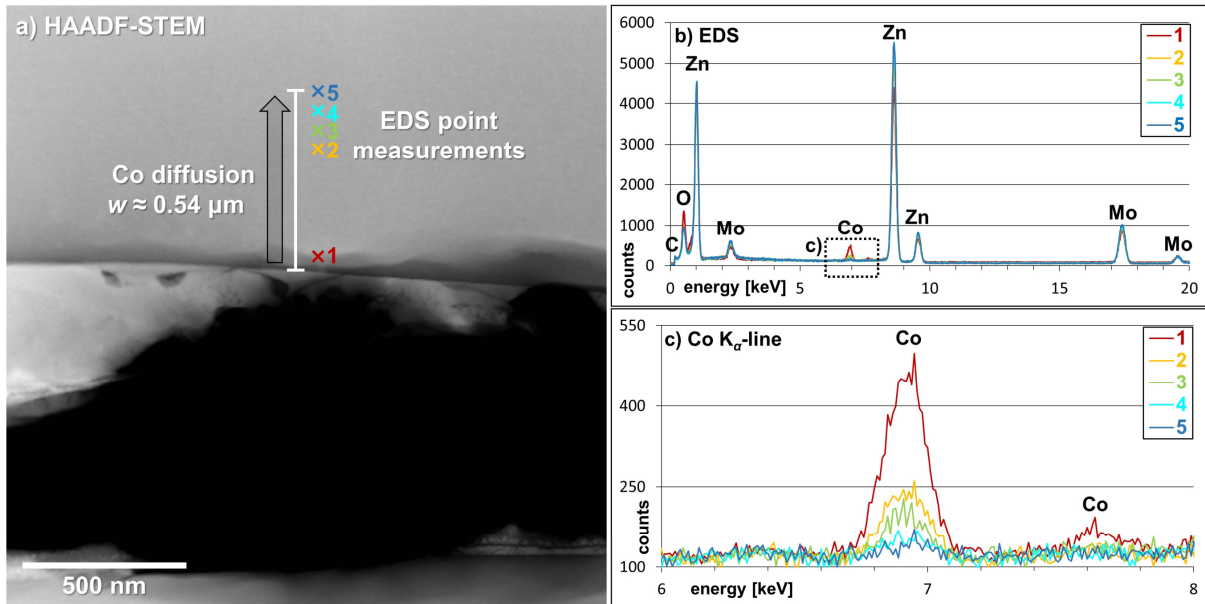


Figure 4-18: a) BF-STEM image of the interface and adjacent bulk region in bicrystal DB-III. This sample could be utilized to evaluate the diffusion width of cobalt into the ZnO lattice, which was determined by EDS point measurements to be at least $0.54 \mu\text{m}$. b) Stacked EDS spectra corresponding to the EDS point measurements as depicted in a). In figure c), the cobalt K_{α} -peak is enlarged for a better depiction of its decreasing height from about 500 counts at measurement point 1 down to the background level at measurement point 5. All measurements were performed using the same settings for the electron beam, detector angle and live time.

Five EDS point measurements were recorded starting near the interface between the ZnO bulk and the dopant layer, where a well-visible cobalt signal was detected. Subsequent measurement points were shifted toward the inner bulk regions yielding successively smaller Co-peaks, which dropped down to the background level at a distance of about $0.54 \mu\text{m}$ to the interface. Considering the EDS detection limit of about 1 mol%, this distance does not represent the true diffusion width, which is naturally larger, but nevertheless provides a useful indication for the minimum distance covered by bulk diffusion of Co at the respective synthesis conditions (1 h @ $1000 \text{ }^{\circ}\text{C}$ plus heating and cooling). Moreover, by confirming the suggested solution and dilution of Co into ZnO, this simple and straightforward experiment explains its strong depletion at the bicrystal interfaces, as it was observed in the successfully bonded bicrystals DB-I and DB-II (cf. p. 60 and 62). The varistor properties are directly related to and rely on the sufficient doping of ZnO interfaces, which applies not only to Bi but also to Co and other transition metals (cf. pp. 14). Therefore, such a depletion of dopants is seen as detrimental and needs to be thoroughly considered in (future) bicrystal design.

4.2.4. I-V measurements

All three doped diffusion-bonded samples were subjected to I - V measurements to determine the degree of varistor behavior (non-linearity). The results are shown in Figure 4-19. Whereas samples DB-II and DB-III exhibit weak non-linear I - V characteristics ($\alpha_{\text{max}} \approx 3.1$ and $\alpha_{\text{max}} \approx 2.3$), sample DB-I shows an almost perfectly linear, ohmic response ($\alpha_{\text{max}} \approx 1$).

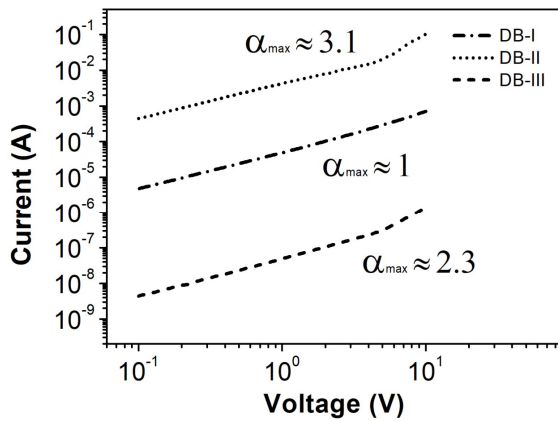


Figure 4-19: I-V characteristics of the DB bicrystals. Weak non-linear characteristics were observed for samples DB-II ($\alpha_{\max} \approx 3.1$) and DB-III ($\alpha_{\max} \approx 2.3$), whereas ohmic behavior was observed for DB-I ($\alpha_{\max} \approx 1.0$). The leakage current (measured at 0.1 V) is considerably different for all three samples, with DB-II having the highest with $4 \cdot 10^{-4}$ A and DB-III the lowest with $4 \cdot 10^{-9}$ A. DB-I exhibits $5 \cdot 10^{-6}$ A.

The breakdown voltage is $V_B \approx 5$ V for both DB-II and DB-III and therefore, slightly higher than the expected ~ 3.5 V for a single grain boundary.^{90, 221}

However, this value reflects the average, more or

less randomly oriented single barrier in polycrystalline ZnO varistors. In consequence, it might be limited in its relevance for individual bicrystal boundaries, beyond being a reference for comparison. The leakage currents of the three DB samples (measured at 0.1 V) are different by several orders of magnitude. In contrast to DB-III, which exhibits $4 \cdot 10^{-9}$ A and hence, the lowest leakage current, a comparably high current of $4 \cdot 10^{-4}$ A was observed for DB-II, while $5 \cdot 10^{-6}$ A was measured for sample DB-I.

In addition to the stress-free experiments, sample DB-III was subjected to load-dependent *I-V* measurements. As shown in Figure 4-20, the response to a load increase from 5 MPa to 100 MPa is contrary to what is expected for an O|O bicrystal (cf. pp. 18). Instead of a decrease, an increase in non-linearity was observed up to $\alpha_{\max} \approx 3.3$. Interestingly, the leakage current remains nearly unchanged. However, a further load increase causes the opposite effect on the non-linear characteristics, which are gradually reduced until a nearly linear behavior is obtained at 300 MPa with $\alpha_{\max} \approx 1.8$. At the same time, the leakage current is increased by two orders of magnitude up to $4 \cdot 10^{-7}$ A. The breakdown voltage of $V_B \approx 5$ V remains constant up to 100 MPa. At 150 MPa, when the response reverses and the barrier starts to decrease, it is shifted to $V_B \approx 4.1$ V.

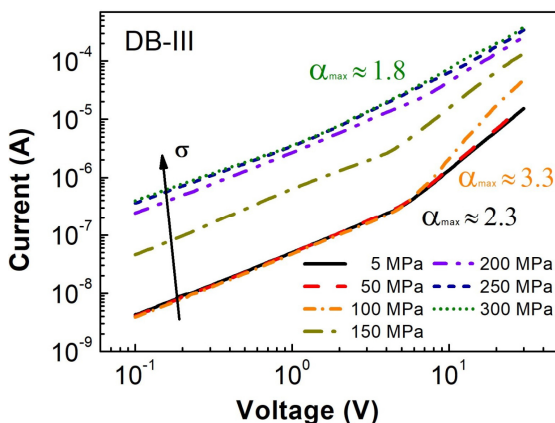


Figure 4-20: Load dependent I-V characteristics of sample DB-III. From 5 MPa to 100 MPa, the observed change in α_{\max} is counter-intuitive as it increases up to $\alpha_{\max} = 3.3$, instead of decreasing. The leakage current (measured at 0.1 V) remains nearly unaltered. However, with increasing load from 100 MPa to 300 MPa, the response is as expected and the coefficient of non-linearity is gradually lowered down to $\alpha_{\max} = 1.8$. Simultaneously, the leakage current increases by two orders of magnitude up to $4 \cdot 10^{-7}$ A. The breakdown voltage is $V_B \approx 5$ V up to 100 MPa and $V_B \approx 4.1$ V for 150 MPa and higher loads.

Considering that samples DB-II and DB-III both feature bismuth at the interface, the observed occurrence of non-ohmic behavior correlates well with the TEM results. The amount of bismuth segregated to the interface in sample DB-II is obviously sufficient to create at least a weak varistor-type potential barrier. Likewise, the large and dopant-rich interlayer in DB-III must

involve enough trap states for the barrier formation. However, it is unclear for DB-III if these trap states are located within the interlayer material itself, as the sputtered layer contained ~80 mol% ZnO, or at the “interlayer|bulk” interface. The unexpected behavior in the load-dependent measurements is attributed to the presence of randomly oriented ZnO grains in the interlayer. According to this explanation, it is assumed that some grains were accidentally oriented in such a way that the initial load increase caused the accumulation of negative charges at the potential barrier, similar to the Zn|Zn case. However, a further load increase reverted this process and positive charges dominated, hence lowering the barrier. This might be due to two circumstances: Firstly, the large polycrystalline interlayer probably caused a locally inhomogeneous stress distribution, which additionally might have changed with increasing load, e.g., due to cracking and (micro)fracture. In consequence, different grains might have contributed differently at different stress levels. The observed shift of V_B from 5 V to 4.1 V supports this consideration, as it reflects the number of active grain boundaries and indicates a change in this regard.^{90, 221} Secondly, lowering varistor-type potential barriers via mechanical load is much more efficient than increasing them (cf. pp. 77).^{101, 199} For an increase, the barrier height must be lifted effectively along the entire interface, whereas for a decrease, the barrier height needs to be reduced only locally, as the current path will take the route of the lowest resistance. Therefore, even if the (initial) load-increase preferably affected Zn|Zn-like oriented grains, it might be overcome by the more efficient barrier-lowering effect of O|O-like grains. However, there still are some inconsistencies, as the breakdown voltage of $V_B \approx 5$ V is ambiguous and neither distinctively indicates one or two boundaries nor a polycrystalline situation as suggested above.^{90, 221} In summary, the situation for sample DB-III is quite complex and it should be noted that it definitely cannot be considered a true bicrystal, according to the TEM measurements. In contrast to that, the correlation between I - V characteristics and TEM observations is straightforward for sample DB-I. As shown in section 4.2.1 (pp. 58), bismuth is entirely retracted from the boundary, hence no potential barrier can be formed and the resulting electric behavior is ohmic. As the current path will take the route of lowest resistance, additional ohmic barriers between ZnO and Bi₂O₃ grains will be bypassed, hence the latter can be regarded as electrically inactive secondary phases. Although no varistor-type barrier is formed, the electrical conductivity appears to be, nonetheless, determined by the inversion boundary, considering the leakage current being low in comparison to the reference sample B-III (cf. p. 54).

4.2.5. Discussion and Summary

Dopant-layer thickness and bonding

The TEM results indicate that large thicknesses of the sputtered interfacial dopant layer complicate the successful bonding and alignment of DB bicrystals. For samples DB-I and DB-II, which featured thin to medium dopant layers of 75 nm and 300 nm, an atomically well-bonded interface was observed. In contrast, sample DB-III with a dopant layer of 500 nm thickness was incompletely bonded (if the bonding process had started at all). Independent of their respective

layer thicknesses, all DB samples were bonded for 1 h @ 1000 °C. However, since the sputtered dopant layer is polycrystalline or amorphous and mainly consists of ZnO, the bonding duration must be sufficiently long to ensure a complete recrystallization, which is expected to afford more time in case of a higher thickness, which could explain why sample DB-III was incompletely bonded. Likewise, sample DB-II was most likely successfully bonded because it was additionally annealed for 2 h @ 1100 °C. Therefore, it is concluded that the duration of the bonding step should be adjusted to the layer thickness for future bicrystals syntheses and that the presented data can be used as guiding values. In addition, with > 500 nm and > 1 μm, it should be noted that the actual layer thickness was (unintentionally) much larger than the expected 300 nm and 500 nm, in both DB-II and DB-III, respectively. Since the EDS measurements in sample DB-III clearly show that Co diffuses and dilutes into the ZnO bulk in significant amounts, even after only 1 h @ 1000 °C (plus heating and cooling), it is also recommended to sputter rather highly doped, but thin layers, in order to minimize the required bonding duration. Since sufficient doping of interfaces is essential for good varistor properties, long bonding durations and related diffusion processes can be regarded as generally detrimental; not only in the case of cobalt but for other dopants as well. An additional option to attenuate diffusion is lowering the bonding temperature, which naturally reduces the speed of the process, but also lowers – in the case of cobalt and other transition metals – the solid solubility in ZnO and hence, might restrict the unwanted diffusion more than the desired recrystallization.²³⁹ However, according to the author's knowledge, the minimum temperature required for bonding has never been clearly determined. In fact, the applied temperature and holding time of 1 h @ 1000 °C is already rather low compared to other bicrystal studies.^{140, 168} Nevertheless, a further temperature reduction might be beneficial for the synthesis of doped ZnO bicrystals.

Bicrystal alignment and bismuth segregation

As detailed in section 1.7 (pp. 18), Sato et al. observed a distinct relationship between grain-boundary coherency and the amount of segregated praseodymium to the bicrystal interface.¹⁴⁰ A similar relation is found for the doped DB bicrystals. As the coherency of a grain boundary is naturally reduced with increasing misalignment, sample DB-I is regarded as highly coherent, whereas DB-II and DB-III are seen as rather incoherent. This consideration is confirmed by the TEM images featuring an almost distortion and defect-free interface in DB-I. Like praseodymium, bismuth is insoluble in ZnO and hence, a similar segregation behavior is expected, which requires a certain degree of incoherency to provide suitable segregation sites.^{4, 5, 241} Indeed, the actual bicrystal interface in DB-I is free from any segregated bismuth, although it is theoretically higher doped than sample DB-II, which in contrast, features a Bi decoration at the grain boundary as well as non-linear characteristics. Due to the highly coherent bonding and hence, the lack of segregation sites in sample DB-I, the entire bismuth content was retracted from the interface and formed non-wetting δ -Bi₂O₃ inclusions.¹³³ In consequence, no potential barrier was formed and the bicrystal responded completely ohmic in the *I-V* measurements. In

the case of samples DB-II and DB-III, the misalignment and the polycrystalline interlayer, respectively, introduced incoherency as well as the possibility to incorporate at least low amounts of Bi and hence, caused the emergence of varistor behavior. The necessity of appropriate segregation sites becomes even more obvious considering that the bonding temperature of 1000 °C is significantly higher than the melting point of Bi₂O₃ at 824 °C and the entire Bi content is liquified and highly mobile during bicrystal synthesis.^a In addition, the high-T modification δ -Bi₂O₃, which forms first upon cooling,^b exhibits poor wetting properties of ZnO grain boundaries compared to the low-T α -modification.¹³³ This might intensify the problem of segregation since it facilitates the retraction of bismuth from the interface. Even after a (hypothetical) recrystallization to the α -phase, a redistribution of bismuth along the grain boundary will not occur, because this would imply a diffusion-controlled solid-state process, at which compact, stable Bi₂O₃ grains disintegrate into thin films or individual atoms; a process considered impossible under the respective conditions. Furthermore, all investigated Bi₂O₃ grains in DB-I unambiguously belonged to the δ -modification and no indications were found for a phase transition to α -Bi₂O₃. In contrast to that, α -Bi₂O₃ was the only Bi-oxide phase observed in sample DB-III, which implies a better wetting of ZnO by Bi₂O₃ and correlates well with the observed non-linearity in the *I-V* measurements. Unfortunately, a comparison of DB-I and DB-III is limited in its relevance, as the latter is not really a bicrystal, since it still features a wide polycrystalline interlayer. In the case of sample DB-II, no distinct Bi-phase has formed at the interface (though they might exist as over-grown inclusions in the bulk). This also indicates that neither a distinct Bi-phase nor a Bi-containing film is necessary to obtain varistor-type potential barriers (cf. pp. 14), although the corresponding coefficient of non-linearity ($\alpha = 2.3$) is rather low.

^a Please note, peritectic and eutectic points exist in the system Bi₂O₃-ZnO at 756 °C and 737 °C, respectively. Thus, the melting of Bi-phases within the dopant layer theoretically starts already earlier, below 824 °C.²³⁵

^b Zn₂Sb₃Bi₃O₁₄ pyrochlore is reported to be the first Bi-rich phase to crystallize from the melt upon cooling in commercial, multi-doped polycrystalline varistor ceramics.²³⁸ However, no pyrochlore formation is reported for the system Zn-Bi-Co-O.

DOPED DB BICRYSTALS - SUMMARY

- ABF-STEM was used to successfully verify the O|O orientation of sample DB-I.^a
- Samples DB-I and DB-II featured straight and atomically well-bonded interfaces without the presence of continuous interfacial films or phases. In contrast, sample DB-III still contained the sputtered polycrystalline dopant layer.
- SAED was used to determine the bicrystal misalignment, which was 0° (DB-I) and 2.8° (DB-II), while being undeterminable, but probably large in DB-III.
- For DB-II and DB-III, the thicknesses of the sputtered dopant layers were highly underestimated and nearly twice as large as intended, with >500 nm instead of 300 nm (DB-II) and 1 μm instead of 500 nm (DB-III).
- Large thicknesses of sputtered dopant layers (>300 nm) hinder the bonding process or at least require an extended bonding duration.
- Sample DB-I features a highly coherent, low-defect and Bi-free interface. This is explained by the absence of suitable segregation sites. Upon disintegration of the sputtered dopant layer, Bi was completely retracted and formed non-wetting,¹³³ electrically inactive δ -Bi₂O₃ grains. As a result, the electrical behavior is purely ohmic with $\alpha_{\max} \approx 1$.
- Due to the misalignment of 2.8°, sample DB-II features a less coherent interface, which implies local distortions and (probably) dislocations, providing segregations sites for Bi atoms. Consistently, Bi was detected at the interface and *I-V* measurements yielded a non-linearity coefficient of $\alpha_{\max} \approx 3.1$.
- For sample DB-III, non-linear behavior ($\alpha_{\max} \approx 2.3$) was observed as well, which is attributed to the retained polycrystalline dopant layer containing α -Bi₂O₃, which exhibits better wetting properties.¹³³ This condition also implies a reduced coherency.
- In all samples, cobalt was found to dissolve into the ZnO lattice, leading to a depletion at the interface, which is expected to be detrimental to the varistor properties. Sample DB-III could be utilized to evaluate this process via EDS point measurements, yielding a diffusion width of >0.54 μm after 1 h @ 1000°C plus heating and cooling.

^a Not conducted for samples DB-II and DB-III, as respective TEM specimens exhibited rather low quality, thus being of limited relevance and not appropriate for advanced TEM measurements.

4.3. EST bicrystal

Only the EST sample in tail-to-tail (O|O) orientation could be subjected to TEM measurements, as the corresponding head-to-head (Zn|Zn) sample was incompletely bonded and still polycrystalline (cf. p. 28). Nevertheless, the results of the stress-dependent I - V measurements are presented for both bicrystals for comparative reasons. In contrast to the DB samples, the EST samples are doped with a typical commercial varistor composition, including Bi, Co, Mn, Cr and Ni (cf. p. 27).

4.3.1. EST bicrystal in O|O orientation

Figure 4-21 features a BSE-SEM image of the tail-to-tail oriented EST-O|O bicrystal after being etched in a 10 % HCl_{aq} solution for about 1 s, which was found to be an effective method to reveal grain boundaries and different grain orientations in ZnO (cf. p. 28). As indicated by the dashed white line, only one single grain boundary is observed in the former polycrystalline layer, confirming the successful transformation from a single-poly-single-crystalline stack into a bicrystal, although small polycrystalline regions persisted at the bicrystal edges (not shown here). However, these can be neglected regarding the electrical properties, which are solely determined by the bicrystalline interface, as discussed in section 4.2.4 (pp. 64).

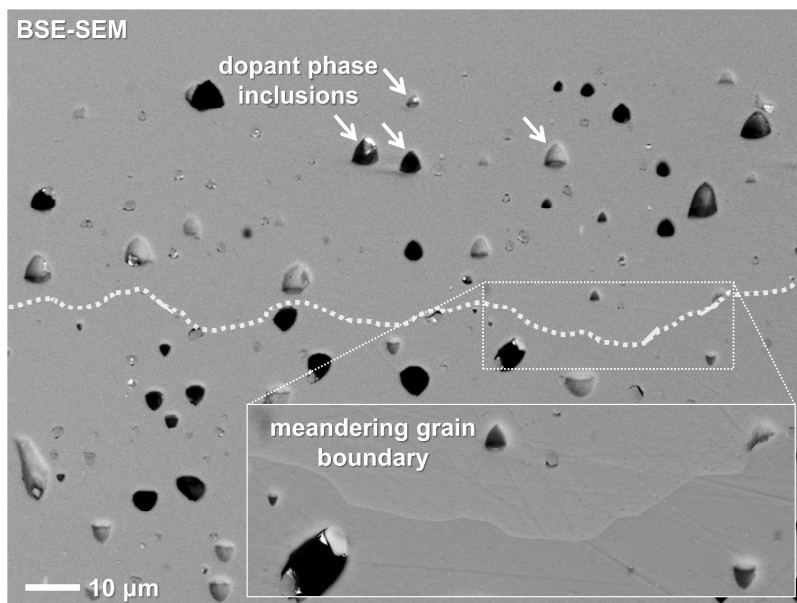


Figure 4-21: BSE-SEM image of the meandering bicrystal grain-boundary (white dashed line) in sample EST-O|O. The interface is mainly free from dopant inclusions, which, however, are numerous observed in the bulk. Homogenous contrast for the bicrystal halves indicates a successful transformation into a bicrystal. Amorphous or crystalline films at the interface were not observed. The sample was etched for about 1 s in a 10 % HCl_{aq} solution for a better accentuation of the grain boundary.

The small difference in brightness for the upper and lower side, as depicted by the

inset in Figure 4-21, indicates a slight misorientation of the bicrystal halves, causing a minor intensity variation due to electron-channeling and back-scatter diffraction effects. A characteristic feature of the grain boundary is its meandering shape, which is in strong contrast to the straight interfaces of the diffusion-bonded bicrystals (cf. pp. 58). Over a wide section, the grain boundary is free from dopant phase inclusions and inflection points do mostly not coincide with respective grains, although they might represent former triple points of the polycrystalline sacrificial layer. Crystalline or amorphous films at the interface were not observed. In the bulk regions, dopant inclusions are found numerously on both sides of the grain boundary, which further confirms the bicrystal interface being located in the center region of the transformed

sacrificial layer. In consequence, similar growth kinetics must have prevailed for both sides during synthesis, since the interface corresponds to the location where the two growth fronts encountered each other.

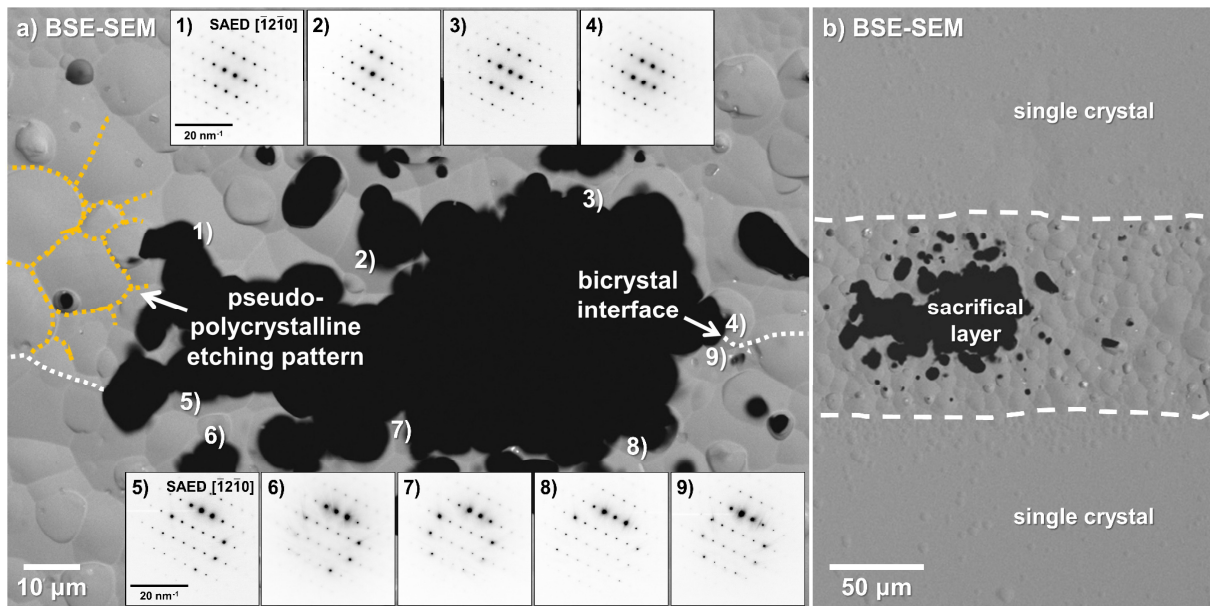


Figure 4-22: a) BSE-SEM image of the meandering grain boundary (white dashed line) in sample EST-O|O after TEM preparation. Upon ion-milling, etching patterns were formed resembling a polycrystalline structure. However, SAED measurements, recorded at position 1) – 9), evidence true single-crystallinity for both bicrystal halves. Please note, all SAED patterns were recorded using the same sample-beam orientation. Since the lower bicrystal half is slightly tilted, patterns 5) – 9) feature the circular intersection of the ZOLZ with the Ewald sphere. Variations within groups 1) – 4) and 5) – 9) are due to thickness variations and bending of the TEM sample thin-foil. b) BSE-SEM overview image of the pseudo-polycrystalline etching pattern, which is limited to the region of the (former) sacrificial interlayer.

Whereas no indication for remaining polycrystallinity was observed previous to TEM preparation (Figure 4-21), a conspicuous etching pattern was formed upon ion-milling. As highlighted in Figure 4-22, this pattern is restricted to the region of the sacrificial layer and resembles a polycrystalline structure. Considering that etching rates are typically different for bulk regions vs. grain boundaries and additionally can be influenced by the local chemistry, this finding revived the question if the transformation to a bicrystalline state was successful and how this pattern is related to the former polycrystalline structure. To answer this question, several SAED patterns were recorded at different measurement points, which are shown as insets in Figure 4-22 a). All measurements were performed using exactly the same beam-to-sample orientation (double-tilt holder: $\alpha, \beta = \text{const}$), which was adjusted to the $[\bar{1}2\bar{1}0]$ zone axis at point 1). As expected for an O|O bicrystal, all images featured the very same zone axis pattern. Whereas patterns 1) – 4) are in precise on-axis orientation, the circular intersection of the Ewald sphere with the ZOLZ in patterns 5) – 9) indicates a small misalignment between the bicrystal halves. Other small differences between the patterns are due to thickness variations and bending of the thin foil. Neither was any correlation with the pseudo grain boundaries of the etching pattern observed nor was any other discrepancy to a true bicrystalline state found, hence the successful transformation is confirmed.

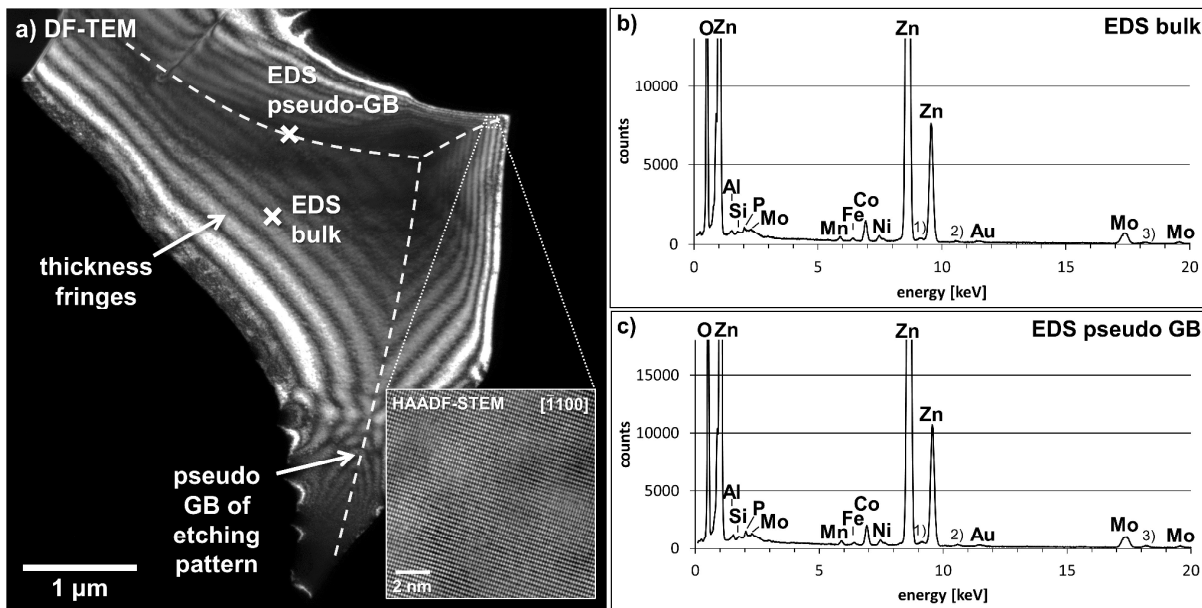


Figure 4-23: a) Two-beam DF-TEM image with $\vec{g} = (0002)$ of sample EST-O|O recorded in the region of the former polycrystalline interlayer, with a small objective aperture applied. Thickness fringes indicate a steep sample topography, at which the ridges correspond to the pseudo-GBs of the etching pattern, as shown in Figure 4-22. The inset depicts an atom-resolved HAADF-STEM image revealing a defect-free, single crystalline structure. Neither any kind of grain- or sub-grain boundary, nor a significant chemical difference is observed. b) and c) are EDS spectra recorded on and off the pseudo-GB, confirming the same chemistry for both sites. The different total intensities (counts) of the spectra are related to the unequal sample thickness. Peaks labeled with 1), 2) and 3) are sum peaks of $\text{ZnK}_\alpha + \text{OK}_\alpha$, $\text{ZnL}_\alpha + \text{ZnK}_\beta$ and $\text{ZnK}_\alpha + \text{ZnK}_\beta$, respectively. The Fe signals originate from the pole piece and the Au signals from the holder. Al, Si and P indicate a minor contamination during or before synthesis.

DF-TEM two-beam imaging with $\vec{g} = (0002)$ revealed that the etching pattern corresponds to a steep and pronounced sample topography, as shown in Figure 4-23. A small objective aperture was applied increasing the contrast and visibility of thickness fringes, which can be interpreted as isolines of the (projected) sample thickness, hence illustrating the topography. This observation is confirmed by AFM imaging in height-sensor mode, which indicates large steps in the region of a few microns (Figure 4-24).

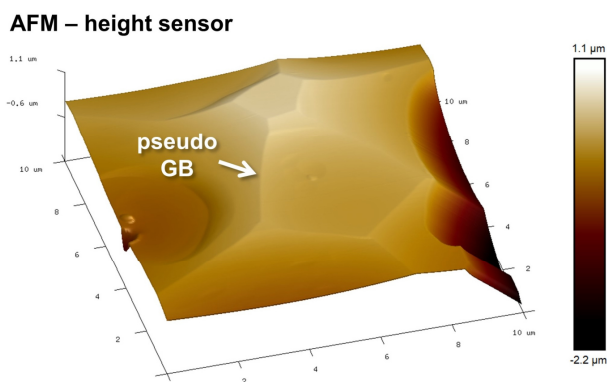


Figure 4-24: AFM image of the pseudo-polycrystalline etching pattern observed in the region of the sacrificial interlayer of sample EST-O|O after ion-milling. The height-sensor mode was used for image generation and revealed a notably uneven sample topography with trench- and ridge-like features of large height differences in the region of microns. The ridges equal the pseudo-GBs of the etching pattern.

Atom-resolved HAADF-STEM (inset Figure 4-23) showed neither indications for a grain or sub-grain boundary nor any Z^2 -contrast features related to a chemical difference between sites on and off the pseudo-GBs. Likewise, no chemical difference was detected by EDS measurements. As a side remark, it should be noted that these EDS measurements also confirm the formation of a solid solution of ZnO and the dopant elements Mn, Co and Ni. In summary, the occurrence of the pseudo-

polycrystalline etching pattern is considered to be of no further relevance for the piezotronic and varistor properties of EST bicrystals. Nevertheless, it must be related to the polycrystalline sacrificial layer in one way or another, since it was not formed in the regions of the original single crystals. Most likely, dopants and dopant phase inclusions are responsible, initially causing locally different etching rates and thus, an uneven topography from the very beginning, which is subsequently intensified or at least maintained during the procedure of ion-milling.

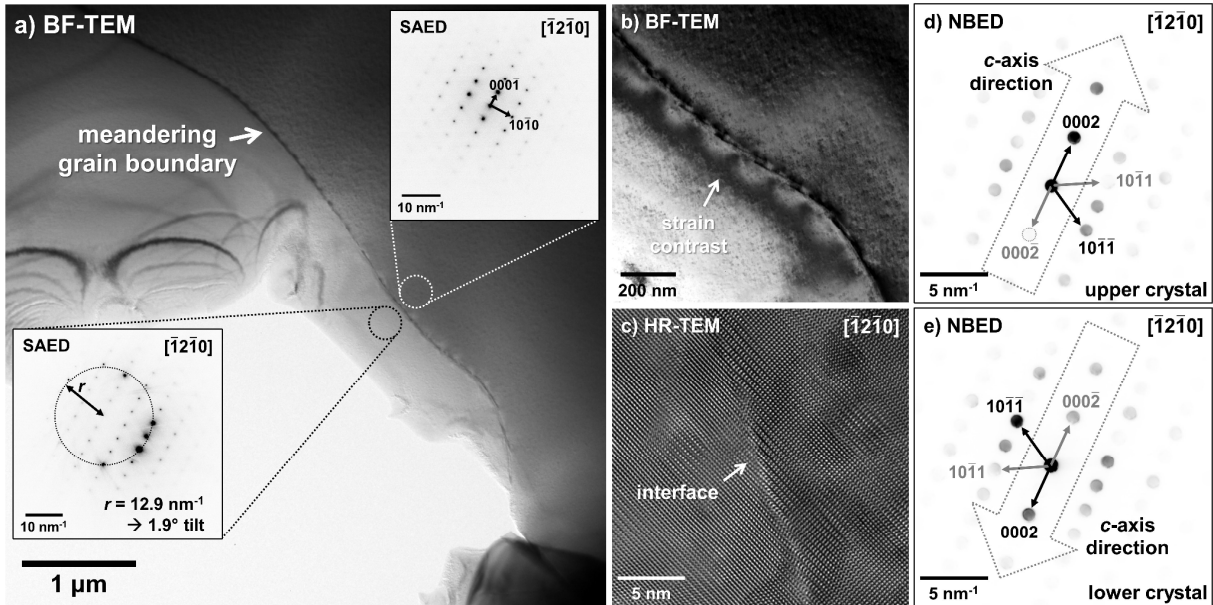


Figure 4-25: a) BF-TEM image of the meandering grain boundary in sample EST-O|O in $\vec{g} = (0002)$ two-beam condition. A misalignment of about 1.9° tilt between the $[\bar{1}2\bar{1}0]$ zone-axes is measured by electron diffraction (SAED insets). b) Two-beam BF-imaging using a small objective aperture reveals periodic strain contrast along the curved interface. c) HR-TEM image in $[\bar{1}2\bar{1}0]$ zone-axis orientation shows an atomically well-bonded interface, without any indications for amorphous or crystalline interfacial films. d) and e) depict NBED measurements, which prove the O|O orientation.

Figure 4-25 a) features a $\vec{g} = (0002)$ two-beam BF-TEM image of the meandering grain boundary in the EST-O|O bicrystal. The misalignment between the bicrystal halves was determined by electron diffraction measurements to be 1.9° tilt between the $[\bar{1}2\bar{1}0]$ zone axes (SAED insets). As shown by Figure 4-25 b), a typical feature of the meandering GB is a periodic strain contrast along the boundary, as revealed by two-beam imaging with a small objective aperture applied. Although the strain contrast appears on only one side of the interface in Figure 4-25 b), it is actually present on both sides. However, the misalignment between the bicrystal halves impeded the simultaneous adjustment of a proper two-beam condition for both sides, hence it could be observed only on one side at once. HR-TEM imaging of the grain boundary shows an atomically well-bonded interface free of any kind of amorphous or crystalline films (Figure 4-25 c)). In order to verify the intended tail-to-tail O|O orientation of the EST bicrystal, NBED diffraction measurements were performed as illustrated in Figure 4-25 d) and e). The violation of Friedel's law, which causes a distinct intensity variation between (0002) & (000 $\bar{2}$) and (10 $\bar{1}1$) & (10 $\bar{1}\bar{1}$) reflection pairs, clearly proves the tail-to-tail orientation.

In addition, this finding was double-checked and confirmed by ABF-STEM imaging of the oxygen positions as highlighted in Figure 4-26. Likewise, the observation of a film-free interface was reproduced.

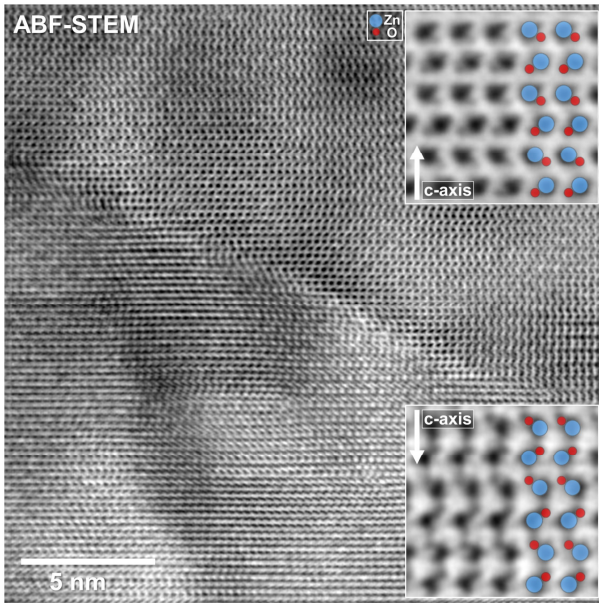


Figure 4-26: FFT-filtered ABF-STEM image of the interface in sample EST-O|O in $[1\bar{2}\bar{1}0]$ zone-axis orientation. Due to bicrystal misalignment, only the upper side is in zone-axis orientation. No indications for any kind of amorphous or crystalline interfacial film are observed. The directions of the Zn-O dumbbells verify the tail-to-tail orientation (insets).

As it can be seen in Figure 4-27 a), the grain boundary meanders not only in the image plane but in all three dimensions. It should be noted that the seemingly varying width of the grain boundary does not represent the true, but only the projected width, hence indicating different inclinations of the interface plane. This is especially well visible in Figure 4-27 b), where the interface is successively less inclined from left to right, almost reaching an edge-on orientation. In consequence, the projected width decreases from tenths of nanometers down to a fine line. Besides its 3D-meandering shape, a further characteristic feature of the grain boundary is the occurrence of a fish-scale-like contrast, which is indicative of the presence of a dislocation network (inset Figure 4-27 a)).

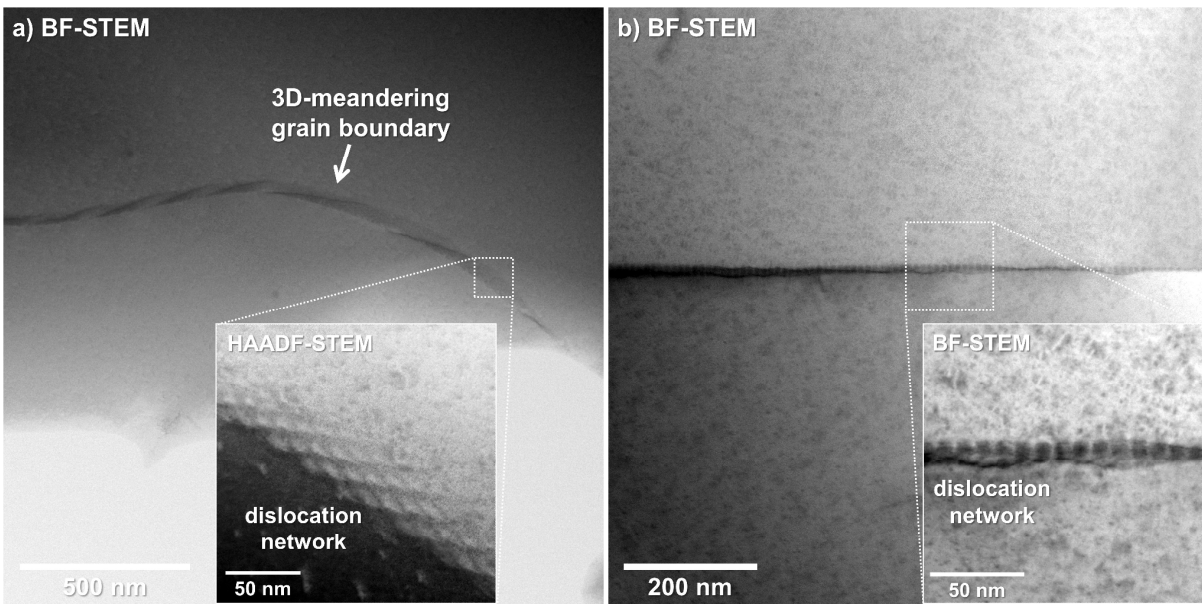


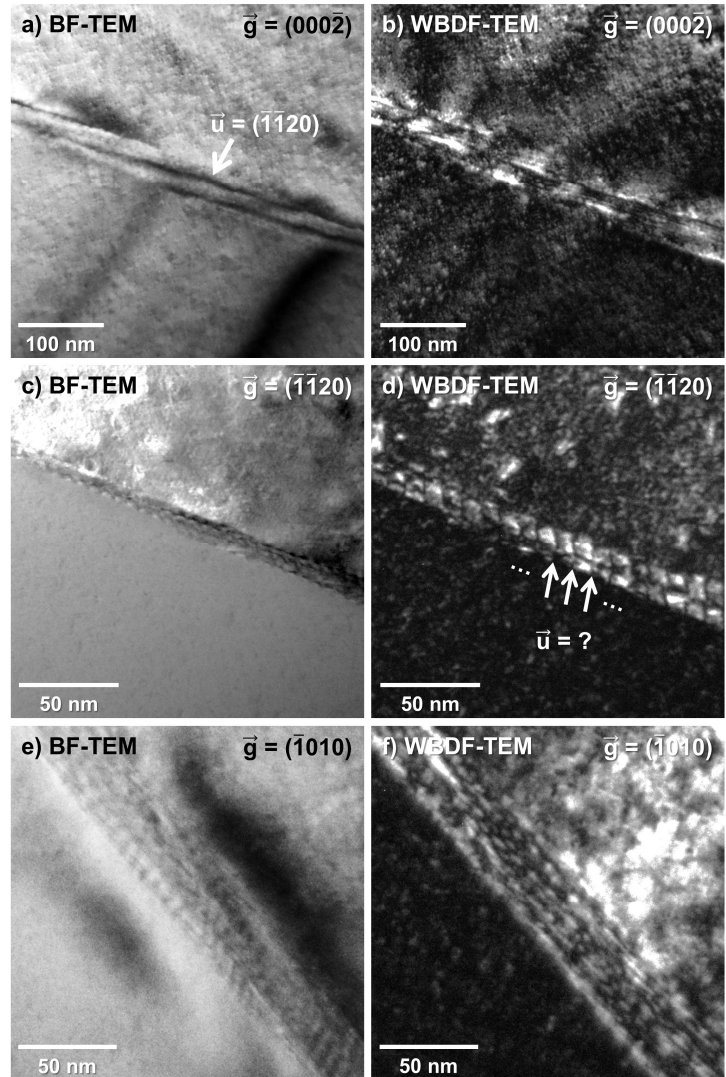
Figure 4-27: a) BF-STEM image of the curved grain boundary in sample EST-O|O. The 3D-meandering nature is depicted by the varying width of the interface. Due to its projection along the direction of view, a smaller or larger width represents a less or more inclined state. A dislocation network has formed throughout the curved interface, as indicated by the characteristic fish-scale-like contrast in the HAADF-STEM inset. b) BF-STEM image of a grain-boundary section being successively less inclined from left to right, almost reaching an edge-on orientation.

This dislocation network was found throughout the entire investigated grain boundary but strictly limited to the interface plane, being best visible for low-inclined interface sections while hardly recognizable near edge-on orientations (Figure 4-27 b)). Consequently, it is seen as an exclusive feature of the interface, which does not expand into the bulk. Considering the bicrystal misalignment, the EST synthesis as well as the observed strain contrast, it is suggested that this network is composed of misfit dislocations.

In order to examine the dislocation network more closely, WBDF-TEM (cf. pp. 33) was applied using different \vec{g} vectors. The results are shown in Figure 4-28.

Figure 4-28: a) – f) Series of corresponding two-beam BF- and WBDF-TEM images of the meandering grain boundary in sample EST-O|O, using different \vec{g} vectors to characterize the (presumed) dislocation network. Although the contrast is unusual for dislocation lines, the observed features are interpreted as two types of dislocations, which are either visible for $\vec{g} = (000\bar{2})$ or $\vec{g} = (\bar{1}\bar{1}20) / \vec{g} = (\bar{1}010)$, indicating Burger's vectors $\vec{b}_1 = (0001)$ and $\vec{b}_2 = \frac{1}{3}(\bar{1}\bar{1}20)$. While no distinct dislocation-line direction \vec{u} can be determined for the dislocations with \vec{b}_2 , those with \vec{b}_1 feature $\vec{u}_1 = (\bar{1}\bar{1}20)$ and hence, are pure edge dislocations.

Normally, individual dislocations occur as fine, bright lines in WBDF images, as long as they are not invisible due to the $\vec{g} \cdot \vec{b}$ criterion. In general, this criterion also allows to deduce the respective Burger's vector \vec{b} , when a dislocation line's (in)visibility is compared for a set of two-beam images with appropriately chosen \vec{g} . However, in the case of the dislocation network in the EST-O|O bicrystal, the situation appears to be more complex. On the one hand, different linear features are observed, which are inversely visible and invisible for $\vec{g} = (000\bar{2})$ and $\vec{g} = (\bar{1}\bar{1}20) / \vec{g} = (\bar{1}010)$. On the other hand, these linear features do not exhibit the typical qualities of dislocation lines in WBDF images, i.e., a bright line on a dark background. In fact, with dark lines, rather the opposite is observed. Then again, the situation of a strained, disordered 3D meandering interface of two misaligned crystals is significantly different from the "regular case" of an individual dislocation in an undisturbed bulk lattice and interference of these properties might cause the unusual contrast. Therefore, despite the ambiguities, it is suggested that a dislocation network is present with at least two



different types of dislocations with Burger's vectors $\vec{b}_1 \cdot (\bar{1}\bar{1}20) = 0$, $\vec{b}_1 \cdot (000\bar{2}) \neq 0$ and $\vec{b}_2 \cdot (000\bar{2}) = 0$, $\vec{b}_2 \cdot (\bar{1}\bar{1}20) \neq 0$, $\vec{b}_2 \cdot (\bar{1}010) \neq 0$. Since Burger's vectors typically correspond to basic lattice vectors, as shorter \vec{b} are energetically favorable, the most likely candidates are $\vec{b}_1 = [0001]$ and $\vec{b}_2 = \frac{1}{3}[\bar{1}\bar{1}20]$,^a which agrees well with the TEM investigations by Müller et al.,⁶⁶ who observed $\vec{b} = \frac{1}{3}\langle 11\bar{2}0 \rangle$ misfit dislocations in ZnO/Al₂O₃ heterostructures.^b For the dislocations with \vec{b}_1 , the direction of the dislocation lines corresponds to $\vec{u}_1 = [\bar{1}\bar{1}20]$ in good approximation, indicating pure edge dislocations, since $\angle(\vec{b}_1, \vec{u}_1) = 90^\circ$ (cf. pp. 33). However, for the dislocations with \vec{b}_2 , the direction of \vec{u}_2 is indistinct, as it was not found to follow any specific (low-indexed) lattice vector, which might be caused by the strained, disordered conditions but could also be seen as an indication of a mixed dislocation character.

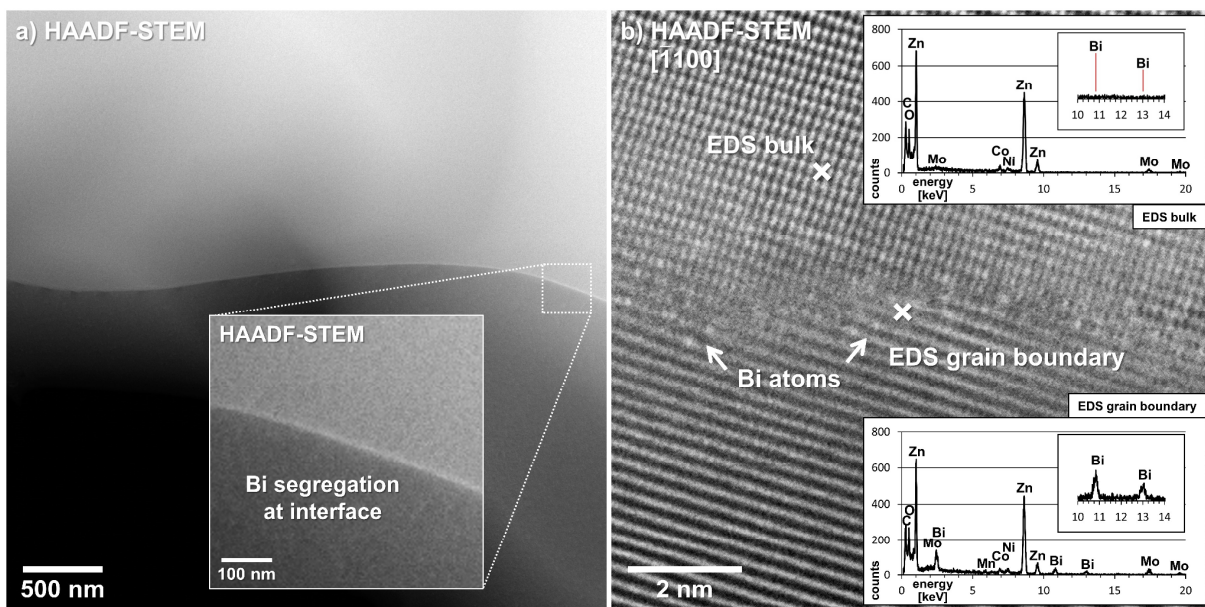


Figure 4-29: a) HAADF-STEM image of the meandering grain boundary in sample EST-O|O close to an edge-on orientation. As shown by the inset, the interface exhibits a significantly higher intensity compared to the bulk regions, hence indicating the presence of bismuth (Z²-contrast). The intensity difference between the upper (zone-axis orientation) and lower part (off-axis orientation) is an electron-channeling effect due to the misalignment of the bicrystal halves. b) FFT-filtered HAADF-STEM image in $[\bar{1}\bar{1}00]$ orientation featuring a rather irregular interface structure with several bright spots (atom columns) indicating the incorporation of bismuth (Z²-contrast). Corresponding EDS measurements verify its presence. While Bi (and a small Mn peak) were detected at the interface only, Co and Ni were found in the bulk as well, while Cr was not detected.

Figure 4-29 shows a section of the meandering grain boundary being close to a perfect edge-on orientation. The Z²-contrast of HAADF-STEM imaging clearly indicates the presence of bismuth at the interface, both at the mesoscale in a) as well as at the atomic scale in b). In the latter case, individual atom columns in close vicinity to the grain boundary feature a higher intensity compared to the local background, which depicts the location of the bismuth incorporation. The

^a $\vec{b}_2 = \frac{1}{3}[\bar{1}\bar{1}20]$ equates to $\vec{b}_2 = [\bar{1}\bar{1}0] = a_3$ in Miller notation and hence also to $\vec{b}_2 = [100] = a$ and $\vec{b}_2 = [010] = b$.

^b Müller et al. also report on amphoteric dislocation states compensating p-type properties in ZnO.⁶⁶ Being amphoteric, such dislocation states could probably interfere with both donor (bulk) and acceptor states (varistor grain-boundary) in piezotronic bicrystals. However, in this regard, the situation in the EST-O|O bicrystal remains intractable complex and it is unclear if such an interference would be positive or negative for the barrier formation and resulting varistor properties.

structure at the interface appears rather disordered and no distinct interfacial plane can be accounted for. This is attributed to the combination of misalignment, 3D meandering, related lattice distortions and the probably high dislocation density at the interface. As verified by corresponding EDS measurements, bismuth is present at the interface exclusively, while being absent in the bulk. In addition, a small Mn-signal was detected only at the interface, whereas the other dopants Co and Ni were found in the bulk as well. In these measurements, Cr was not detected at all, although it was occasionally found at the EST interface and in the bulk.¹⁹⁹ It should be noted that the intensity difference between the upper and lower bicrystal halves in Figure 4-29 a) is caused by diffraction and electron-channeling effects due to the bicrystal misalignment impeding a simultaneous zone-axis orientation for both sides.

4.3.2. I-V measurements

As shown in Figure 4-30 a), increasing mechanical stress has a distinct and well-pronounced effect on the electrical characteristics of the EST-O|O sample.

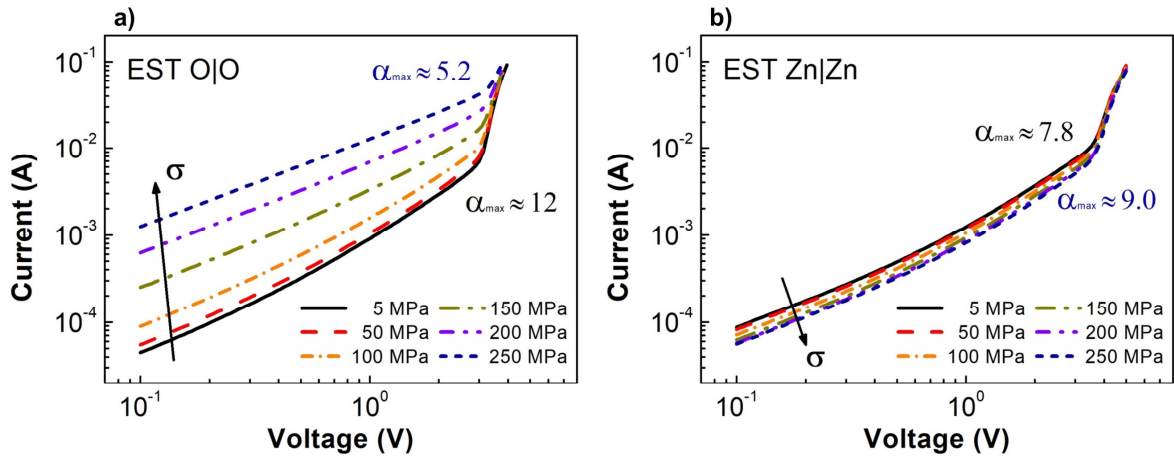


Figure 4-30: Load-dependent I-V characteristics of the two EST samples in a) tail-to-tail (O|O) and b) head-to-head (Zn|Zn) orientation. For the EST-O|O sample, increasing the mechanical load from 5 MPa to 250 MPa causes a successive decrease of $\alpha_{\max} = 12$ down to $\alpha_{\max} = 5.2$ and a simultaneous increase of the leakage current (measured at 0.1 V) from $5 \cdot 10^{-5}$ A up to $1 \cdot 10^{-3}$ A. The EST-Zn|Zn sample exhibits the reverse effect, though it is significantly less pronounced. The non-linearity coefficient increases from $\alpha_{\max} = 7.8$ up to $\alpha_{\max} = 9.0$, while the leakage current drops slightly from $9 \cdot 10^{-5}$ A to $6 \cdot 10^{-5}$ A.

Whereas the non-linear coefficient decreases successively from $\alpha_{\max} \approx 12$ down to $\alpha_{\max} \approx 5.2$, the leakage current (measured at 0.1 V) rises from $5 \cdot 10^{-5}$ A up to $1 \cdot 10^{-3}$ A upon a load increase from 5 MPa to 250 MPa. The breakdown voltage of $V_B = 3.25$ V remains nearly constant and agrees well with values reported for single grain boundaries in polycrystalline ZnO varistors.^{90, 221} Due to its reverse orientation, the contrary effect is expected for the EST-Zn|Zn sample and was indeed observed, though it is in comparison much less pronounced (Figure 4-30 b)). The non-linearity increases from $\alpha_{\max} \approx 7.8$ to $\alpha_{\max} \approx 9.0$, while the leakage current drops slightly from $9 \cdot 10^{-5}$ A to $6 \cdot 10^{-5}$ A. This significantly weaker effect is explained by the fact that the barrier height needs to be increased everywhere along the interface in order to be effective since the current flow follows the route of least resistance. For the same reason, in the O|O sample, the barrier only needs to be reduced locally to obtain an effective barrier lowering. The breakdown

voltage in the Zn|Zn sample is constant and with $V_B = 3.95$ V slightly higher as for the EST-O|O sample, but nevertheless, close to reported values.^{90, 221} Since the overall breakdown voltage scales with the number of active grain boundaries,⁹⁰ the observed breakdown voltages indicate for both samples that additional phase boundaries between ZnO and secondary oxide grains in the bulk or at the interface either do not measurably affect the I - V characterization or are not included in the current path. For the EST-Zn|Zn sample in particular, this implies that, albeit being still partly polycrystalline, it has formed locally a “bicrystalline” grain boundary, which connects the single crystals and bypasses the other grains. Therefore, in both samples, the overall electrical response is regarded to be determined only by the electrical properties of those bicrystal interface sections, which are free of secondary phases, since they represent the actual ZnO–ZnO bicrystal boundary.

It should be noted that among all investigated samples, the EST bicrystals (EST-O|O in particular) feature not only the highest non-linearity and hence, the strongest varistor behavior, but they also exhibit the strongest and most distinct response upon mechanical load. This observation is not only considered a successful proof of principle for the piezotronic tuning of ZnO varistor bicrystals or related devices, but it also shows that the EST method is well-suited for the synthesis of such bicrystals and probably superior to sputtering and diffusion-bonding.

4.3.3. Discussion and Summary

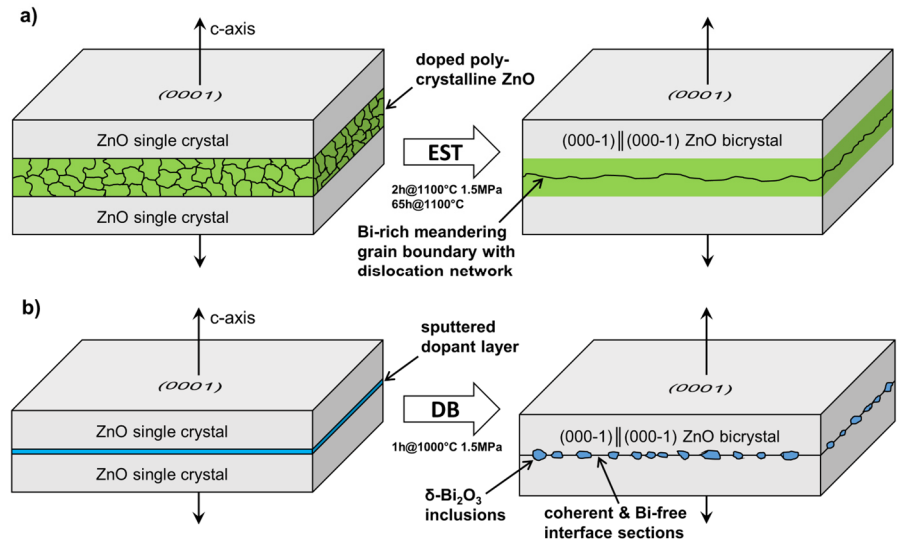
The core results of this thesis, which were published as a full paper,²⁰⁰ are derived from a comparison of the samples EST-O|O and DB-I, contrasting grain boundary structure, coherency and bismuth segregation, with respect to the underlying synthesis method as well as to the resulting I - V characteristics. In addition, thermodynamical aspects of interface coherency and grain-boundary segregation were considered as well as comparative examples from the literature, in order to point out the general relevance of the described relationship. The following sections are an extended reproduction of the discussion as given in the corresponding publication.²⁰⁰

EST vs. DB-I – Interface coherency and bismuth segregation

Both samples feature macroscopically the same O|O orientation and both are, in principle, sufficiently doped to obtain varistor-type properties.^a Therefore, previous to the TEM investigation, a highly coherent grain boundary and a similar segregation behavior were expected for both samples, as well as the occurrence of non-linear I - V characteristics. However, besides the common feature of being atomically well-bonded bicrystals, without any kind of continuous interfacial film or phases, some significant differences were revealed comparing the two samples.

^a In fact, the doping is very different for these two samples regarding both the absolute amount as well as the variety of dopant elements. Whereas the EST bicrystal has a dopant composition typical for a commercial varistor (cf. pp. 27), the DB-I sample is only doped by a 75 nm layer containing 5 mol% Bi₂O₃ and 5 mol% Co₃O₄. Nevertheless, the data obtained from the even lower doped DB-II bicrystal strongly indicate that this is sufficient to obtain varistor behavior (cf. p. 65), provided that Bi segregation occurs. Therefore, a qualitative comparison of EST-O|O and DB-I is justified.

Figure 4-31: Illustration of the different bismuth segregation behavior in samples EST-O|O vs. DB-I, depending on the respective synthesis method. a) A low-coherent meandering grain boundary with a Bi incorporating dislocation network is formed in the EST-O|O bicrystal. b) In the DB-I bicrystal, Bi accumulates to nonwetting δ - Bi_2O_3 inclusions with highly coherent and Bi-free interface sections in between.²⁰⁰



In the EST-bicrystal, bismuth originates from Bi_2O_3 phases in the sacrificial polycrystalline layer and then distributes at the interface, which is formed during the epitaxial grain growth. Bi-free interface sections were not observed and the incorporation occurred independently of the formation of secondary phases. On the contrary, the DB-I bicrystal starts with a continuous Bi-rich dopant layer at the interface, which then disintegrates upon bonding and annealing. While cobalt forms a solid solution in the ZnO lattice and rapidly diffuses into the bulk, bismuth retracts from the interfaces, accumulates and forms non-wetting secondary δ - Bi_2O_3 grains. The actual bicrystalline interface of sample DB-I is coherent and bismuth free, hence no varistor behavior can occur, as confirmed by the electrical measurements. In contrast to that, the meandering grain boundary in the EST-bicrystal is locally strongly curved, hence much less coherent and has a notable amount of bismuth incorporated at the interface, which correlates well with the observed non-linearity of $\alpha_{\text{max}} = 12$. The continuous network of misfit dislocations at this interface plays an important role in providing segregation sites and retaining bismuth at the interface. The comparably large quantity of local structural defects and corresponding lattice distortions creates special positions with an excess free volume sufficient for the stable incorporation of the large bismuth ions. Although the macroscopical bicrystal misalignment of 1.9° contributes to it, the curvature of the grain boundary is seen as the main reason for the high defect density. Accordingly, the DB-I bicrystal features the inverse relationship by exhibiting a straight, quasi defect-free grain boundary without any bismuth segregation. A comparison regarding the duration of annealing steps strengthens this relation and indicates the stability and permanence of the bismuth doping in the EST bicrystal. Whereas the sputtered dopant layer is already withdrawn from the interface after only 1 h @ 1000 °C, the dislocation network and the incorporated bismuth are still present after 65 h @ 1100 °C. A graphical summary of these results is provided in Figure 4-31. In addition, this observation correlates well with the stability of comparable impurity-decorated dislocation networks reported for polycrystalline Cu-doped ZnO.²⁴² In this case, the formation of stable impurity-related dislocation networks, was attributed to two effects. Firstly, the solid solubility of a dopant is lowered during cooling and hence, respective atoms concentrate at certain regions, causing

stress, which in turn, leads to the formation of dislocations and dislocation networks. The dopant atoms cannot leave such regions, since this would cause an even higher stress level. The second effect is that insoluble dopants diffuse preferentially along already existing dislocations. In doing so, the segregation of dopant atoms and the dislocation formation are mutually dependent. These considerations are also applicable to the case of bismuth atoms at an incoherent, defect-rich grain boundary. Since the high defect density and thus, the dislocation network itself are attributed to the curvature, both are seen as a consequence of the synthesis method. During epitaxial solid-state transformation, the fronts of the opposing single crystals grow towards each other until complete consumption of the intermediate doped sacrificial layer. Regarding the growth rates, this process is not completely uniform along the progressing boundaries, considering that different sizes and orientations of ZnO crystallites are present as well as the various secondary phases. In consequence, a 3D meandering grain boundary is formed in the final step, since the single crystalline fronts encounter each other at different positions and angles. Due to the local curvature (and the observed mismatch), misfit dislocations are formed, which constitute the observed dislocation network at the interface. A process which is likely facilitated and stabilized by the presence and incorporation of the insoluble bismuth atoms.

Thermodynamic aspects of interface coherency and segregation

A qualitative understanding of the thermodynamic aspects of the observed Bi segregation can be attained by applying Gibbs adsorption isotherm,²⁴³ as provided in Eq. 4.1 and 4.2 for the straight and the curved interface, respectively.^a

$$d\gamma(\textit{straight}) = -\Gamma_{\textit{sat}(\textit{straight})} \cdot d\mu(\textit{straight}) \quad \text{Eq. 4.1}$$

$$d\gamma(\textit{curved}) = -\Gamma_{\textit{sat}(\textit{curved})} \cdot d\mu(\textit{curved}) \quad \text{Eq. 4.2}$$

$d\gamma$ = change in interfacial energy, $\Gamma_{\textit{sat}}$ = interfacial excess concentration (saturated interface), $d\mu$ = change in chemical potential of bismuth

These equations provide the change of interfacial energy, $d\gamma$, as a function of interfacial excess $\Gamma_{\textit{sat}}$ of the segregating species (here bismuth) and the change of its chemical potential, $d\mu$. In general, the anisotropy^b of segregation depends on five macroscopic degrees of freedom,^c including the relative orientation of bulk phases as well as the relative orientation of the interface with respect to these.²⁴⁴ Therefore, a general discussion quickly becomes intractable and very case-specific. However, for the compared bicrystals EST-O|O and DB-I, the orientation

^a The original adsorption isotherm for molecules of type A dissolved in or adsorped by a material of type B is $d\gamma = -\Gamma_A d\mu_A$ or $\frac{\partial \gamma}{\partial \mu} \Big|_{n_B, T, a} = -\Gamma_A$. The amount of B, n_B , is constant as well as temperature T and surface/interface area a .

^b The term “anisotropy” relates to the general anisotropy of crystals and crystal surfaces. Depending on their orientation, crystal surfaces have a different energy, although belonging to the same crystal or grain. In consequence, surface or interface segregation is different as well, i.e., it is anisotropic.

^c Three degrees of freedom (DoF) specify the orientation of one crystal relative to the other, e.g., by the three Euler angles ψ , θ , φ (3 DoFs) or alternatively, by a rotation around one specific axis o (2 DoFs) and an angle α (1 DoF). Two further DoFs specify the orientation of the boundary plane relative to one of the crystals, either by two angles α and β , or by the corresponding plane normal (2 DoFs).

of the bulk material is fixed at both sides of the interface and the grain-boundary orientation takes on two extremes. On the one hand, it is fixed by the orientation of the prior interface for the DB-I bicrystal resulting in a perfectly straight interface. On the other hand, it renders maximum local variation with respect to all three grain-boundary angles for the EST bicrystal due to the 3D meandering interface, which is the consequence of the random microstructure of the sacrificial polycrystalline dopant layer. Segregation in general requires the consideration of the solute concentration in the bulk to include the variation in configurational entropy if the solute atoms diffuse from bulk to interface.^{244, 245} However, as bismuth is virtually insoluble in ZnO,^{4, 5} a solid solution of bismuth in the bulk ZnO can be neglected. Instead, Bi is considered to be available in a quasi-infinite reservoir, since it is already present at the grain boundary in sufficient amounts.^a In the case of the DB-I bicrystal, this reservoir is formed by precipitates of the sputtered dopant layer and in the case of the EST-O|O bicrystal, it is provided by bulk precipitates from the sacrificial layer. In consequence, the chemical potential μ , or rather the value of $d\mu$, is (in approximation) only determined by the given situation of a certain interface and the corresponding (possible) energy change upon segregation ($d\gamma = \gamma_{sat} - \gamma_0$), as expressed by Eq. 4.3

$$d\mu = d\gamma / -\Gamma_{sat} = (\gamma_{sat} - \gamma_0) / -\Gamma_{sat} \quad \text{Eq. 4.3}$$

$d\mu$ = change in chemical potential, $d\gamma$ = change in interfacial energy, Γ_{sat} = interfacial excess concentration (saturated interface), γ_{sat} = interfacial energy (saturated interface), γ_0 = interfacial energy (reference state "before segregation")

It should be noted that this comprises two important implications. Firstly, segregation is never hindered by a lack of Bi atoms, i.e., a low(ered) $d\mu$. Secondly, what is more important, effectively increasing $d\mu$, by simply providing more segregating atoms, i.e. higher doping, is not possible. Therefore, the bicrystals DB-I and EST-O|O combine two extreme cases, that is, a straight vs. a curved interface of identical average orientation, with the simple case of segregation where an infinite source feeds the segregating species without the interference of a bulk solute. Hence, the simple equations Eq. 4.1 and 4.2 suffice. From the TEM investigations, it is obtained that for the case of the straight interface, segregation does not occur and the bismuth interfacial excess, Γ_{sat} , is equal to zero. For the case of the curved interface, segregation is strongly promoted due to the lower grain-boundary coherency. This high degree of segregation is reflected and confirmed by the TEM findings as well as by the large nonlinearity factor of $\alpha_{max} = 12$. For the case of the curved interface, grain-boundary reconstruction is likely to occur. This reconstruction typically includes the formation of dislocations, steps, and terraces, which encompass excess free volume promoting the incorporation of large atom species, such as Bi. Upon segregation, the interfacial energy γ is lowered by decorating the meandering interface of the EST-O|O bicrystal with Bi atoms. In contrast, no further reduction in total free

^a Please note, most literature on the general thermodynamics of grain-boundary segregation focus on the question if segregation from the bulk to an interface or surface occurs at all for a certain solute within a solid solution. In this sense, the segregation of Bi is already concluded, since it is insoluble and located at the interface anyhow. Therefore, in this thesis, the term "segregation" is employed with a slightly different connotation, as it is used to distinguish interface decoration from the formation of Bi₂O₃ grains.

energy is possible in the DB-I bicrystal due to the already low-energy state of its interface and the lack of dislocations or excess free volume. Accordingly, there is a large volume fraction of bismuth in the form of secondary phases, i.e., $\delta\text{-Bi}_2\text{O}_3$, available, but no bismuth was found to segregate. In addition, the dihedral angles θ of $\delta\text{-Bi}_2\text{O}_3$ at the grain boundary, i.e., at triple junctions with ZnO, depend on the free energy γ of ZnO|ZnO in relation to ZnO| $\delta\text{-Bi}_2\text{O}_3$ interfaces and hence can be used to estimate the relative energies of the straight interface in the DB-bicrystal with and without wetting using Eq. 4.4.²²⁹

$$\cos\left(\frac{\theta}{2}\right) = \frac{\gamma(\text{ZnO}|\text{ZnO})}{2\gamma(\text{ZnO}|\text{Bi}_2\text{O}_3)} \Leftrightarrow \gamma(\text{ZnO}|\text{Bi}_2\text{O}_3) = \frac{\gamma(\text{ZnO}|\text{ZnO})}{2\cos\left(\frac{\theta}{2}\right)} \quad \text{Eq. 4.4}$$

With a dihedral angle $\theta = 138^\circ$ and taking into account that two ZnO| Bi_2O_3 interfaces are present in the case of a $\delta\text{-Bi}_2\text{O}_3$ grain at the grain boundary, Eq. 4.4 yields $\gamma(\text{ZnO}|\text{Bi}_2\text{O}_3) = 1.4\gamma(\text{ZnO}|\text{ZnO})$. This result does not only confirm the low-energy state of the non-wetted DB-I interface, but it is also consistent with the described necessity of an increased interfacial energy to provide a sufficient segregation potential, e.g., by the introduction of curvature, defects, mismatch, etc. as in the EST-O|O bicrystal. With respect to the high sintering temperatures during bonding and annealing, bismuth is rendered highly mobile and any kinetic constraints preventing a segregation that is determined by the thermodynamic equilibrium are excluded. In consequence, the straight interface is devoid of any varistor-type potential barrier and non-linearity ($\alpha \approx 1$).

Coherency-related anisotropy of segregation in other material systems

As shown in the following, the presented thermodynamic considerations are perfectly consistent with various literature examples, in particular with the results by Sato et al.¹⁴⁰ as discussed and presented in section 1.7 (pp. 18). They studied a Pr-Co doped (0001)|(0001) bicrystal, which exhibited a straight and highly coherent interface without any detectable Pr segregation and quasi-linear characteristics ($\alpha = 1.2$). Furthermore, they also reported that the bicrystal with the highest non-linearity ($\alpha > 20$) and strongest Pr segregation had the highest grain-boundary incoherency. Although the incoherency was not introduced via interface curvature in this case, but with a specific tilt of the crystals, it can be considered a defect-/distortion-rich high-energy interface, where Pr segregation lowers γ , in contrast to the coherent bicrystal, which already has a low γ . The same is true for the various Σ boundaries featuring special periodic segregation sites, which were also part of their study. The respective semicoherent bicrystals represent the medium case in terms of interfacial energy and lie in between the extreme cases of maximal vs. minimal coherency. Consistently, they exhibit a medium segregation and intermediate *I-V* characteristics.

Furthermore, the observed anisotropy of segregation is similar to examples from other material systems aside from ZnO bicrystals. Wynblatt and Chatain found the segregation of Au atoms to interfaces in an fcc Pt-1 at.% Au alloy to be higher with increasing grain-boundary energy and higher indexed boundary planes.²⁴⁴ Although not explicitly mentioned in their paper, their

results implicate that the Au segregation increases with decreasing interfacial coherency. Concerning the influence of dislocations, Choudhury et al. describe a distinct segregation of Cr to misfit dislocations at Fe|Y₂O₃ interfaces under oxidizing conditions.²⁴⁶ In addition, their experiments on YAl_xCr_{1-x}O₃ particles embedded in a Fe_{0.78}Al_{0.06}Cr_{0.16} matrix revealed Cr to be enriched at low-coherent interfaces with misfit dislocations, in contrast to highly coherent defect-free interfaces. The results of Herbig et al. on the anisotropic segregation of carbon in ferrite clearly demonstrate that the carbon content at the interfaces increases with the misorientation angle ω in the small-angle grain boundary regime ($\omega < 14^\circ$).²⁴⁷ For high-angle grain boundaries, the data clearly indicate the influence of boundary coherency and misfit dislocations. Thus, at $\Sigma 3$ and $\Sigma 5$ boundaries, which represent rather low-energy interfaces, the carbon excess is significantly lower compared to interfaces deviating from the perfect Σ orientations and hence, include misfit dislocations. This agreement between results from highly diverse materials and the findings presented in this study point out that the underlying principles are not limited to Bi-ZnO or Pr-ZnO compositions. In particular, this implies that the described mechanism of retaining insoluble, otherwise dewetting elements at interfaces is also adaptable to other material systems.

Implications for the bicrystal synthesis

Both the structural as well as the thermodynamic considerations on the segregation of bismuth bear an important implication for the synthesis of piezotronic and varistor-type bicrystals via diffusion bonding of single crystals. In order to obtain or enhance the non-linear characteristics, it is not sufficient to simply increase the amount of dopants, it is also necessary to avoid highly coherent interfaces, i.e., low $d\gamma$, and introduce suitable segregation sites instead, i.e., enabling large Γ_{sat} . Otherwise, the additional dopant atoms will be added to the already quasi-infinite reservoir without effectively changing γ . This is illustrated by the I - V characteristics of samples DB-I and DB-IV.^a

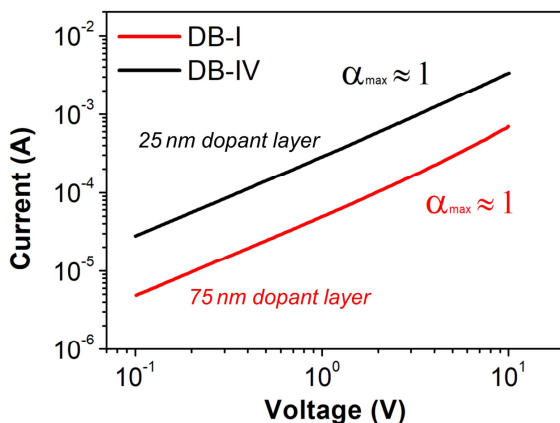


Figure 4-32: I - V characteristics of samples DB-I and DB-IV. Although DB-I featured a 3x higher doping, non-linear behavior could not be induced and both samples were found to be completely ohmic ($\alpha_{\text{max}} \approx 1$).

As shown in Figure 4-32, both samples exhibit an almost perfectly linear, ohmic behavior despite the fact that the dopant layer thickness and thus, the total amount of dopants was increased by a factor of three in sample DB-I. While the EST synthesis method represents one way to meet the

requirements for an effective Bi incorporation, reduced coherency can also be achieved in diffusion-bonded bicrystals by purposefully adding certain misalignments, as shown in the following chapter.

^a Sample DB-IV was destroyed during TEM preparation, hence no images or measurements exist. Chronologically, it is the predecessor of sample DB-I, which was higher doped, since DB-IV did not show any non-linear behavior.

EST BICRYSTALS - SUMMARY

- ABF-STEM and NBED were used to successfully verify the O|O orientation of the EST sample.
- A bicrystal misalignment of 1.9° was determined by SAED.
- SEM and TEM imaging as well as SAED verified a complete epitaxial transformation (EST).
- Dopant phases form electrically inactive grains located in the bulk or at the interface.
- The etching pattern in the TEM sample, resembling a polycrystalline structure, was identified as an ion-milling artifact, causing a trench- & ridge-like topography, as confirmed by AFM measurements.
- A 3D-meandering grain boundary was formed during the EST process, with the following properties:
 - macroscopically, an O|O orientation
 - microscopically, a strained interface with local curvature → reduced coherency
 - no amorphous or crystalline interfacial film (as known from commercial varistors)
 - continuous dislocation network at the interface with two types of (misfit) dislocations corresponding to Burger's vectors $\vec{b}_1 = [0001]$ and $\vec{b}_2 = \frac{1}{3}[\bar{1}\bar{1}20]$
 - suitable segregation sites cause stable incorporation of Bi atoms at the interface.
- The other dopant elements Cr, Mn, Co and Ni were found in varying amounts at the interface as well as in the bulk, which is attributed to the formation of solid solutions with ZnO.
- *I-V* measurements of samples EST-O|O and EST-Zn|Zn yielded high non-linearity coefficients $\alpha_{\max} \approx 12$ and $\alpha_{\max} \approx 7.8$, respectively, at breakdown voltages $V_B = 3.25$ V and $V_B = 3.95$ V, which indicates a single (bicrystal) grain-boundary for both samples. The electrical properties of both samples could successfully be piezotronically tuned by mechanical load.
- A comparison of samples EST-O|O and DB-I yielded the following insights:
 - Both samples feature a sufficient doping and macroscopically the same O|O orientation. Yet, interface structure, Bi doping and resulting electrical properties are highly different.
 - Their interfaces represent extreme cases of straight & coherent vs. curved & incoherent.
 - Straight, highly coherent $(000\bar{1})|(000\bar{1})$ interfaces do not feature Bi segregation sites, hence no varistor-like potential barriers were formed.
 - The curvature of 3D-meandering interfaces implies reduced coherency, dislocations and lattice distortions, which provide Bi segregation sites and in consequence, varistor behavior.
 - A thermodynamical description of the different segregation behavior is attained by applying Gibbs' adsorption isotherm:

$$d\gamma(\text{straight}) = -\Gamma_{\text{sat}(\text{straight})} \cdot d\mu(\text{straight})$$

$$d\gamma(\text{curved}) = -\Gamma_{\text{sat}(\text{curved})} \cdot d\mu(\text{curved})$$

Previous to segregation, the curved & incoherent interface is considered a high-energy interface, whereas the straight & coherent interface is considered to have low-energy. Segregation and incorporation of Bi atoms ("adsorption") ($\Gamma_{\text{sat}} > 0$) lowers the interfacial energy. Thus, it occurs for the curved interface ($d\gamma < 0$), while it is absent in case of the straight interface, since no further energy lowering is possible ($d\gamma = 0$). The latter corresponds to the lack of segregations sites, which fixes $\Gamma_{\text{sat}} = 0$.

- Large dihedral angles of non-wetting $\delta\text{-Bi}_2\text{O}_3$ grains in DB-I confirm the assigned low-energy state of the straight interface.
- Structural and thermodynamic considerations are adaptable to other material systems.
- Non-linear behavior cannot be increased by just adding a higher amount of dopants. Suitable segregation sites at the interface (incoherency) must be provided as well.

4.4. Doped DB bicrystals with reduced coherency

Chronologically, the tilted bicrystals were devised and fabricated last, in consequence of the discovered relationship between grain-boundary coherency and Bi segregation. Transferring it to the application in piezotronic bicrystals, the tilted DB samples pick up the idea of Sato et al. to use specific misorientations to maximize the incoherency and thus, facilitate segregation as well as potential-barrier formation.^{140, 176} In contrast to the somewhat arbitrary results of the EST method, more control on the actual grain-boundary configuration is provided using the diffusion bonding procedure for the bicrystals synthesis, which is beneficial in tailoring it for possible applications. All tilted DB bicrystals were sputter-doped with a typical varistor composition for the target, including Bi, Co, Mn, Cr and Ni (cf. p. 26). The orientation used for sample DB-a|c, with parallel a - and c -axes and a $(000\bar{1})|(2\bar{1}\bar{1}0)$ interface, is directly adopted from Sato et al.,¹⁴⁰ since this orientational configuration is easy in preparation, hence reliably reproduced and furthermore, it notably showed the second best results regarding Pr segregation and potential barrier formation ($\alpha_{\max} \approx 3.9$). In contrast, the 26° asymmetric tilt for sample DB-26 was specifically chosen to obtain the best compromise between reduced coherency and maximum piezoelectric response. Whereas an optimized piezo-response demands a parallel alignment of inversed c -axes (e.g., O|O for the strongest piezotronic response), incoherency requires a certain misorientation.

Why 26° tilt? – A discussion based on results from CRLP

The specification of 26° tilt as the best compromise between incoherency and piezo-response, was derived from literature reports as described in the following. For the design of their Pr-doped bicrystal with maximum incoherency, Sato et al. utilized the so-called *coincidence of reciprocal lattice points* (CRLP) method, in which the coherency of two crystals is measured by means of overlapping of reciprocal lattice points.^{140, 248, 249} A finite spherical volume is assigned to each point and the sum of the overlapping volume reflects the quality of the coincidence for these two crystals. In other words, it reflects the coherency of the lattices, since each lattice point stands for a set of lattice planes, and the coincidence of reciprocal points implies the same orientation in real space for the corresponding lattice planes. The underlying idea is that the more lattice planes share the same orientation, the better is the fitting and hence, the higher is the coherency between two crystals. This approach might be considered the reciprocal equivalent of the real-space *coincidence site lattice* (CSL) theory and can be applied to both cases of grains of identical and grains of different crystal structures. The finite size of the spherical volumes can be adjusted to allow certain deviations, e.g., to take small-angle grain boundaries and minor compensating lattice distortions into account, in order to avoid an overestimation of the actual incoherency. For the actual calculation of the CRLP, a computer program was used by the authors. It should be noted that, according to the CRLP approach (as well as to the CSL theory), the orientation of the interface plane between two grains does not play any role in determining their orientation relationship (although it naturally influences segregation, stability and local structure).

In the case of ZnO bicrystals, a comprehensive CRLP analysis of special grain boundaries was conducted by Wunderlich, who investigated – among other configurations – the coherency of symmetrical tilt boundaries rotated around the a_3 -axis $[11\bar{2}0]$ (Figure 4-33).²⁴⁹ Due to the symmetry of space group $P6_3mc$, these results also apply to a rotation around a_1 or a_2 . Thus, a 0° misorientation angle represents parallel and a 180° angle anti-parallel c -axis configurations, as known from the $\{0001\}$ IBs investigated in this thesis. Therefore, these data can be used to find the best compromise for the orientation of diffusion-bonded bicrystals, simultaneously providing a minimized coherency as well as an optimized piezotronic response by staying as close to the ideal $\{0001\}$ IB as possible.

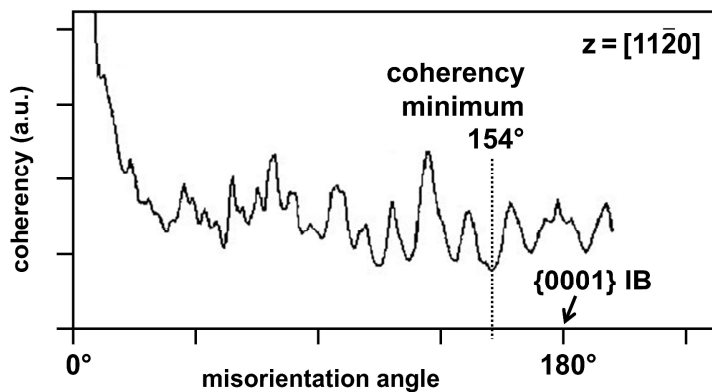


Figure 4-33: The coherency of symmetrical tilt boundaries in ZnO bicrystals rotated around the $[11\bar{2}0]$ axis according to the CRLP theory. A misorientation angle of 0° corresponds to a parallel and 180° to an anti-parallel c -axis configuration. The latter equals the conditions implied in $\{0001\}$ IBs. Reworked after "Fig.2" by Wunderlich (1998).²⁴⁹

According to the CRLP theory, the lowest coherency for these kinds of tilted bicrystals is found at a

misorientation angle of 154° , which equates to a 26° tilt of a $\{0001\}|\{0001\}$ -type bicrystal. Another suitable coherency minimum exists at 168° , which, however, was considered to be too close to the ideal $\{0001\}$ IB with only 12° tilt, probably leading to the formation of a small-angle grain boundary. In this case, the straight interface would split up into several highly coherent sections separated by (periodic) misfit dislocations, hence limiting the number of segregation sites. There is no definite limit value for the occurrence of small-angle grain boundaries, but it is commonly assigned to $<15^\circ$, hence the 26° was preferred to the 12° tilt configuration, despite the fact that it is farther away from the ideal $\{0001\}$ IB. Please note, one might argue that no small-angle boundary formed in sample DB-II, although it featured only 2.8° misalignment. However, the tilt in DB-II was not a simple symmetric rotation around one basic axis, but a mixture of two basic rotations (tilt & twist), as it can be deduced from the transverse position of the ZOLZ intersection circle with respect to the primary beam and the pattern symmetry (Figure 4-16, p. 62). In contrast, the formation of a semi-coherent small-angle grain boundary is assumed much more likely in the case of a pure 12° tilt, compared to the arbitrary and completely unsymmetric tilt in DB-II. Finally, it should be noted, that the calculations by Wunderlich were dedicated to symmetrical tilt bicrystals, where both single crystals are rotated by half of the misorientation angle, maintaining a mirror symmetry at the interface. However, for the sake of a simplified preparation,^a it was decided to use an

^a Regarding the preparation and synthesis, two main advantages over symmetrical bicrystals were seen for the asymmetrical bicrystals. Firstly, only one crystal needs to be ground and polished, which not only reduces the effort necessary but also avoids additional misorientation probably introduced by a second grinding step. Secondly, $\{0001\}$ single crystals with a sputtered dopant layer were already prepared and could readily be used for the DB-a|c as well as for the DB-26 bicrystal.

asymmetrical tilt for the DB-26 bicrystal, with one single crystal fixed in a $\{0001\}$ orientation, while the other is rotated by the respective angle. With regard to the general independence of the CRLP theory to the orientation of the actual interface, the orientation relationship between the crystal lattices as well as the expected (in-)coherency is theoretically the same for both symmetrical and asymmetrical tilt bicrystals. Therefore, the application of the results by Wunderlich and the derived 26° tilt orientation is justified.

4.4.1. Doped DB bicrystal in a|c orientation (DB-a|c)

Figure 4-34 a) features a two-beam BF-TEM image with $\vec{g} = (0002)$ of the DB-a|c bicrystal with parallel a - and c -axes. A straight grain boundary is observed as expected for a diffusion-bonded bicrystal. Special contrast features, such as strain contrast, for example, were observed neither in two-beam nor in zone-axis condition.

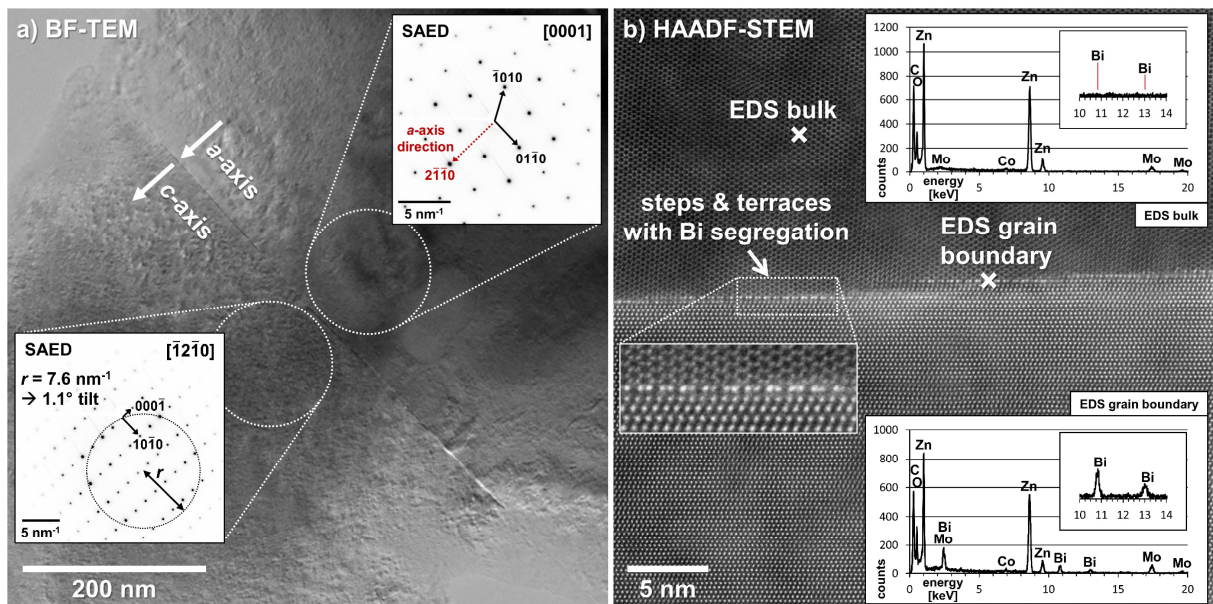


Figure 4-34: a) $\vec{g} = (0002)$ two-beam BF-TEM image of the interface in sample DB-a|c with a $(000\bar{1})|(2\bar{1}\bar{1}0)$ interface, which corresponds to the c -axis of one side and the a -axis of the other being aligned perpendicular to the interface plane. The orientation is verified by SAED (insets), however, a small misalignment of 1.1° tilt from the ideal a|c configuration is measured. b) FFT-filtered HAADF-STEM image in $[\bar{1}2\bar{1}0]$ zone-axis orientation revealing an interface with step- and terrace-like sections, featuring semi-periodic decorations by bismuth atoms (Z^2 -contrast), as verified by corresponding EDS measurements. Whereas Bi was detected exclusively at the interface, Co was also found in the bulk. Other dopants were not detected. No indications for crystalline or amorphous interfacial films were observed.

As illustrated by the insets, SAED was used to determine a misalignment of 1.1° tilt and to verify the formation of a $(000\bar{1})|(2\bar{1}\bar{1}0)$ -type interface. The HAADF-STEM image in Figure 4-34 b) shows a characteristic step-and-terrace-like interface structure, featuring a well-pronounced Bi decoration of the terrace-like sections, as revealed by the higher brightness of the respective atom columns (Z^2 -contrast). Corresponding EDS measurements verify both the presence of Bi at the interface and its absence in the bulk, while Co was found at both measurement points. No indications for a crystalline or amorphous interfacial film were detected. In contrast to the arbitrary formation of Bi segregation sites, such as in the case of the EST bicrystal (cf. p. 76), a semi-periodic substitution of Zn sites by Bi is observed in the DB-a|c sample. On the $(000\bar{1})$

side (Figure 4-35 a), Bi substitutes Zn in approximately every second column of the interfacial (0002) Zn layer. This periodicity is maintained throughout individual “terrace” sections but interrupted at the step-like structures with an irregular, apparently lower Bi content. At other interface sections, the semi-periodic segregation was found to occur on the $(2\bar{1}\bar{1}0)$ side (Figure 4-35 b), where Bi is incorporated in quasi every atom column of the interfacial $(2\bar{1}\bar{1}0)$ layer.

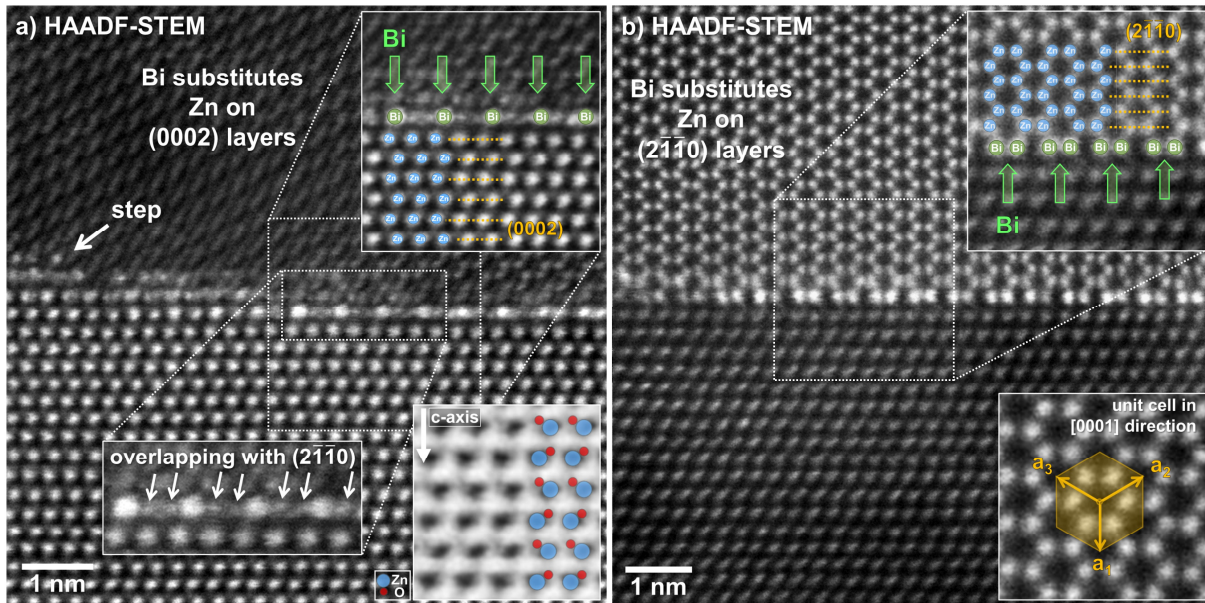


Figure 4-35: a) FFT-filtered HAADF-STEM image of the DB-a|c interface with the lower bicystal half in $[\bar{1}2\bar{1}0]$ zone-axis orientation. Due to the misalignment, the upper side is in off-axis condition. Bi semi-periodically occupies every second atom column of the inner (0002) Zn-layer of the lower crystal (upper inset). Additional spots in between the atom columns indicate an overlapping with the $(2\bar{1}\bar{1}0)$ layer of the upper crystal. At interface steps, the periodicity is interrupted, exhibiting an apparently lower, irregular Bi segregation. The inset on the lower right depicts an ABF-STEM image verifying the “tail” c -axis direction of the lower crystal. b) FFT-filtered HAADF-STEM image of a different interface section with the upper bicystal half in $[0001]$ zone-axis orientation. Due to the misalignment, the lower side is in off-axis condition. Z^2 -contrast reveals the atom columns of the innermost $(2\bar{1}\bar{1}0)$ layer being occupied by Bi atoms. The inset on the lower right depicts a projection of the hexagonal unit cell in $[0001]$ direction.

While the inset in Figure 4-35 a) shows an ABF-STEM image confirming the negative c -axis direction pointing towards the interface, the other insets in Figure 4-35 highlight and illustrate the Bi segregation and orientation of the DB-a|c bicrystal. Due to the 1.1° misalignment, it is not possible to bring both sides in zone-axis orientation simultaneously, hence optimized atomic resolution is only possible for one side at once. Nevertheless, the images suffice to show that the two Bi substituted layers (0002) and $(2\bar{1}\bar{1}0)$ overlap at the interface. If there were two separated Bi-containing layers, i.e., one for each side, this would be visible in Figure 4-35 b) by an increased intensity of the first (0002) layer of the lower crystal. Moreover, the (0002) layer in Figure 4-35 a) features some additional small bright spots between the actual atom columns, which are attributed to an overlapping with the $(2\bar{1}\bar{1}0)$ layer of the upper crystal. As illustrated in Figure 4-36 a), the overlapping of (0002) and $(2\bar{1}\bar{1}0)$ lattice planes is semi-coherent and periodically features *coincidence site lattice points* (CSLP), which act as Bi segregation sites. Both periodicity and semi-coherence are the consequence of the two bicrystal sides being arranged with equally (coherently) aligned $\{1\bar{1}00\}$ lattice planes. However, due to the a|c orientation, this in principle perfect match of lattice planes, i.e., the Bravais lattice, is not shared by the

atomic structure, at which only every second Zn site on the (0002) plane actually coincides with a Zn site from the ($2\bar{1}\bar{1}0$) plane. In between, the Zn columns from both sides need to be arranged side by side, which explains the small weak intensities between the CSLPs, as shown by the inset in Figure 4-35 a).

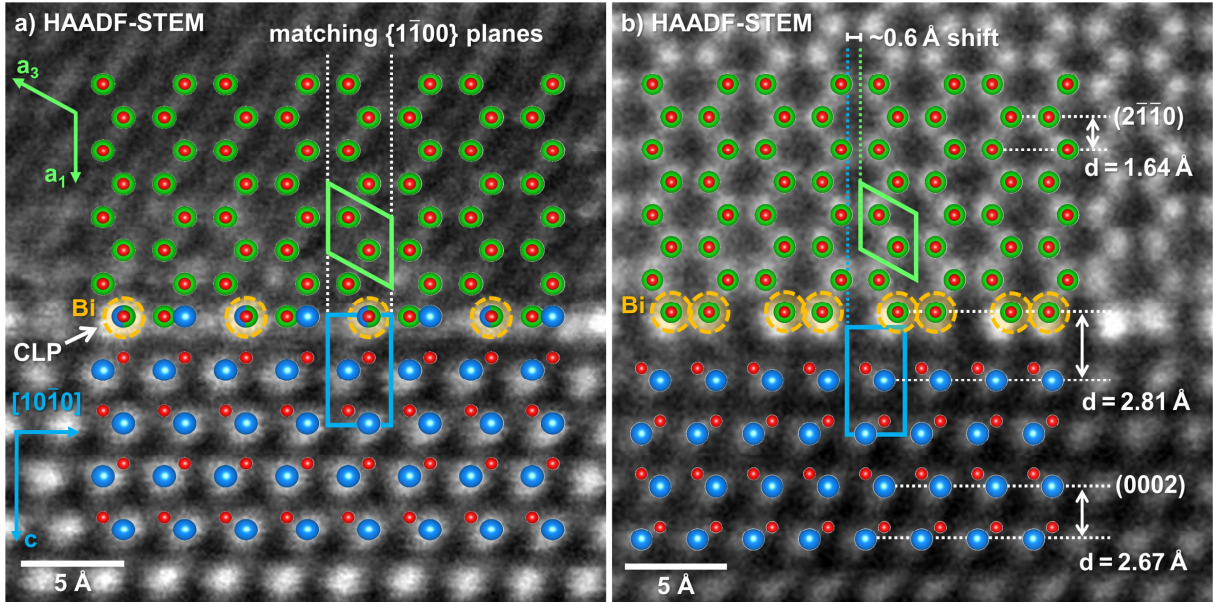


Figure 4-36: Higher magnification of the interface sections featured in Figure 4-35 a) and b) overlaid with the ZnO atomic structure (Zn = blue, green O = red). a) The periodic Bi segregation sites (orange) correspond to coincidence lattice points (CSLP) of both bicrystal halves, which are oriented with perfectly matching $\{1\bar{1}00\}$ lattice planes. Unit cells are shown as green and blue boxes. b) A local displacement of about the 0.6 Å with respect to the $\{1\bar{1}00\}$ lattice planes is evident, impeding the formation of CSLPs. It is suggested that this leads to the observed increased interface width of 2.81 Å between the terminating (0002) and ($2\bar{1}\bar{1}0$) layers, which in turn enables the Bi segregation on the Zn columns of the ($2\bar{1}\bar{1}0$) side, by providing sufficient space and probably a higher coordination.

The reason for the CSLPs being appropriate segregation sites for the large Bi atoms is attributed to the wider space and higher coordination by oxygen atoms, unlike in the ZnO bulk. Similar observations and considerations were reported by Sato et al. for the case of semi-coherent symmetric-tilt Σ -boundaries, where periodic structural units with more space and higher coordination number were determined as the preferred segregation sites for Pr.^{140, 177} However, the situation is different for the interface section shown in Figure 4-35 b). Here, the bicrystal halves are displaced with respect to each other by about 0.6 Å. Furthermore, no CSLPs are observed, but a widened interface with a distance of 2.81 Å between the terminating (0002) and ($2\bar{1}\bar{1}0$) lattice planes (Figure 4-36 b)).^a It should be noted that the widening is important for the Bi segregation, since it allows the incorporation of large atoms in the Zn columns of the terminating ($2\bar{1}\bar{1}0$) layer. In summary, the (local) misorientation, i.e., the 0.6 Å displacement, impeded the formation of CSLPs and hence, the formation of a widened interface between the terminating (0002) and ($2\bar{1}\bar{1}0$) planes was favored. This in turn allowed the incorporation of Bi atoms, probably stabilizing this configuration, similar to the mutual stabilization of dopant

^a For clarification, the value of 2.81 Å perfectly matches the distance of $\{1\bar{1}00\}$ lattice planes, which, however, cannot be oriented parallel to the interface plane in an $a|c$ configuration. Therefore, this is seen as an accidental coincidence of numerical values without further meaning.

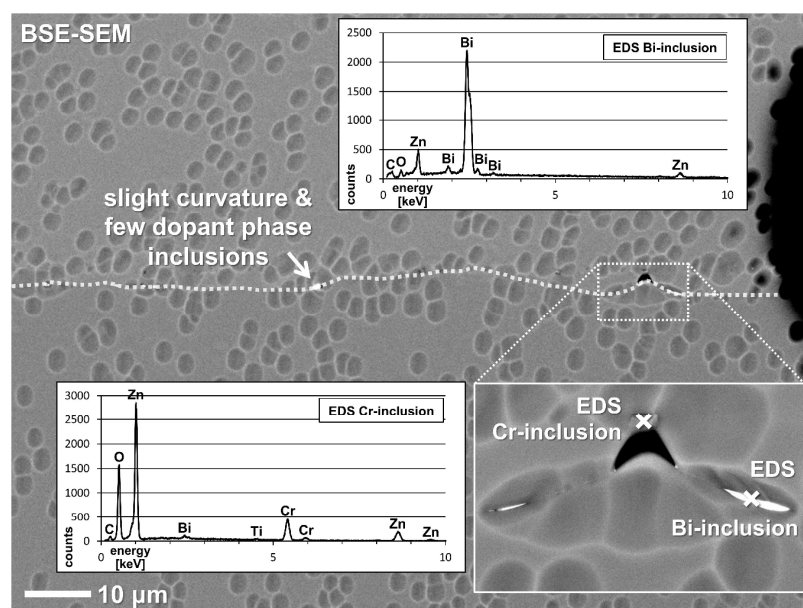
and dislocation network as in the EST-O|O sample (cf. pp. 70).^{200, 242} However, it should be noted that the situation for the oxygen columns or interstitials and therefore, the actual coordination of the segregation sites, could not be revealed by the conducted TEM investigations.^a Nevertheless, it is assumed that for all sites providing sufficient space for the incorporation of Bi atoms, a higher coordination is realized as well.

4.4.2. Doped DB bicrystal in Zn|Zn orientation with 26° tilt (DB-26)

Prior to the TEM investigation, but after the ion-milling procedure, sample DB-26 was subjected to SEM measurements to obtain overview images. As shown in Figure 4-37, the grain boundary features a slight curvature and occasionally isolated dopant inclusions, which were found to be either Bi- or Cr-rich phases. The latter also included minor amounts of Ti.

Figure 4-37: BSE-SEM image of the interface in the Zn|Zn oriented doped tilt-bicrystal DB-26 subsequent to TEM-sample preparation and ion-milling. The interface is slightly curved with a few isolated Bi-rich and Cr/Ti-rich inclusions forming secondary phases. The crater-like structures are preparation artifacts of the ion-milling procedure.

In contrast to the curvature observed in the SEM, TEM investigations revealed a (locally) straight grain boundary, as shown in Figure 4-38 a). SAED was used to measure both the adjusted tilt angle, which was found to be 29° instead of 26°, and the additional unintended misalignment of 2.7° tilt (Figure 4-38 b). Strain contrast or other special contrast features were observed neither in two-beam nor in zone-axis condition. Likewise, no indications were found for a crystalline or amorphous interfacial film (Figure 4-38 c). However, the HR-TEM image reveals that the close vicinity of the interface is notably disordered and – at least at this local position – not a true (0001) interface, as illustrated by the (0002) lattice planes which are slightly inclined with respect to the interface plane. This inclination is a consequence of the curvature and therefore varies along the grain boundary. Figure 4-38 d) and e) show NBED measurements, which were conducted to determine the absolute directions of the *c*-axes and verify their inversion. In doing so, it was revealed that the bicrystal actually has a Zn|Zn orientation instead of the originally intended O|O orientation.



^a ABF-STEM is in principle capable of revealing O atoms, but (at least with the employed ARM 200F) this was found to be possible only for the ordered oxygen columns in the bulk. The complex, more or less disordered situation at interfaces, probably including O interstitials, was found to be practically impossible to image.

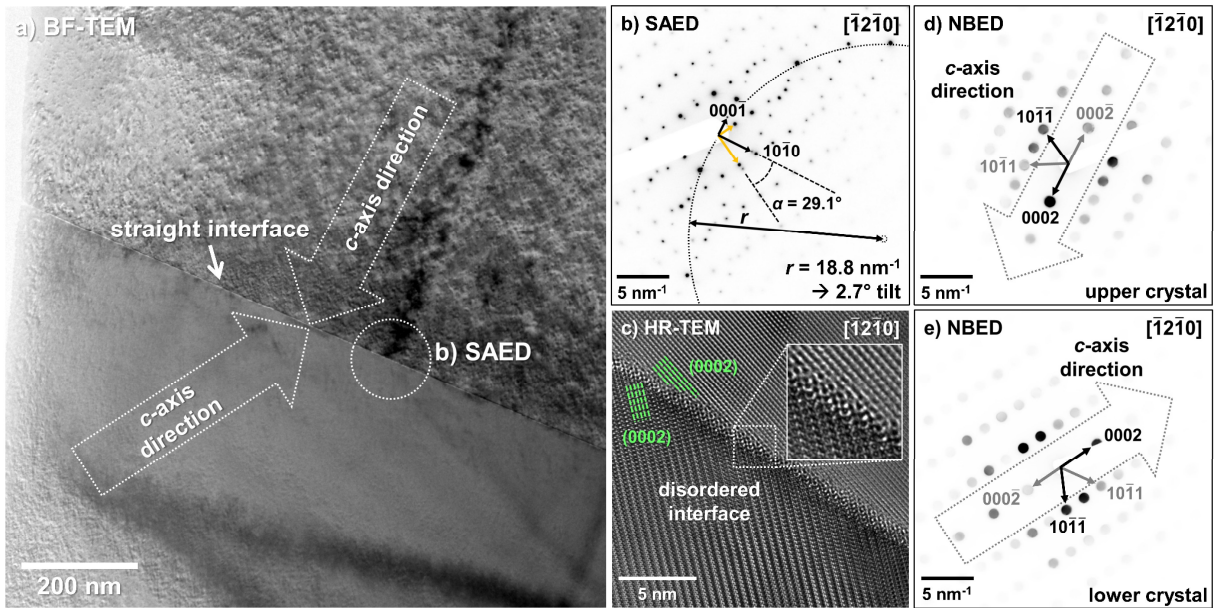


Figure 4-38: a) BF-TEM image of the interface in bicrystal DB-26 in $\vec{g} = (0002)$ two-beam condition. b) electron diffraction indicates a Zn|Zn orientation with 29.1° bicrystal-tilt (rotation around the a-axis) and 2.7° zone-axis tilt (misalignment). c) HR-TEM image in $[\bar{1}2\bar{1}0]$ zone-axis orientation showing an atomically well-bonded interface, without any indications for amorphous or crystalline interfacial films. d), e) NBED measurements revealing a tilted head-to-head orientation via the violation of Friedel's law.

HAADF-STEM imaging (Z^2 -contrast) indicates a large Bi segregation at the interface, which is visible already at medium magnifications, as shown in Figure 4-39 a). Atomic resolution HAADF-STEM and corresponding EDS measurements verify this finding, as given in Figure 4-39 b). Within the disordered interface region, the incorporation of Bi is observed, while it is absent in the bulk. With the exception of Ni, other dopant elements were not detected, being probably diluted below the EDS detection limit.

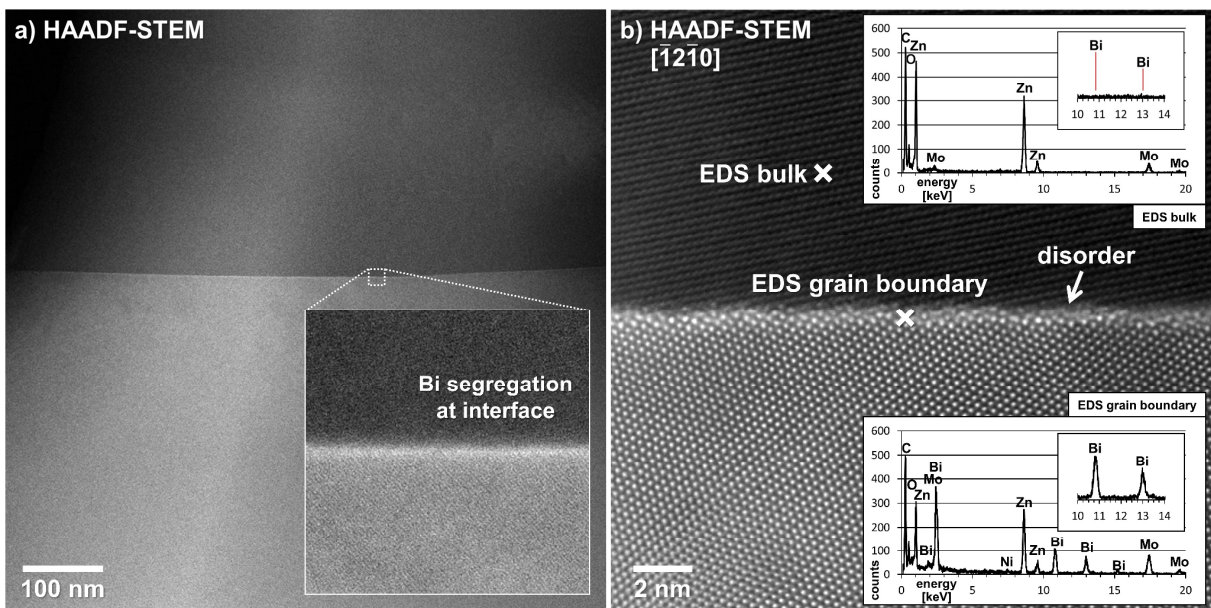


Figure 4-39: a) HAADF-STEM image of sample DB-26. The comparably high image brightness of the interface region indicates the presence of bismuth (Z^2 -contrast). The lower bicrystal half is in zone-axis orientation, hence it appears brighter due to electron channeling. b) Higher magnified HAADF-STEM image revealing a Bi decorated and slightly disordered interface. EDS measurements (insets) verify the presence of Bi at the interface, while it is absent in the bulk. Regarding the other dopants, only a very small Ni signal was detected at the interface.

Due to the 2.7° misalignment, a simultaneous zone-axis alignment of both bicrystal sides is not possible, hence atomic resolution can only be obtained for one side at a time. In order to clarify whether Bi segregation occurred on both sides, corresponding image pairs were recorded, as shown in Figure 4-40.

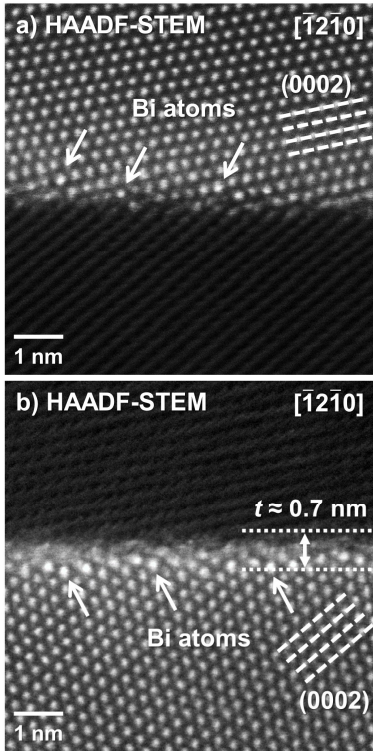


Figure 4-40: a) and b) are HAADF-STEM images of the DB-26 bicrystal interface, with the upper and lower bicrystal side being in $[\bar{1}2\bar{1}0]$ zone-axis orientation, respectively. It is revealed that Bi occupies Zn-sites of (0002) lattice planes on both sides of the interface. However, a preference of Bi substituting Zn-sites of the lower, higher-tilted bicrystal half is observed. The Bi-containing interface structure is disordered and exhibits an approximately constant width of 0.7 nm. (0002) lattice planes are highlighted for a better depiction of the crystal tilt.

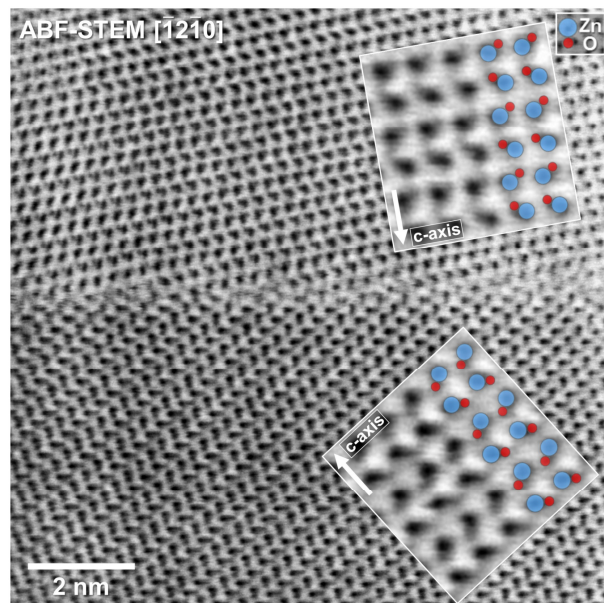
The Z^2 -contrast of the HAADF-STEM images clearly reveals that Bi occupies Zn sites on both sides of the interface, however, with a tendency towards the higher tilted bicrystal half. This tendency is attributed to the likewise higher degree of lattice disorder, which is present at this side of the interface (Figure 4-40 b)) and hence expected to provide more segregation sites.

In order to double-check the results of the NBED measurements, which indicated a Zn|Zn orientation, additional ABF-STEM images were recorded. Figure 4-41 features an interface section located close to the sample edge, where the thickness is very low (<20 nm) and thin-foil bending and relaxation occurred in such

a way that both sides of the interface could be brought in zone-axis orientation simultaneously.^a As illustrated by the insets highlighting the orientation of the Zn-O dumbbells, the Zn|Zn orientation of the bicrystal was confirmed.

Figure 4-41: ABF-STEM image of the interface in sample DB-26 verifying a tilted tail-to-tail (Zn|Zn) orientation by revealing the directions of the Zn-O dumbbells.

As it can be seen in Figure 4-39 and Figure 4-40, the Bi segregation to the interface is predominantly homogeneous with a rather constant width of about 0.7 nm. Therefore, in contrast to the other doped samples, DB-26 was considered suitable for the application of the CEP method to quantify the local Bi content. Two measurement series were recorded at two different positions. As shown in Figure 4-42 a), an $R(r)$ plot of series A



^a The very low sample thickness also limits the absolute intensity of the Z^2 -contrast in corresponding HAADF-STEM images, i.e., the intensity difference between Bi-substituted and pure Zn columns. Therefore, this interface section was well-suited for the determination of the c -axes direction via ABF-STEM, but not for evidencing the Bi segregation.

yields $R^2 > 0.95$ for the linear fit and a derived chemical width of $d = 0.1370$ nm. The high value for R^2 is seen as an indication of the solubility criterion of $x \approx 0 \ll 20$ ppm being fulfilled, as expected for Bi in ZnO.^{4,5} This is confirmed by the $R^{-1}(r^{-1})$ plot in Figure 4-42 b), which indicates a solubility limit close to zero ($0.0006 \approx 0$). Thus, the chemical width can and should be determined from $R(r)$ plots (cf. pp. 43).

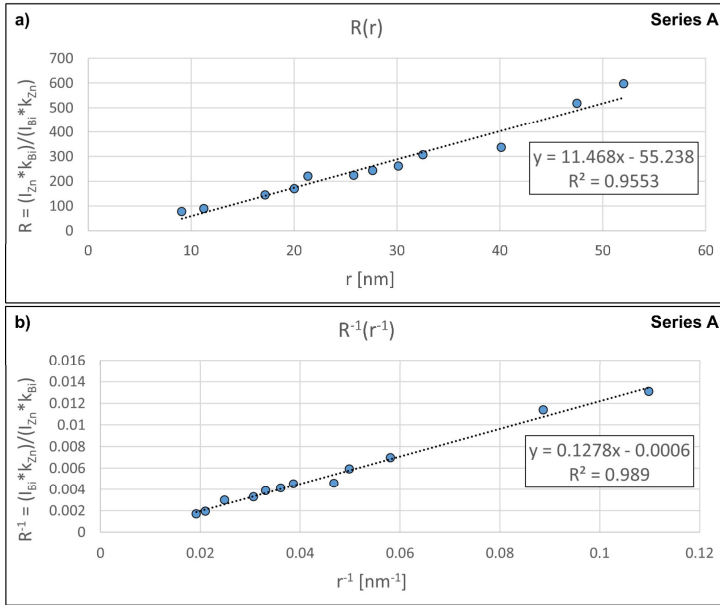


Figure 4-42: a) $R(r)$ plot of CEP measurement series A with $R^2 > 0.95$ indicating the $x \approx 0$ criterion being fulfilled. b) The linear regression of an $R^{-1}(r^{-1})$ plot of the same measurement series confirms this by yielding a solid solubility limit of $x = 0.0006 \approx 0$. Therefore, the chemical width $d = \pi / (2 * 11.468) = 0.1370$ nm is determined from the $R(r)$ plot.

In agreement with series A, a linear fit of measurement series B (Figure 4-43) yields similar values with $R^2 > 0.98$ and $d = 0.1739$ nm. Assuming a constant width of 0.7 nm for the Bi-containing interface, the chemical widths of

series A and B correspond to Zn-site occupancies of 20 % and 25 %, respectively. However, due to tilt and lattice disorder, these occupancies cannot be related to distinct Zn layers, as it was done, for example, in the case of the Si contamination in sample B-II (cf. pp. 50). Nevertheless, these values are regarded as a reliable quantification of the average interfacial Bi content.

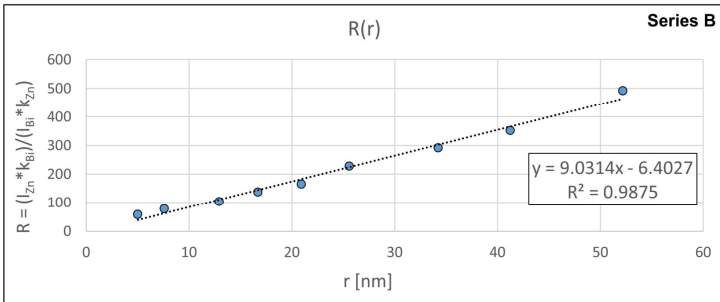


Figure 4-43: $R(r)$ plot of CEP measurement series B with $R^2 > 0.98$. The chemical width is $d = \pi / (2 * 9.0314) = 0.1739$.

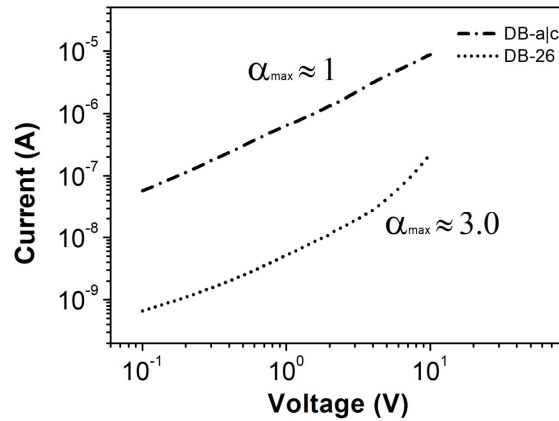
4.4.3. I-V measurements

Both tilted DB bicrystals were subjected to I - V measurements in order to quantify the degree of non-linearity in the stress-free state (Figure 4-44), while sample DB-26 was additionally subjected to load-dependent measurements (Figure 4-45). It should be noted that the original DB-26 sample failed during the I - V measurement by continuously showing zero resistance, which indicates short-circuiting. However, the reason for this could not be revealed. In

consequence, the measurements were repeated with a second DB-26 bicrystal identical in synthesis and configuration.^a

For both bicrystals, the results of the I - V measurements were somewhat unexpected. Sample DB-a|c showed an almost perfect linear behavior with $\alpha_{\max} \approx 1$, although a clear and distinct Bi segregation at the interface was observed. For comparison, $\alpha_{\max} \approx 3.9$ was reported by Sato et al. for a Pr- and Co-doped bicrystal in a|c orientation.¹⁴⁰

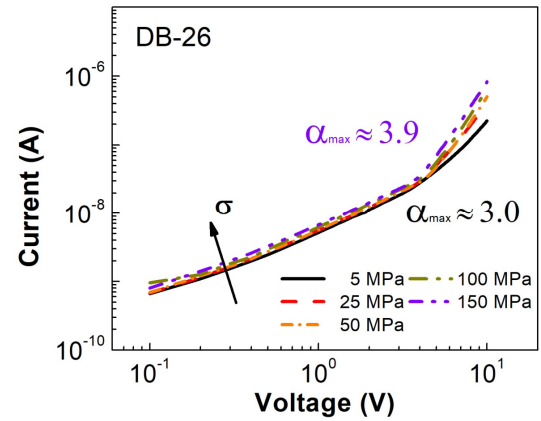
Figure 4-44: I - V characteristics of the tilted DB samples with reduced coherency. Despite the observed Bi segregation in sample DB-a|c, the electrical behavior is almost perfectly linear with $\alpha_{\max} \approx 1$. Sample DB-26 shows a distinct non-linear behavior with $\alpha_{\max} \approx 3.0$, which is, however, a lower value than expected. The breakdown voltage of $V_B = 3.7$ V agrees with the situation of a single bicrystal grain-boundary.



The linear characteristics observed for DB-a|c might be the consequence of an incomplete decoration of the bicrystal interface by Bi, considering that the step-like structures interrupt the semi-periodic segregation (cf. p. 88). In consequence, a high quantity of grain-boundary sections without a potential barrier might be present, allowing the current flow to bypass the “terrace” sections, which are, in contrast, expected to feature sufficient Bi and thus, a local barrier. However, the latter cannot be verified and in addition, other (undetected) reasons for the ohmic behavior might exist as well. In contrast, sample DB-26 clearly shows non-linear behavior with $\alpha_{\max} \approx 3.0$ and a breakdown voltage of $V_B = 3.7$ V being plausible for a single grain boundary.^{90, 221} With respect to the apparently high Bi incorporation at the interface, however, an even higher value of α was expected, since $\alpha_{\max} \approx 3.1$ was already achieved by sample DB-II, which only featured a slight misorientation and presumably a lower Bi content. Yet, this discrepancy might be rationalized by the fact that only an infinitesimally small fraction of the entire interface can actually be probed by the TEM investigations. Thus, the observed slight curvature of sample DB-26 is seen as a possible reason for the comparably low α -value. In contrast to the EST sample, no indication of a dislocation network stabilizing the Bi incorporation was found and the Bi segregation sites are solely attributed to the disorder created at the grain boundary. Since the degree and width of the disorder probably vary with the curvature, the TEM investigations might have been conducted at an interface section of locally higher Bi segregation. For example, the investigated sample regions featured (0002) lattice planes being inclined to the interface plane for both bicrystal sides (cf. p. 92). Interface sections, where the curvature results in (0002) planes being aligned parallel to the interface plane, potentially feature a locally lower disorder and hence a reduced Bi segregation. In consequence, the potential barrier would be lower at these locations, resulting in an overall lowered α -value.

^a This second sample, however, was not investigated by TEM. Thus, it should be kept in mind that despite the fact that both samples are regarded and treated as identical, minor differences might exist, such as a slightly different tilt angle, for example. However, small differences are not expected to significantly change the Bi segregation in this case, since (in)coherency and grain-boundary structure are mainly governed by the in either case large tilt of $\sim 26^\circ$.

Figure 4-45: Load-dependent I-V characteristics of sample DB-26. With increasing mechanical load, the coefficient of non-linearity increases from $\alpha_{\max} \approx 3.0$ at 5 MPa to $\alpha_{\max} \approx 3.9$ at 150 MPa, while $V_B = 3.7$ V remains constant. While this is in perfect agreement with a Zn|Zn-like oriented bicrystal, the leakage current (measured at 0.1 V) increases slightly from $7 \cdot 10^{-10}$ A to $1 \cdot 10^{-9}$ A, instead of being decreased as expected from the simultaneously increased barrier height.



Regarding the stress-dependent measurements, sample DB-26 shows the expected behavior for most aspects except the leakage current (Figure 4-45), which slightly increases from $7 \cdot 10^{-10}$ A to $1 \cdot 10^{-9}$ A

(measured at 0.1 V). A decrease would theoretically be more plausible, considering the bicrystal's Zn|Zn orientation and the corresponding increase in barrier height. The latter is, however, in good agreement with the theoretical expectations (cf. pp. 18) as well as with the results from the EST samples (cf. p. 77) and reflected by the coefficient of non-linearity rising from $\alpha_{\max} \approx 3.0$ to $\alpha_{\max} \approx 3.9$, while the breakdown voltage $V_B = 3.7$ V remains constant and independent of the applied load.

4.4.4. Discussion and Summary

The TEM results for both samples DB-a|c and DB-26 confirm that using specific misorientation in order to reduce coherency and hence, increase (or actually induce) grain-boundary segregation is a workable as well as promising approach in tailoring varistor or piezotronic bicrystals. As revealed by HAADF-STEM imaging, these two bicrystals featured the most distinct and well-pronounced Bi segregation among all investigated samples, despite the fact that the respective interface sections were (locally) almost perfectly flat like in the case of the coherent, Bi-free sample DB-I (cf. pp. 58). This finding is qualitatively verified by EDS and, in the case of sample DB-26, also quantitatively supported by CEP measurements, which indicated up to ~ 25 % Bi at the interface with respect to the total metal content. In contrast to the EST-O|O sample, no dislocation network was formed, which shows that this is not necessarily required to obtain an interfacial segregation of Bi. In fact, three different mechanisms providing suitable segregation sites can be distinguished, which are all related to a reduced coherency and a deviation from the ideal (bi)crystal structure:

EST-O|O: Synthesis procedure leads to a strong GB curvature and a continuous Bi-containing dislocation network at the interface, with the dislocation network and its incorporation of Bi mutually stabilizing each other.

DB-a|c: Semi-coherent interface configurations provide (semi-)periodic segregation sites of sufficient space and coordination at the interface. CSLPs in particular can act as such segregation sites.

DB-26: Specific misorientation, i.e., macroscopic tilt, minimizes coherency and causes irregular lattice disorder at the interface, which allows the incorporation of Bi.

Although these three types of segregation sites are structurally different, the same thermodynamic considerations as discussed for samples DB-I and EST-O|O (cf. pp. 80) apply. In each case, an interface is formed featuring Bi-decorated segregation sites, i.e., $\Gamma_{\text{sat}} \gg 0$, which corresponds to a certain change in interfacial energy $d\gamma$. Since $d\gamma$ refers to the difference between the saturated and the undecorated state of the very same interface^a, it becomes clear that the introduction of structural incoherencies, such as defects, disorder or CSLs & CSLPs, via interface curvature or tilt boundaries, defines both Γ_{sat} and $d\gamma$. However, it should be kept in mind that these considerations are only valid for the special case of insoluble dopants available in near-infinite quantity with respect to the number of segregation sites.

Interestingly, the successful doping of the bicrystal interfaces with Bi, as shown by the TEM results, is only partly reflected by the I - V measurements. While low non-linear characteristics ($\alpha_{\text{max}} \approx 3.0$) were obtained for sample DB-26, sample DB-a|c actually exhibited pure ohmic behavior ($\alpha_{\text{max}} \approx 1$), despite the fact that the TEM findings strongly indicate a sufficient doping for both samples. In the case of DB-a|c, however, the Bi incorporation is probably discontinuous, which could explain the linear characteristics. Nevertheless, the load-dependent measurements of sample DB-26, in conjunction with EDS and HAADF-STEM imaging, qualitatively and unequivocally proved the successful doping as well as the piezotronic modulation.

^a It should be noted that the undecorated state is energetically unfavorable and hence exists only theoretically.

DOPED DB BICRYSTALS WITH REDUCED COHERENCY - SUMMARY

- ABF-STEM successfully verified the (000 $\bar{1}$) O-terminated “tail” orientation of the c -axis in DB-a|c.
- ABF-STEM and NBED revealed a Zn|Zn type orientation for sample DB-26.
- SAED was used to determine a bicrystal misalignment of 1.1° and 2.7° for samples DB-a|c and DB-26, respectively. The intended 26° tilt of DB-26 was found to be 29.1°.
- Both samples DB-a|c and DB-26 feature an atomically well-bonded interface free from any kind of crystalline or amorphous interfacial film.
- In sample DB-a|c, a semi-coherent interface is formed with the following properties:
 - predominantly flat, but with steps & terrace-like sections on the atomic scale
 - at such steps, the structure is disordered with irregular, (probably) lower Bi segregation
 - the straight terrace section feature either periodic CSLPs (Zn sites) acting as Bi segregation sites or exhibit a widened interface allowing continuous Bi incorporation on the Zn columns of the a -axis side, i.e., the terminating (2 $\bar{1}\bar{1}$ 0) plane.
- In sample DB-26, an incoherent interface was formed with the following properties:
 - predominantly flat, but with a slight curvature on the μm scale
 - continuous, strongly disordered structure with a width of about 0.7 nm
 - high Bi segregation; Bi substitutes on Zn columns of both sides
 - CEP measurements indicate 20 – 25 % Bi on Zn sites.
- Stress-dependent I-V measurements revealed non-linear characteristics ($\alpha_{\text{max}} \approx 3.0$) as well as a barrier-increasing piezotronic response for sample DB-26, while sample DB-a|c exhibited completely ohmic behavior ($\alpha_{\text{max}} \approx 1$), which is seen as the consequence of the Bi segregation being discontinuous at the step-like interface sections.
- Based on a comparison of samples DB-a|c, DB-26 and EST-O|O, three structurally different types of Bi segregation-site formation are distinguished:
 1. strong GB curvature with continuous dislocation network (macroscopically coherent, but locally reduced coherency)
 2. semi-coherent, low-disorder interface with (semi-)periodic segregation sites, e.g., CSLPs
 3. highly incoherent and disordered interface structure.
- For all three types of segregation-site formation, the same thermodynamical considerations (cf. pp. 80) apply: The Bi-segregation (Γ_{sat}) corresponds to a lowering of an otherwise high interfacial energy γ . In consequence of the special case of an insoluble dopant available in quasi-infinite amounts, interface structure and segregation-site abundance (almost) exclusively determine the quantity of the segregation via Γ_{sat} and $d\gamma$ according to

$$d\gamma = -\Gamma_{\text{sat}} \cdot d\mu$$

5. ZnO Hexagonal Platelets & Rod-shaped Twins – Results & Discussion

5.1. Hexagonal platelets

Figure 5-1 a) features a BF-TEM image of the typical mineralization products after 15 min reaction time using a 30:70 ethanol/water mixture. Larger crystallites clearly show a hexagonal platelet-like morphology, which is, however, irregular and uneven in most cases. SAED verifies a wurtzite ZnO crystal structure and reveals the platelets being formed perpendicular to the c -axis with $\{10\bar{1}0\}$ hexagonal facets. Although these facets follow $\{10\bar{1}0\}$ planes on average, they feature a high surface roughness on the atomic scale, as shown by the HR-TEM image in Figure 5-1 b). In addition to the hexagonal crystallites, a large amount of matrix material is present in this sample.

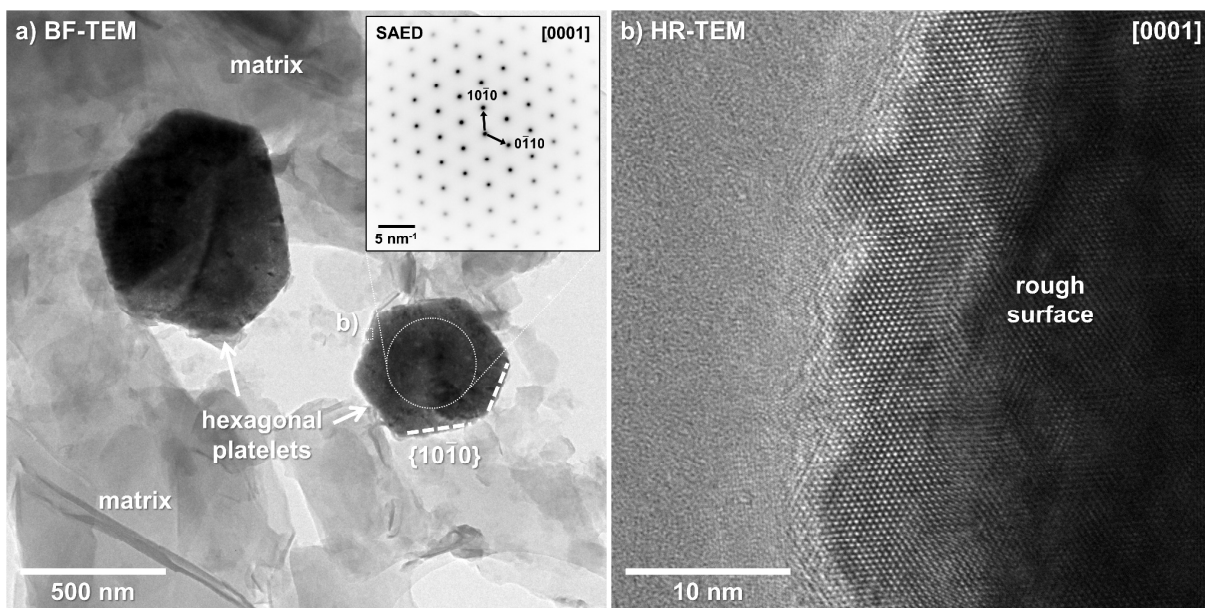


Figure 5-1: a) BF-TEM image of hexagonal ZnO platelets after 15 min reaction time. As shown in by inset, SAED verifies a wurtzite crystal structure and a $[0001]$ zone-axis orientation. The hexagonal facets correspond to crystallographic $\{10\bar{1}0\}$ planes. However, the hexagonal shape of most individuals is irregular and uneven. In addition, a significant amount of residual matrix is still present. b) HR-TEM image showing a distinctively pronounced surface roughness of the $\{10\bar{1}0\}$ facets.

This matrix material itself is partly amorphous, as indicated by the irregular, blurry contrast in respective HR-TEM images (Figure 5-2 a)),^a and partly nanocrystalline, as revealed by the observation of various lattice fringes. The measured lattice-fringe distances agree well with ZnO lattice planes $\{0002\}$, $\{10\bar{1}0\}$ and $\{10\bar{1}1\}$. In addition, Debye-Scherrer rings, which could unambiguously be attributed to ZnO, were observed in SAED images of the matrix material, confirming both its polycrystallinity as well as the wurtzite ZnO crystal structure for the corresponding nanocrystals (Figure 5-2 b)).

^a The supporting (holey) carbon film of the employed TEM grids is also amorphous and thus, exhibits a similar contrast. Therefore, attention was placed on recording HR-TEM images only at sample regions “overhanging” into holes of the carbon film.

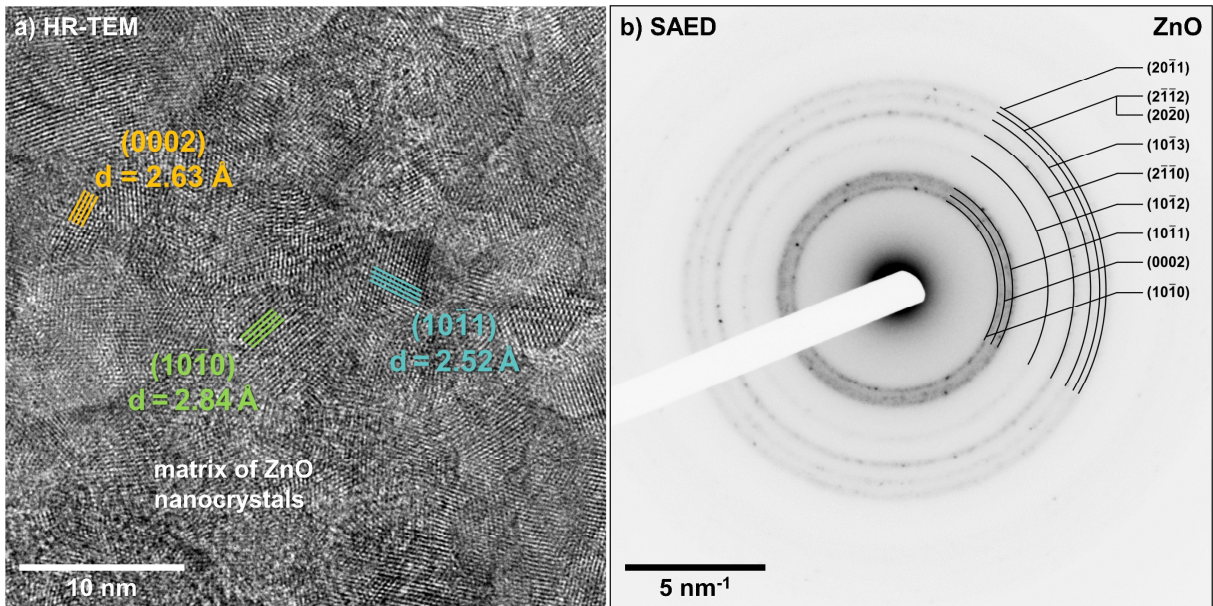


Figure 5-2: a) HR-TEM image of the matrix after 15 min reaction time, revealing a high density of ZnO nanocrystals (<10 nm) interspersed with amorphous material (indicated by irregular, blurry contrast). For illustration, some ZnO lattice planes are highlighted in the image. b) Corresponding SAED image showing Debye-Scherrer rings, confirming both the polycrystallinity of the matrix and the wurtzite crystal structure of the nanocrystals.

Applying a prolonged reaction time of 45 min, a significantly higher quality of the hexagonal platelets is obtained, as shown in Figure 5-3 a).

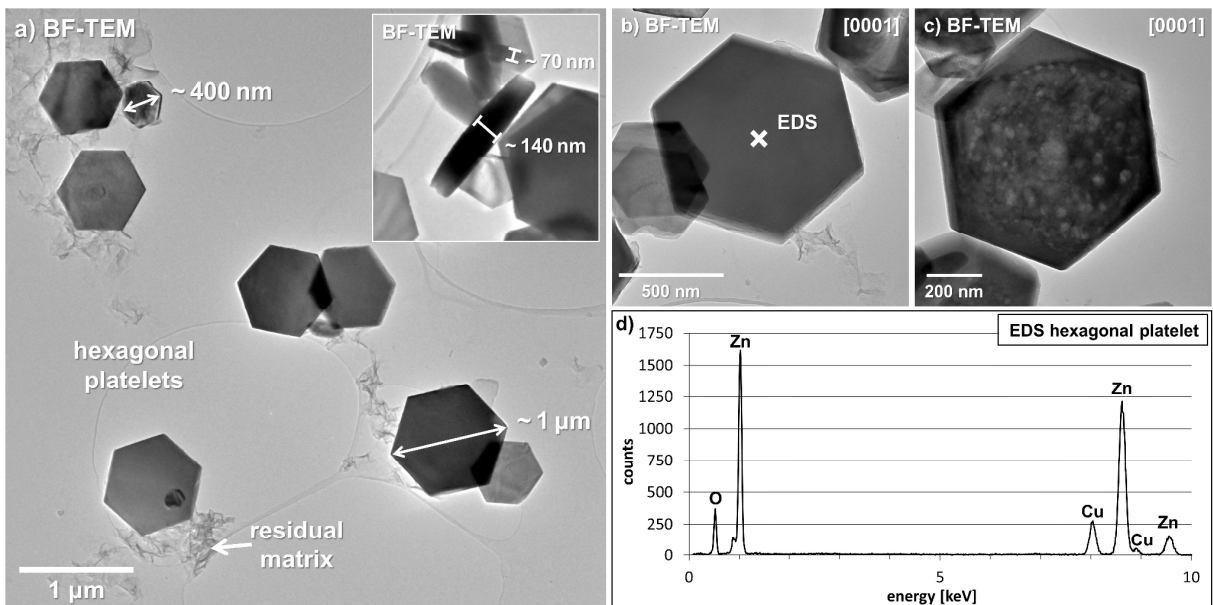


Figure 5-3: a) BF-TEM overview image of hexagonal ZnO platelets after 45 min reaction time. The majority of platelets feature a well-pronounced hexagonal shape with a diameter of about 400 nm – 1 μm and a thickness of 80 – 140 nm. Only small amounts of residual matrix material are present. b) ZnO hexagon in [0001] zone-axis orientation with uniform contrast, indicating a high crystallinity with low to zero defects and pores, being typical for most individuals in this sample. In contrast, some platelets contain a rather high amount of defects and pores, despite their well-pronounced hexagonal shape, as shown in c). d) EDS point measurement corresponding to b), revealing a quasi-pure Zn-O composition. Co was not detected. The Cu signal originates from the supporting TEM grid.

The majority of crystallites exhibits a well-pronounced, uniform hexagonal morphology and only minor amounts of matrix residuals are present. The typical diameter is in the range of 400 nm – 1 μm and the thickness is 80 – 140 nm. Whereas most individual crystallites show a

uniform contrast in zone-axis BF-TEM images (Figure 5-3 b)), others clearly feature pores and defects (Figure 5-3 c)), despite their well-pronounced hexagonal shape. Corresponding EDS measurements indicate a quasi-pure Zn-O composition (Figure 5-3 d)). Cobalt was not detected but is considered to be present in low concentrations below the EDS detection limit, according to complementary investigations.²⁰¹ A typical feature observed for nearly all ZnO hexagons in the 45 min sample, is a surface coverage of the $\{10\bar{1}0\}$ facets by a mixture of amorphous and nanocrystalline material attributed to matrix residuals, as shown in Figure 5-4. Observed lattice-fringe distances agree well with $\{10\bar{1}0\}$ ZnO lattice planes and EDS point measurements reveal a Co-rich Zn-O composition. Although the $\{10\bar{1}0\}$ facets appear even and well-crystallized on the mesoscopic scale, higher magnified images depict a rather rough surface below the surface coverage.

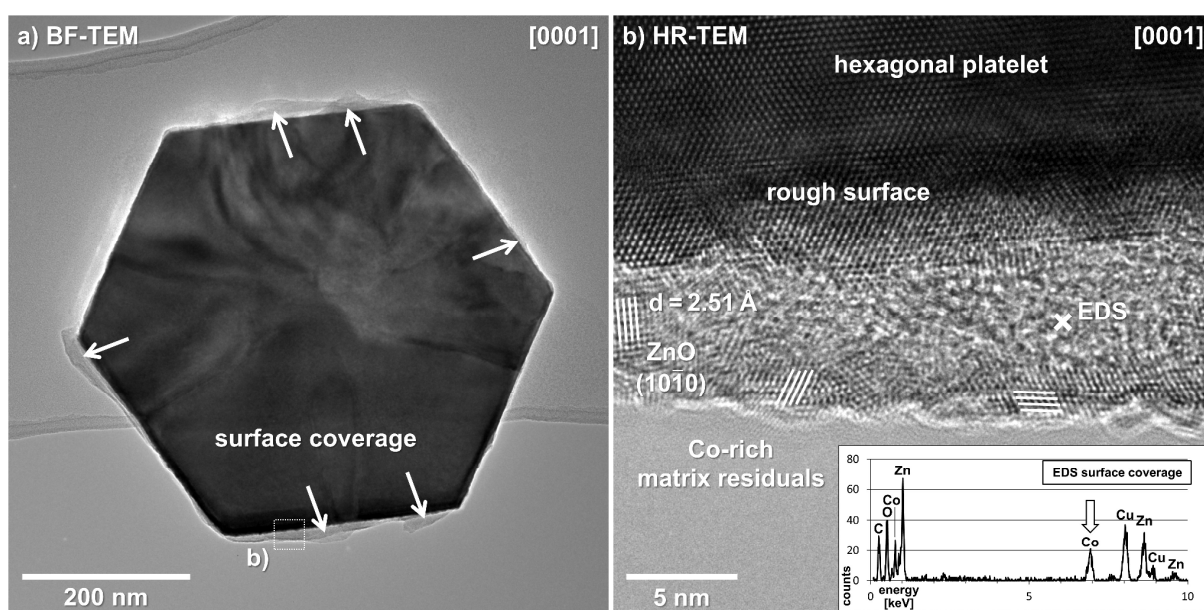


Figure 5-4: a) BF-TEM image of a typical ZnO hexagon of the 45 min sample in $[0001]$ zone-axis orientation. Attributed to matrix residuals, a distinct surface coverage of nearly all $\{10\bar{1}0\}$ facets is observed. b) HR-TEM image revealing these surface coverages consisting of amorphous material (blurry contrast) and nanocrystalline ZnO, as identified by wurtzite $\{10\bar{1}0\}$ lattice planes. Although well-pronounced $\{10\bar{1}0\}$ facets have formed, the hexagon's surface still features a certain roughness. The EDS point measurement indicates a Co-rich Zn-O composition of the surface coverage. The Cu signal originates from the supporting TEM grid.

In consequence of these observations, the 45 min sample was additionally subjected to a $300\text{ }^{\circ}\text{C}$ calcination step in air. As exemplarily shown in Figure 5-5 a), this procedure successfully removed the surface coverage from the ZnO hexagons. Moreover, the surface roughness was reduced, leading to almost atomically flat hexagonal $\{10\bar{1}0\}$ facets for the majority of the investigated crystallites.

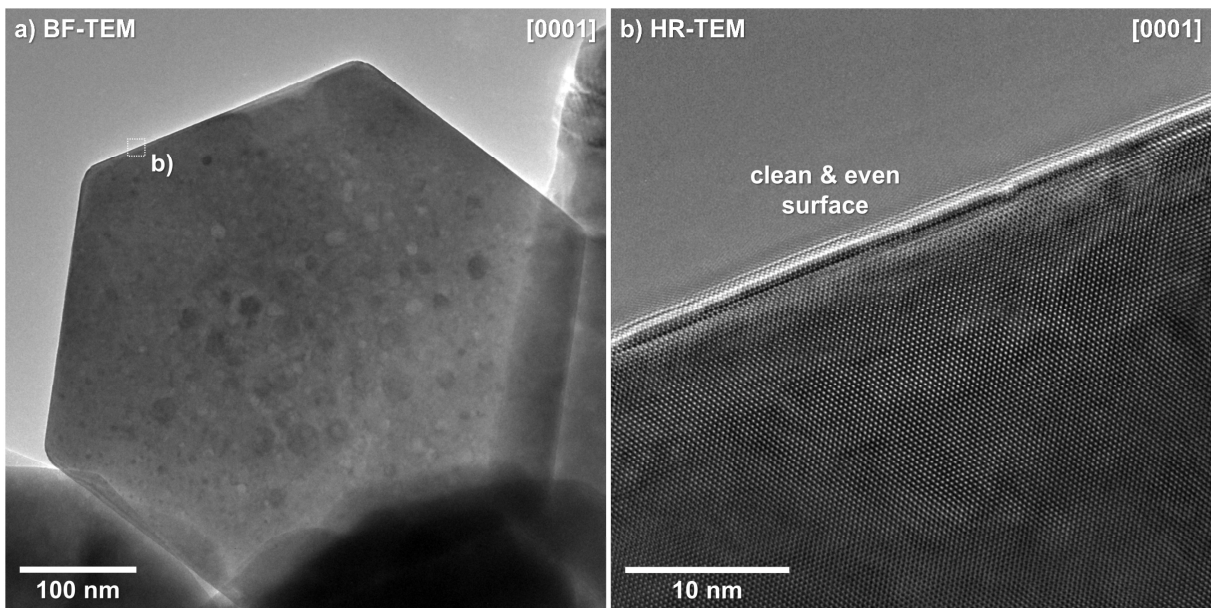


Figure 5-5: BF-TEM image in [0001] zone-axis orientation of a typical ZnO hexagon after 45 min reaction time and a subsequent calcination at 300 °C in air. Some pores and probably defects are present in the bulk. No indication of any residual surface coverage is observed. b) HR-TEM image revealing a clean and almost atomically flat surface for the {10 $\bar{1}0$ } facets.

In order to verify chemical homogeneity, hexagons from the 300 °C annealed 45 min sample were subjected to STEM-EDS mappings, as shown in Figure 5-6.

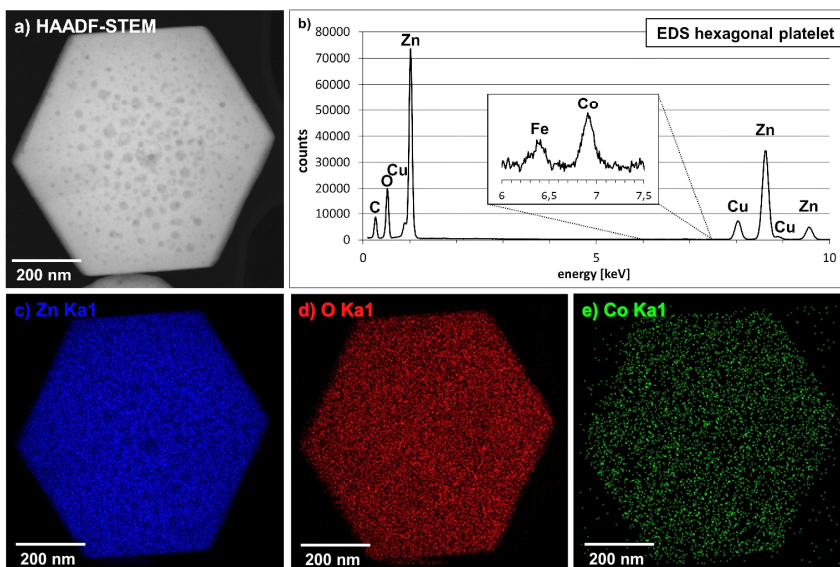


Figure 5-6: STEM EDS-mapping a), c), d), e) and corresponding sum spectrum b) of a typical ZnO hexagonal platelet after 45 min reaction time and a subsequent calcination at 300 °C in air. The contrast inhomogeneities in a) are attributed to pores. A low amount of Co is detected, as shown by the inset in b). The Fe signal originates from the pole piece in the TEM. Despite small intensity variations related to the pores, the ZnO hexagon is chemically perfectly homogeneous.

The results confirm both the chemical homogeneity as well as the presence of cobalt, which, however, was solely detected in the mapping's sum spectrum, since it is only present in very low amounts.^a This low Co concentration is in notable agreement with both the complementary measurements as well as the reported low solid solubility in larger, near micrometer-sized

^a In contrast to regular EDS point measurements, such as shown in Figure 5-3 d), which were typically conducted with 1 – 2 min live time, the EDS mappings were recorded over an extended period of about 30 min. Therefore, even small amounts of cobalt, present in concentrations near the detection limit of ~ 1 wt%, could be detected.

nanoparticles^a at low temperatures ≤ 550 °C.^{201, 239, 250-252} Nevertheless, this is seen as a confirmation of the successful doping of ZnO with Co, which is additionally confirmed by the greenish color of the mineralization product (cf. pp. 28).²⁵³

Cross-sections of ZnO hexagons were prepared for TEM investigation in order to verify their single crystallinity with absolute certainty. In the case of *c*-axis inversion twinning, a stack of two equally oriented platelets of the same size would most likely be unrecognizable in and near [0001] zone-axis orientation. Considering that inversion twinning was observed as a common feature for all other investigated solvent/dopant combinations, as shown in Figure 3-6 (p. 28), such a configuration, which would conceal its twinned nature in [0001] orientation, appears not unlikely.²⁰¹ Therefore, hexagons were investigated in $[10\bar{1}0]$ zone-axis direction and subjected to NBED measurements, which unambiguously verified the same *c*-axis direction for both sides, i.e., top and bottom of the platelet (Figure 5-7 a)). In addition, HR-TEM images were recorded to reveal possible twin-, grain- or subgrain-boundaries. However, no indications for such boundaries were observed and single crystallinity was confirmed (Figure 5-7 b)).

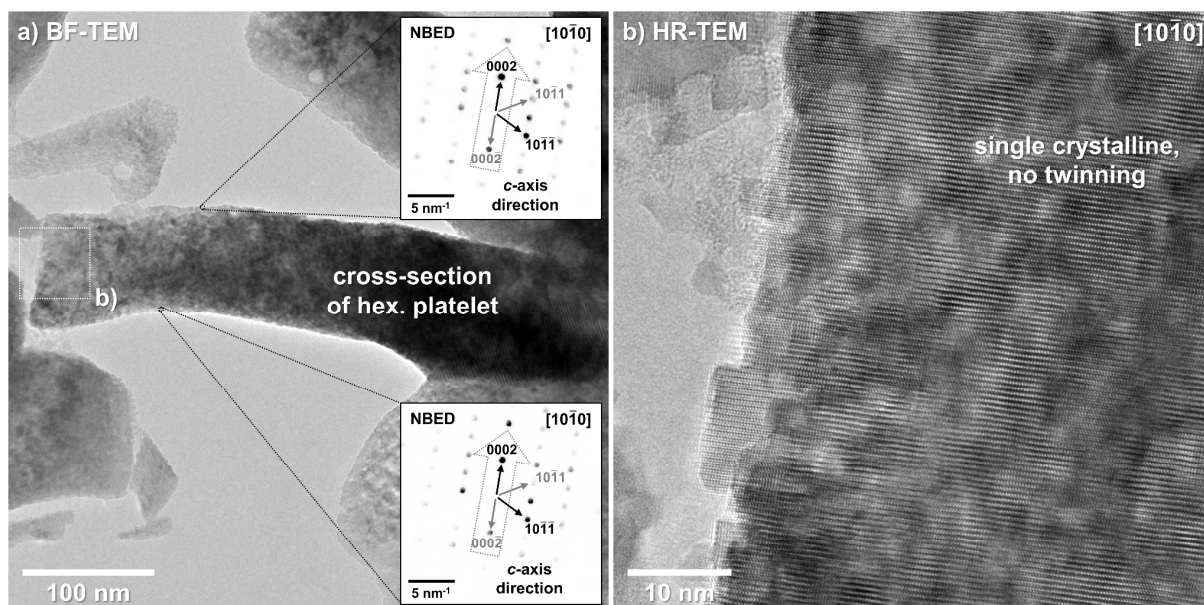


Figure 5-7: a) and b) BF-TEM and $[10\bar{1}0]$ HR-TEM image of a cross-section of a hexagonal platelet after 45 min reaction time and subsequent to the 300 °C calcination. No indications for any kind of (sub)grain-boundary or twinning are observed. In addition, NBED verifies the same *c*-axis direction for both the upper and lower side, hence inversion twinning is ruled out and single crystallinity is confirmed. The blurry contrast in b) is attributed to a contamination by the epoxy resin used for embedding.

^a The solid-solubility limit of Co in ZnO is not only strongly dependent on the temperature but also on the crystal size in the case of nanoparticles. While up to 33 at% are reported for particles < 20 nm (at 550 °C), it is below 2 at% for larger crystals > 100 nm at the same temperature.^{250, 251} However, it should be noted that this large increase in solubility is attributed by the authors to Co accumulation at GBs and free surfaces in nanocrystalline ZnO films. Therefore, its relevance for “real” bulk solubilities might be questionable. On the other hand, the authors observed a distinct and linear increase of the lattice spacing up to 33 at% by XRD, which indicates a “true” dissolution of Co into the ZnO lattice.

5.2. Rod-shaped twins

Since the development of a synthesis route for uniform hexagonal ZnO platelets was the original goal, the rod-shaped nanotwins were rather a side-product of these experiments. Nevertheless, they are considered to be also relevant in the context of nanoparticles, as they were fabricated with notable uniform size, hexagonal rod-shape and a distinct inversion twinning.²⁰¹ Independent of an optional cobalt doping, they are obtained as mineralization products from the same thermohydrolysis as the hexagons, if water instead of an ethanol/water mixture is used as a solvent (cf. pp. 28). The characteristic inversion twinning is already indicated by their morphology with a symmetric tapering towards the center of the elongated crystals, as shown in the BF-TEM image in Figure 5-8 a). Similar to the bicrystal studies, NBED was used to verify the inversion character of the presumed twinning and determine its orientational configuration. In all cases, the nanorods were found to be tail-to-tail (O|O) *c*-axis inversion twins. The actual twin-boundary was investigated by HR-TEM, as shown in Figure 5-8 b), revealing an atomically well-bonded interface apparently free of any kind of interfacial film or secondary phases.

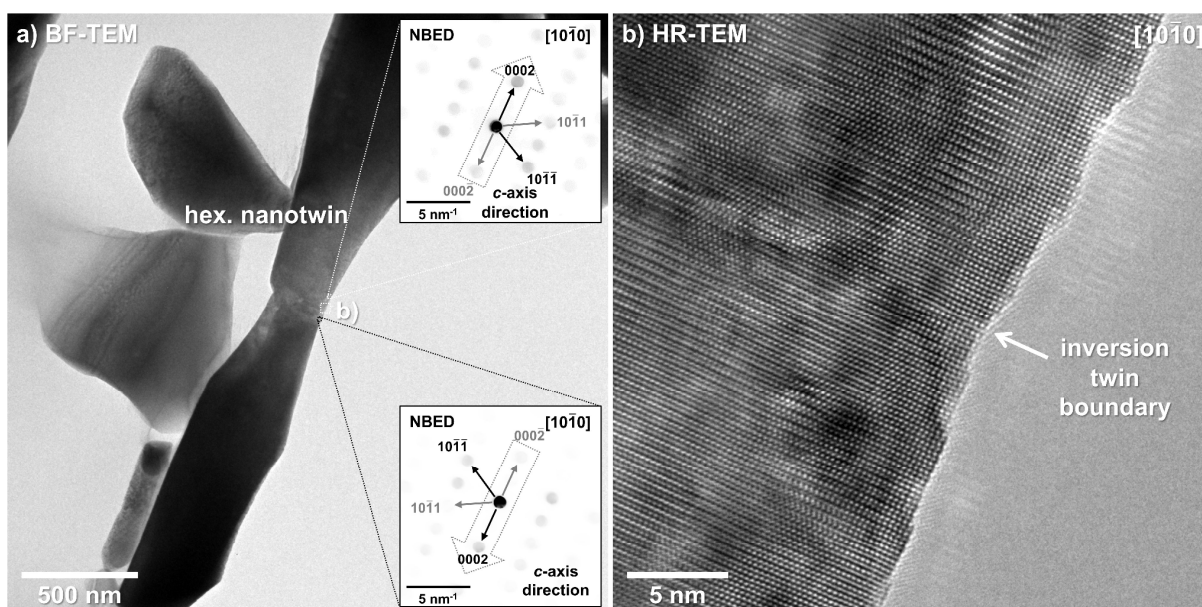


Figure 5-8: a) BF-TEM image of a hexagonal rod-shaped nanotwin. The tapering shape indicates the position of the twin boundary. NBED measurements verify a tail-to-tail *c*-axis inversion twinning and the rods being parallel to the *c*-axes in length. b) HR-TEM image in $[10\bar{1}0]$ zone-axis orientation revealing an atomically well-bonded twin boundary. No interfacial films or phases were observed.

HAADF-STEM investigations were conducted in addition, showing that these twin boundaries are slightly meandering and irregular (Figure 5-9 a)). Thus, they do not correspond to even $(000\bar{1})|(000\bar{1})$ interfaces, although the *c*-axis inversion itself is accurate with no measurable misorientation between both sides (Figure 5-8 a)). Consistent with this irregular boundary, the lattice is notably distorted in the vicinity of the interface, as it can be seen in Figure 5-9 b)). Interestingly, despite C-rich contaminations, which are attributed to the epoxy resin used for embedding, EDS measurements (not shown) did not detect any kind of dopant (cobalt) accumulation or incorporation at the twin boundary. As illustrated by the insets in Figure 5-9 b)),

ABF-STEM was used to double-check and successfully confirm the tail-to-tail orientation of the inversion twinning via imaging of the Zn-O dumbbell orientation.

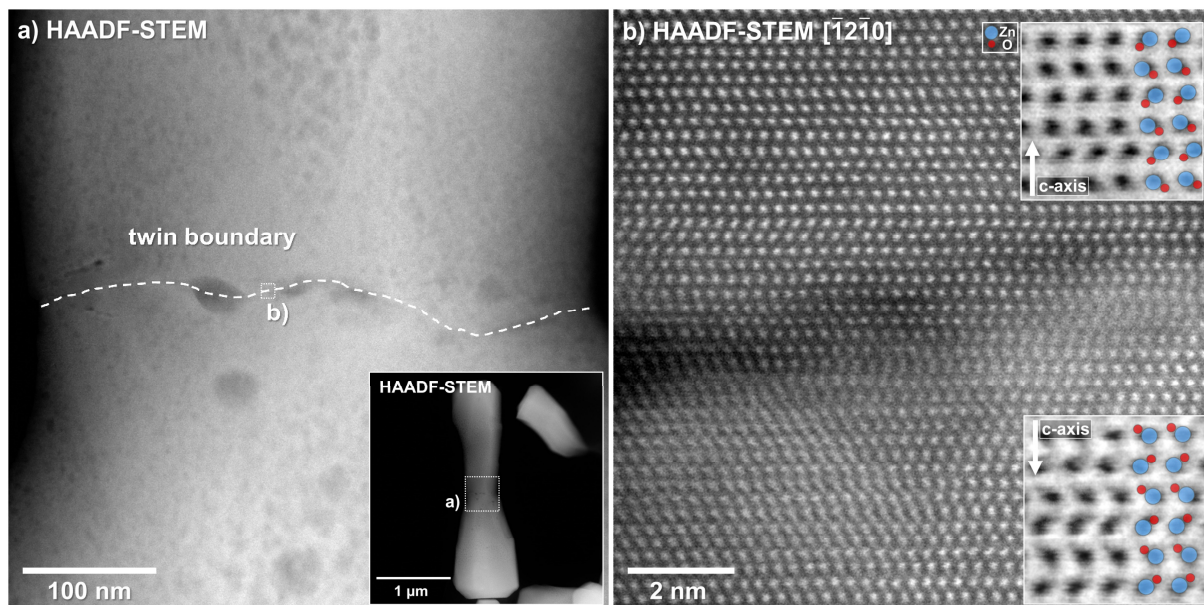


Figure 5-9: a) HAADF-STEM image of a hexagonal rod-shaped nanotwin (inset) showing a slightly meandering twin boundary. The spot-like contrast variations are attributed to pores and residual epoxy resin. b) HAADF-STEM image of the twin boundary in $[12\bar{1}0]$ zone-axis orientation, revealing an atomically well-bonded but curved interface featuring distinctive lattice distortions. ABF-STEM verifies a tail-to-tail c-axis inversion twinning, as illustrated by the insets.

5.3. Discussion and Summary

The TEM results verify a successful synthesis of Co-doped single-crystalline hexagonal ZnO platelets, which exhibit both uniform morphology ($\{10\bar{1}0\}$ facets) and chemistry. Inversion-twinning, as observed for all other mineralization products (cf. p. 28),²⁰¹ could be ruled out. It was shown that well-pronounced hexagons were precipitated after 45 min of reaction time. However, these crystallites typically featured a surface coverage of residual matrix material, which is related to the simultaneously observed surface roughness of the hexagon facets. Based on these findings, a subsequent calcination step at 300 °C in air was added to the synthesis procedure, which lead to a remarkable increase in crystal quality. The calcinated hexagons were not only free of surface coverages but also featured almost atomically flat and well-crystallized $\{10\bar{1}0\}$ facets. Both is regarded as highly beneficial for the aspired tessellation via Langmuir-Blodgett deposition since surface contaminations might influence (local) surface tension as well as hinder a close fitting of adjoined crystallites. Nevertheless, the size variation with diameters of 400 nm – 1 μm and thicknesses of 80 – 140 nm was still found to be rather large, considering that larger, well-tessellated layers demand a uniform size of the hexagons, in particular, when self-assembling is desired. This might be one reason for the actually unsuccessful Langmuir-Blodgett deposition, which lead to tessellations of only very small patches of about 12 – 14 crystallites.²⁰¹ However, as described in the corresponding publication, other parameters, such as the coating of the glass substrate or the electrokinetic potential of the particles in water, were also found to influence and probably dominate the deposition.

Regarding the rod-shaped twins, it was shown that they are exclusively tail-to-tail (O|O) *c*-axis inversion twins, which are accurately oriented with atomically well-bonded interfaces, although the latter are slightly irregular and hence, do not represent perfect $(000\bar{1})|(000\bar{1})$ boundaries. The interfaces appeared free from dopant phases or other impurities but exhibited a certain lattice disorder. Nevertheless, similar to the hexagons (cf. p. 101), the twinned crystallites are expected to feature a low Co-content as a bulk solute, which is, however, below the EDS detection limit. Being rather a side-product in the course of the optimization of the hexagon synthesis, the rod-shaped twins were not subjected to further investigations. Nevertheless, against the background of the early work by Wang et al. on ZnO piezotronics,^{154, 155, 161} which was conducted utilizing nanowires, and under the consideration that their O|O inversion twinning represents a similar configuration as for the EST-O|O bicrystal (cf. pp. 70), the rod-shaped twins are seen as an interesting type of nanocrystal by their own right, with possible application scenarios similar to piezotronic bicrystals. With respect to their irregular, disordered interfaces, they are probably capable of incorporating large-ion dopants at the interface and a consideration of respective precipitation experiments, including doping with Bi, for example, is seen as probably worthwhile. In consequence, it might be possible to obtain accurately oriented varistor-type nano-bicrystals, which additionally can be piezotronically modified, similar to the nanowires.

HEXAGONS AND ROD-SHAPED TWINS - SUMMARY

- Thermohydrolysis of zinc-cobalt acetates (95 °C, 15 – 60 min) yields hexagonal platelets if a 30:70 ethanol/water mixture is used and rod-shaped twins if water only is used as a solvent.
- ZnO hexagonal platelets at three different reaction stages were investigated by TEM:
 - a) 15 min:
Rough crystals with irregular proto-hexagonal shape; large amount of residual matrix being partly amorphous and partly nanocrystalline ZnO.
 - b) 45 min:
Well-pronounced hexagonal crystals with $\{10\bar{1}0\}$ facets and 400 nm – 1 μm diameter at a thickness of 80 – 140 nm in *c*-direction [0001]; rough surface covered by Co-rich matrix residuals being partly amorphous and partly nano-crystalline ZnO; some crystals featured pores.
 - c) 45 min + 300°C calcination in air:
Well-pronounced hexagonal crystals with $\{10\bar{1}0\}$ facets; same size as in b), but with clean, straight and atomically flat surfaces; STEM-EDS mappings indicate chemical homogeneity and a low Co content <1 at%; single-crystallinity is verified by HR-TEM and NBED investigation of cross-sectioned hexagons → No inversion twinning.
- The TEM results revealed the necessity of an additional heat treatment to obtain clean and flat surfaces as required for an undisturbed tessellation of the hexagons.
- Synthesis of ZnO hexagons was successful, but the size variation is probably too large → Possible reason why tessellation was found to occur only in small patches.²⁰¹
- Cross sections of the rod-shaped nanotwins were investigated by TEM (60 min reaction time):
 - Twin boundaries are atomically well-bonded; no indications for interfacial films or dopant accumulations were observed.
 - NBED and ABF-STEM revealed exclusively tail-to-tail (O|O) inversion twinning; head-to-head (Zn|Zn) twins were not observed.
 - Perfect *c*-axis inversion, but interfaces are slightly curved, hence they do not correspond to ideal $(000\bar{1})|(000\bar{1})$ configurations.
- Rod-shaped nanotwins resemble the configuration of accurately oriented O|O bicrystals, with an irregular, disordered interface probably capable of incorporating large-ion dopants, e.g., Bi.
→ Potential for the synthesis of piezotronic/varistor-type nano-bicrystals.

6. Final Summary, Conclusive Remarks and Outlook

As detailed in the introduction (cf. pp. 18), piezotronic ZnO bicrystals hold a large potential for the development of novel devices for various applications. They are based on varistor-type ZnO bicrystals featuring doped {0001} inversion boundary configurations, as required to obtain both non-linear electrical characteristics as well as an optimum piezoelectric response. However, the straightforward synthesis approach of simply diffusion-bonding two single crystals with an intermediate dopant layer was found to be inadequate, since it implies highly coherent arrangements of flat interfaces inhibiting an effective doping. In varistor ceramics, the essential dopants are Bi or Pr, which are both large-ion elements insoluble in ZnO. This is the reason why increasing their concentration is ineffective, as long as suitable segregation sites are not provided. For coherent configurations, the interface conditions are similar to the ZnO bulk where Bi cannot be incorporated (cf. pp. 58). Incoherent arrangements, however, feature excess free volume sufficient for large ions. In good agreement with previous studies,¹⁴⁰ the TEM results of this work verified that structural incoherency is mandatory for the formation of Bi segregation sites at ZnO interfaces. Being naturally fulfilled in the case of polycrystalline varistor ceramics, where grains are arbitrarily oriented, these requirements were never found to be problematic nor were their importance for the resulting electrical properties fully noticed. However, coherent configurations, such as the (0001)-IB bicrystals, need appropriate synthesis procedures to meet these demands. The application of epitaxial solid-state transformation was found to be especially successful since the ideal coherent O|O configuration could be maintained macroscopically, while the interface itself featured a locally reduced coherency related to its strong curvature, strained state and continuous dislocation network (cf. pp. 70).^{101, 199} Furthermore, Bi incorporation and dislocation network are considered to mutually stabilize each other.²⁴² If deviations from the ideal O|O or Zn|Zn orientation are accepted, special tilt orientations can alternatively be applied to reduce the coherency of diffusion-bonded bicrystals, such as the investigated a|c or 26° configuration (cf. pp. 85). In doing so, a semi-coherent low-disorder interface was formed in sample DB-a|c, with semi-periodic Bi segregation sites at those interfacial Zn columns which are either CSLPs or feature a widened lattice plane distance. The 26° tilt set-up^a corresponds to a case of minimal coherency, which is reflected by a highly disordered interface structure of uniform width and a local Bi content of up to 25 %. These samples also encompass the three different types of segregation site formation observed in this work, which are a) *curvature in interplay with strain and dislocations*, b) *semi-coherent configurations (such as CSLs)* and c) *irregular disorder*. A graphical summary is provided in Figure 6-1.

^a Please note, a tilt of 29.1° was measured in the actual bicrystal sample DB-26. Nevertheless, regarding the grain-boundary structure and Bi segregation, the findings were as expected from the 26° tilt set-up (cf. pp. 80).

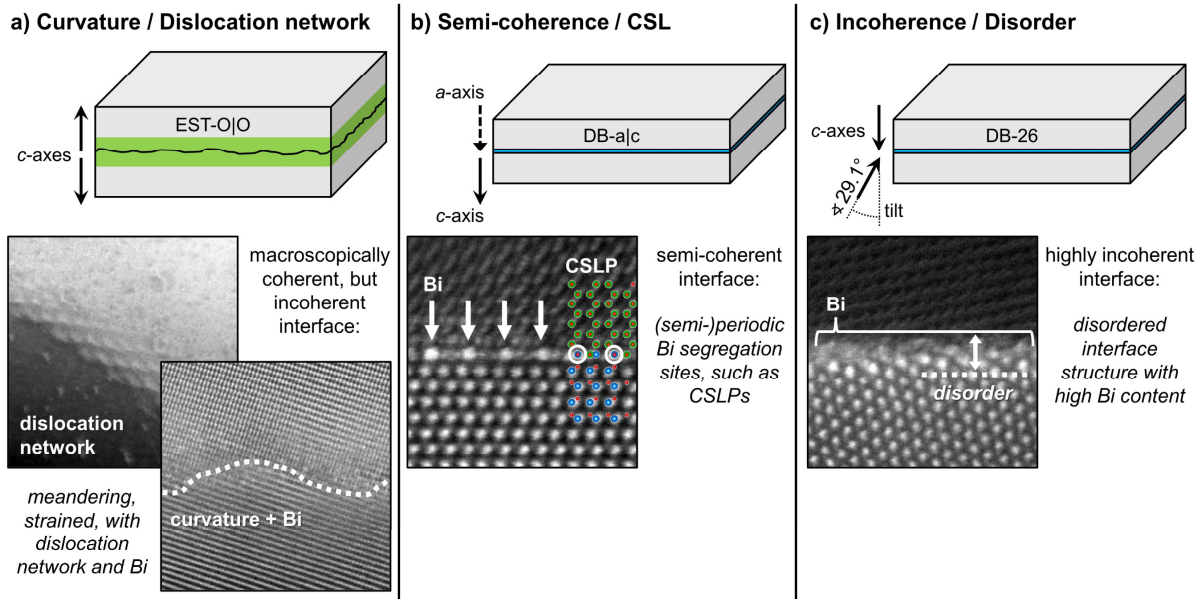


Figure 6-1: Graphical summary of the three structurally different types of Bi segregation site formation, as observed by TEM investigations of samples a) EST-O|O, b) DB-a|c and c) DB-26.

Whereas the main results of the TEM investigations concern the issues of Bi doping, there were also clear indications found that large dopant-layer thicknesses are disadvantageous for the diffusion-bonding process. While the bonding itself was unproblematic for the undoped samples and most samples with layer thicknesses ≤ 300 nm, the samples featuring 500 nm layers were mechanically rather unstable, i.e., they broke apart along the interface upon load-dependent measurements or TEM preparation. Furthermore, as recrystallization of thicker dopant layers is expected to require more annealing time than their thinner counterparts, it is more likely to obtain incomplete, i.e., still polycrystalline samples such as DB-III (cf. p. 63). However, increasing the annealing time also strongly increases the bulk diffusion and dilution of other important but soluble dopants, such as Co, whose concentration would then be lowered at the interface, which in turn can be detrimental to the electrical properties. Therefore, rather thin and highly doped layers are recommended in order to optimize the synthesis of DB-type bicrystals.

A further problematic feature of all bicrystals is the perfect cleavage along $\{10\bar{1}0\}$ planes and parting on $\{0001\}$ faces of ZnO. As large mechanical loads of about 250 MPa and more were required to significantly modify the potential barrier heights, multiple cracking and fracture were observed in nearly all samples.^a Against this background, applications of such bicrystalline devices appear challenging, as either an increased (mechanical) stability or a drastic reduction of the required force must be realized, especially if a load-induced switching between an on/off or a conductive/non-conductive state is desired. The stability issue might be addressed by synthesizing perfectly oriented, well-bonded and secondary-phase free interfaces and applying the force as uniformly and homogeneously as possible, i.e., without shear components and perfectly normal to both sides. However, as cleavage is an immanent property, improvements

^a 250 MPa = 25000 N/cm². This equals the pressure of 2.55 tons of weight applied on an area of 1 cm² or 25.5 kg on 1 mm².

via this approach are naturally limited. In consequence, a force reduction is required, which can be attained by optimizing the electrical properties via doping or voltage biasing. For example, in polycrystalline ZnO films or nanoparticles, doping with Mg/Cu or Eu, respectively, is reported to significantly increase d_{33} .^{254, 255, 256} In contrast, Co and Ni – being typical varistors dopants – were actually found to reduce the piezoelectric coefficients.^{255, 257} However, it is unclear to what extent these data are transferable to the case of ZnO single- or bicrystals. Additionally, further investigation should address the issue of Si contamination, which was frequently observed and might interfere with the effects of other dopants regarding the potential barrier formation. Anyhow, independent of doping effects, the barrier height can also be adjusted by the application of electric fields, which might allow bringing respective piezotronic devices via specific bias voltages into states being more sensitive to mechanical manipulation (cf. pp. 16).¹⁶⁵

The following criteria for the successful synthesis of piezotronic bicrystals represent the quintessence of the TEM-based results of this work:

1. Bi-segregation to the interface, i.e., the decoration of special segregation sites, is mandatory for the formation of varistor-type potential barriers and must be distinguished from a Bi-segregation forming inactive Bi-oxide phases instead.
2. The formation of the essential segregation sites implies semi- or incoherent interface configurations, being necessary to provide the excess free volume required for the incorporation of large-ion dopants such as Bi or Pr. This can be achieved either macroscopically via bicrystal tilt (DB) or microscopically (locally) via interface curvature (EST).
3. This type of segregation corresponds to a lowering of interfacial energy ($d\gamma < 0$) via interfacial excess of dopant atoms ($\Gamma_{sat} > 0$) according to Gibbs adsorption isotherm:

$$d\gamma = -\Gamma_{sat} \cdot d\mu$$

Presupposed that the dopant species is insoluble in the bulk and abundantly available (quasi-infinite reservoir), this segregation is determined exclusively by Γ_{sat} and $d\gamma$ without any interference with $d\mu$.

4. Thickness of sputtered dopant layers for DB-type bicrystals should be kept low (<100 nm) to facilitate bonding.
5. Bonding- and annealing time of DB-type bicrystals should be kept as low as possible to limit dopant depletion via bulk diffusion but nevertheless, needs to be adjusted to the dopant layer thickness to ensure a complete recrystallization.

In addition, it should be highlighted that the rod-shaped twins featured interfaces with a certain degree of disorder and irregularity, which implies a certain degree of incoherence. Considering these similarities to the EST bicrystal, it might be possible that they incorporate Bi or other large-ion dopants at the twin boundary. Thus, the development of a respective, specifically

tailored precipitation process might be worthwhile, in particular, as such doped twins hold potential for the synthesis of piezotronic or varistor-type nano-bicrystals.

Finally, it should be noted that both the structural as well as thermodynamic considerations regarding the segregation of large, insoluble dopants, as observed in the investigated bicrystals, rely exclusively on basic principles and hence, are considered to be perfectly transferable to other material systems. This also applies to the determination of silicon's "true" solid-solubility in ZnO, using the CEP method, which is in principle applicable to arbitrary material systems, where a certain solute species with a low to zero solubility is abundantly present at a straight interface.

7. References

1. J. A. Hedvall, "Über Rinmans Grün," *Zeitschrift für anorganische Chemie*, 86[1] 201-24 (1914).
2. J. A. Hedvall, "Studien über Rinmansgrün," *Chemisches Zentralblatt*, 2[15] 1273-74 (1913).
3. P. Walden, "Chronologische Übersichtstabellen: Zur Geschichte der Chemie von den Ältesten Zeiten bis zur Gegenwart." Springer-Verlag: Berlin, Göttingen, Heidelberg, (1952).
4. J. H. Hwang, T. O. Mason, and V. P. Dravid, "Microanalytical Determination of ZnO Solidus and Liquidus Boundaries in the ZnO-Bi₂O₃ System," *J Am Ceram Soc*, 77[6] 1499-504 (1994).
5. J. P. Guha, S. Kune, and D. Suvorov, "Phase equilibrium relations in the binary system Bi₂O₃-ZnO," *J Mater Sci*, 39[3] 911-18 (2004).
6. H. Karzel, W. Potzel, M. Köfferlein, W. Schiessl, M. Steiner, U. Hiller, G. M. Kalvius, D. W. Mitchell, T. P. Das, P. Blaha, K. Schwarz, and M. P. Pasternak, "Lattice dynamics and hyperfine interactions in ZnO and ZnSe at high external pressures," *Phys Rev B*, 53[17] 11425-38 (1996).
7. "Zincite (Zn,Mn²⁺)O." in Handbook of mineralogy. Edited by J. W. Anthony, R. A. Bideaux, K. W. Bladh, and M. C. Nichols. Mineralogical society of America: Chantilly, VA, USA, 2001.
8. R. M. Lavinsky, "<https://upload.wikimedia.org/wikipedia/commons/5/56/Zincite-21552.jpg>." Rob Lavinsky, – CC-BY-SA-3.0, CC BY-SA 3.0 <<https://creativecommons.org/licenses/by-sa/3.0/>>, Wikimedia Commons, 2010.
9. R. M. Lavinsky, "<https://upload.wikimedia.org/wikipedia/commons/a/a4/Zincite-rare08-20a.jpg>." Rob Lavinsky, – CC-BY-SA-3.0, CC BY-SA 3.0 <<https://creativecommons.org/licenses/by-sa/3.0/>>, Wikimedia Commons, 2010.
10. W. L. Bragg and J. A. Darbyshire, "The structure of thin films of certain metallic oxides," *Transactions of the Faraday Society*, 28 522-29 (1932).
11. C. H. Bates, R. Roy, and W. B. White, "New High-Pressure Polymorph of Zinc Oxide," *Science*, 137[3534] 993 (1962).
12. T. Kogure and Y. Bando, "Formation of ZnO nanocrystallites on ZnS surfaces by electron beam irradiation," *J Electron Microsc*, 47[2] 135-41 (1998).
13. A. B. M. A. Ashrafi, A. Ueta, A. Avramescu, H. Kumano, I. Suemune, Y. W. Ok, and T. Y. Seong, "Growth and characterization of hypothetical zinc-blende ZnO films on GaAs(001) substrates with ZnS buffer layers," *Appl Phys Lett*, 76[5] 550-52 (2000).
14. S. K. Kim, S. Y. Jeong, and C. R. Cho, "Structural reconstruction of hexagonal to cubic ZnO films on Pt/Ti/SiO₂/Si substrate by annealing," *Appl Phys Lett*, 82[4] 562-64 (2003).
15. Ü. Özgür, Y. I. Alivov, C. Liu, A. Teke, M. A. Reshchikov, S. Dogan, V. Avrutin, S. J. Cho, and H. Morkoc, "A comprehensive review of ZnO materials and devices," *J Appl Phys*, 98[4] 041301 (2005).
16. T. Hidaka, "Paulings Ionicity and Phillips Ionicity," *J Phys Soc Jpn*, 44[4] 1204-07 (1978).
17. H. Morkoç and Ü. Özgür, "General Properties of ZnO." in Zinc Oxide: Fundamentals, Materials and Device Technology. John Wiley & Sons, Hoboken, NJ, USA, 2008.

18. E. H. Kisi and M. M. Elcombe, "*u*-Parameters for the Wurtzite Structure of ZnS and ZnO Using Powder Neutron Diffraction," *Acta Crystallogr C*, 45 1867-70 (1989).
19. M. Catti, Y. Noel, and R. Dovesi, "Full piezoelectric tensors of wurtzite and zinc blende ZnO and ZnS by first-principles calculations," *Journal of Physics and Chemistry of Solids*, 64[11] 2183-90 (2003).
20. Y. Noel, C. M. Zicovich-Wilson, B. Civalleri, P. D'Arco, and R. Dovesi, "Polarization properties of ZnO and BeO: An *ab initio* study through the Berry phase and Wannier functions approaches," *Phys Rev B*, 65[1] 014111 (2002).
21. J. E. Jaffe and A. C. Hess, "Hartree-Fock Study of phase changes in ZnO at high pressure," *Phys Rev B*, 48[11] 7903-09 (1993).
22. K. Momma and F. Izumi, "VESTA 3 for three-dimensional visualization of crystal, volumetric and morphology data," *J Appl Crystallogr*, 44 1272-76 (2011).
23. O. Dulub, U. Diebold, and G. Kresse, "Novel Stabilization Mechanism on Polar Surfaces: ZnO(0001)-Zn," *Phys Rev Lett*, 90[1] 016102 (2003).
24. G. Kresse, O. Dulub, and U. Diebold, "Competing stabilization mechanism for the polar ZnO(0001)-Zn surface," *Phys Rev B*, 68[24] 245409 (2003).
25. S. T. King, S. S. Parihar, K. Pradhan, H. T. Johnson-Steigleman, and P. F. Lyman, "Observation of a ($\sqrt{3} \times \sqrt{3}$)R30° degrees reconstruction on O-polar ZnO surfaces," *Surf Sci*, 602[22] L131-L34 (2008).
26. J. H. Lai, S. H. Su, H. H. Chen, J. C. A. Huang, and C. L. Wu, "Stabilization of ZnO polar plane with charged surface nanodefects," *Phys Rev B*, 82[15] 155406 (2010).
27. A. Waag, "Growth," pp. 39-76. in *Zinc Oxide: From Fundamental Properties Towards Novel Applications*. Springer, Berlin, Heidelberg, 2010.
28. W. J. Li, E. W. Shi, W. Z. Zhong, and Z. W. Yin, "Growth mechanism and growth habit of oxide crystals," *J Cryst Growth*, 203[1-2] 186-96 (1999).
29. H. Iwanaga, N. Shibata, O. Nittono, and M. Kasuga, "Crystal growth in *c* direction and crystallographic polarity in ZnO crystals," *J Cryst Growth*, 45[1] 228-32 (1978).
30. W. Jo, S. J. Kim, and D. Y. Kim, "Analysis of the etching behavior of ZnO ceramics," *Acta Mater*, 53[15] 4185-88 (2005).
31. A. N. Mariano and R. E. Hanneman, "Crystallographic Polarity of ZnO Crystals," *J Appl Phys*, 34[2] 384-8 (1963).
32. W. Kleber, H.-J. Bausch, and J. Bohm, "Einführung in die Kristallographie," 19 ed. Edited by J. Bohm and D. Klimm. Oldenbourg Wissenschaftsverlag: München, (2010).
33. J.-F. Li, "Fundamentals of Piezoelectricity," pp. 1-18. in *Lead-Free Piezoelectric Materials*. Edited by J.-F. Li. Wiley-VCH, Weinheim, 2021.
34. J. Geurts, "Crystal Structure, Chemical Binding, and Lattice Properties," pp. 7-37. in *Zinc Oxide: From Fundamental Properties Towards Novel Applications*. Edited by K. Ellmer, A. Klein, and B. Rech. Springer, Berlin, Heidelberg, 2010.
35. F. Bernardini, V. Fiorentini, and D. Vanderbilt, "Spontaneous polarization and piezoelectric constants of III-V nitrides," *Phys Rev B*, 56[16] 10024-27 (1997).
36. S. Massidda, R. Resta, M. Posternak, and A. Baldereschi, "Polarization and dynamical charge of ZnO within different one-particle schemes," *Phys Rev B*, 52[24] 16977-80 (1995).

-
37. H. Jaffe and D. A. Berlincourt, "Piezoelectric Transducer Materials," *Proceedings of the IEEE*, 53[10] 1372-86 (1965).
 38. A. R. Hutson, "Piezoelectricity and Conductivity in ZnO and CdS," *Phys Rev Lett*, 4[10] 505-07 (1960).
 39. D. F. Crisler, J. J. Cupal, and A. R. Moore, "Dielectric, Piezoelectric, and Electromechanical Coupling Constants of Zinc Oxide Crystals," *Proceedings of the IEEE*, 56[2] 225-26 (1968).
 40. I. B. Kobiakov, "Elastic, Piezoelectric and Dielectric Properties of ZnO and CdS Single Crystals in a Wide Range of Temperatures," *Solid State Commun*, 35[3] 305-10 (1980).
 41. V. Srikant and D. R. Clarke, "On the optical band gap of zinc oxide," *J Appl Phys*, 83[10] 5447-51 (1998).
 42. D. C. Reynolds, D. C. Look, B. Jogai, C. W. Litton, G. Cantwell, and W. C. Harsch, "Valence-band ordering in ZnO," *Phys Rev B*, 60[4] 2340-44 (1999).
 43. D. C. Look, J. W. Hemsky, and J. R. Sizelove, "Residual Native Shallow Donor in ZnO," *Phys Rev Lett*, 82[12] 2552-55 (1999).
 44. G. Heiland, E. Mollwo, and F. Stöckmann, "Electronic Processes in Zinc Oxide," pp. 191-323. in *Solid State Physics*. Edited by F. Seitz and D. Turnbull. Academic Press: London, Oxford, Boston, New York, San Diego, 1959.
 45. F. A. Kröger, "The chemistry of imperfect crystals." North-Holland Publishing Company: Amsterdam, Netherlands, (1974).
 46. A. Waag, "Electrical Conductivity and Doping," pp. 95-119. in *Zinc Oxide: From Fundamental Properties Towards Novel Applications*. Springer, Berlin, Heidelberg, 2010.
 47. S. B. Zhang, S. H. Wei, and A. Zunger, "Intrinsic *n*-type versus *p*-type doping asymmetry and the defect physics of ZnO," *Phys Rev B*, 63[7] 075205 (2001).
 48. A. Janotti and C. G. Van de Walle, "Native point defects in ZnO," *Phys Rev B*, 76[16] 165202 (2007).
 49. A. Janotti and C. G. Van de Walle, "New insights into the role of native point defects in ZnO," *J Cryst Growth*, 287[1] 58-65 (2006).
 50. A. Janotti and C. G. Van de Walle, "Fundamentals of zinc oxide as a semiconductor," *Reports on Progress in Physics*, 72[12] 126501 (2009).
 51. J. L. Lyons, A. Janotti, and C. G. Van de Walle, "Role of Si and Ge as impurities in ZnO," *Phys Rev B*, 80[20] 205113 (2009).
 52. C. G. Van de Walle, "Hydrogen as a Cause of Doping in Zinc Oxide," *Phys Rev Lett*, 85[5] 1012-15 (2000).
 53. M. H. Du and K. Biswas, "Anionic and Hidden Hydrogen in ZnO," *Phys Rev Lett*, 106[11] 115502 (2011).
 54. D. G. Thomas and J. J. Lander, "Hydrogen as a Donor in Zinc Oxide," *J Chem Phys*, 25[6] 1136-42 (1956).
 55. G. A. Shi, M. Saboktakin, M. Stavola, and S. J. Pearton, "'Hidden hydrogen' in as-grown ZnO," *Appl Phys Lett*, 85[23] 5601-03 (2004).

-
56. E. V. Lavrov, F. Herklotz, and J. Weber, "Identification of Hydrogen Molecules in ZnO," *Phys Rev Lett*, 102[18] 185502 (2009).
57. S. G. Koch, E. V. Lavrov, and J. Weber, "Interplay between interstitial and substitutional hydrogen donors in ZnO," *Phys Rev B*, 89[23] 235203 (2014).
58. Y. S. Kim and C. H. Park, "Rich Variety of Defects in ZnO via an Attractive Interaction between O Vacancies and Zn Interstitials: Origin of *n*-Type Doping," *Phys Rev Lett*, 102[8] 086403 (2009).
59. G. A. Shi, M. Stavola, S. J. Pearton, M. Thieme, E. V. Lavrov, and J. Weber, "Hydrogen local modes and shallow donors in ZnO," *Phys Rev B*, 72[19] 195211 (2005).
60. K. Ellmer and A. Klein, "ZnO and Its Applications," pp. 1-33. in *Transparent Conductive Zinc Oxide: Basics and Applications in Thin Film Solar Cells*. Edited by K. Ellmer, A. Klein, and B. Rech. Springer, Berlin, Heidelberg, 2008.
61. N. H. Nickel and E. Terukov, "Zinc Oxide - A Material for Micro- and Optoelectronic Applications." Springer: Dordrecht, Netherlands, (2005).
62. C. F. Klingshirn, A. Waag, A. Hoffmann, and J. Geurts, "Zinc Oxide: From Fundamental Properties Towards Novel Applications." Springer: Berlin, Heidelberg, (2010).
63. Z. L. Wang, "Towards Self-Powered Nanosystems: From Nanogenerators to Nanopiezotronics," *Adv Funct Mater*, 18[22] 3553-67 (2008).
64. M. D. McCluskey and S. J. Jokela, "Defects in ZnO," *J Appl Phys*, 106[7] 071101 (2009).
65. Y. L. Wang, H. S. Kim, D. P. Norton, S. J. Pearton, and F. Ren, "Dielectric passivation effects on ZnO light emitting diodes," *Appl Phys Lett*, 92[11] 112101 (2008).
66. E. Müller, D. Livinov, D. Gerthsen, C. Kirchner, A. Waag, N. Oleynik, A. Dadgar, and A. Krost, "Properties of Dislocations in Epitaxial ZnO Layers Analyzed by Transmission Electron Microscopy," pp. 99-111. in *Zinc Oxide — A Material for Micro- and Optoelectronic Applications*. Edited by N. H. Nickel and E. Terukov. Springer: Dordrecht, Netherlands, (2005).
67. O. Schmidt, P. Kiesel, C. G. Van de Walle, N. M. Johnson, J. Nause, and G. H. Döhler, "Effects of an Electrically Conducting Layer at the Zinc Oxide Surface," *Japanese Journal of Applied Physics Part 1-Regular Papers Brief Communications & Review Papers*, 44[10] 7271-74 (2005).
68. O. Schmidt, A. Geis, P. Kiesel, C. G. Van de Walle, N. M. Johnson, A. Bakin, A. Waag, and G. H. Döhler, "Analysis of a conducting channel at the native zinc oxide surface," *Superlattice Microst*, 39[1-4] 8-16 (2006).
69. D. C. Look, "Quantitative analysis of surface donors in ZnO," *Surf Sci*, 601[23] 5315-19 (2007).
70. S. J. Jokela and M. D. McCluskey, "Unambiguous identification of nitrogen-hydrogen complexes in ZnO," *Phys Rev B*, 76[19] 193201 (2007).
71. A. Kobayashi, O. F. Sankey, and J. D. Dow, "Deep energy levels of defects in the wurtzite semiconductors AlN, CdS, CdSe, ZnS, and ZnO," *Phys Rev B*, 28[2] 946-56 (1983).
72. C. H. Park, S. B. Zhang, and S. H. Wei, "Origin of *p*-type doping difficulty in ZnO: The impurity perspective," *Phys Rev B*, 66[7] 073202 (2002).
73. E. V. Kalinina, A. E. Cherenkov, G. A. Onushkin, Y. I. Alivov, D. C. Look, B. M. Ataev, A. K. Omaev, and C. M. Chukichev, "ZnO/AlGaIn Ultraviolet Light Emitting Diodes," pp.

-
- 211-16. in Zinc Oxide — A Material for Micro- and Optoelectronic Applications. Edited by N. H. Nickel and E. Terukov. Springer: Dordrecht, Netherlands, (2005).
74. S. Mohammadi and M. Zavvari, "High performance *n*-ZnO/*p*-metal-oxides UV detector grown in low-temperature aqueous solution bath," *Thin Solid Films*, 626 173-77 (2017).
75. H. S. Kim, F. Lugo, S. J. Pearton, D. P. Norton, and F. Ren, "Dependence of Zn_{1-x}Mg_xO : P film properties on magnesium concentration," *J Vac Sci Technol B*, 26[3] 968-72 (2008).
76. K. S. Ahn, T. Deutsch, Y. Yan, C. S. Jiang, C. L. Perkins, J. Turner, and M. Al-Jassim, "Synthesis of band-gap-reduced *p*-type ZnO films by Cu incorporation," *J Appl Phys*, 102[2] 023517 (2007).
77. S. Limpijumnong, X. N. Li, S. H. Wei, and S. B. Zhang, "Substitutional diatomic molecules NO, NC, CO, N₂, and O₂: Their vibrational frequencies and effects on *p* doping of ZnO," *Appl Phys Lett*, 86[21] 211910 (2005).
78. E. C. Lee, Y. S. Kim, Y. G. Jin, and K. J. Chang, "Compensation mechanism for N acceptors in ZnO," *Phys Rev B*, 64[8] 085120 (2001).
79. K. Iwata, P. Fons, A. Yamada, K. Matsubara, and S. Niki, "Nitrogen-induced defects in ZnO : N grown on sapphire substrate by gas source MBE," *J Cryst Growth*, 209[2-3] 526-31 (2000).
80. M. M. Su, T. L. Zhang, J. Su, Z. Wang, Y. M. Hu, Y. H. Gao, H. S. Gu, and X. H. Zhang, "Homogeneous ZnO nanowire arrays *p*-*n* junction for blue light-emitting diode applications," *Opt Express*, 27[16] A1207-A15 (2019).
81. M. S. Oh, S. H. Kim, and T. Y. Seong, "Growth of nominally undoped *p*-type ZnO on Si by pulsed-laser deposition," *Appl Phys Lett*, 87[12] 122103 (2005).
82. H. Shen, C. X. Shan, Q. Qiao, J. S. Liu, B. H. Li, and D. Z. Shen, "Stable surface plasmon enhanced ZnO homojunction light-emitting devices," *J Mater Chem C*, 1[2] 234-37 (2013).
83. Y. H. Leung, Z. B. He, L. B. Luo, C. H. A. Tsang, N. B. Wong, W. J. Zhang, and S. T. Lee, "ZnO nanowires array *p*-*n* homojunction and its application as a visible-blind ultraviolet photodetector," *Appl Phys Lett*, 96[5] 053102 (2010).
84. S. B. Wang, C. Y. Huang, L. Pan, Y. Chen, X. W. Zhang, Fazal-e-Aleem, and J. J. Zou, "Controllable fabrication of homogeneous ZnO *p*-*n* junction with enhanced charge separation for efficient photocatalysis," *Catal Today*, 335 151-59 (2019).
85. L. Pan, S. B. Wang, W. B. Mi, J. J. Song, J. J. Zou, L. Wang, and X. W. Zhang, "Undoped ZnO abundant with metal vacancies," *Nano Energy*, 9 71-79 (2014).
86. B. D. Boruah, S. N. Majji, S. Nandi, and A. Misra, "Doping controlled pyro-phototronic effect in self-powered zinc oxide photodetector for enhancement of photoresponse," *Nanoscale*, 10[7] 3451-59 (2018).
87. Y. Zhang, C. H. Liu, J. B. Liu, J. Xiong, J. Y. Liu, K. Zhang, Y. D. Liu, M. Z. Peng, A. F. Yu, A. H. Zhang, Y. Zhang, Z. W. Wang, J. Y. Zhai, and Z. L. Wang, "Lattice Strain Induced Remarkable Enhancement in Piezoelectric Performance of ZnO-Based Flexible Nanogenerators," *Acs Appl Mater Inter*, 8[2] 1381-87 (2016).
88. E. Fortunato, L. Raniero, L. Silva, A. Goncalves, A. Pimentel, P. Barquinha, H. Aguas, L. Pereira, G. Goncalves, I. Ferreira, E. Elangovan, and R. Martins, "Highly stable

transparent and conducting gallium-doped zinc oxide thin films for photovoltaic applications," *Sol Energ Mat Sol C*, 92[12] 1605-10 (2008).

89. Y. R. Park, J. Kim, and Y. S. Kim, "Effect of hydrogen doping in ZnO thin films by pulsed DC magnetron sputtering," *Appl Surf Sci*, 255[22] 9010-14 (2009).
90. D. R. Clarke, "Varistor Ceramics," *J Am Ceram Soc*, 82[3] 485-502 (1999).
91. L. O. Grondahl and P. H. Geiger, "A New Electronic Rectifier," *Journal of the A.I.E.E.*, 46[3] 215-22 (1927).
92. C. Frosch, "Improved silicon carbide varistors," *Bell Lab Rec*, 32 336 (1954).
93. H. Dienel, "Silicon carbide varistors: properties and construction," *Bell Lab. Rec*, 34 407 (1956).
94. M. Matsuoka, "Nonohmic Properties of Zinc Oxide Ceramics," *Jpn J Appl Phys*, 10[6] 736-46 (1971).
95. J. He, "Introduction of Varistor Ceramics," pp. 1-30. in *Metal Oxide Varistors*. Edited by J. He. Wiley-VCH, Weinheim, 2019.
96. J. He, "Conduction Mechanisms of ZnO Varistors," pp. 31-65. in *Metal Oxide Varistors*. Edited by J. He. Wiley-VCH, Weinheim, 2019.
97. P. N. Butcher, N. H. March, and M. P. Tosi, "Crystalline Semiconducting Materials and Devices." Springer Science & Business Media: New York, (1986).
98. F. Thuselet, "Metall-Halbleiter-Kontakte und Feldeffekt-Transistoren," pp. 255-305. in *Physik der Halbleiterbauelemente: Einführendes Lehrbuch für Ingenieure und Physiker*. Edited by F. Thuselet. Springer, Berlin, Heidelberg, 2005.
99. W. Schottky, "Halbleitertheorie der Sperrschicht," *Naturwissenschaften*, 26[52] 843-43 (1938).
100. N. F. Mott, "The theory of crystal rectifiers," *Proceedings of the Royal Society of London. Series A. Mathematical and Physical Sciences*, 171[944] 27-38 (1939).
101. P. Keil, "Mechanically tuned conductivity in piezoelectric semiconductors," Ph.D. thesis. Institute of Material Science, Technische Universität Darmstadt, Darmstadt, (2019).
102. M. Reisch, "Kontakte," pp. 47-112. in *Halbleiter-Bauelemente*. Edited by M. Reisch. Springer, Berlin, Heidelberg, 2007.
103. C. Funck and S. Menzel, "An atomistic view on the Schottky barrier lowering applied to SrTiO₃/Pt contacts," *Aip Adv*, 9[4] (2019).
104. J. Bardeen, "Surface States and Rectification at a Metal Semi-Conductor Contact," *Phys Rev*, 71[10] 717-27 (1947).
105. R. T. Tung, "Formation of an electric dipole at metal-semiconductor interfaces," *Phys Rev B*, 64[20] (2001).
106. R. T. Tung, "Recent advances in Schottky barrier concepts," *Mat Sci Eng R*, 35[1-3] 1-138 (2001).
107. G. E. Pike and C. H. Seager, "The dc voltage dependence of semiconductor grain-boundary resistance," *J Appl Phys*, 50[5] 3414-22 (1979).
108. G. E. Pike, "Semiconducting Polycrystalline Ceramics," pp. 731-53. in *Material Science and Technology*. Edited by M. V. Swain. VCH, Weinheim, Germany, 1994.

-
109. G. Blatter and F. Greuter, "Carrier transport through grain boundaries in semiconductors," *Phys Rev B*, 33[6] 3952-66 (1986).
 110. F. Greuter and G. Blatter, "Electrical properties of grain boundaries in polycrystalline compound semiconductors," *Semicond Sci Tech*, 5[2] 111-37 (1990).
 111. S. S. Li, "Metal–Semiconductor Contacts," pp. 284-333. in *Semiconductor Physical Electronics*. Edited by S. S. Li. Springer, New York, NY, 2006.
 112. G. Blatter and F. Greuter, "Electrical breakdown at semiconductor grain boundaries," *Phys Rev B*, 34[12] 8555-72 (1986).
 113. J. He, "Praseodymium/Vanadium/Barium-Based ZnO Varistor Systems," pp. 281-305. in *Metal Oxide Varistors*. Edited by J. He. Wiley-VCH, Weinheim, 2019.
 114. T. D. Chen, J. R. Lee, H. L. Tuller, and Y. M. Chiang, "Grain boundary dopant and heat treatment effects on the electrical properties of polycrystalline ZnO," *Mater Res Soc Symp P*, 411 295-300 (1996).
 115. F. Greuter, G. Blatter, M. Rossinelli, and F. Schmückle, "Bulk and grain boundary defects in polycrystalline ZnO," *Mater Sci Forum*, 10-12 235-40 (1986).
 116. J. C. Simpson and J. F. Cordaro, "Defect clusters in zinc oxide," *J Appl Phys*, 67[11] 6760-63 (1990).
 117. A. Rohatgi, S. K. Pang, T. K. Gupta, and W. D. Straub, "The deep level transient spectroscopy studies of a ZnO varistor as a function of annealing," *J Appl Phys*, 63[11] 5375-79 (1988).
 118. J. P. Gambino, W. D. Kingery, G. E. Pike, H. R. Philipp, and L. M. Levinson, "Grain boundary electronic states in some simple ZnO varistors," *J Appl Phys*, 61[7] 2571-74 (1987).
 119. K. Tsuda and K. Mukae, "Interface States of Zinc Oxide Varistors," *High Tech Ceramics. (Part B)* 1781-90 (1986).
 120. J. M. Carlsson, H. S. Domingos, P. D. Bristowe, and B. Hellsing, "An Interfacial Complex in ZnO and Its Influence on Charge Transport," *Phys Rev Lett*, 91[16] (2003).
 121. Y. Sato, J. P. Buban, T. Mizoguchi, N. Shibata, M. Yodogawa, T. Yamamoto, and Y. Ikuhara, "Role of Pr Segregation in Acceptor-State Formation at ZnO Grain Boundaries," *Phys Rev Lett*, 97[10] 106802 (2006).
 122. F. Oba, T. Yamamoto, Y. Ikuhara, I. Tanaka, and H. Adachi, "First-Principles Calculations of Co Impurities and Native Defects in ZnO," *Mater Trans*, 43[7] 1439-43 (2002).
 123. J. He, "Tuning Electrical Characteristics of ZnO Varistors," pp. 67-124. in *Metal Oxide Varistors*. Edited by J. He. Wiley-VCH, Weinheim, 2019.
 124. F. A. Selim, T. K. Gupta, P. L. Hower, and W. G. Carlson, "Low voltage ZnO varistor - Device process and defect model," *J Appl Phys*, 51[1] 765-68 (1980).
 125. R. Einzinger, "Metal oxide varistor action - a homojunction breakdown mechanism," *Appl Surf Sci*, 1[3] 329-40 (1978).
 126. F. Stucki and F. Greuter, "Key role of oxygen at zinc oxide varistor grain boundaries," *Appl Phys Lett*, 57[5] 446-48 (1990).
 127. E. Sonder, M. M. Austin, and D. L. Kinser, "Effect of oxidizing and reducing atmospheres at elevated temperatures on the electrical properties of zinc oxide varistors," *J Appl Phys*, 54[6] 3566-72 (1983).

-
128. P. R. Bueno, E. R. Leite, M. M. Oliveira, M. O. Orlandi, and E. Longo, "Role of oxygen at the grain boundary of metal oxide varistors: A potential barrier formation mechanism," *Appl Phys Lett*, 79[1] 48-50 (2001).
 129. Y. M. Chiang, H. Wang, and J. R. Lee, "HREM and STEM of intergranular films at zinc oxide varistor grain boundaries," *J Microsc-Oxford*, 191 275-85 (1998).
 130. D. R. Clarke, "Grain-boundary segregation in a commercial ZnO-based varistor," *J Appl Phys*, 50[11] 6829-32 (1979).
 131. W. D. Kingery, J. B. V. Sande, and T. Mitamura, "A Scanning Transmission Electron Microscopy Investigation of Grain-Boundary Segregation in a ZnO-Bi₂O₃ Varistor," *J Am Ceram Soc*, 62[3-4] 221-22 (1979).
 132. J. Wong, "Sintering and varistor characteristics of ZnO-Bi₂O₃ ceramics," *J Appl Phys*, 51[8] 4453-59 (1980).
 133. M. Elfving, R. Österlund, and E. Olsson, "Differences in Wetting Characteristics of Bi₂O₃ Polymorphs in ZnO Varistor Materials," *J Am Ceram Soc*, 83[9] 2311-14 (2000).
 134. H. F. Wang and Y. M. Chiang, "Thermodynamic Stability of Intergranular Amorphous Films in Bismuth-Doped Zinc Oxide," *J Am Ceram Soc*, 81[1] 89-96 (1998).
 135. W. Onreabroy, N. Sirikulrat, A. P. Brown, C. Hammond, and S. J. Milne, "Properties and intergranular phase analysis of a ZnO-CoO-Bi₂O₃ varistor," *Solid State Ionics*, 177[3-4] 411-20 (2006).
 136. D. R. Clarke, "Microstructural location of intergranular metal-oxide phase in a zinc oxide varistor," *J Appl Phys*, 49[4] 2407-11 (1978).
 137. P. Williams, O. L. Krivanek, G. Thomas, and M. Yodogawa, "Microstructure-property relationships of rare-earth zinc-oxide varistors," *J Appl Phys*, 51[7] 3930-34 (1980).
 138. Y. Sato, T. Mizoguchi, F. Oba, M. Yodogawa, T. Yamamoto, and Y. Ikuhara, "Identification of native defects around grain boundary in Pr-doped ZnO bicrystal using electron energy loss spectroscopy and first-principles calculations," *Appl Phys Lett*, 84[26] 5311-13 (2004).
 139. Y. Sato, F. Oba, M. Yodogawa, T. Yamamoto, and Y. Ikuhara, "Grain boundary dependency of nonlinear current-voltage characteristics in Pr and Co doped ZnO bicrystals," *J Appl Phys*, 95[3] 1258-64 (2004).
 140. Y. Sato, T. Yamamoto, and Y. Ikuhara, "Atomic Structures and Electrical Properties of ZnO Grain Boundaries," *J Am Ceram Soc*, 90[2] 337-57 (2007).
 141. T. Takemura, M. Kobayashi, Y. Takada, and K. Sato, "Effects of Bismuth Sesquioxide on the Characteristics of ZnO Varistors," *J Am Ceram Soc*, 69[5] 430-36 (1986).
 142. E. Olsson and G. L. Dunlop, "The effect of Bi₂O₃ content on the microstructure and electrical properties of ZnO varistor materials," *J Appl Phys*, 66[9] 4317-24 (1989).
 143. K. Eda, "Electrical Properties of ZnO-Bi₂O₃ Metal Oxide Heterojunction — A Clue of a Role of Intergranular Layers in ZnO Varistors," *MRS Proceedings*, 5 381-92 (1981).
 144. J. Y. Li, S. T. Li, P. F. Cheng, and M. A. Alim, "Advances in ZnO-Bi₂O₃ based varistors," *J Mater Sci-Mater El*, 26[7] 4782-809 (2015).
 145. L. M. Levinson, H. R. Philipp, and G. D. Mahan, "Evidence for parallel conduction paths in ZnO varistors," pp. 145-54. in *Ceramics Transactions, Advances in Varistor*

Technology. Edited by L. M. Levinson. The American Ceramic Society: Westerville, OH, 1989.

146. L. M. Levinson and H. R. Philipp, "Zinc Oxide Varistors - A Review," *Am. Ceram. Soc. Bull.*, 65[4] 639 (1986).
147. R. Einzinger, "Grain junction properties of ZnO varistors," *Appl Surf Sc*, 3[3] 390-408 (1979).
148. J. Hu, J. L. He, W. C. Long, and J. Liu, "Temperature Dependences of Leakage Currents of ZnO Varistors Doped with Rare-Earth Oxides," *J Am Ceram Soc*, 93[8] 2155-57 (2010).
149. J. L. He, R. Zeng, Q. H. Chen, S. M. Chen, Z. C. Guan, S. W. Han, and H. G. Cho, "Nonuniformity of Electrical Characteristics in Microstructures of ZnO Surge Varistors," *Ieee T Power Deliver*, 19[1] 138-44 (2004).
150. J. Han, P. Q. Mantas, and A. M. R. Senos, "Grain growth in Mn-doped ZnO," *J Eur Ceram Soc*, 20[16] 2753-58 (2000).
151. T. Senda and R. C. Bradt, "Grain Growth of Zinc Oxide during the Sintering of Zinc Oxide-Antimony Oxide Ceramics," *J Am Ceram Soc*, 74[6] 1296-302 (1991).
152. M. Lei, S. Li, J. Li, and M. A. Alim, "The role of CeO₂ in the high electric field ZnO varistors," *J Appl Sci*, 6[8] 1671-78 (2006).
153. C. C. Zhang, Y. X. Hu, W. Z. Lu, M. H. Cao, and D. X. Zhou, "Influence of TiO₂/Sb₂O₃ ratio on ZnO varistor ceramics," *J Eur Ceram Soc*, 22[1] 61-65 (2002).
154. Z. L. Wang, "Nanopiezotronics," *Adv Mater*, 19[6] 889-92 (2007).
155. X. D. Wang, J. Zhou, J. H. Song, J. Liu, N. S. Xu, and Z. L. Wang, "Piezoelectric Field Effect Transistor and Nanoforce Sensor Based on a Single ZnO Nanowire," *Nano Lett*, 6[12] 2768-72 (2006).
156. Z. L. Wang, "From nanogenerators to piezotronics-A decade-long study of ZnO nanostructures," *Mrs Bull*, 37[9] 814-27 (2012).
157. Z. L. Wang and W. Z. Wu, "Piezotronics and piezo-phototronics: fundamentals and applications," *Natl Sci Rev*, 1[1] 62-90 (2014).
158. Z. L. Wang, X. Y. Kong, Y. Ding, P. X. Gao, W. L. Hughes, R. S. Yang, and Y. Zhang, "Semiconducting and Piezoelectric Oxide Nanostructures Induced by Polar Surfaces," *Adv Funct Mater*, 14[10] 943-56 (2004).
159. Z. L. Wang, "Nanostructures of zinc oxide," *Mater Today*, 7[6] 26-33 (2004).
160. W. Z. Wu, Y. G. Wei, and Z. L. Wang, "Strain-Gated Piezotronic Logic Nanodevices," *Adv Mater*, 22[42] 4711-5 (2010).
161. Y. Zhang, Y. Liu, and Z. L. Wang, "Fundamental Theory of Piezotronics," *Adv Mater*, 23[27] 3004-13 (2011).
162. L. Pintilie and M. Alexe, "Metal-ferroelectric-metal heterostructures with Schottky contacts. I. Influence of the ferroelectric properties," *J Appl Phys*, 98[12] 124103 (2005).
163. P. M. Verghese and D. R. Clarke, "Piezoelectric contributions to the electrical behavior of ZnO varistors," *J Appl Phys*, 87[9] 4430-38 (2000).

-
164. N. Raidl, P. Supancic, R. Danzer, and M. Hofstätter, "Piezotronically Modified Double Schottky Barriers in ZnO Varistors," *Adv Mater*, 27[12] 2031-35 (2015).
165. R. Baraki, N. Novak, M. Hofstätter, P. Supancic, J. Rödel, and T. Frömling, "Varistor piezotronics: Mechanically tuned conductivity in varistors," *J Appl Phys*, 118[8] 085703 (2015).
166. U. Schwing and B. Hoffmann, "ZnO single crystals with an intermediate layer of metal oxides - a macroscopic varistor model," *J Appl Phys*, 51[8] 4558-60 (1980).
167. U. Schwing and B. Hoffmann, "Model experiments describing the microcontact of ZnO varistors," *J Appl Phys*, 57[12] 5372-79 (1985).
168. J. S. Lee and J. Maier, "High barrier effects of (000 $\bar{1}$)|(000 $\bar{1}$) zinc oxide bicrystals: Implication for varistor ceramics with inversion boundaries," *J Mater Res*, 20[8] 2101-09 (2005).
169. C. L. Cheng, J. L. He, and J. Hu, "Naturally asymmetrical double-Schottky barrier model: Based on observation of bicrystal," *Appl Phys Lett*, 101[17] 173508 (2012).
170. C. L. Cheng, J. Hu, and J. L. He, "Characterization of dielectric behavior in ZnO electroceramic: Superior grain boundary, inferior grain boundary and grain," *Mater Lett*, 132 240-42 (2014).
171. C. L. Cheng, J. L. He, and J. Hu, "Observation of the charged defect migration that causes the degradation of double-Schottky barriers using a nondestructive quantitative profiling technique," *Appl Phys Lett*, 105[13] 133508 (2014).
172. Y. Sato, F. Oba, T. Yamamoto, Y. Ikuhara, and T. Sakuma, "Current-Voltage Characteristics across [0001] Twist Boundaries in Zinc Oxide Bicrystals," *J Am Ceram Soc*, 85[8] 2142-44 (2002).
173. Y. Sato, T. Tanaka, F. Oba, T. Yamamoto, Y. Ikuhara, and T. Sakuma, "Non-linear current-voltage characteristics related to native defects in SrTiO₃ and ZnO bicrystals," *Sci Technol Adv Mat*, 4[6] 605-11 (2003).
174. F. Oba, H. Ohta, Y. Sato, H. Hosono, T. Yamamoto, and Y. Ikuhara, "Atomic structure of [0001]-tilt grain boundaries in ZnO: A high-resolution TEM study of fiber-textured thin films," *Phys Rev B*, 70[12] 125415 (2004).
175. Y. Sato, F. Oba, M. Yodogawa, T. Yamamoto, and Y. Ikuhara, "Current-Voltage Characteristic and Grain Boundary Structure in Undoped and Pr and Co doped ZnO Bicrystals," *Mater Sci Forum*, 475-479 3867-70 (2005).
176. Y. Sato, M. Yodogawa, T. Yamamoto, N. Shibata, and Y. Ikuhara, "Dopant-segregation-controlled ZnO single-grain-boundary varistors," *Appl Phys Lett*, 86[15] 152112 (2005).
177. Y. Sato, T. Mizoguchi, N. Shibata, T. Yamamoto, T. Hirayama, and Y. Ikuhara, "Atomic-scale segregation behavior of Pr at a ZnO [0001] Σ 49 tilt grain boundary," *Phys Rev B*, 80[9] 094114 (2009).
178. A. Recnik, N. Daneu, T. Walther, and W. Mader, "Structure and Chemistry of Basal-Plane Inversion Boundaries in Antimony Oxide-Doped Zinc Oxide," *J Am Ceram Soc*, 84[11] 2657-68 (2001).
179. N. Daneu, A. Recnik, and S. Bernik, "The application of electron microscopy methods in the study of inversion boundaries in ZnO-based varistors," *Inform Midem*, 30[4] 228-32 (2000).

-
180. A. Recnik, S. Bernik, and N. Daneu, "Microstructural engineering of ZnO-based varistor ceramics," *J Mater Sci*, 47[4] 1655-68 (2012).
 181. T. Yamazaki, N. Nakanishi, A. Recnik, M. Kawasaki, K. Watanabe, M. Ceh, and M. Shiojiri, "Quantitative high-resolution HAADF-STEM analysis of inversion boundaries in Sb₂O₃-doped zinc oxide," *Ultramicroscopy*, 98[2-4] 305-16 (2004).
 182. M. A. McCoy, R. W. Grimes, and W. E. Lee, "Inversion domain boundaries in ZnO ceramics," *J Mater Res*, 11[8] 2009-19 (1996).
 183. J. C. Kim and E. Goo, "Inversion Twin Boundaries in Zinc Oxide," *J Am Ceram Soc*, 73[4] 877-84 (1990).
 184. J. C. Kim and E. Goo, "Morphology and formation mechanism of the pyrochlore phase in ZnO varistor materials," *J Mater Sci*, 24[1] 76-82 (1989).
 185. J. Rohrer and K. Albe, "Thermodynamic stability and electronic structure of pristine wurtzite ZnO {0001} inversion domain boundaries," *Phys Rev Mater*, 5[2] 023601 (2021).
 186. D. Lincot, "Solution growth of functional zinc oxide films and nanostructures," *Mrs Bull*, 35[10] 778-89 (2010).
 187. A. Kolodziejczak-Radzimska and T. Jesionowski, "Zinc Oxide - From Synthesis to Application: A Review," *Materials*, 7[4] 2833-81 (2014).
 188. P. K. Kannan, D. J. Late, H. Morgan, and C. S. Rout, "Recent developments in 2D layered inorganic nanomaterials for sensing," *Nanoscale*, 7[32] 13293-312 (2015).
 189. T. Ohtake, "Bottom-up approaches for material and device designing using practical aspects of self-assembled molecular architectures," *Mol Syst Des Eng*, 3[5] 804-18 (2018).
 190. T. D. Clark, J. Tien, D. C. Duffy, K. E. Paul, and G. M. Whitesides, "Self-Assembly of 10- μ m-Sized Objects into Ordered Three-Dimensional Arrays," *J Am Chem Soc*, 123[31] 7677-82 (2001).
 191. T. D. Clark, R. Ferrigno, J. Tien, K. E. Paul, and G. M. Whitesides, "Template-Directed Self-Assembly of 10- μ m-sized Hexagonal Plates," *J Am Chem Soc*, 124[19] 5419-26 (2002).
 192. R. Z. Ma, M. Osada, L. F. Hu, and T. Sasaki, "Self-Assembled Nanofilm of Monodisperse Cobalt Hydroxide Hexagonal Platelets: Topotactic Conversion into Oxide and Resistive Switching," *Chem Mater*, 22[23] 6341-46 (2010).
 193. S. Cho, J. W. Jang, S. H. Jung, B. R. Lee, E. Oh, and K. H. Lee, "Precursor Effects of Citric Acid and Citrates on ZnO Crystal Formation," *Langmuir*, 25[6] 3825-31 (2009).
 194. M. Wang, S. H. Hahn, J. S. Kim, J. S. Chung, E. J. Kim, and K. K. Koo, "Solvent-controlled crystallization of zinc oxide nano(micro)disks," *J Cryst Growth*, 310[6] 1213-19 (2008).
 195. N. Qin, Q. Xiang, H. B. Zhao, J. C. Zhang, and J. Q. Xu, "Evolution of ZnO microstructures from hexagonal disk to prismoid, prism and pyramid and their crystal facet-dependent gas sensing properties," *Crystengcomm*, 16[30] 7062-73 (2014).
 196. S. Hussain, T. M. Liu, M. Kashif, S. X. Cao, W. Zeng, S. B. Xu, K. Naseer, and U. Hashim, "A simple preparation of ZnO nanocones and exposure to formaldehyde," *Mater Lett*, 128 35-38 (2014).

-
197. K. Ada, M. Gökgöz, M. Önal, and Y. Sarikaya, "Preparation and characterization of a ZnO powder with the hexagonal plate particles," *Powder Technol*, 181[3] 285-91 (2008).
198. M. R. Alenezi, A. S. Alshammari, T. H. Alzanki, P. Jarowski, S. J. Henley, and S. R. P. Silva, "ZnO Nanodisk Based UV Detectors with Printed Electrodes," *Langmuir*, 30[13] 3913-21 (2014).
199. P. Keil, M. Trapp, N. Novak, T. Frömling, H.-J. Kleebe, and J. Rödel, "Piezotronic Tuning of Potential Barriers in ZnO Bicrystals," *Adv Mater*, 30[10] 1705573 (2018).
200. M. Trapp, P. Keil, T. Frömling, J. Rödel, and H.-J. Kleebe, "Segregation and properties at curved vs straight (000 $\bar{1}$) inversion boundaries in piezotronic ZnO bicrystals," *J Am Ceram Soc* 103[4] 2817-27 (2020).
201. R. C. Hoffmann, M. Trapp, E. Erdem, M. Kratzer, C. Teichert, H.-J. Kleebe, and J. J. Schneider, "Synthesis and Assembly of Zinc Oxide Microcrystals by a Low-Temperature Dissolution-Reprecipitation Process: Lessons Learned About Twin Formation in Heterogeneous Reactions," *Chem-Eur J*, 26[42] 9319-29 (2020).
202. D. B. Williams and C. B. Carter, "Transmission Electron Microscopy: A Textbook for Materials Science," 2nd ed. Springer: New York, (2009).
203. J. Thomas and T. Gemming, "Analytische Transmissionselektronenmikroskopie - Eine Einführung für den Praktiker," 1 ed. Springer-Verlag: Wien, (2013).
204. S. J. Pennycook and P. D. Nellist, "Scanning Transmission Electron Microscopy: Imaging and Analysis." Springer Science & Business Media: New York, Dordrecht, Heidelberg, London, (2011).
205. H.-J. Kleebe, S. Lauterbach, and M. Müller, "Transmission electron microscopy (TEM)," pp. 168-78. in *Bunsenmagazin*, Vol. 5. Deutsche Bunsen-Gesellschaft für physikalische Chemie e.V., Frankfurt, 2010.
206. A.-K. Fetzer, M. Trapp, S. Lauterbach, and H.-J. Kleebe, "Introduction to Transmission Electron Microscopy; The Basics," pp. 578-99. in *Encyclopedia of Materials: Technical Ceramics and Glasses*, Vol. 1. Edited by M. Pomeroy. Elsevier, Oxford, 2021.
207. W. Mader and A. Recnik, "Determination of Crystal Polarity by Electron Diffraction from Thin Crystals," *Phys Status Solidi A*, 166[1] 381-95 (1998).
208. J. Liu and J. M. Cowley, "High-resolution scanning transmission electron microscopy," *Ultramicroscopy*, 52[3-4] 335-46 (1993).
209. V. Grillo, "Quantitative evaluation of strain effects in STEM HAADF contrast," *Microscopie*, 11[1] 61-68 (2009).
210. M. de la Mata, C. Magen, J. Gazquez, M. I. B. Utama, M. Heiss, S. Lopatin, F. Furtmayr, C. J. Fernandez-Rojas, B. Peng, J. R. Morante, R. Rurali, M. Eickhoff, A. F. I. Morral, Q. H. Xiong, and J. Arbiol, "Polarity Assignment in ZnTe, GaAs, ZnO, and GaN-AlN Nanowires from Direct Dumbbell Analysis," *Nano Lett*, 12[5] 2579-86 (2012).
211. C. T. Koch, "Determination of Core Structure Periodicity and Point Defect Density along Dislocations," Ph.D. thesis. Arizona State University, (2002).
212. C. A. Schneider, W. S. Rasband, and K. W. Eliceiri, "NIH Image to ImageJ: 25 years of image analysis," *Nat Methods*, 9[7] 671-75 (2012).
213. K. Zuiderveld, "Contrast limited adaptive histogram equalization," pp. 474-85. in *Graphics Gems IV*. Edited by P. S. Heckbert. Academic Press: San Diego, London, San Francisco, 1994.

-
214. T. Walther, "Development of a new analytical electron microscopy technique to quantify the chemistry of planar defects and to measure accurately solute segregation to grain boundaries," *J Microsc-Oxford*, 215 191-202 (2004).
215. T. Walther, A. Recnik, and N. Daneu, "A Novel Method of Analytical Transmission Electron Microscopy for Measuring Highly Accurately Segregation to Special Grain Boundaries or Planar Interfaces," *Microchim Acta*, 155[1-2] 313-18 (2006).
216. T. Walther, M. Hopkinson, N. Daneu, A. Recnik, Y. Ohno, K. Inoue, and I. Yonenaga, "How to best measure atomic segregation to grain boundaries by analytical transmission electron microscopy," *J Mater Sci*, 49[11] 3898-908 (2014).
217. T. Walther, N. Daneu, and A. Recnik, "A New Method to Measure Small Amounts of Solute Atoms on Planar Defects and Application to Inversion Domain Boundaries in Doped Zinc Oxide," *Interface Sci*, 12[2-3] 267-75 (2004).
218. T. Walther, "Linear least-squares fit evaluation of series of analytical spectra from planar defects: extension and possible implementations in scanning transmission electron microscopy," *J Microsc-Oxford*, 223 165-70 (2006).
219. T. Walther and M. Hopkinson, "Quantitative investigation of the onset of islanding in strained layer epitaxy of InAs/GaAs by X-ray mapping in STEM," *J Phys Conf Ser*, 209 012035 (2010).
220. J. I. Goldstein, "Principles of Thin Film X-Ray Microanalysis." pp. 83-120. in *Introduction to Analytical Electron Microscopy*. Edited by J. J. Hren, J. I. Goldstein, and D. C. Joy. Springer, New York, NY, 2013.
221. J. T. C. Vankemenade and R. K. Eijthoven, "Direct determination of barrier voltage in ZnO varistors," *J Appl Phys*, 50[2] 938-41 (1979).
222. M. Gehringer, "Preparation of varistor-type bicrystal interfaces by sputter deposition of dopants," MSc. thesis. Institute of Material Science, Technische Universität Darmstadt, Darmstadt, (2018).
223. Y. F. Yan, G. M. Dalpian, M. M. Al-Jassim, and S. H. Wei, "Energetics and electronic structure of stacking faults in ZnO," *Phys Rev B*, 70[19] 193206 (2004).
224. E. Jak, S. Degterov, P. Wu, P. C. Hayes, and A. D. Pelton, "Thermodynamic Optimization of the Systems PbO-SiO₂, PbO-ZnO, ZnO-SiO₂ and PbO-ZnO-SiO₂," *Metall Mater Trans B*, 28[6] 1011-18 (1997).
225. R. Hansson, B. J. Zhao, P. C. Hayes, and E. Jak, "A Reinvestigation of Phase Equilibria in the System Al₂O₃-SiO₂-ZnO," *Metall Mater Trans B*, 36[2] 187-93 (2005).
226. J. Clatot, M. Nistor, and A. Rougier, "Influence of Si concentration on electrical and optical properties of room temperature ZnO:Si thin films," *Thin Solid Films*, 531 197-202 (2013).
227. W. Z. Zhou, D. A. Jefferson, M. Alariofranco, and J. M. Thomas, "Superlattices in Ternary Oxides Derived from Bi₂O₃: New Families of Ordered Phases Based on the Fluorite Structure," *J Phys Chem*, 91[3] 512-14 (1987).
228. R. Miida and M. Tanaka, "A Modulated Structure in a Fluorite-Type Fast-Ion-Conductor δ -(Bi₂O₃)_{1-x}(Nb₂O₅)_x," *Jpn J Appl Phys 1*, 29[6] 1132-38 (1990).
229. C. S. Smith, "Some elementary principles of polycrystalline microstructure," *Metallurgical Reviews*, 9[1] 1-48 (1964).

-
230. S. M. Hosseini, A. Alemi, and Z. Rezvani, "Preparation and Study of Bismuth Oxide Doped and co-Doped with Cobalt(III) and Holmium(III) via Sol-Gel Method," *Iran J Chem Chem Eng*, 34[4] 53-59 (2015).
231. G. Viruthagiri and P. Kannan, "Visible light mediated photocatalytic activity of cobalt doped Bi₂O₃ nanoparticles," *J Mater Res Technol*, 8[1] 127-33 (2019).
232. G. Y. Huo, J. Lu, and L. X. Ren, "Phase relations in the Bi₂O₃-CoO_y-SnO₂ system at room temperature," *J Alloy Compd*, 368[1-2] 126-29 (2004).
233. D. Poleti, L. Karanovic, and A. Hadzi-Tonic, "Doped γ -Bi₂O₃: synthesis of microcrystalline samples and crystal chemical analysis of structural data," *Z Kristallogr*, 222[2] 59-72 (2007).
234. H. Y. Deng, W. C. Hao, and H. Z. Xu, "A Transition Phase in the Transformation from α -, β - and ϵ - to δ -Bismuth Oxide," *Chinese Phys Lett*, 28[5] 056101 (2011).
235. S. Serena, M. A. De la Rubia, A. C. Caballero, and Y. A. Caballero, "Thermodynamic study of the rich-Bi₂O₃ region of the Bi₂O₃-ZnO system," *Bol Soc Esp Ceram V*, 45[3] 150-53 (2006).
236. A. Watanabe, "Is It Possible to Stabilize δ -Bi₂O₃ by an Oxide Additive?," *Solid State Ionics*, 40-1 889-92 (1990).
237. A. Watanabe, "Phase equilibria in the system Bi₂O₃-Y₂O₃: No possibility of δ -Bi₂O₃ stabilization," *Solid State Ionics*, 86-8 1427-30 (1996).
238. E. Olsson, G. L. Dunlop, and R. Österlund, "Development of interfacial microstructure during cooling of a ZnO varistor material," *J Appl Phys*, 66[10] 5072-77 (1989).
239. C. H. Bates, W. B. White, and R. Roy, "Solubility of Transition Metal Oxides in Zinc Oxide and Reflectance Spectra of Mn²⁺ and Fe²⁺ in Tetrahedral Fields," *J Inorg Nucl Chem*, 28[2] 397-405 (1966).
240. S. Y. Chun, N. Wakiya, K. Shinozaki, and N. Mizutani, "Investigation of the solidus boundaries and microstructure in the ZnO-PrO_{1.5}-CoO system," *J Mater Res*, 13[8] 2110-16 (1998).
241. S. Y. Chun, N. Wakiya, H. Funakubo, K. Shinozaki, and N. Mizutani, "Phase Diagram and Microstructure in the ZnO-Pr₂O₃ system," *J Am Ceram Soc*, 80[4] 995-98 (1997).
242. N. Raghu and T. R. N. Kutty, "The influence of dislocations on the nonlinearity of ZnO : Cu varistors," *J Mater Sci-Mater El*, 1[2] 84-86 (1990).
243. J. W. Gibbs, "The collected works of J. Willard Gibbs." Longmans, Green and Co.: New York, (1928).
244. P. Wynblatt and D. Chatain, "Anisotropy of Segregation at Grain Boundaries and Surfaces," *Metall Mater Trans A*, 37a[9] 2595-620 (2006).
245. R. Kirchheim, "Reducing grain boundary, dislocation line and vacancy formation energies by solute segregation. I. Theoretical background," *Acta Mater*, 55[15] 5129-38 (2007).
246. S. Choudhury, J. A. Aguiar, M. J. Fluss, L. L. Hsiung, A. Misra, and B. P. Uberuaga, "Non-uniform Solute Segregation at Semi-Coherent Metal/Oxide Interfaces," *Sci Rep*, 5 (2015).
247. M. Herbig, D. Raabe, Y. J. Li, P. Choi, S. Zaefferer, and S. Goto, "Atomic-Scale Quantification of Grain Boundary Segregation in Nanocrystalline Material," *Phys Rev Lett*, 112[12] (2014).

-
248. Y. Ikuhara and P. Pirouz, "Orientation Relationship in Large Mismatched Bicrystals and Coincidence of Reciprocal Lattice Points (CRLP)," *Mater Sci Forum*, 207-209 121-24 (1996).
249. W. Wunderlich, "Atomic Structure of Symmetrical Tilt Grain Boundaries in Zinc Oxide with High Coincidence," *Phys Status Solidi A*, 170[1] 99-111 (1998).
250. B. B. Straumal, A. A. Mazilkin, S. G. Protasova, P. B. Straumal, A. A. Myatiev, G. Schütz, E. Goering, and B. Baretzky, "Ferromagnetism of Nanostructured Zinc Oxide Films," *Phys Met Metallogr+*, 113[13] 1244-56 (2012).
251. B. B. Straumal, A. A. Mazilkin, S. G. Protasova, A. A. Myatiev, P. B. Straumal, and B. Baretzky, "Increase of Co solubility with decreasing grain size in ZnO," *Acta Mater*, 56[20] 6246-56 (2008).
252. C. C. Ma and A. Navrotsky, "Thermodynamics of the CoO-ZnO System at Bulk and Nanoscale," *Chem Mater*, 24[12] 2311-15 (2012).
253. M. Gaudon, O. Toulemonde, and A. Dernourgues, "Green Coloration of Co-doped ZnO Explained from Structural Refinement and Bond Considerations," *Inorg Chem*, 46[26] 10996-1002 (2007).
254. Y. J. Chen, S. Brahma, C. P. Liu, and J. L. Huang, "Enhancement of the piezoelectric coefficient in hexagonal $Mg_xZn_{1-x}O$ films at lower Mg compositions," *J Alloy Compd*, 728 1248-53 (2017).
255. X. B. Wang, C. Song, D. M. Li, K. W. Geng, F. Zeng, and F. Pan, "The influence of different doping elements on microstructure, piezoelectric coefficient and resistivity of sputtered ZnO film," *Appl Surf Sci*, 253[3] 1639-43 (2006).
256. H. Yadav, N. Sinha, S. Goel, and B. Kumar, "Eu-doped ZnO nanoparticles for dielectric, ferroelectric and piezoelectric applications," *J Alloy Compd*, 689 333-41 (2016).
257. D. D'Agostino, C. Di Giorgio, A. Di Trollo, A. Guarino, A. M. Cucolo, A. Vecchione, and F. Bobba, "Piezoelectricity and charge trapping in ZnO and Co-doped ZnO thin films," *Aip Adv*, 7[5] 055010 (2017).

List of Figures

- Figure 1-1: a) and b) zincite specimens from Sterling Mine, Sterling Hill, Ogdensburg, Franklin Mining District, Sussex County, New Jersey, USA. The red color is due to iron and manganese impurities. Reworked after Robert M. Lavinsky.^{8,9} 1
- Figure 1-2: The crystal structure of wurtzite ZnO. Zinc and oxygen atoms form interpenetrative hcp and mutually occupy one-half of their tetrahedral sites. In contrast to an ideal tetrahedral coordination, the close-packings are slightly shifted along the c-axis, leading to non-uniform bond lengths l and l' in c-axis and off-axis direction, respectively. 2
- Figure 1-3: a) and b) BSE-SEM images of the interface layer in an EST bicrystal (cf. pp. 27) before and after etching with 10 % HCl_{aq} for about 1 s. Etching indicates the incomplete transformation to a bicrystal by revealing the polycrystalline state of the interfacial layer by highlighting grain boundaries as well as the different orientation of ZnO grains, as reflected by the etching pits and hillocks (inset), which occur exclusively at the O-terminated $[000\bar{1}]$ side..... 3
- Figure 1-4: a) Illustration of the hexagonal unit cell according to Bravais notation using three equivalent axes a_1 , a_2 , a_3 and the unique c-axis. The small circles mark Bravais lattice points. As highlighted by the grey color, the regular primitive hexagonal unit cell hP is set up by $a_1 = a$, $a_2 = b$ and c . b) Projection of the hexagonal unit cell along the c-axis, for a better depiction of the equivalence of a_1 , a_2 and a_3 4
- Figure 1-5: Illustration of the four different types of the piezoelectric effect, which are classified by the two components of the corresponding piezoelectric coefficient d . These components are the applied force F , which is either a normal or a shear force, and the direction of the resulting polarization P , which is either longitudinal or transversal to F . Redrawn after "Bild. 4.12" by Kleber.³² 6
- Figure 1-6: Illustration of the components of the stress tensor σ_{jk} for wurtzite ZnO. The directions and planes indicated by j and k correspond to an orthonormal coordination system, which relates to the hexagonal unit cell as shown in the figure. Normal and shear components are highlighted in blue and green color, respectively. Reworked after "Bild 4.10" by Kleber.³² 7
- Figure 1-7: Typical I-V curve of a commercial polycrystalline varistor. In the pre-switch and high-current regime, where the current is controlled by the grain boundaries and the grain's bulk properties, respectively, the electrical behavior is quasi-ohmic with $\alpha \approx 1$. In the switching region, the current I increases proportionally to V^α . Reworked after Fig 1 by Clarke.⁹⁰ 11
- Figure 1-8: Band diagram of a Schottky barrier at a metal/n-type semiconductor junction a) before and b) after contacting. Due to $\Phi_M > \Phi_S$, electrons are transferred to the metal side in the course of Fermi level equalization, which causes band bending and formation of a potential barrier Φ_{SB} and a depletion layer W_D . Reworked after Figure 2-3 by Keil.¹⁰¹ 11
- Figure 1-9: Band diagram of a double Schottky barrier at a varistor-type interface a) before and b) after contacting. a) Two n-type ZnO grains are separated by GB material with additional unoccupied trap states N_i and hence a lower Fermi level. Upon contacting and Fermi level equalization, the trap states get filled by electrons from both sides, leading to a negative sheet charge Q_i at the interface, depletion layers W_D on both sides and, in consequence, the formation of a double Schottky barrier. Reworked after Figure 14-6 by Pike.¹⁰⁸ 12
- Figure 1-10: Illustration of the breakdown mechanism for varistor-type potential barriers under voltage application. Below the critical voltage V_C , the band structure is deformed and unoccupied trap states get successively filled, counteracting a barrier decrease. Current is

governed by thermionic emission. Reaching the critical voltage, hot electrons occur, which ionize valence states and thus, generate electron-hole pairs. Being attracted by the electrostatic field, h^+ diffuse to and counteract the negative sheet charge, leading to an exponentially fast lowering of the potential barrier. Reworked after Figure 14-10 by Pike.¹⁰⁸

- 13
- Figure 1-11: Piezotronic application of a single ZnO nanowire as a strain-gated transistor. Two contacts suffice since the gate voltage is adjusted via mechanical load. a) Compressive stress: piezoelectric charges increase the Schottky barrier at one side (left) while decreasing the other (right). b) Tensile stress: reversed piezo-charges and impact on the Schottky barriers, hence inverse operation of the transistor is possible..... 16
- Figure 1-12: Illustration of the two main configurations of ZnO bicrystals investigated in this work: a) Zn|Zn terminated bicrystal with an (0001)|(0001) interface corresponding to a head-to-head orientation of the c-axes. b) O|O terminated bicrystal with an (000 $\bar{1}$)|(000 $\bar{1}$) interface corresponding to a tail-to-tail orientation of the c-axes. Both orientations provide an optimized piezoelectric response (polarization P) upon compressive stress applied along the c-axes, causing the accumulation of negative and positive piezo-charges at the interface for a Zn|Zn and O|O configuration, respectively..... 19
- Figure 3-1: Illustration of the bicrystal synthesis via diffusion bonding. Two single crystals in O|O, Zn|Zn or Zn|O orientation with an optional sputtered dopant layer are hot-pressed for 1 h @ 1000°C, 1.5 MPa..... 25
- Figure 3-2: Illustration of the tilted DB-bicrystals. An asymmetrical tilt is introduced, at which one crystal with a sputtered dopant layer remains fixed in “head” or “tail” position, while the other is rotated by a specific angle α . For the rotated crystals, larger specimens were used, which allowed cutting them to match the size of the fixed crystal and to obtain a plain and flat interface. 26
- Figure 3-3: Some examples of bicrystals, as provided for this thesis. All bicrystals featured cracks and fractures as a consequence of zinc oxide’s perfect {10 $\bar{1}$ 0} cleavage and the load during bonding or I-V measurements. a) Sample B-II; no I-V measurement performed; cracks are from bonding. b) Sample DB-a|c; highly fractured from load-dependent I-V measurements. c) DB-IV bicrystal in O|O orientation with conchoidal fracture; destroyed during TEM sample preparation. d) Second DB bicrystal in a|c orientation; destroyed during TEM sample preparation; direction of view (and applied force) is along the a-axis, which caused additional parting along {0001}..... 26
- Figure 3-4: Illustration of epitaxial solid-state transformation (EST). Two single crystals in O|O or Zn|Zn orientation with a doped polycrystalline interlayer of 100 μ m thickness form a single-poly-single crystalline stack bonded for 2 h @ 1100°C, 1.5 MPa. Upon the subsequent annealing step of 25 h (Zn|Zn) or 65 h (O|O) @ 1100°C, the single crystals grow at the expense of the sacrificial interlayer, which is epitaxially transformed until a bicrystal is obtained. 27
- Figure 3-5: a) PLM image of the EST-Zn|Zn bicrystal after polishing. It is revealed that the sacrificial interlayer is still polycrystalline. b) Corresponding BSE-SEM image of the interlayer after etching with 10 % HCl_{aq} for about 1 s, which highlights grain boundaries as well as different grain orientations. 28
- Figure 3-6: Simplified overview of the reaction products obtained from thermohydrolysis of Zn/Co-acetates, depending on the employed solvent and optional cobalt doping. Whereas the application of water lead to the formation of rod-shaped nanotwins, independent of Co doping, the latter was found to be mandatory to suppress the twinning of hexagons, which were formed using a water/ethanol mixture. Redrawn after Figure 1 by Hoffmann et al.²⁰¹
- 28

Figure 3-7: Schematic of the ion-milling procedure. A thin-foil TEM sample is placed between opposing ion guns, where Ar ⁺ ions are accelerated on the rotating specimen under a certain milling angle α and an acceleration voltage ΔkV . Sample material is continuously removed until one or more holes are generated featuring electron transparent regions at their edges.	29
Figure 3-8: a), b) Samples DB-a c and EST-O O after ion-milling. Grain-boundary and interlayer were carefully positioned parallel & centered with respect to a row of meshes. In consequence, several holes formed along the interface upon ion-milling, thus providing a maximum yield of electron transparent regions.	30
Figure 3-9: Schematic sketch of a typical SEM. An electron gun generates an electron beam focused by a set of lenses and scanned across the sample. Within a certain pear-shaped excitation volume, beam-matter interactions cause (among other effects) the generation of secondary and back-scattered electrons as well as characteristic X-rays, whose detection is used for imaging and chemical analysis.	31
Figure 3-10: Components and general setup of a TEM, showing the Jeol 2100F instrument used for this work. The electron gun generates an electron beam, which is focused by electromagnetic lenses. In order to adjust brightness, spot size and beam convergence, the condenser lens system and aperture can be used, while the objective lens system and aperture allow adjustment of image contrast and DF-imaging. The intermediate lens features the ability to switch instantaneously between image and diffraction mode. If required, the SAED aperture limits the sample area contributing to the diffraction pattern. Typically, a double-tilt holder is used, which allows tilting of the sample to desired zone axes or directions. The resulting image or diffraction pattern is magnified and displayed on the viewing screen or CCD camera by the projector lens system. For scanning mode, special scan coils (condenser system) and STEM detectors are used. Both TEM and STEM images can be complemented by chemical analysis via EDS.	32
Figure 3-11: a) Sketch illustrating the formation of a bright-field TEM image (BF-TEM). The objective aperture is centered on the primary beam and absorbs scattered and diffracted beams depending on its diameter. The smaller the diameter is, the more electrons are absorbed and the higher is the resulting image contrast. b) For dark-field imaging (DF-TEM), a small objective aperture is shifted on the position of a diffracted beam excluding the primary beam. In the corresponding image, only those parts of the sample, which contribute to the diffracted beam, appear bright and the background is dark.	33
Figure 3-12: Illustration of the Ewald sphere and diffraction in TEM. A 2D cross-section of the reciprocal lattice is shown with Zero, First, Second, ..., and Higher Order Laue Zones (ZOLZ, etc.). The Ewald sphere has radius $k = \lambda^{-1}$ pointing to the (000) reflection, i.e., the spot of the primary beam. Diffraction occurs for all reciprocal lattice points (hkl) intersecting the sphere's surface with $k' = k + g_{hkl}$. Due to thin-foil effects, lattice points are elongated to relrods, allowing a certain excitation error s , which relaxes the diffraction condition to $K = g_{hkl} + s$ and $k' = k + K$	36
Figure 3-13: a) Intensity difference of Friedel pair (0002) & (000 $\bar{2}$) and Bijvoet pairs {10 $\bar{1}\bar{1}$ } & {10 $\bar{1}1$ } due to multiple scattering in very thin samples. b) Sketch of the resulting diffraction pattern which allows to deduce the c-axis polarity. Reworked after Fig. 4 by Recnik et al. ¹⁸⁰	38
Figure 3-14: a) Sketch illustrating a typical STEM setup with an EDS detector. Via special scanning coils, a small convergent electron beam (probe) is scanned across the sample. BF and DF detectors are located below the sample collecting transmitted beams within a certain angular width. b) By changing the (virtual) camera length, the acceptance angles θ of the detectors can be adjusted, e.g., for HAADF or Z ² -contrast conditions.	39

- Figure 3-15: FFT-filtered HAADF-STEM image of alternating layers of TiNiSn and HfNiSn. Both layer types feature exactly the same crystal structure but a different average atomic weight Z . Therefore, they exhibit a strong Z^2 -contrast due to $I \sim Z^2$ 40
- Figure 3-16: a) ABF-STEM image of wurzite ZnO in $[\bar{1}2\bar{1}0]$ zone-axis orientation recorded with a C_s -corrected ARM 200F at a camera length of 6 cm and with the beam stopper inserted, which limits the BF acceptance angles to 11 – 22 mrad. b) Corresponding QSTEM image simulation for a ZnO slab of 30 nm thickness, an acceptance angle of 11 – 22 mrad, a beam convergence angle of 24 mrad, $C_s = 0.001$, $C_c = 1.4$ and an energy spread of $\Delta E = 0.8$ eV. A comparison of both images verifies the ABF-STEM technique to be capable of identifying the absolute c-axis direction via the orientation of the Zn-O dumbbells, as highlighted in b)..... 41
- Figure 3-17: Illustration of the FFT filtering procedure used to increase the quality of HR-(S)TEM images. a) Raw HAADF-STEM image of ZnO in $[\bar{1}100]$ zone-axis condition. b) FFT of the HAADF-STEM image. Similar to reflections in a diffraction pattern, spots occur related to periodic image features, such as atomic columns or lattice planes, e.g., (0002) and $(\bar{1}\bar{1}20)$. c) The same FFT after the application of a mask filtering out background noise and amorphous contributions. d) Inverse FFT recreating the filtered real space image. . 41
- Figure 3-18: Sketch illustrating the CEP method for the quantification of solute segregation to planar defects or interfaces. A series of EDS or EELS measurements is recorded using different radii r for the electron beam, which is centered on the planar defect in edge-on orientation. In consequence, different matrix/solute ratios are probed. From the obtained data, the chemical width d of the solute-covered planar defect can be calculated, which allows quantifying the segregation. The main advantage of the CEP method is its independence from beam broadening $r + \Delta r$, which can, depending on the thickness t , be a large obstacle for EDS or EELS point measurements. Redrawn after Figure 1 by Walther et al.²¹⁷ 43
- Figure 3-19: Plot of a CEP measurement series (EDS). The intensity ratios $R = I_m \cdot k_s / I_s \cdot k_m$ are plotted against the respective beam radius. The slope $\partial R(r) / \partial r$ of a linear regression function yields the chemical width d according to Eq. 3.3..... 44
- Figure 3-20: Sketch of the setup for the load-dependent I-V measurements used for the electrical characterization of the ZnO bicrystals. All measurements were performed using the d_{33} -arrangement, at which load is applied parallel to the c-axes..... 46
- Figure 4-1: a) BF-TEM image of the interface in the O|O oriented undoped bicrystal B-I in $[\bar{1}2\bar{1}0]$ zone-axis orientation. SAED reveals a misalignment of 1° tilt (insets). b) FFT-filtered HAADF-STEM image of the interface showing a lower intensity for the grain boundary compared to the bulk, which indicates a locally lower average atomic weight. EDS measurements verify the presence of silicon ($Z = 14$) at the grain boundary, whereas no silicon was detected in the bulk. Except for minor lattice distortions, the interface is predominantly straight and defect free. 47
- Figure 4-2: FFT-filtered ABF-STEM image of the interface in sample B-I in $[\bar{1}2\bar{1}0]$ zone-axis orientation showing a predominantly straight and well-bonded grain boundary. Here, a stacking fault is observed as presented in the large inset in the middle. The two small ABF insets on the right verify the tail-to-tail orientation by revealing the direction of the Zn-O dumbbells. 48
- Figure 4-3: a) BF-TEM image of the interface in the Zn|Zn oriented undoped bicrystal B-II in $g = (0002)$ two-beam condition. SAED measurements indicate a misalignment of 2.8° tilt between the $[\bar{1}2\bar{1}0]$ zone axes (insets). The periodic contrast variations at the interface are interpreted as strain contrast generated by the large mismatch. b) FFT-filtered HAADF-

STEM image of the interface in $[\bar{1}2\bar{1}0]$ orientation, which appears straight and rather defect-free. Due to the large misalignment, only the lower crystal is in zone-axis orientation with resolvable atom columns. Z^2 -contrast and EDS measurements reveal a distinct Si enrichment at the interface..... 49

Figure 4-4: FFT-filtered ABF-STEM image of the interface in bicrystal B-II in $[\bar{1}2\bar{1}0]$ zone-axis orientation. In contrast to Figure 4-3 b), ABF imaging indicates a rather disordered interface with diffuse atom columns. However, the disordered region is limited to two Zn layers, hence corresponding to the dimensions of one unit cell in c-axis direction. The ABF insets depict the head-to-head orientation by revealing the direction of the Zn-O dumbbells. 49

Figure 4-5: a) $R(r)$ plot of CEP measurement series A conducted in TEM mode. The low R^2 value is seen as an indication of a solid solubility of Si in ZnO $\gg 20$ ppm. b) The linear regression of an $R^{-1}(r^{-1})$ plot of the same measurement series confirms this consideration by indicating a solid solubility limit of $x = 0.0033 = 3300$ ppm. In consequence, the chemical width $d = (\pi \cdot 0.1077)/2 = 0.1692$ is determined from $R^{-1}(r^{-1})$ instead of $R(r)$ 50

Figure 4-6: a) $R^{-1}(L^{-1})$ plot of CEP measurement series B conducted in STEM mode. The R^2 value of the respective linear regression is considerably low, although a solubility $x \gg 20$ ppm is already considered. This is attributed to a varying Si concentration at the interface. However, the obtained values $x = 0.0041$ and $d = 0.1918$ are in the same region as for series A & C and hence appear plausible. b) $R^{-1}(L^{-1})$ plot of CEP measurement series C conducted in STEM mode. The solubility of Si and the chemical width were determined as $x = 0.0054$ and $d = 0.2805$ 51

Figure 4-7: a) BF-TEM image of the interface in the head-to-tail (Zn|O) oriented undoped bicrystal B-III in $g = (0002)$ two-beam condition. SAED indicates a quasi-perfect fitting with zero tilt (insets). Nevertheless, a small displacement of bending contours at the interface indicates a very slight mismatch, which however is non-measurable and estimated to be $\ll 1^\circ$. b) FFT-filtered HAADF-STEM image of the interface in $[\bar{1}100]$ orientation. Consistent with the observed tilt-free configuration, the interface appears straight and defect-free. However, Z^2 -contrast and EDS measurements reveal a distinct Si enrichment, which varies along the boundary, according to the alternating darker and brighter regions. The width of the Si-containing interface comprises approximately three Zn layers $3 \cdot d_{(0002)} = 0.78$ nm..... 52

Figure 4-8: a) FFT-filtered ABF-STEM image of the interface in bicrystal B-III in $[\bar{1}2\bar{1}0]$ zone-axis orientation. Imaging along $[\bar{1}2\bar{1}0]$ provides to possibility to identify basal-plane stacking faults (large inset in the middle) as well as the Zn-O dumbbell orientation (insets on the right). Contrary to the intended Zn|Zn orientation, ABF imaging revealed a Zn|O bicrystal. As shown in b) and c), NBED revealing the violation of Friedel's law was applied, verifying this finding. 53

Figure 4-9: a) and b) $R^{-1}(r^{-1})$ plots of CEP measurement series A and B conducted in TEM mode. Whereas the obtained values for the solubility limit $x = 0.0032$ and $x = 0.0034$ are in the same region as the results from the Zn|Zn bicrystal (cf. pp. 50), the chemical widths $d = (\pi \cdot 0.0623)/2 = 0.0979$ and $d = (\pi \cdot 0.0623)/2 = 0.1323$ are significantly lower. The R^2 -values are both < 0.9 , which is seen as a consequence of the non-uniform silicon segregation along the interface non-uniform silicon segregation along the interface..... 53

Figure 4-10: Stress-dependent I-V characteristics of the undoped reference bicrystal B-III. An ideal ohmic behavior ($\alpha_{\max} \approx 1.0$) is observed independent of the applied mechanical load ranging from 5 MPa to 100 MPa. Likewise, the leakage current of $8 \cdot 10^{-4}$ A (measured at 0.1 V) remains unchanged..... 54

- Figure 4-11: BSE-SEM image of the interface in the O|O oriented doped bicrystal DB-I subsequent to TEM-sample preparation and ion-milling. A straight interface is revealed, decorated by Bi-rich inclusions, as determined by EDS measurements (upper inset). A small silicon signal was detected in addition to bismuth. The crater-like structure of the interface region is a preparation artifact due to ion-milling. 58
- Figure 4-12: a) HAADF-STEM image of the Bi-rich inclusions at the interface of the O|O oriented bicrystal DB-I, doped by sputtering a 75 nm dopant layer with 5 mol% Bi₂O₃ and 5 mol% Co₃O₄ (target composition). δ-Bi₂O₃ is clearly and unambiguously identified by EDS and electron diffraction (lower & upper inset). The superlattice reflections at 1/3 (hkl) positions are characteristic for the δ-modification of Bi₂O₃.²²⁷ b) HAADF-STEM image of an individual δ-Bi₂O₃ grain revealing a large dihedral angle of $\theta = 138^\circ$ at the interface, which indicates a non-wetting behavior.²²⁹ 59
- Figure 4-13: a) FFT-filtered ABF-STEM image of δ-Bi₂O₃ in $[\bar{1}10]$ orientation depicting the 3x3x3 supercell compared to the regular unit cell. b) FFT of the ABF-STEM image showing the crystallographic directions as well as small additional spots at 1/3 (hkl) positions corresponding to the 3x3x3 superlattice. c) and d) show plots of the intensity profiles along the $[112]$ and the $[\bar{1}\bar{1}2]$ directions illustrating the threefold-periodic intensity variation defining the supercell in the ABF-STEM image. 59
- Figure 4-14: a) BF-TEM image of the interface in the O|O bicrystal DB-I in $[\bar{1}2\bar{1}0]$ zone-axis orientation. Electron diffraction indicates a perfect alignment of the bicrystal halves with zero zone-axis tilt (SAED insets). b) FFT-filtered HAADF-STEM image of the interface section between the δ-Bi₂O₃ inclusion revealing an atomically well-bonded and coherent grain boundary. No interfacial films or any kind of distinct Bi segregation is observed. However, silicon is detected at the interface indicating a Si segregation as previously observed in undoped bicrystals (cf. pp. 47), which explains the reduced intensity (Z²-contrast) at the interface. 60
- Figure 4-15: FFT-filtered ABF-STEM image of the interface in bicrystal DB-I in $[\bar{1}2\bar{1}0]$ zone-axis orientation. Except for a single edge dislocation and minor lattice distortions, the interface is predominantly straight and atomically well-bonded. The two small ABF insets on the right depict a tail-to-tail orientation as revealed by the directions of the Zn-O dumbbells. 61
- Figure 4-16: a) HAADF-STEM image of the interface in the O|O oriented doped bicrystal DB-II in $[\bar{1}100]$ zone-axis orientation. The sample was doped by sputtering a (nominal) 300 nm thick dopant layer with 1 mol% Bi₂O₃ and 1 mol% Co₃O₄ (target composition). SAED was used to determine a misalignment of 2.8° tilt (insets). Dopant phases were found as inclusions in the near bulk, but not at the actual interface and only on one side, indicating a one-directional (over)growth. b) FFT-filtered HAADF-STEM images (Z²-contrast) indicate the presence of heavy elements, i.e., Bi. EDS measurements comparing bulk and interface reveal a distinct Bi accumulation at the grain boundary. Due to the large misalignment, the atomic structure of the interface could hardly be resolved. 62
- Figure 4-17: a) BF-STEM image of the interface in the O|O oriented doped bicrystal DB-III revealing an incomplete bonding. Doping was achieved by sputtering a 500 nm layer on the interface prior to bonding with 10 mol% Bi₂O₃ and 10 mol% Co₃O₄ (target composition). The thickness of the dopant layer was, however, determined to be about 1 μm (lower inset). The interfacial material mainly consists of polycrystalline Zn- and Bi-rich grains according to EDS measurements (upper inset). b) α-Bi₂O₃ is identified by high-resolution HAADF-STEM and corresponding FFT images (insets). 63
- Figure 4-18: a) BF-STEM image of the interface and adjacent bulk region in bicrystal DB-III. This sample could be utilized to evaluate the diffusion width of cobalt into the ZnO lattice,

which was determined by EDS point measurements to be at least 0.54 μm . b) Stacked EDS spectra corresponding to the EDS point measurements as depicted in a). In figure c), the cobalt K_{α} -peak is enlarged for a better depiction of its decreasing height from about 500 counts at measurement point 1 down to the background level at measurement point 5. All measurements were performed using the same settings for the electron beam, detector angle and live time. 64

Figure 4-19: I-V characteristics of the DB bicrystals. Weak non-linear characteristics were observed for samples DB-II ($\alpha_{\text{max}} \approx 3.1$) and DB-III ($\alpha_{\text{max}} \approx 2.3$), whereas ohmic behavior was observed for DB-I ($\alpha_{\text{max}} \approx 1.0$). The leakage current (measured at 0.1 V) is considerably different for all three samples, with DB-II having the highest with $4 \cdot 10^{-4}$ A and DB-III the lowest with $4 \cdot 10^{-9}$ A. DB-I exhibits $5 \cdot 10^{-6}$ A. 65

Figure 4-20: Load dependent I-V characteristics of sample DB-III. From 5 MPa to 100 MPa, the observed change in α_{max} is counter-intuitive as it increases up to $\alpha_{\text{max}} = 3.3$, instead of decreasing. The leakage current (measured at 0.1 V) remains nearly unaltered. However, with increasing load from 100 MPa to 300 MPa, the response is as expected and the coefficient of non-linearity is gradually lowered down to $\alpha_{\text{max}} = 1.8$. Simultaneously, the leakage current increases by two orders of magnitude up to $4 \cdot 10^{-7}$ A. The breakdown voltage is $V_{\text{B}} \approx 5$ V up to 100 MPa and $V_{\text{B}} \approx 4.1$ V for 150 MPa and higher loads. 65

Figure 4-21: BSE-SEM image of the meandering bicrystal grain-boundary (white dashed line) in sample EST-O|O. The interface is mainly free from dopant inclusions, which, however, are numerous observed in the bulk. Homogenous contrast for the bicrystal halves indicates a successful transformation into a bicrystal. Amorphous or crystalline films at the interface were not observed. The sample was etched for about 1 s in a 10 % HCl_{aq} solution for a better accentuation of the grain boundary. 70

Figure 4-22: a) BSE-SEM image of the meandering grain boundary (white dashed line) in sample EST-O|O after TEM preparation. Upon ion-milling, etching patterns were formed resembling a polycrystalline structure. However, SAED measurements, recorded at position 1) – 9), evidence true single-crystallinity for both bicrystal halves. Please note, all SAED patterns were recorded using the same sample-beam orientation. Since the lower bicrystal half is slightly tilted, patterns 5) – 9) feature the circular intersection of the ZOLZ with the Ewald sphere. Variations within groups 1) – 4) and 5) – 9) are due to thickness variations and bending of the TEM sample thin-foil. b) BSE-SEM overview image of the pseudo-polycrystalline etching pattern, which is limited to the region of the (former) sacrificial interlayer. 71

Figure 4-23: a) Two-beam DF-TEM image with $g = (0002)$ of sample EST-O|O recorded in the region of the former polycrystalline interlayer, with a small objective aperture applied. Thickness fringes indicate a steep sample topography, at which the ridges correspond to the pseudo-GBs of the etching pattern, as shown in Figure 4-22. The inset depicts an atom-resolved HAADF-STEM image revealing a defect-free, single crystalline structure. Neither any kind of grain- or sub-grain boundary, nor a significant chemical difference is observed. b) and c) are EDS spectra recorded on and off the pseudo-GB, confirming the same chemistry for both sites. The different total intensities (counts) of the spectra are related to the unequal sample thickness. Peaks labeled with 1), 2) and 3) are sum peaks of $\text{ZnK}_{\alpha} + \text{OK}_{\alpha}$, $\text{ZnL}_{\alpha} + \text{ZnK}_{\beta}$ and $\text{ZnK}_{\alpha} + \text{ZnK}_{\beta}$, respectively. The Fe signals originate from the pole piece and the Au signals from the holder. Al, Si and P indicate a minor contamination during or before synthesis. 72

Figure 4-24: AFM image of the pseudo-polycrystalline etching pattern observed in the region of the sacrificial interlayer of sample EST-O|O after ion-milling. The height-sensor mode was used for image generation and revealed a notably uneven sample topography with trench-

and ridge-like features of large height differences in the region of microns. The ridges equal the pseudo-GBs of the etching pattern. 72

Figure 4-25: a) BF-TEM image of the meandering grain boundary in sample EST-O|O in $g = (0002)$ two-beam condition. A misalignment of about 1.9° tilt between the $[\bar{1}2\bar{1}0]$ zone-axes is measured by electron diffraction (SAED insets). b) Two-beam BF-imaging using a small objective aperture reveals periodic strain contrast along the curved interface. c) HR-TEM image in $[\bar{1}2\bar{1}0]$ zone-axis orientation shows an atomically well-bonded interface, without any indications for amorphous or crystalline interfacial films. d) and e) depict NBED measurements, which prove the O|O orientation. 73

Figure 4-26: FFT-filtered ABF-STEM image of the interface in sample EST-O|O in $[\bar{1}2\bar{1}0]$ zone-axis orientation. Due to bicrystal misalignment, only the upper side is in zone-axis orientation. No indications for any kind of amorphous or crystalline interfacial film are observed. The directions of the Zn-O dumbbells verify the tail-to-tail orientation (insets). 74

Figure 4-27: a) BF-STEM image of the curved grain boundary in sample EST-O|O. The 3D-meandering nature is depicted by the varying width of the interface. Due to its projection along the direction of view, a smaller or larger width represents a less or more inclined state. A dislocation network has formed throughout the curved interface, as indicated by the characteristic fish-scale-like contrast in the HAADF-STEM inset. b) BF-STEM image of a grain-boundary section being successively less inclined from left to right, almost reaching an edge-on orientation. 74

Figure 4-28: a) – f) Series of corresponding two-beam BF- and WBDF-TEM images of the meandering grain boundary in sample EST-O|O, using different g vectors to characterize the (presumed) dislocation network. Although the contrast is unusual for dislocation lines, the observed features are interpreted as two types of dislocations, which are either visible for $g = (000\bar{2})$ or $g = (\bar{1}\bar{1}20) / g = (10\bar{1}0)$, indicating Burger's vectors $b_1 = (0001)$ and $b_2 = 1/3(\bar{1}\bar{1}20)$. While no distinct dislocation-line direction u can be determined for the dislocations with b_2 , those with b_1 feature $u_1 = (\bar{1}\bar{1}20)$ and hence, are pure edge dislocations. 75

Figure 4-29: a) HAADF-STEM image of the meandering grain boundary in sample EST-O|O close to an edge-on orientation. As shown by the inset, the interface exhibits a significantly higher intensity compared to the bulk regions, hence indicating the presence of bismuth (Z^2 -contrast). The intensity difference between the upper (zone-axis orientation) and lower part (off-axis orientation) is an electron-channeling effect due to the misalignment of the bicrystal halves. b) FFT-filtered HAADF-STEM image in $[\bar{1}100]$ orientation featuring a rather irregular interface structure with several bright spots (atom columns) indicating the incorporation of bismuth (Z^2 -contrast). Corresponding EDS measurements verify its presence. While Bi (and a small Mn peak) were detected at the interface only, Co and Ni were found in the bulk as well, while Cr was not detected. 76

Figure 4-30: Load-dependent I-V characteristics of the two EST samples in a) tail-to-tail (O|O) and b) head-to-head (Zn|Zn) orientation. For the EST-O|O sample, increasing the mechanical load from 5 MPa to 250 MPa causes a successive decrease of $\alpha_{\max} = 12$ down to $\alpha_{\max} = 5.2$ and a simultaneous increase of the leakage current (measured at 0.1 V) from $5 \cdot 10^{-5}$ A up to $1 \cdot 10^{-3}$ A. The EST-Zn|Zn sample exhibits the reverse effect, though it is significantly less pronounced. The non-linearity coefficient increases from $\alpha_{\max} = 7.8$ up to $\alpha_{\max} = 9.0$, while the leakage current drops slightly from $9 \cdot 10^{-5}$ A to $6 \cdot 10^{-5}$ A. 77

Figure 4-31: Illustration of the different bismuth segregation behavior in samples EST-O|O vs. DB-I, depending on the respective synthesis method. a) A low-coherent meandering grain boundary with a Bi incorporating dislocation network is formed in the EST-O|O bicrystal.

b) In the DB-I bicrystal, Bi accumulates to nonwetting δ -Bi₂O₃ inclusions with highly coherent and Bi-free interface sections in between.²⁰⁰ 79

Figure 4-32: I-V characteristics of samples DB-I and DB-IV. Although DB-I featured a 3x higher doping, non-linear behavior could not be induced and both samples were found to be completely ohmic ($\alpha_{\max} \approx 1$)..... 83

Figure 4-33: The coherency of symmetrical tilt boundaries in ZnO bicrystals rotated around the [11 $\bar{2}$ 0] axis according to the CRLP theory. A misorientation angle of 0° corresponds to a parallel and 180° to an anti-parallel c-axis configuration. The latter equals the conditions implied in {0001} IBs. Reworked after “Fig.2” by Wunderlich (1998).²⁴⁹ 86

Figure 4-34: a) $g = (0002)$ two-beam BF-TEM image of the interface in sample DB-a|c with a $(000\bar{1})|(2\bar{1}\bar{1}0)$ interface, which corresponds to the c-axis of one side and the a-axis of the other being aligned perpendicular to the interface plane. The orientation is verified by SAED (insets), however, a small misalignment of 1.1° tilt from the ideal a|c configuration is measured. b) FFT-filtered HAADF-STEM image in $[\bar{1}2\bar{1}0]$ zone-axis orientation revealing an interface with step- and terrace-like sections, featuring semi-periodic decorations by bismuth atoms (Z^2 -contrast), as verified by corresponding EDS measurements. Whereas Bi was detected exclusively at the interface, Co was also found in the bulk. Other dopants were not detected. No indications for crystalline or amorphous interfacial films were observed..... 87

Figure 4-35: a) FFT-filtered HAADF-STEM image of the DB-a|c interface with the lower bicrystal half in $[\bar{1}2\bar{1}0]$ zone-axis orientation. Due to the misalignment, the upper side is in off-axis condition. Bi semi-periodically occupies every second atom column of the inner (0002) Zn-layer of the lower crystal (upper inset). Additional spots in between the atom columns indicate an overlapping with the $(2\bar{1}\bar{1}0)$ layer of the upper crystal. At interface steps, the periodicity is interrupted, exhibiting an apparently lower, irregular Bi segregation. The inset on the lower right depicts an ABF-STEM image verifying the “tail” c-axis direction of the lower crystal. b) FFT-filtered HAADF-STEM image of a different interface section with the upper bicrystal half in [0001] zone-axis orientation. Due to the misalignment, the lower side is in off-axis condition. Z^2 -contrast reveals the atom columns of the innermost $(2\bar{1}\bar{1}0)$ layer being occupied by Bi atoms. The inset on the lower right depicts a projection of the hexagonal unit cell in [0001] direction..... 88

Figure 4-36: Higher magnification of the interface sections featured in Figure 4-35 a) and b) overlaid with the ZnO atomic structure (Zn = blue, green O = red). a) The periodic Bi segregation sites (orange) correspond to coincidence lattice points (CSLP) of both bicrystal halves, which are oriented with perfectly matching {1 $\bar{1}$ 00} lattice planes. Unit cells are shown as green and blue boxes. b) A local displacement of about the 0.6 Å with respect to the {1 $\bar{1}$ 00} lattice planes is evident, impeding the formation of CSLPs. It is suggested that this leads to the observed interface with an increased width of 2.81 Å between the terminating (0002) and $(2\bar{1}\bar{1}0)$ layers, which in turn enables the Bi segregation on the Zn columns of the $(2\bar{1}\bar{1}0)$ side, by providing sufficient space and probably a higher coordination..... 89

Figure 4-37: BSE-SEM image of the interface in the Zn|Zn oriented doped tilt-bicrystal DB-26 sub-sequent to TEM-sample preparation and ion-milling. The interface is slightly curved with a few isolated Bi-rich and Cr/Ti-rich inclusions forming secondary phases. The crater-like structures are preparation artifacts of the ion-milling procedure. 90

Figure 4-38: a) BF-TEM image of the interface in bicrystal DB-26 in $g = (0002)$ two-beam condition. b) electron diffraction indicates a Zn|Zn orientation with 29.1° bicrystal-tilt (rotation around the a-axis) and 2.7° zone-axis tilt (misalignment). c) HR-TEM image in $[\bar{1}2\bar{1}0]$ zone-axis orientation showing an atomically well-bonded interface, without any

- indications for amorphous or crystalline interfacial films. d), e) NBED measurements revealing a tilted head-to-head orientation via the violation of Friedel's law..... 91
- Figure 4-39: a) HAADF-STEM image of sample DB-26. The comparably high image brightness of the interface region indicates the presence of bismuth (Z^2 -contrast). The lower bicrystal half is in zone-axis orientation, hence it appears brighter due to electron channeling. b) Higher magnified HAADF-STEM image revealing a Bi decorated and slightly disordered interface. EDS measurements (insets) verify the presence of Bi at the interface, while it is absent in the bulk. Regarding the other dopants, only a very small Ni signal was detected at the interface. 91
- Figure 4-40: a) and b) are HAADF-STEM images of the DB-26 bicrystal interface, with the upper and lower bicrystal side being in $[\bar{1}2\bar{1}0]$ zone-axis orientation, respectively. It is revealed that Bi occupies Zn-sites of (0002) lattice planes on both sides of the interface. However, a preference of Bi substituting Zn-sites of the lower, higher-tilted bicrystal half is observed. The Bi-containing interface structure is disordered and exhibits an approximately constant width of 0.7 nm. (0002) lattice planes are highlighted for a better depiction of the crystal tilt. 92
- Figure 4-41: ABF-STEM image of the interface in sample DB-26 verifying a tilted tail-to-tail (Zn|Zn) orientation by revealing the directions of the Zn-O dumbbells. 92
- Figure 4-42: a) $R(r)$ plot of CEP measurement series A with $R^2 > 0.95$ indicating the $x \approx 0$ criterion being fulfilled. b) The linear regression of an $R^{-1}(r^{-1})$ plot of the same measurement series confirms this by yielding a solid solubility limit of $x = 0.0006 \approx 0$. Therefore, the chemical width $d = \pi/(2 \cdot 11.468) = 0.1370$ nm is determined from the $R(r)$ plot. 93
- Figure 4-43: $R(r)$ plot of CEP measurement series B with $R^2 > 0.98$. The chemical width is $d = \pi/(2 \cdot 9.0314) = 0.1739$ 93
- Figure 4-44: I-V characteristics of the tilted DB samples with reduced coherency. Despite the observed Bi segregation in sample DB-a|c, the electrical behavior is almost perfectly linear with $\alpha_{\max} \approx 1$. Sample DB-26 shows a distinct non-linear behavior with $\alpha_{\max} \approx 3.0$, which is, however, a lower value than expected. The breakdown voltage of $V_B = 3.7$ V agrees with the situation of a single bicrystal grain-boundary..... 94
- Figure 4-45: Load-dependent I-V characteristics of sample DB-26. With increasing mechanical load, the coefficient of non-linearity increases from $\alpha_{\max} \approx 3.0$ at 5 MPa to $\alpha_{\max} \approx 3.9$ at 150 MPa, while $V_B = 3.7$ V remains constant. While this is in perfect agreement with a Zn|Zn-like oriented bicrystal, the leakage current (measured at 0.1 V) increases slightly from $7 \cdot 10^{-10}$ A to $1 \cdot 10^{-9}$ A, instead of being decreased as expected from the simultaneously increased barrier height..... 95
- Figure 5-1: a) BF-TEM image of hexagonal ZnO platelets after 15 min reaction time. As shown in by inset, SAED verifies a wurtzite crystal structure and a [0001] zone-axis orientation. The hexagonal facets correspond to crystallographic $\{10\bar{1}0\}$ planes. However, the hexagonal shape of most individuals is irregular and uneven. In addition, a significant amount of residual matrix is still present. b) HR-TEM image showing a distinctively pronounced surface roughness of the $\{10\bar{1}0\}$ facets. 98
- Figure 5-2: a) HR-TEM image of the matrix after 15 min reaction time, revealing a high density of ZnO nanocrystals (<10 nm) interspersed with amorphous material (indicated by irregular, blurry contrast). For illustration, some ZnO lattice planes are highlighted in the image. b) Corresponding SAED image showing Debye-Scherrer rings, confirming both the polycrystallinity of the matrix and the wurtzite crystal structure of the nanocrystals..... 99

Figure 5-3: a) BF-TEM overview image of hexagonal ZnO platelets after 45 min reaction time. The majority of platelets feature a well-pronounced hexagonal shape with a diameter of about 400 nm – 1 μm and a thickness of 80 – 140 nm. Only small amounts of residual matrix material are present. b) ZnO hexagon in [0001] zone-axis orientation with uniform contrast, indicating a high crystallinity with low to zero defects and pores, being typical for most individuals in this sample. In contrast, some platelets contain a rather high amount of defects and pores, despite their well-pronounced hexagonal shape, as shown in c). d) EDS point measurement corresponding to b), revealing a quasi-pure Zn-O composition. Co was not detected. The Cu signal originates from the supporting TEM grid. 99

Figure 5-4: a) BF-TEM image of a typical ZnO hexagon of the 45 min sample in [0001] zone-axis orientation. Attributed to matrix residuals, a distinct surface coverage of nearly all {10 $\bar{1}$ 0} facets is observed. b) HR-TEM image revealing these surface coverages consisting of amorphous material (blurry contrast) and nanocrystalline ZnO, as identified by wurtzite {10 $\bar{1}$ 0} lattice planes. Although well-pronounced {10 $\bar{1}$ 0} facets have formed, the hexagon's surface still features a certain roughness. The EDS point measurement indicates a Co-rich Zn-O composition of the surface coverage. The Cu signal originates from the supporting TEM grid. 100

Figure 5-5: BF-TEM image in [0001] zone-axis orientation of a typical ZnO hexagon after 45 min reaction time and a subsequent calcination at 300 °C in air. Some pores and probably defects are present in the bulk. No indication of any residual surface coverage is observed. b) HR-TEM image revealing a clean and almost atomically flat surface for the {10 $\bar{1}$ 0} facets. 101

Figure 5-6: STEM EDS-mapping a), c), d), e) and corresponding sum spectrum b) of a typical ZnO hexagon after 45 min reaction time and a subsequent calcination at 300 °C in air. The contrast inhomogeneities in a) are attributed to pores. A low amount of Co is detected, as shown by the inset in b). The Fe signal originates from the pole piece in the TEM. Despite small intensity variations related to the pores, the ZnO hexagon is chemically perfectly homogeneous. 101

Figure 5-7: a) and b) BF-TEM and [10 $\bar{1}$ 0] HR-TEM image of a cross-section of a hexagonal platelet after 45 min reaction time and subsequent to the 300 °C calcination. No indications for any kind of (sub)grain-boundary or twinning are observed. In addition, NBED verifies the same c-axis direction for both the upper and lower side, hence inversion twinning is ruled out and single crystallinity is confirmed. The blurry contrast in b) is attributed to a contamination by the epoxy resin used for embedding. 102

Figure 5-8: a) BF-TEM image of a hexagonal rod-shaped nanotwin. The tapering shape indicates the position of the twin boundary. NBED measurements verify a tail-to-tail c-axis inversion twinning and the rods being parallel to the c-axes in length. b) HR-TEM image in [10 $\bar{1}$ 0] zone-axis orientation revealing an atomically well-bonded twin boundary. No interfacial films or phases were observed. 103

Figure 5-9: a) HAADF-STEM image of a hexagonal rod-shaped nanotwin (inset) showing a slightly meandering twin boundary. The spot-like contrast variations are attributed to pores and residual epoxy resin. b) HAADF-STEM image of the twin boundary in [1 $\bar{2}$ 10] zone-axis orientation, revealing an atomically well-bonded but curved interface featuring distinctive lattice distortions. ABF-STEM verifies a tail-to-tail c-axis inversion twinning, as illustrated by the insets. 104

Figure 6-1: Graphical summary of the three structurally different types of Bi segregation site formation, as observed by TEM investigations of samples a) EST-O|O, b) DB-a|c and c) DB-26. 108

List of Tables

Table 1-1: Overview of basic directions and planes in wurtzite ZnO in both Miller and Bravais notation. As indicated by the corresponding lengths, lattice plane distances and color code, only Bravais notation allows direct identification of families of symmetry equivalent directions and planes by their shared set of $[uvtw] / (hkil)$ digits..... 5

Acknowledgment

First of all, I would like to thank my supervisor, Prof. Dr. Hans-Joachim Kleebe, for the possibility to complete my doctoral thesis within his working group. I am very grateful for his continuous support, motivation and guidance throughout the last decade, which were in all aspects, but especially at the personal level, far beyond anything a Ph.D. student could ever wish for.

Special thanks go to Prof. Dr. Jürgen Rödel, my second reviewer, who did not only support me regarding the ZnO project but also gave me the valuable opportunity to work with him and his staff on further highly interesting materials and research questions.

Likewise, I would like to thank Prof. Dr. Jörg J. Schneider and Dr. Rudolf C. Hoffmann for the possibility to contribute to their project on hexagonal ZnO platelets.

Together with Prof. Dr. Christoph Schüth, I would also like to thank Prof. Dr. Jörg J. Schneider for contributing as examiners in my defense.

Many thanks go to Peter Keil and Maximilian Gehringer for the synthesis and electrical characterization of the ZnO bicrystals.

For his training and guidance on the TEMs as well as for maintaining and troubleshooting the machines, I would like to give many special thanks to Dr. Stefan Lauterbach.

Last but not least, I would like to thank all members of the Geomaterial Science group for a decade of fun and fascinating research! I enjoyed it very much and will certainly miss it a lot.

This project (KL 615/27-1) was funded by the German Research Foundation (DFG).

Curriculum vitae

Education:

10/2016 – 03/2023	Geomaterial Science, Prof. Dr. Hans-Joachim Kleebe, Technical University Darmstadt: Ph.D. student
10/2012 – 02/2016	MSc Applied Geoscience, Technical University Darmstadt
04/2009 – 09/2012	BSc Geoscience, Goethe University Frankfurt
10/2008 – 03/2009	BSc Chemistry, Saarland University, Saarbrücken
08/1998 – 03/2007	Abitur, Gymnasium Kusel, Kusel

Work experience:

04/2023 – present	HORIBA Jobin Yvon GmbH, Oberursel: Application Specialist for Spectroscopy
08/2016 – 03/2023	Geomaterial Science, Prof. Dr. Hans-Joachim Kleebe, Technical University Darmstadt: Research associate
08/2013 – 07/2016	Geomaterial Science, Prof. Dr. Hans-Joachim Kleebe, Technical University Darmstadt: Student research assistant
09/2012	Umweltgeotechnik GmbH (UGG), Nonnweiler- Otzenhausen: Internship
05/2011 – 07/2011	Department of Geosciences, Goethe University Frankfurt:
08/2010 – 01/2011	Student research assistant
02/2010 – 04/2010	
07/2007 – 03/2008	Haus der Jugend, Kusel: Alternative civilian service

Honors and Awards:

11/2017	Harald Rose-Prize 2017; awarded for outstanding master's theses [...] related to electron microscopy. MSc Thesis: " <i>TEM investigation of CuMn₂O₄ spinel catalyst upon reduction and subsequent reoxidation</i> "
---------	---

Publications:

- M. Höfling, **M. Trapp**, L. Porz, H. Ursic, E. Bruder, H.-J. Kleebe, J. Rödel, and J. Koruza, "Large plastic deformability of bulk ferroelectric KNbO_3 single crystals," *J Eur Ceram Soc*, 41[7] 4098-107 (2021).
- A.-K. Fetzer, **M. Trapp**, S. Lauterbach, and H.-J. Kleebe, "Introduction to Transmission Electron Microscopy; The Basics," pp. 578-99. in *Encyclopedia of Materials: Technical Ceramics and Glasses*, Vol. 1. Edited by M. Pomeroy. Elsevier, Oxford, 2021.
- T. Necke, **M. Trapp**, S. Lauterbach, G. Amthauer, and H.-J. Kleebe, "Electron microscopy investigations on the mineral lorándite (TlAsS_2) from Allchar in Macedonia," *Zeitschrift Für Kristallographie-Crystalline Materials*, 236[3-4] 51-60 (2021).
- J. Peter, **M. Trapp**, S. Lauterbach, P. Golle-Leidreiter, U. Kolb, and H.-J. Kleebe, "Exomorphism of jacobsonite precipitates in bixbyite single crystals from the Thomas Range in Utah," *Am Mineral*, 106[7] 1163-71 (2021).
- R. C. Hoffmann, **M. Trapp**, E. Erdem, M. Kratzer, C. Teichert, H.-J. Kleebe, and J. J. Schneider, "Synthesis and Assembly of Zinc Oxide Microcrystals by a Low-Temperature Dissolution-Reprecipitation Process: Lessons Learned About Twin Formation in Heterogeneous Reactions," *Chem-Eur J*, 26[42] 9319-29 (2020).
- S. Heinz, E. C. Angel, **M. Trapp**, H.-J. Kleebe, and G. Jakob, "Phonon Bridge Effect in Superlattices of Thermoelectric $\text{TiNiSn}/\text{HfNiSn}$ With Controlled Interface Intermixing," *Nanomaterials-Basel*, 10[6] 1239 (2020).
- M. Trapp**, P. Keil, T. Frömling, J. Rödel, and H.-J. Kleebe, "Segregation and properties at curved vs straight $(000\bar{1})$ inversion boundaries in piezotronic ZnO bicrystals," *J Am Ceram Soc* 103[4] 2817-27 (2020).
- F. T. Xie, I. Gonzalo-Juan, H. Breitzke, C. Fasel, **M. Trapp**, G. Buntkowsky, H.-J. Kleebe, R. Riedel, A. R. Boccaccini, and E. Ionescu, "Effect of Ca and B incorporation into silicon oxycarbide on its microstructure and phase composition," *J Am Ceram Soc*, 102[12] 7645-55 (2019).
- P. Keil, **M. Trapp**, N. Novak, T. Frömling, H.-J. Kleebe, and J. Rödel, "Piezotronic Tuning of Potential Barriers in ZnO Bicrystals," *Adv Mater*, 30[10] 1705573 (2018).
- M. Trapp**, M. M. Müller, Z. Nazarpour, and H.-J. Kleebe, "Full reoxidation of CuMn_2O_4 spinel catalyst triggered by epitaxial Mn_3O_4 surface nanocrystals," *J Am Ceram Soc*, 100[11] 5327-34 (2017).

Workshops and conference contributions :

- M. Trapp** and H.-J. Kleebe, "Piezotronic ZnO bicrystals: A TEM study on interfacial segregation and properties of (0001) inversion boundaries," poster presentation, Microscopy Conference (MC) 2023, 26.02. – 02.03.2023, Darmstadt, Germany
- M. Trapp** and H.-J. Kleebe, "Interfaces in piezotronic ZnO bicrystals: A TEM study upon segregation and properties of (0001) inversion boundaries," oral presentation, Material Science and Engineering (MSE) 2020, 22. – 25.09.2020, Darmstadt, Germany
- H.-J. Kleebe and **M. Trapp**, "Structure and chemical composition of (0001) inversion boundaries in piezotronic ZnO bicrystals," oral presentation, 44th International Conference and Exposition on Advanced Ceramics and Composites (ICACC'20), 26. – 31.01.2020, Daytona Beach, Florida, USA
- H.-J. Kleebe and **M. Trapp**, "TEM investigation of piezotronic ZnO bicrystals," oral presentation, 16th Conference of the European Ceramic Society, 16. – 20.06.2019, Torino, Italy
- M. Trapp** and H.-J. Kleebe, " TEM characterization of basal plane inversion boundaries in ZnO bicrystals," poster presentation, International workshop on grain boundaries in semiconducting oxides – organized by A. Klein, TU Darmstadt, 08. – 12.04.2018, Edesheim, Germany
- M. Trapp**, M. M. Müller, and H.-J. Kleebe, "TEM investigation of CuMn₂O₄ spinel catalyst upon reduction & subsequent reoxidation," oral presentation, 25th Annual Meeting of the German Society for Crystallography – DGK, 27. – 30.03.2016, Karlsruhe, Germany